THE UNIVERSITY OF WARWICK

AUTHOR: **Michael Smidman** DEGREE: **Ph.D.**

TITLE: **Superconducting and magnetic properties of non-centrosymmetric systems**

DATE OF DEPOSIT: ....

I agree that this thesis shall be available in accordance with the regulations governing the University of Warwick theses.

I agree that the summary of this thesis may be submitted for publication.

I **agree** that the thesis may be photocopied (single copies for study purposes only).

Theses with no restriction on photocopying will also be made available to the British Library for microfilming. The British Library may supply copies to individuals or libraries. subject to a statement from them that the copy is supplied for non-publishing purposes. All copies supplied by the British Library will carry the following statement:

> "Attention is drawn to the fact that the copyright of this thesis rests with its author. This copy of the thesis has been supplied on the condition that anyone who consults it is understood to recognise that its copyright rests with its author and that no quotation from the thesis and no information derived from it may be published without the author's written consent."

AUTHOR'S SIGNATURE: ....

USER'S DECLARATION

1. I undertake not to quote or make use of any information from this thesis without making acknowledgement to the author.
2. I further undertake to allow no-one else to use this thesis while it is in my care.

DATE SIGNATURE ADDRESS

....

....

....

....

....

Superconducting and magnetic properties of non-centrosymmetric systems

by

Michael Smidman

Thesis

Submitted to the University of Warwick

for the degree of

Doctor of Philosophy

Physics

May 2014

THE UNIVERSITY OF
WARWICK

Contents

List of Tables

List of Figures

Acknowledgments

I would firstly like to thank my supervisors Geetha Balakrishnan and Don Paul for constant support, guidance and patience throughout the Ph.D. I would also like to thank Martin Lees, both for help with performing laboratory measurements and for being willing to answer questions on any subject, particularly the Physical Review Style and Notation Guide. I would like to thank Ravi Singh for help and advice with sample preparation. Thanks to Tom Orton for technical support as well considerable levels of patience and dexterity. Also thanks to Oleg Petrenko for help with the Laue system, Dean Keeble for help with TOPAS software, Steve York for performing EDAX measurements and Vivek Anand for allowing the use of his samples and for a very thorough reading of draft publications. I would also like to thank the other members of the superconductivity and magnetism group, particularly Robert Cook, Olga Young, Pabitra Biswas, Natalia Parzyk and Daniel Brunt, all of whom I shared an office with at various times.

Thanks to those people I worked with at central facilities. Special thanks to Devashibhai Adroja for involving me in his research of CeTX_3 compounds and for teaching me about a multitude of topics, from heavy fermion physics and neutron scattering to data analysis of diffraction data and crystal field levels. I would also like to thank Adrian Hillier for help and assistance on several μSR experiments, as well as carefully reading any draft publications. Thanks also to all the instrument scientists I have worked with, Eugene Goremychkin, Clemens Ritter, Marek Koza, Pascal Manuel, Laurent Chapon, Charles Dewhurst, Bachir Ouladdiaf and Sanghamitra Mukhopadhyay. Finally, I am very grateful to my parents and family for constant support and encouragement over the entire period of the Ph.D.

Declarations

This thesis is submitted to the University of Warwick in support of my application for the degree of Doctor of Philosophy. It has been composed by myself and has not been submitted in any previous application for any degree. The work presented (including data generated and data analysis) was carried out by the author except in the cases outlined below.

All of the polycrystalline samples were prepared by myself except for those of $CeCoGe_3$, and part of the $CePtSi_3$ and $LaPtSi_3$ samples used, which were prepared by Dr. Vivek Anand when at ISIS. The single crystals of $CeCoGe_3$ and $Nb_{0.18}Re_{0.82}$ were prepared by myself and Dr. Ravi Singh under the guidance of Professor Geetha Balakrishnan. EDAX measurements of $CeCoGe_3$ were performed by Steve York at the University of Warwick.

Physical properties measurements were performed by myself at the University of Warwick under the supervision of Dr. Martin Lees. Neutron scattering and muon spin relaxation/rotation measurements were performed at the Institut Laue Langevin, France or the ISIS facility, UK with the assistance of an instrument scientist. For all of the experiments I was the leading member of the experimental team, except for the measurements of $CeCoGe_3$ performed on the MuSR and MARI spectrometers, which were collected by Dr Devashibhai Adroja. The analysis of the crystal electric field model of $CeCoGe_3$ in chapter 4 was performed in collaboration with Dr Devashibhai Adroja. The remaining data from central facilities was analyzed by myself under the guidance of academic staff and instrument scientists, particularly Dr Devashibhai Adroja and Dr Adrian Hillier.

Parts of this thesis has formed the basis for the following publications.

- *'Investigations of the superconducting states of noncentrosymmetric LaPdSi$_3$ and LaPtSi$_3$'*, M. Smidman, A. D. Hillier, D. T. Adroja, M. R. Lees, V. K. Anand, R. P. Singh, R. I. Smith, D. M. Paul and G. Balakrishnan, Physical Review B, **89**, 094509 (2014).

- *'Neutron scattering and muon spin relaxation measurements of the noncentrosymmetric antiferromagnet CeCoGe$_3$'*, M. Smidman, D. T. Adroja, A. D. Hillier, L. C. Chapon, J. W. Taylor, V. K. Anand, R. P. Singh, M. R. Lees, E. A. Goremychkin, M. M. Koza, V. V. Krishnamurthy. D. M. Paul and G. Balakrishnan, Physical Review B, **88**, 134416 (2013).

- *'Crystal growth of the non-centrosymmetric superconductor Nb$_{0.18}$Re$_{0.82}$'*, R. P. Singh, M. Smidman, M. R. Lees, D. M. Paul and G. Balakrishnan, Journal of Crystal Growth, **361**, pp 129 – 131 (2012).

- *'Is CeCoSi$_3$ a superconductor?'*, M. Smidman, R. P. Singh, M. R. Lees, D. M. Paul, D. T. Adroja and G. Balakrishnan, Journal of Physics: Conference Series, **391**, 012068 (2012).

- *'Neutron scattering studies of non-centrosymmetric CeTX$_3$'*, M. Smidman, D. T. Adroja, M. R. Lees, V. K. Anand, R. P. Singh, E. A. Goremychkin, M. M. Koza, S. Mukhopadhyay, D. M. Paul and G. Balakrishnan, (under preparation).

Parts of this thesis has also been presented at the following meetings.

- *'Investigations of the noncentrosymmetric superconductors LaTSi$_3$'*, Frontiers in Unconventional Superconductivity and Magnetism, Bristol, UK, January 2014 – **Talk**.

- *'Neutron scattering and μSR investigations on noncentrosymmetric heavy fermions CeTX$_3$'*, Theoretical and Experimental Magnetism Meeting, Abingdon, UK, July 2013 – **Talk**.

- *'Muon spin rotation studies of the noncentrosymmetric superconductors* $LaPdSi_3$ *and* $LaPtSi_3$*'*, Strongly Correlated Electron Systems 2013, Tokyo, Japan, August 2013 – **Poster**.

- *'Neutron scattering studies of non-centrosymmetric heavy fermions* $CeTX_3$*'*, International Conference on Neutron Scattering 2013, Edinburgh, UK, July 2013 – **Poster**.

- *'Is* $CeCoSi_3$ *a superconductor?'*, Strongly Correlated Electron Systems 2011, Cambridge, UK, September 2011 – **Poster**.

Abstract

Non-centrosymmetric superconductors (NCS) and related compounds have been studied using magnetic, specific heat and transport measurements as well as by neutron scattering and muon spin relaxation/rotation (μSR). The crystal structures of NCS lack inversion symmetry and in the presence of a finite antisymmetric spin orbit coupling, the Cooper pairs are a mixture of spin-singlet and spin-triplet states. In particular, the cerium based NCS have been reported to display unconventional superconductivity.

Two different approaches for studying NCS are used. Firstly, the ground states of materials in the CeTX_3 (T = transition metal, X = Si or Ge) family have been studied. CeCoGe$_3$ is an antiferromagnet at ambient pressures and becomes superconducting at $p > 4.3$ GPa and was studied using inelastic neutron scattering (INS), muon spin relaxation/rotation (μSR), neutron diffraction and magnetic susceptibility measurements. The crystal electric fields (CEF) were studied using INS and magnetic susceptibility and the CEF scheme was evaluated. From this a ground state magnetic moment of 1.01 μ_B/Ce along the c axis was predicted. However, a magnetic moment of 0.405 μ_B/Ce along the c axis was observed in single crystal neutron diffraction measurements, indicating a reduced magnetic moment due to hybridization between the cerium f-electrons and the conduction band. The INS response was compared to the isostructural CePdSi$_3$, CePtSi$_3$ and CeRuSi$_3$. The former two order antiferromagnetically and the Kondo temperatures were evaluated from the quasielastic scattering. CeRuSi$_3$ is non-magnetic and there is a broad peak in the magnetic scattering at 59 meV.

Another approach is to study weakly correlated NCS to look for evidence of unconventional behaviour. In particular, systems where the spin-orbit coupling can be varied by the substitution of heavier atoms into non-centrosymmetric positions were considered. LaPdSi$_3$ and LaPtSi$_3$ are superconductors with $T_\mathrm{c} = 2.65$ and 1.52 K respectively and crystallize in the same crystal structure as the CeTX_3 compounds. Magnetization, specific heat and μSR measurements reveal that both compounds are weakly coupled, fully gapped s-wave superconductors but LaPdSi$_3$ is a type-I material while LaPtSi$_3$ is type-II with a Ginzburg-Landau parameter of 2.49. The superconducting properties of single crystals of Nb$_{0.18}$Re$_{0.82}$ have been investigated and are discussed.

Chapter 1

Introduction

Following the discovery of superconductivity by Kamerlingh Onnes in 1911 [1], it became to be understood that superconductivity arises from the condensation of pairs of electrons, bound by an attractive interaction. The discovery of the isotope effect [2, 3] gave considerable support to the idea that the electron phonon interaction was responsible for the formation of the superconducting condensate [4]. The microscopic theory of Bardeen, Cooper and Schrieffer (BCS) [5, 6] describes superconductivity arising from an attractive interaction between electrons in the vicinity of the Fermi level, mediated by the exchange of phonons. The electron pairs form in the spin singlet s-wave state and an isotropic energy gap opens in the single particle excitation spectrum. The variation in the superconducting transition temperature (T_{c}) of elements and alloys were often explained in terms of a set of empirical rules called the Matthias rules [7, 8]. One of the rules was that superconductivity does not occur in non-metallic systems, nor does it occur in ferromagnets, antiferromagnets or rare earth systems with unpaired electrons. In addition to this it was suggested that T_{c} primarily depended on the atomic mass, the atomic volume and the number of valence electrons (n). T_{c} was determined to increase monotonically with n for non-transitional metals and peak for $n = 3, 5$ and 7 for transition metals, with superconductivity only occurring for $2 \leq n \leq 8$. Interestingly, both Refs. [7] and [8] remark that superconductors where the crystal structure lacks inversion symmetry have not been found. However, soon after the publication of Ref [8], superconductivity was reported in several non-centrosymmetric compounds with α-Mn and hexagonal structures [9, 10], although this aspect of their crystal structure was not remarked upon. Although the crystal structure was otherwise considered of lesser importance in determining the superconducting properties, it was noted that cubic or hexagonal structures appeared to be preferable. Soon after the introduction of

BCS theory, it was recognized that the theory could qualitatively explain many of these rules [8]. Even within the framework of strong coupling BCS theory, the upper limit of T_c was believed to be around 30 K [11].

1.0.1 Unconventional superconductivity

The first unambiguous example of unconventional superconductivity was found in 1979 following the discovery of superconductivity in the heavy fermion compound $CeCu_2Si_2$ [12, 13, 14], although as pointed out in Ref. [14], superconducting signals had previously been reported in several uranium based compounds but were either not widely considered or believed to result from filaments of elemental uranium [15, 16]. $CeCu_2Si_2$ consists of a lattice of Ce^{3+} ions, each with an unpaired f electron and it was observed to be superconducting at around 0.5 K, whereas no superconductivity was observed in the non-magnetic, isostructural $LaCu_2Si_2$. As a result of the Kondo interaction, which arises from hybridization between the conduction band and f electrons (Sec. 2.1.4), the electronic co-efficient of the specific heat (γ) is enhanced in heavy fermion compounds and reaches around 1 J/mol K^2 in $CeCu_2Si_2$. The fact that the jump in the specific heat at the superconducting transition is enhanced by a similar factor is a strong indication that the Cooper pairs are formed from electrons within these 'heavy' hybridized bands, as was the suppression of superconductivity by a small concentration of non-magnetic impurities [13]. Also of interest was the proximity of the system to magnetic order. The observed properties are highly sample dependent, with some samples displaying antiferromagnetic order, some superconductivity and others displaying both properties [17]. Although this indicates the very close proximity between magnetism and superconductivity, μSR measurements show a lack of microscopic coexistence [18], suggesting that there is competition between the two phases.

A more ubiquitous picture of the relationship between heavy fermion superconductivity and magnetic order emerged from Ref. [19], where it was demonstrated that $CeIn_3$ and $CePd_2Si_2$ order antiferromagnetically at ambient pressure but become superconducting under applied pressure. In both cases, the magnetic ordering temperature is suppressed with pressure before superconductivity emerges as a dome in the temperature-pressure phase diagram, which itself terminates at sufficiently large pressures. This was taken to be evidence that the attractive interaction between superconducting electrons is mediated by magnetic interactions. Subsequently this behaviour has been observed in additional cerium based heavy fermion compounds and in recent years there has been considerable research interest in the role of quantum critical phenomena in determining the existence of a superconducting dome [20]. In fact, subsequent measurements indicate the presence of two superconducting domes in $CeCu_2Si_2$, with the dome at lower pressure being associated with the suppression of magnetic order [21].

An even more dramatic departure from the rules of Matthias and BCS theory was observed upon the discovery in 1986 of superconductivity in Ba doped La_2CuO_4 [22], with a T_c of around 30 K. Higher values of T_c were subsequently observed in related systems, with a maximum of 93 K in the $YBa_2Cu_3O_{7-x}$ system [23]. Several classes of cuprate superconductors have been discovered with a maximum T_c at ambient pressure of ∼133 K [24] and 164 K under applied pressure [25] in the Hg-Ba-Ca-Cu-O system. All cuprate superconductors crystallize in either tetragonal or orthorhombic structures with layers consisting of CuO_2 planes perpendicular to the c axis. The observation of strongly enhanced superconductivity in a doped oxide consisting of weakly coupled two dimensional layers contradicts the rules for conventional systems where isotropic, metallic materials were believed to be favoured. In fact a similar picture emerges from heavy-fermion superconductors, where T_c increases from a maximum of 0.2 K in the cubic $CeIn_3$ to 2.3 K in the quasi-two-dimensional $CeCoIn_5$ [26]. Further similarities between heavy fermion and cuprate superconductors are observed in the phase diagrams. The undoped cuprates order antiferromagnetically, which is suppressed upon doping and a superconducting dome is observed in this region. In the superconducting state, the Cooper pairs are believed to have *d*-wave symmetry [27] and evidence for nodes in the gap functions has been observed. This is again in contrast to weakly coupled BCS theory, where the highly symmetric *s*-wave state is energetically favourable.

The properties of a second class of high temperature superconductors have been the subject of intensive study in recent years after the discovery of superconductivity at $T_c = 26$ K in the iron arsenide compound $LaO_{1-x}F_xFeAs$ [28]. Several further pnictide superconductors have been discovered with higher transition temperatures. These all have crystal structures consisting of different arrangements of FeAs layers. In several pnictide compounds, superconductivity emerges from altering the carrier concentration by the doping of the parent compound, which orders antiferromagnetically [14, 29]. The magnetic transition is accompanied by a structural transition from a tetragonal to an orthorhombic structure. Once again magnetic order is suppressed with increased doping before a superconducting dome emerges, coinciding with the disappearance of the structural transition. Despite the layered nature of the crystal structure, the materials have more of a three dimensional electronic structure than the cuprates and more isotropic superconducting properties [30, 31]. The Cooper pairs are believed to condense in the extended *s*-wave state

[32] which is nodeless, unlike the *d*-wave pairing of the cuprates.

There are therefore striking similarities and differences between superconductivity in heavy fermion, cuprate and pnictide systems. The superconducting phase diagrams for these systems frequently display a superconducting dome close to the region where magnetic order is suppressed, although magnetic ordering is not observed in the parent compounds of all pnictide superconductors. The superconductivity in these compounds is believed to be mediated by magnetic interactions rather than the electron-phonon coupling of conventional BCS theory, although there is currently not a widely accepted theory which accounts for the superconducting behaviour.

All the systems discussed up to this point are centrosymmetric, that is the crystal structure has a centre of inversion. The result of inversion symmetry is that the Cooper pairs have a definite parity and therefore can be classified as either spin singlet or spin triplet. This is not necessarily the case for non-centrosymmetric superconductors and in the presence of a finite antisymmetric spin-orbit coupling (ASOC), parity is no longer a good quantum number and therefore the superconducting states may no longer be classified as spin singlet or triplet but an admixture of the two [33].

In the next section, non-centrosymmetric cerium based heavy fermion superconductors are firstly discussed. It was the novel superconducting properties of these systems that triggered the intensive experimental and theoretical study of non-centrosymmetric superconductors. For example, the theory of mixed parity pairing in non-centrosymmetric systems was outlined in Ref. [33] in 2001. As of April 2014 there have been 303 citations of this work, with only nine of these occurring prior to the discovery of heavy fermion superconductivity in non-centrosymmetric $CePt_3Si$ [34, 35]. In addition, the superconducting properties of weakly correlated systems are discussed. These studies were motivated by both the experimental and theoretical difficulties associated with understanding the behaviour of the non-centrosymmetric heavy fermion systems. The aim is to isolate the effects of inversion symmetry on the superconducting properties, without also needing to account for strongly correlated behaviour.

1.1 Non-centrosymmetric superconductors

1.1.1 Heavy fermion non-centrosymmetric superconductors

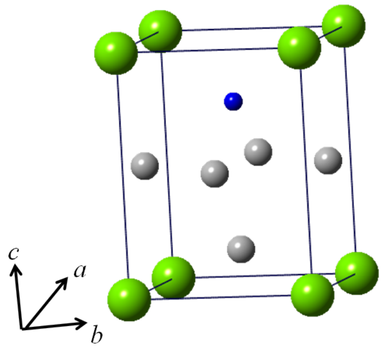

Figure 1.1: Crystal structure of $\mathrm{CePt_3Si}$ with cerium atoms in green, platinum in grey and silicon in blue.

$\mathrm{CePt_3Si}$ was the first non-centrosymmetric, heavy fermion superconductor to be reported and the only one unambiguously shown to display superconductivity at ambient pressure [34, 35, 36]. $\mathrm{CePt_3Si}$ crystallizes in a primitive, non-centrosymmetric tetragonal structure (space group $P4mm$), which is displayed in Fig. 1.1. The lack of a mirror plane perpendicular to the c axis removes inversion symmetry and results in a potential gradient along c. The system magnetically orders at $T_{\mathrm{N}} = 2.2$ K and undergoes a superconducting transition at $T_{\mathrm{c}} = 0.75$ K. The cerium atoms order with a propagation vector of $\mathbf{k} = (0, 0, \frac{1}{2})$, with the magnetic moments pointing along [100] [37]. The expected magnetic moment from the crystal electric field scheme is $\sim 0.5\ \mu_{\mathrm{B}}$ [38], but a moment of only $0.16\ \mu_{\mathrm{B}}$ is observed in neutron diffraction measurements. Such a reduction in the ordered moment is evidence for the strength of the Kondo interaction, as is the large value of $\gamma = 390$ mJ/mol K^2. Unlike $\mathrm{CeCu_2Si_2}$, μSR measurements reveal that all muons are implanted in magnetic regions, indicating microscopic coexistence of the superconducting and magnetic states [39].

Apart from the coexistence with magnetic order, a number of unusual properties of the superconducting state were identified. Thermal conductivity, specific heat and penetration depth measurements all indicate the presence of line nodes in the superconducting gap [40, 41, 42]. From nuclear magnetic resonance (NMR) measurements, the spin susceptibility (χ_s) remains constant across the superconducting transition for all orientations [43] and the upper critical field is nearly isotropic at around 5 T, in excess of the Pauli paramagnetic limiting field of 1.4 T. For a spin

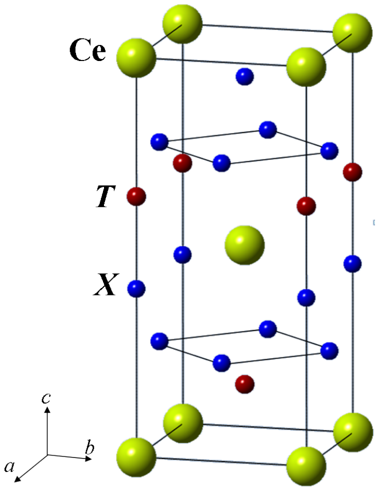

Figure 1.2: Crystal structure of CeTX_3, where T = transition metal and X = Si or Ge.

singlet superconductor, χ_s is expected to decrease to zero below T_c. For a triplet superconductor, it is expected to remain constant for one orientation only [36]. The possibility of spin triplet superconductivity was of particular interest since it had previously been noted that inversion symmetry was necessary for spin-triplet superconductivity [44], although there is one direction in a crystal structure along which triplet states with a parallel $\mathbf{d}(\mathbf{k})$ are protected [45]. The protected triplet state has point rather than line nodes but the latter may arise from the mixing of spin singlet and triplet states, for a sufficiently strong triplet component [46].

Pressure induced superconductivity is also observed in CeRhSi$_3$ ($p > 1.2$ GPa) [47], CeIrSi$_3$ ($p > 1.8$ GPa) [48], CeCoGe$_3$ ($p > 4.3$ GPa) [49] and CeIrGe$_3$ ($p > 20$ GPa) [50]. These crystallize in a body-centred, non-centrosymmetric tetragonal BaNiSn$_3$ type structure (space group $I4mm$), as displayed in Fig. 1.2. Like the crystal structure of CePt$_3$Si, inversion symmetry is broken due to the loss of mirror symmetry along the c axis.

At ambient pressure, CeRhSi$_3$ orders antiferromagnetically at $T_N = 1.6$ K [52, 51]. Neutron diffraction measurements reveal that the ordered moments are orientated in the ab plane in a spin density wave type structure with an incommensurate propagation vector $\mathbf{k} = (0.215, 0, \frac{1}{2})$ [53]. Since de Haas-van Alphen measurements indicate that the Ce $4f$ electrons are itinerant even at ambient pressure [54, 55], this was ascribed to a spin density wave type structure rather than local moment magnetism. Further evidence for the strength of the Kondo interaction arises from

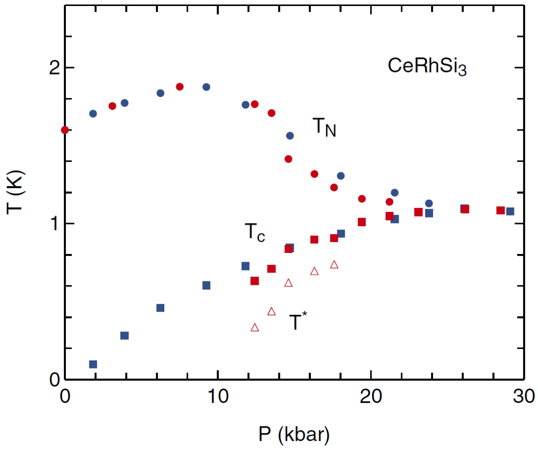

Figure 1.3: Temperature - pressure phase diagram of CeRhSi$_3$ from resistivity measurements. The ordering temperature (T_N), superconducting transition temperature (T_c) are displayed. T^* denotes the position at which a kink in the resistivity is observed below T_c. From Ref. [51].

the enhanced value of $\gamma = 110$ mJ/mol K^4 and the small ordered moment of ~0.1 μ_B/Ce compared to 0.92 μ_B/Ce from the CEF scheme [56].

The temperature-pressure phase diagram of CeRhSi$_3$ is shown in Fig. 1.3. T_N initially increases with pressure until about 1 GPa when it starts to decrease, before merging with the superconducting dome. Superconductivity is observed for pressures above 1.2 GPa. The blue points in Fig. 1.3 show the superconducting dome extending down to ambient pressures. These points correspond to measurements of the resistivity with currents along the c axis and a broad superconducting transition is observed at lower pressures [51]. μSR measurements under pressure reveal the suppression of both the ordered moment and T_N to zero temperature at a quantum critical point for $p = 2.36$ GPa [57].

Similar behaviour is observed in CeIrSi$_3$, which both has a higher ordering temperature of $T_\mathrm{N} = 5$ K [52] and becomes superconducting at higher pressures. The temperature-pressure phase diagram is shown in Fig. 1.4. A maximum T_c of 1.6 K is observed at 2.5 GPa, which is near to where T_N and T_c coincide. Much like CeRhSi$_3$, the cerium 4f electrons in CeIrSi$_3$ display itinerant behaviour [58] and an incommensurate spin density wave structure is observed with $\mathbf{k} = (0.265, 0, 0.43)$ [59].

An interesting contrast to the behaviour of these two compounds is observed in CeCoGe$_3$, which orders at a much higher temperature of $T_\mathrm{N1} = 21$ K [60] and

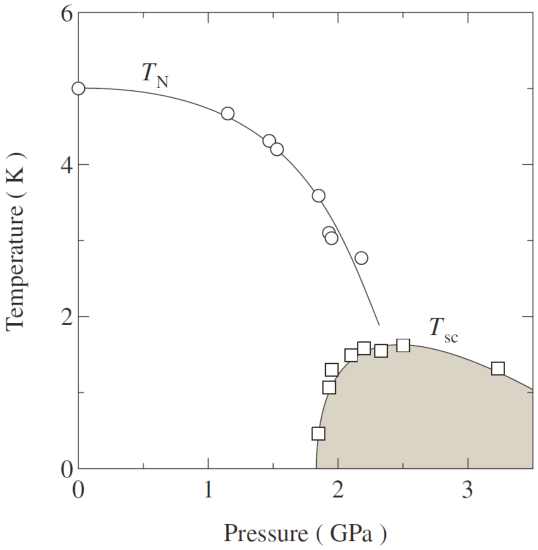

Figure 1.4: Temperature - pressure phase diagram of $CeIrSi_3$. From Ref. [48].

becomes superconducting at a higher pressure again of 4.3 GPa [49]. A more detailed discussion of the properties of this compound is given in Sec. 4.1. However it is interesting that there is no evidence for the itinerancy of the $4f$ electron, since the same branches are observed in both $CeCoGe_3$ and non-magnetic $LaCoGe_3$ [61, 62]. Furthermore, the magnetically ordered state consists of magnetic moments ordered along the c axis and the magnetization as a function of a field along [001] shows three step-like metamagnetic transitions [60]. These are readily interpreted as transitions between magnetic phases resulting from the flipping of localized Ce spins. It is not known if local moment magnetism is present at pressures close to the region of the superconducting dome.

The ground state properties of several other isostructural $CeTX_3$ compounds have also been reported. Several other compounds including $CeRhGe_3$ ($T_N = 14.6$ K) [52], $CeIrGe_3$ ($T_N = 8.7$ K) [52], $CePtSi_3$ ($T_N = 4.8$ K) [64] and $CePdSi_3$ ($T_N = 5.2$ K) [65] order antiferromagnetically at ambient pressure. Of these $CeIrGe_3$ becomes superconducting for $p > 20$ GPa [50], while $CeRhGe_3$ and $CePtSi_3$ do not become superconducting up to at least 8.0 GPa [63, 66]. Other compounds such as $CeRuSi_3$, $CeOsSi_3$ and $CeCoSi_3$ do not order magnetically and are believed to be intermediate valence compounds [63]. The range of behaviours in the series are often explained in terms of the Doniach phase diagram [67]. There is competition between the intersite Ruderman-Kittel-Kasuya-Yosida (RKKY) interaction, which leads to magnetic

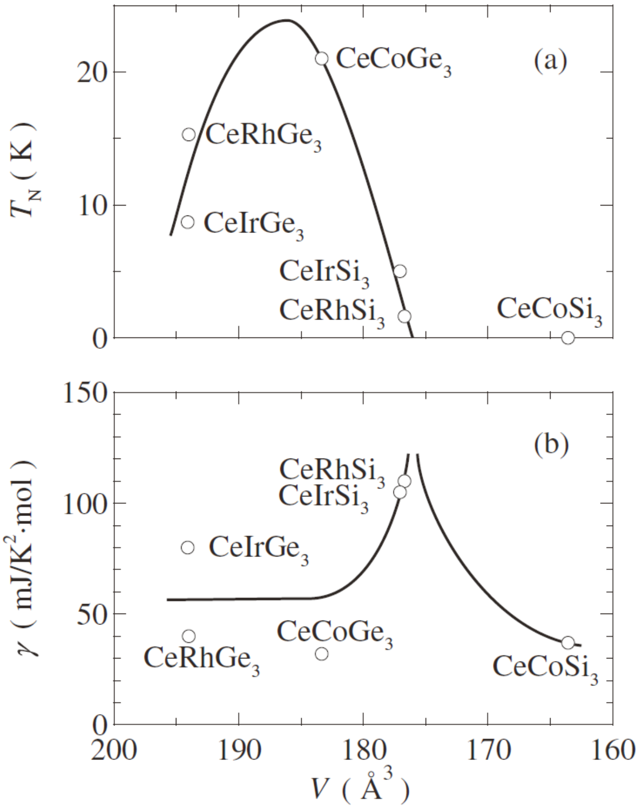

Figure 1.5: The dependence of (a) T_{N} and (b) γ, as a function of unit cell volume for selected CeTX_3. From Ref. [63].

order and the onsite Kondo interaction, which favours a non-magnetic ground state. In this case, altering the composition either expands or contracts the unit cell which either strengthens or weakens the coupling between the $4f$ and conduction electrons. This is shown in Fig. 1.5, where the ordering temperature and γ have been plotted as a function of unit cell volume. Going from left to right, the volume decreases corresponding to an increase in chemical pressure. The solid lines illustrate the expected behaviour of the Doniach phase diagram. Increasing the coupling initially enhances the RKKY interaction and therefore T_{N}. However, with increased pressure the Kondo interaction dominates and T_{N} is suppressed to zero at a quantum critical point (QCP). It is also around this region where there is a greater enhancement of γ. It can be seen that these diagrams appear to encapsulate the relative behaviour of several members of the series including the pressure induced superconductors. However, this simplified picture does not readily explain the behaviour of all compounds. For example, CeFeGe$_3$ does not order magnetically and has a relatively large value of $\gamma = 150$ mJ/mol K^2, yet with a unit cell volume of 186.6 Å^3 it would be expected to be in the magnetically ordered regime. The unit cell volumes of CeRuSi$_3$ and CePtSi$_3$ are 175.7 and 175.5 Å^3 respectively, despite the latter being deep in the ordered regime and the latter being non-magnetic and probably an intermediate valence compound.

The most notable feature of the superconducting states of these compounds are the large, anisotropic upper critical fields. For example, the upper critical field of CeRhSi$_3$ reaches ∼7 T for fields in the *ab* plane but is significantly larger along the *c* axis, possibly reaching up to 30 T for $p = 2.9$ GPa [68]. Similarly in CeIrSi$_3$, a zero temperature value of 9.5 T is obtained perpendicular to *c*, while it exceeds 30 T along *c* at 2.65 GPa [69]. Much like CePt$_3$Si, the BCS Pauli limiting field is greatly exceeded in all directions but in this case there is a much greater anisotropy. The B_{c2} curve also turns up at low temperatures for fields along *c*, while the curve for fields perpendicular to this resembles conventional behaviour. This suggests that paramagnetic limiting is absent for fields along the *c* axis and greatly reduced for perpendicular fields. In the absence of paramagnetic limiting, B_{c2} is determined solely by the orbital limiting value, which may be greatly enhanced in the region of a QCP [70, 71]. This behaviour is consistent with the calculated spin susceptibility for the permitted triplet state of the non-centrosymmetric crystal structure [72], whereas the consistency of the spin susceptibility of CePt$_3$Si in all directions remains more difficult to account for.

While initially it was only the heavy fermion non-centrosymmetric superconductors which were the subject of intense study, in recent years the properties of weakly correlated non-centrosymmetric superconductors have been increasingly examined. Several reasons can be identified for this. Firstly, the number of known heavy fermion non-centrosymmetric superconductors is small, with only CePt$_3$Si, CeTX_3 and UIr [73] being reported. Of these, only CePt$_3$Si becomes superconducting at ambient pressures and the ability to characterize the superconducting states under pressure is much more limited. Even in the case of CePt$_3$Si, the low T_c, sample dependence [74] and coexistent magnetic order further restrict measurements of the superconducting properties. There are also difficulties in separating the effects of unconventional pairing states and other phenomena such as coexistent magnetic order and strong electronic correlations. For example in the case of CePt$_3$Si, the presence of line nodes and a constant spin susceptibility are often taken as evidence of mixed singlet and triplet pairing. However, the line nodes have also been explained as resulting from coupling with magnetic order [75] and strong electronic correlations may also enhance the spin susceptibility to the normal state value in all directions [76]. Therefore it may be the case that in weakly correlated systems, the effects of a lack of inversion symmetry on the pairing symmetries can be more readily isolated.

1.1.2 Weakly correlated non-centrosymmetric superconductors

In this section, the properties of weakly correlated non-centrosymmetric superconductors are discussed. The aim is to look for evidence of mixed pairing states resulting from the loss of inversion symmetry. It will be of particular interest to examine systems where the ASOC can be varied by the substitution of heavy atoms on non-centrosymmetric positions [77].

Perhaps the canonical example of such compounds are Li_2Pd_3B ($T_c = 7$ K) and Li_2Pt_3B ($T_c = 2.7$ K) [78, 79, 36]. These both crystallize in a cubic non-centrosymmetric perovskite type structure and γ values of 9 and 7 mJ/mol K^2 respectively [80] indicate a lack of strong electronic correlations. Specific heat [81], magnetic penetration depth [82] and NMR [83] measurements are consistent with fully gapped s-wave superconductivity in Li_2Pd_3B. Upon the substitution of the heavier Pt for Pd, there is an increase in the ASOC. At low temperatures, there is a quadratic dependence of the electronic specific heat and a linear dependence of the penetration depth, indicating the presence of line nodes. NMR measurements indicate no change in χ_s at T_c, suggesting spin-triplet superconductivity. In Ref. [82] the magnetic penetration depth of both compounds is modelled with a superconducting gap consisting of an admixture of an isotropic singlet state and a triplet state compatible with the spin-orbit coupling of the crystal structure. One of the gaps of the resulting two gap structure has line nodes for a sufficiently large triplet component. The model contains a parameter ν, which is the ratio of the magnitude of the singlet and triplet components. Values of $\nu = 4$ for Li_2Pd_3B and $\nu = 0.6$ for Li_2Pt_3B were obtained, indicating that upon increasing the ASOC the triplet component of the pairing increases, leading to line nodes in one of the superconducting gaps. It has also been suggested that Li_2Pt_3B is dominated by a singlet $s_\pm$ state which arises from nesting of the Fermi surface [84]. In this case, the difference between the two compounds arises from changes in the Fermi surface from the additional contribution of platinum $5d$ bands. It should be noted that neither of these models predict χ_s to remain unchanged for a polycrystalline sample at T_c and this result is yet to be accounted for.

Unconventional superconductivity has also been reported in the orthorhombic compound $LaNiC_2$ ($T_c = 2.7$ K) [85]. Magnetic penetration depth measurements indicate both the presence of point nodes [86] and a fully gapped, two gap structure [87]. Ref. [86] ascribes the discrepancy as arising from the effect of magnetic impurities. The most dramatic experimental result is the observation of spontaneous fluctuating magnetic fields below T_c, from muon spin relaxation measurements [88]. This indicates that time reversal symmetry is broken in the superconducting state. Time reversal symmetry is only broken by a subset of spin-triplet states which are known as non-unitary and the Cooper pairs are spin polarized [89]. A symmetry analysis reveals that while there are three non-unitary states compatible with the crystal structure, none of these are allowed in the presence of a sizeable ASOC [90]. This suggests that the ASOC in $LaNiC_2$ is negligible and that the unconventional pairing state arises despite the non-centrosymmetric crystal structure, rather than as a consequence of it. This is further supported by the observation of time reversal symmetry breaking in the related but centrosymmetric superconductor $LaNiGa_2$ [91].

Time reversal symmetry breaking was also reported for non-centrosymmetric Re_6Zr [92] with the α-Mn structure. Unlike $LaNiC_2$, the crystal structure contains a large number of heavy atoms in non-centrosymmetric positions and therefore a negligible ASOC is unlikely. However, in this instance the non-unitary state is saved in the presence of ASOC, as a result of the higher symmetry of the cubic α-Mn structure and a state with the mixing of singlet and triplet states was identified.

An admixture of singlet and triplet states will not necessarily lead to nodal structures, in which case a two-band, fully gapped structure would be anticipated. These gaps would be expected to be anisotropic, particularly on the Δ_- surface (Eq. 2.47). An example of a system where such a structure has been deduced is BiPd ($T_c = 3.8$ K) [93], which is weakly correlated with $\gamma = 4$ mJ/mol K^2. Two gap superconductivity is revealed by both point contact Andreev reflection [94] and penetration depth measurements [95] of single crystals. Single crystals are necessary for the former and with the latter different field directions can be measured, allowing greater information of the gap anisotropy to be obtained. The penetration depth data can be fitted with one isotropic and one anisotropic gap and this is consistent with an ASOC which is estimated to be smaller than $CePt_3Si$ and Li_2Pt_3B.

Several non-centrosymmetric superconductors have also been reported with properties consistent with BCS s-wave superconductivity. These include T_2Ga_9 ($T =$ Rh, Ir) [96, 97], Re_3W [98], $Re_{24}Ti_5$ [99] and $LaPt_3Si$ [42]. There has been a particular focus on compounds of the form RTX_3 ($R =$ Sr, Ba, La, Ca; $T =$ transition metal; $X =$ Si,Ge), which crystallize in the $BaNiSn_3$ structure, the same as the pressure induced heavy fermion superconductors discussed in Sec. 1.1.1. It will therefore be of interest to determine whether similar unconventional behaviour is observed in isostructural, weakly correlated materials. $SrPdGe_3$ ($T_c = 1.49$ K), $SrPtGe_3$ ($T_c = 1$ K) [100], $BaPtSi_3$ ($T_c = 2.25$ K) [101], $CaPtSi_3$ ($T_c = 2.3$ K), $CaIrSi_3$ ($T_c = 3.6$ K) [102] and $LaIrSi_3$ ($T_c = 0.9$ K) [69] all contain $5d$ transition metals and are type-II superconductors. The specific heats of $BaPtSi_3$, $CaPtSi_3$ and $CaIrSi_3$ are all consistent with an isotropic superconducting gap of the magnitude predicted by BCS theory. A relatively low upper critical field of 64 mT was reported for $BaPtSi_3$ with a Ginzburg Landau parameter (κ) of 2.6, while larger values of were reported for $CaIrSi_3$ and $CaPtSi_3$ respectively. One possible reason for this difference is that for the latter two compounds, the upper critical field was measured using the onset of T_c, while the $BaPtSi_3$ values were bulk values from muon spin rotation measurements. In fact, upper critical field values obtained from resistivity measurements are significantly larger in all three materials and there is a positive curvature at low temperatures, possibly as a result of the significant broadening of the in-field transition. Single crystals of $LaIrSi_3$ have been grown and there is only a small anisotropy in the upper critical field, in contrast to the massively anisotropic values in the cerium based compounds. Different behaviour is observed in $LaRhSi_3$, which is a dirty type-I superconductor, as revealed through muon spin rotation, specific heat and magnetization measurements [103]. The specific heat data are also compatible with weakly coupled BCS superconductivity and the estimated value of κ puts the material in the type-I regime.

Electronic structure calculations of $BaPtSi_3$ [36, 101] reveal that the main contributions to the density of states at the Fermi level are from Si-$3p$ and Pt-$5d$ states. The presence of $5d$ states might indicate that the bands will be significantly affected by spin-orbit coupling. However, while relativistic calculations show that there is significant spin-orbit splitting of the bands at around -1.5 eV, there is only weak splitting of the bands at the Fermi level. Since it is electrons in the region of the latter which condense to form Cooper pairs, it is unlikely the spin-orbit coupling plays a significant role in determining the superconducting properties of $BaPtSi_3$.

These results give some indication of the range of properties observed in weakly correlated non-centrosymmetric superconductors. These range from systems where the strong spin-orbit coupling leads to unusual nodal gap structures, to those where fully gapped, two-band behaviour is observed and those which are consistent with single band BCS superconductivity. While a two gap structure is expected to be a generic feature of non-centrosymmetric superconductors, for weak spin-orbit coupling both gaps may be nearly isotropic and very similar in magnitude. The example of $LaNiC_2$ is also important, since despite displaying highly unconventional behaviour, this does not appear to arise as a result of strong ASOC and theoretical calculations indicate the non-unitary state is only permitted when it is weak. This shows that while studying weakly correlated non-centrosymmetric superconductors has allowed progress to be made in disentangling the effects of strong electronic correlations and inversion symmetry breaking, unconventional properties can not necessarily be ascribed to the latter.

Table 1.1: Normal state and superconducting properties of selected non-centrosymmetric superconductors. The values are given for ambient pressure unless otherwise stated. A more in depth review of non-centrosymmetric superconductivity is given in Ref. [36].

Compound	Space group	T_c (K)	γ (mJ/ mol K^2)	Superconducting state	Reference
$CePt_3Si$	$I4mm$	0.75	390	Line nodes, isotropic $H_{c2} > H_P$.	[35, 40, 41, 42]
$CeRhSi_3$ ($p > 1.2$ GPa)	$I4mm$	1.05 ($p = 3$ GPa)	110	Anisotropic $H_{c2} > H_P$.	[47, 68]
$CeIrSi_3$ ($p > 1.8$ GPa)	$I4mm$	1.6 ($p = 2.5$ GPa)	100	Anisotropic $H_{c2} > H_P$.	[48, 69]
$CeCoGe_3$ ($p > 4.3$ GPa)	$I4mm$	0.64 ($p = 7.1$ GPa)	32	Anisotropic $H_{c2} > H_P$.	[49, 104]
Li_2Pd_3B	$P4_332$	7	9	Anisotropic, fully gapped.	[79, 82]
Li_2Pt_3B	$P4_332$	2.7	7	Anisotropic, line nodes.	[79, 82]
Y_2C_3	$I\bar{4}3d$	11.5 - 18	6.3	Two gaps/nodes.	[105, 106, 107]
$LaNiC_2$	$Amm2$	2.7	7.7	TRS Breaking. Two gaps/point nodes.	[85, 86, 87, 88]
BiPd	$P2_1$	3.8	4	Two gaps.	[93, 94, 95]
Re_6Zr	$I\bar{4}3m$	6.75	26	TRS Breaking, fully gapped.	[92]
Re_3W	$I\bar{4}3m$	7.8	15.9	One gap.	[108]
$BaPtSi_3$	$I4mm$	2.25	5.7	One gap.	[101]
$CaPtSi_3$	$I4mm$	2.3	4	One gap.	[102]
$CaIrSi_3$	$I4mm$	3.6	5.8	One gap.	[102]
Rh_2Ga_9	Pc	1.95	7.64	One gap.	[96, 97]
Ir_2Ga_9	Pc	2.25	7.32	One gap.	[96, 97]

Therefore, two different approaches for understanding the behaviour of non-centrosymmetric superconductors are outlined in sections 1.1.1 and 1.1.2. That is the properties of the CeTX_3 compounds can be studied directly, or weakly correlated non-centrosymmetric superconductors can be examined. Examples of both approaches are given in this thesis, which is structured as follows. Chapter 2 contains a theoretical background, mainly detailing selected topics in superconductivity, magnetism and neutron scattering. Details of experimental techniques are given in chapter 3. The following four chapters contain the experimental results of this work. Chapters 4 and 5 are concerned with the ground state properties of CeTX_3 at ambient pressure. Chapter 4 details neutron scattering, muon spin relaxation and magnetic susceptibility measurements of the antiferromagnetic, pressure-induced superconductor $\mathrm{CeCoGe_3}$. Chapter 5 contains neutron scattering measurements of the antiferrogmagnets $\mathrm{CePdSi_3}$ and $\mathrm{CePtSi_3}$, as well as $\mathrm{CeRuSi_3}$, which does not display magnetic order. Chapters 6 and 7 are concerned with the properties of weakly correlated non-centrosymmetric superconductors. Results of investigations into the superconducting properties of $\mathrm{LaPdSi_3}$ and $\mathrm{LaPtSi_3}$ are given in chapter 6, whereas chapter 7 is concerned with the superconducting properties of a single crystal of $\mathrm{Nb_{0.18}Re_{0.82}}$.

Chapter 2

Theoretical background

2.1 Magnetic properties of f electron systems

2.1.1 Isolated ion properties

This section gives an overview of some of the magnetic properties of f electron systems, that is compounds containing elements with partially filled f-electron shells. The solution of the non-relativistic, time independent Schrödinger equation for a hydrogen atom gives a set of wave functions ψ_{nlm} where n, l and m are the principal, orbital and magnetic quantum numbers. Along with the spin quantum number, these can uniquely describe the state of an electron in the system. For atoms other than hydrogen, there is an additional term in the Hamiltonian due to the Coulomb interaction between electrons. Calculations of the radial wave functions for lanthanide elements show a peak for the $4f$ states at low radii, below that of the $5s$, $5d$ and $6s$ orbitals. Moving across the period, the increasing nuclear charge is poorly screened by the f electrons and the orbitals become increasing contracted and localized. However, the $4f$ wave function of cerium has a long tail which reaches into the outer shells.

Atomic states may be described by the total angular momentum $\mathbf{J}$ which is the sum of the orbital angular momentum $\mathbf{L}$ and spin angular momentum $\mathbf{S}$

$$\mathbf{J} = \mathbf{L} + \mathbf{S}, \tag{2.1}$$

which takes values between $|L\ +\ S|$ and $|L\ -\ S|$ [109]. The subsequent magnetic moments are given by

$$\mu = g_J \mu_{\mathrm{B}} \sqrt{J(J\ +\ 1)}, \tag{2.2}$$

where g_J is the Landé g-factor given by

$$g_J = \frac{3}{2} + \frac{S(S\ +\ 1) - L(L\ +\ 1)}{2J(J\ +\ 1)}. \tag{2.3}$$

Since J can take a range of values, determining the moment requires knowledge of which is the ground state. This requires considering the configuration of unfilled shells, since $J\ = 0$ for a filled one. This can be estimated from Hund's rules which are

1. Select the largest value of S for the electronic configuration.
2. Select the largest value of L for the electronic configuration.
3. $J\ =\ |\mathrm{L}\ -\ \mathrm{S}|$ for a less than half filled shell and $|\mathrm{L}\ +\ \mathrm{S}|$ otherwise.

The first rule minimizes the Coulomb repulsion by preventing electrons from occupying the same position. The second also minimizes Coulomb interactions and can be understood qualitatively as preventing the crossing of electron orbits. The third rule is from minimizing the spin-orbit energy which arises from a term proportional to $\mathbf{L} \cdot \mathbf{S}$ in the Hamiltonian, when relativistic corrections are taken into account. Ce^{3+} has a $4f^1$ configuration and applying Hund's rules, $S\ =\ \frac{1}{2}$, $L\ =\ 3$ and $J\ =\ \frac{5}{2}$. For this state, $g_J\ =\ \frac{6}{7}$ and $\mu = 2.54\ \mu_\mathrm{B}$. The $J\ =\ \frac{7}{2}$ state is well separated by typical energies of $\sim$ 3000 K [110] and therefore does not play a significant role in the magnetic properties.

2.1.2 Crystal electric fields

In addition to the atomic properties, it is necessary to consider the local environment of an ion sitting in a regular atomic lattice. This will contribute an additional electrostatic interaction termed the crystal electric field (CEF). In a metal, this will arise not only from the point like charges of surrounding nuclei but the broad distribution from surrounding conduction electrons. The appropriate method of dealing with this field depends on the magnitude of the effect. Since f orbitals lie quite close to the nucleus, the effect of the local electric field is relatively weak compared to the spin-orbit coupling. In this case, all three of Hund's rules are expected to hold and the effect of this field is to act as a perturbation which lifts the degeneracy of the $(2J + 1)$ states of the ground state multiplet.

This can be analyzed using the method of Stevens operator equivalents [111, 112]. This approach is valid under the condition that the other multiplets are sufficiently well separated from the one in consideration. Once the perturbing potential is expressed as a function of Cartesian co-ordinates (x, y, z), the Wigner-Eckhart theorem can be applied which allows the replacement of (x, y, z) with the projections of the angular momentum operators (J_x, J_y, J_z), provided the non-commutation of the angular momentum operators is taken into account. In this case, the perturbing CEF Hamiltonian ($\mathscr{H}_{\mathrm{CEF}}$) is

$$\mathscr{H}_{\mathrm{CEF}} = \sum_{n,m} B_m^n O_m^n, \tag{2.4}$$

where the coefficients B_m^n are Stevens parameters and O_m^n are Stevens operator equivalents which depend only on the angular momentum operators. For a cerium ion in a tetragonal CEF, $\mathscr{H}_{\mathrm{CEF}}$ takes the form of

$$\mathscr{H}_{\mathrm{CEF}} = B_2^0\mathrm{O}_2^0 + B_4^0\mathrm{O}_4^0 + B_4^4\mathrm{O}_4^4. \tag{2.5}$$

For the $J = \frac{5}{2}$ multiplet, the higher order parameters B_6^n are all zero. The three Stevens operator equivalents in Eq. 2.5 are given by

$$O_2^0 = 3J_z^2 - J(J+1) \tag{2.6}$$

$$O_4^0 = 35J_z^4 - 30J(J+1)J_z^2 + 25J_z^2 - 6J(J+1) + 3J^2(J+1)^2 \tag{2.7}$$

$$O_4^4 = \frac{1}{2}(J_+^4 + J_-^4). \tag{2.8}$$

$J_\pm$ are raising and lowering operators. The $J = \frac{5}{2}$ multiplet has six states $|m_J>$, where m_J runs from $-\frac{5}{2}$ to $\frac{5}{2}$. Using these as a set of a basis states a matrix can be constructed with elements $< m'_J|\mathscr{H}_{\mathrm{CEF}}|m_J >$ which is given by

$$\begin{pmatrix}
10B_2^0{+}60B_4^0 & 0 & 0 & 0 & 12\sqrt{5}B_4^4 & 0 \\
0 & -2B_2^0{-}180B_4^0 & 0 & 0 & 0 & 12\sqrt{5}B_4^4 \\
0 & 0 & -8B_2^0{+}120B_4^0 & 0 & 0 & 0 \\
0 & 0 & 0 & -8B_2^0{+}120B_4^0 & 0 & 0 \\
12\sqrt{5}B_4^4 & 0 & 0 & 0 & -2B_2^0{-}180B_4^0 & 0 \\
0 & 12\sqrt{5}B_4^4 & 0 & 0 & 0 & 10B_2^0{+}60B_4^0
\end{pmatrix}$$

This can be diagonalized and the eigenvectors and eigenvalues give the CEF wave functions and their corresponding energies. The forms of the operators and their matrix elements are tabulated in Ref. [112]. It can be seen that the only off-diagonal elements are proportional to B_4^4 since $< m'_J|O_2^0|m_J >$ and $< m'_J|O_4^0|m_J >$ are zero for $m'_J \neq m_J$, whereas $< m'_J|O_4^4|m_J >$ is only non zero for $m'_J - m_J = 4$. Therefore, if B_4^4 is non-zero, there will be mixing of the $|\frac{5}{2}>$ and $|-\frac{3}{2}>$, and $|-\frac{5}{2}>$ and $|\frac{3}{2}>$ states. There are no terms that mix the $|\pm\frac{1}{2}>$ states. The level scheme will consist of three doublets. This is a result of Kramer's theorem which states that if the Hamiltonian for a non-integer spin does not break time reversal symmetry, then the energy levels will be at least doubly degenerate. Electric fields do not break time reversal symmetry but magnetic fields do, so in the absence of a field there exist protected Kramer's doublets but in an applied field these levels may split.

It can be seen that even before the magnetic interactions between $4f$ ions are considered, the perturbing effect of the surrounding charge distribution can lead to strongly anisotropic properties. These are often termed single-ion anisotropic effects which can strongly influence magnetic properties up until temperatures where the thermal energy greatly exceeds the energy of the CEF splittings. To the lowest order, the anisotropy energy (E_a) of a tetragonal system is given by

$$E_\mathrm{a} = K_1 \sin^2\theta, \tag{2.9}$$

where θ is the angle between the direction of the magnetic moments and the c axis [113]. So if $K_1 < 0$, E_a is minimized for moments in the ab plane and if $K_1 > 0$, E_a is minimized for moments along the c axis. Within this CEF model for a cerium ion, K_1 is given by

$$K_1 = -\left(\frac{3}{2}B_2^0 < O_2^0 > +5B_4^0 < O_4^0 >\right). \tag{2.10}$$

Typically the sign of K_1 is dominated by the sign of $B_2^0 < O_2^0 >$. The projections of the ground state magnetic moment in the ab plane ($\langle\mu_x\rangle$) and along the c axis are given by

$$\langle\mu_z\rangle = \langle\psi_1^\pm|g_J J_z|\psi_1^\pm\rangle \tag{2.11}$$

$$\langle\mu_x\rangle = \langle\psi_1^\pm|\frac{g_J}{2}(J^+ + J^-)\left|\psi_1^\pm\right\rangle, \tag{2.12}$$

where $\left|\psi_1^\pm\right\rangle$ are the wave functions of the ground state doublet. It is therefore possible for a range of ground state moments to arise purely from single-ion anisotropy. One technique in which anisotropic properties will be readily apparent is in magnetic susceptibility measurements of single crystals.

Single crystal susceptibility

In the absence of CEF splittings, the low field magnetic susceptibility of a paramagnetic ion is given by

$$\chi = \frac{\mu_0 \mu_{\text{eff}}^2}{3k_{\text{B}}T}, \tag{2.13}$$

where μ_{eff} is the effective moment and can be estimated from Eq. 2.2 [109]. The experimentally observed value for Ce^{3+} is 2.51 μ_{B} compared to the theoretical value of 2.54 μ_{B}. Taking into account the CEF splitting, the magnetic susceptibility of an ion along the axis i given by [114]

$$\begin{aligned}\chi_{\text{CEF}} = \chi_0 + (g_J\mu_{\text{B}})^2 Z^{-1} \Bigg(& \sum_{j\neq k} | < \psi_j|J_i|\psi_k > |^2 \frac{1-\mathrm{e}^{\frac{E_k-E_j}{k_{\text{B}}T}}}{E_k - E_j} \mathrm{e}^{\frac{E_j}{k_{\text{B}}T}} \\ & + \frac{1}{k_{\text{B}}T} \sum_j | < \psi_j|J_i|\psi_j > |^2 \mathrm{e}^{\frac{E_j}{k_{\text{B}}T}} \Bigg),\end{aligned} \tag{2.14}$$

where E_j is the energy of the jth level and $E_j = 0$ for the ground state. $Z = \sum\limits_j \mathrm{e}^{\frac{E_j}{k_{\text{B}}T}}$ is the partition function. As $T \rightarrow 0$, only the term on the right hand state for the ground state remains and the susceptibility is reduces to Eq. 2.13 with an effective moment determined by the ground state doublet. Eq. 2.14 models the magnetic susceptibility taking into account single-ion anisotropy from CEF. However, it does not take into account two-ion interactions. The high temperature magnetic susceptibility of magnetically ordered compounds is significantly different above the ordering temperature since instead of Eq. 2.13, $\chi \propto (T - \theta_{\text{CW}})^{-1}$, where θ_{CW} is the Curie-Weiss temperature. Magnetic ordering evidently must arise from two-ion interactions and this can be accounted for by the addition of a molecular field (λ). The magnetic susceptibility is then given by [114].

$$\chi = \chi_0 + \frac{\chi_{\text{CEF}}}{1 - \lambda\chi_{\text{CEF}}} \tag{2.15}$$

The molecular field parameters can also be anisotropic and this represents two-ion anisotropic exchange interactions. The CEF parameter B_2^0 can also be related to the high temperature susceptibility for isotropic exchange interactions by [115]

$$B_2^0 = \frac{10k_B(\theta_{ab} - \theta_c)}{3(2J-1)(2J+3)}, \tag{2.16}$$

where θ_{ab} and θ_c are the Curie Weiss temperatures perpendicular and parallel to the c axis respectively. In the next section, two-ion interactions and magnetic ordering are discussed more fully.

2.1.3 Magnetic order

For magnetic order to occur there must be interactions between magnetic moments. The Hamiltonian for such an interaction is given for the Heisenberg model by

$$\mathscr{H} = -\sum_{i,j} J_{ij}\mathbf{S_i}\cdot\mathbf{S_j}, \tag{2.17}$$

where J_{ij} is the exchange interaction between the ith and jth spins [109]. Considering a nearest neighbour model where $J_{ij} = J$ for neighbouring spins and is zero otherwise, the energy will be minimized when neighbouring spins align for $J > 0$ and antialign for $J < 0$, and the former describe ferromagnetic interactions while the latter describe antiferromagnetic interactions. In an Ising model, the spins can no longer point in any direction and are constrained to point along a single axis. In this case, $\mathbf{S_i}\cdot\mathbf{S_j}$ in Eq. 2.17 can be replaced with just the component along one axis $S_i^z S_j^z$.

The most straightforward interaction between a pair of localized spins is the dipolar interaction. The energy scale is of this interaction is at most of the order of 1 K and in metallic materials the localized moments are surrounded by a cloud of conduction electrons. It is the interaction between the f electrons and the conduction band that gives rise to magnetic exchange interactions in many of these systems. The $\mathbf{q}$ dependent paramagnetic susceptibility of an electron gas in three dimensions is given by [109]

$$\chi(\mathbf{q}) = \frac{\chi_{\mathrm{P}}}{2}\left(1 + \frac{1-\tilde{q}^2}{2\tilde{q}}\ln\left|\frac{\tilde{\mathrm{q}}+1}{\tilde{\mathrm{q}}-1}\right|\right), \tag{2.18}$$

where χ_{P} is the Pauli paramagnetic susceptibility and $\tilde{q} = q/2k_{\mathrm{F}}$ is the ratio of wave vector to twice the Fermi wave vector. χ_{P} is the response of an electron gas to a uniform magnetic field. As a result, the electron gas at distance $\mathbf{r}$ from a perfectly localized spin $\mathbf{S_1}$ has a spin polarization $\mathbf{s}(\mathbf{r})$ given by [116]

$$\mathbf{s}(r) \propto \sum_{\mathbf{q}} \chi(\mathbf{q})\mathrm{e}^{i\mathbf{q}\cdot r}\mathbf{S_1} \propto J_{\mathrm{cf}}\left(\frac{-2k_{\mathrm{F}}r\cos 2k_{\mathrm{F}}r + \sin 2k_{\mathrm{F}}r}{16(k_{\mathrm{F}}r)^4}\right), \tag{2.19}$$

where J_{cf} is the on site exchange interaction between $\mathbf{S_1}$ and a conduction electron. The polarized conduction electrons can then couple to another localized spin $\mathbf{S_2}$

which leads to an effective interaction between a pair of local moments mediated by the conduction electrons. This is the Ruderman-Kittel-Kasuya-Yosida (RKKY) interaction

$$\mathscr{H}_{\mathrm{RKKY}} \propto J_{\mathrm{cf}}\, \mathbf{s}(\mathbf{r}) \cdot \mathbf{S_1} \propto J_{\mathrm{cf}}^2 \left(\frac{-2k_{\mathrm{F}} r \cos 2k_{\mathrm{F}} r + \sin 2k_{\mathrm{F}} r}{16(k_{\mathrm{F}} r)^4} \right) \mathbf{S_1} \cdot \mathbf{S_2}. \tag{2.20}$$

This can be identified as a form of the Hamiltonian in Eq. 2.17 with an exchange interaction of the form shown in Fig. 2.1. The interaction is strong and ferromagnetic for short separations. However, with increasing interatomic distances, J_{RKKY} oscillates and therefore the interactions can either be ferromagnetic or antiferromagnetic. Furthermore, a structure can display both ferromagnetic and antiferromagnetic interactions when different pairs of ions are considered and this can lead to competing magnetic interactions. Fig. 2.2 illustrates how for a face-centred lattice, interactions can be ferromagnetic between nearest neighbours and antiferromagnetic between next nearest neighbours. The extreme example of this is when the moments are randomly positioned in a conducting medium and this leads to a spin-glass behaviour [109]. As $k_{\mathrm{F}} \rightarrow 0$, the interaction is ferromagnetic and $J_{\mathrm{RKKY}} \sim 1/r^3$. $k_{\mathrm{F}} = 0$ corresponds to the disappearance of the Fermi surface and therefore the absence of conduction electrons and the form of Eq. 2.20 reduces to the dipolar interaction.

This type of two-ion interaction can explain much of the magnetic behaviour of f electron systems. The strength of the interaction scales with J_{cf}^2 and therefore upon increasing the coupling between the local moments and the conduction electrons, the RKKY interaction would be expected to be enhanced. However, as discussed in the next section, increasing the coupling in some systems enhances the Kondo interaction which competes with magnetic ordering.

2.1.4 Kondo Interaction

The behaviour of localized magnetic moments in a metallic host can be described by the Anderson impurity model given by [116]

$$\mathscr{H} = \sum_{\mathbf{k},\sigma} \epsilon_{\mathbf{k}} c^{\dagger}_{\mathbf{k},\sigma} c_{\mathbf{k},\sigma} + \sum_{\sigma} \epsilon_f f^{\dagger}_{\sigma} f_{\sigma} + U f^{\dagger}_{\uparrow} f_{\uparrow} f^{\dagger}_{\downarrow} f_{\downarrow} + \sum_{\mathbf{k},\sigma} \left(V_{\mathbf{k}} c^{\dagger}_{\mathbf{k},\sigma} f_{\sigma} + \mathrm{h.c.} \right). \tag{2.21}$$

$c^{\dagger}_{\mathbf{k},\sigma}$ and $c_{\mathbf{k},\sigma}$ are creation and annihilation operators for conduction electrons with a band energy $\epsilon_{\mathbf{k}}$ and spin σ, while $f^{\dagger}_{\sigma}$ and f_{σ} are creation and annihilation operators

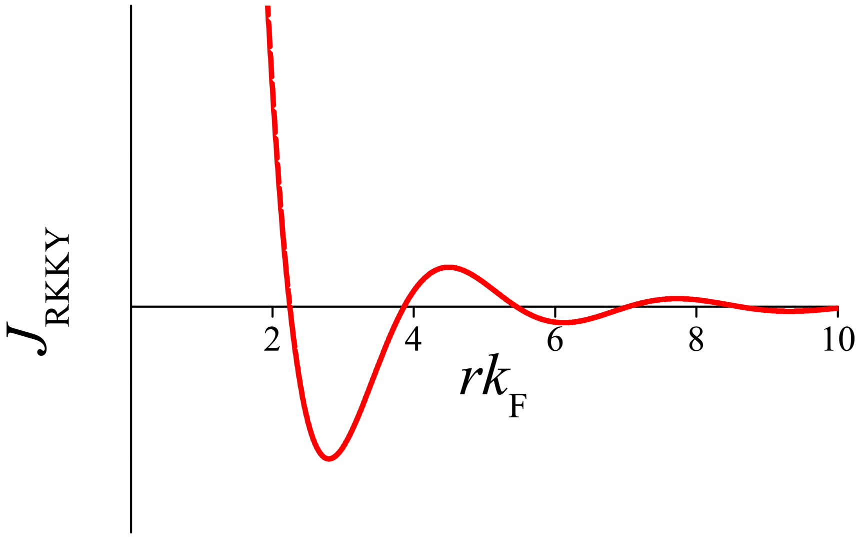

Figure 2.1: The functional form of the exchange interaction for the RKKY interaction.

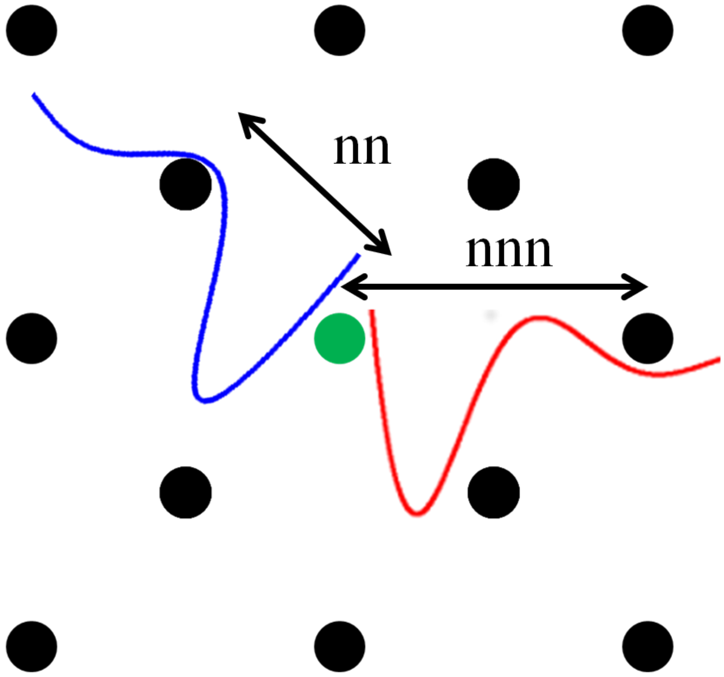

Figure 2.2: An illustration of how the RKKY interaction can lead to ferromagnetic interactions (blue) between nearest neighbours (nn) and antiferromagnetic interactions (red) between next nearest neighbours on a face-centred lattice.

for localized electrons with an energy ϵ_f. The dispersion of a conduction band in the free electron model is $\propto k^2$ while it has no k dependence for a perfectly localized electron. U is the Coulomb repulsion on the localized electron site and describes the energy cost of the level being doubly occupied. The last term describes the hybridization of the conduction and localized electrons, the strength of which is given by the matrix element $V_{\mathbf{k}}$. It can be shown that in the limit of a large U and small $V_{\mathbf{k}}$ [117], the Hamiltonian in Eq. 2.21 takes the form of the Kondo interaction $\mathscr{H} \sim J\mathbf{s} \cdot \mathbf{S}$ between the spins of a conduction and localized electron. This is an antiferromagnetic coupling, the strength of which is proportional to the square of the hybridization strength V^2 and is inversely proportional to $(\epsilon_F - \epsilon_f)$, the difference in energy between the Fermi level and the localized electron levels.

The Kondo model can be used to study the properties of certain f electron systems. In the case of strongly localized f electrons, ϵ_f is too far below the Fermi level. The poorly screened nuclear charge ensures that the wave function lies very close to the core with a negligible amplitude further out. However, cerium ions in particular often have ϵ_f close to the Fermi level and although the wave function peaks close to the core, there is a longer tail to greater distances [115]. Therefore, the Kondo interaction plays a dominant role in the magnetic properties of many cerium based systems. Although the model in Eq. 2.21 can account for much of the behaviour of these compounds, a fundamental difference is that in these compounds the localized moments are often arranged in a regular lattice. Since the Anderson impurity model describes the interaction of a single impurity spin, it will be unable to account for coherence effects which may be very important for describing the wide range of unusual phenomena observed in heavy-fermion and intermediate valence compounds.

Upon reducing the temperature, the conduction electrons increasingly screen the magnetic moment of the localized electrons. At temperatures far below a characteristic energy scale called the Kondo temperature (T_{K}), there is strong coupling between the localized and conduction electrons and there is screening of the local moment. They can be thought of as forming a non-magnetic singlet state with a binding energy

$$k_{\mathrm{B}}T_{\mathrm{K}} \sim \epsilon_{\mathrm{F}}\mathrm{e}^{-1/\mathrm{J}\rho(\epsilon_{\mathrm{F}})}, \tag{2.22}$$

where $\rho(\epsilon_{\mathrm{F}})$ is the density of states at the Fermi level. The crossover between local moments and the Kondo singlet can be observed in the magnetic susceptibility which displays Curie like behaviour at high temperatures (Eq. 2.13) and a constant susceptibility of order $1/T_{\mathrm{K}}$ at low ones [118]. There is a large resonance in the density of states around ϵ_{F} which is reflected in massively enhanced values of γ, up to the order of ~ 1 J/mol K [119]. This corresponds to the conduction bands having a 'heavy' f like character. That is the bands have a weak dispersion corresponding to large effective electron masses. With increased coupling J, the model of the Kondo interaction can not be applied and in particular, the $4f$ level is no longer fully occupied. This is the intermediate valence regime where the f electron fluctuates between occupying f orbitals and the conduction band, so that $0 < n_f < 1$ and properties such as the low temperature susceptibility and γ are moderately enhanced but not to the extent of the heavy-fermion regime [116].

2.1.5 Doniach phase diagram and quantum criticality

From considering the coupling of localized f electrons to the conduction band, two very different possible behaviours emerge. It is possible for magnetic exchange interactions to be realized between magnetic moments following Eq. 2.20, yet it is also possible for hybridization between f electrons and the conduction bands to lead to the screening of the moment and the formation of an effective singlet state. These are two fundamentally different ground states and the competition between these interactions are often described within the framework of the Doniach phase diagram [67]. In this model, the coupling constant J_{cf} in Eq. 2.20 is identified with the Kondo coupling constant. Therefore the magnetic ordering temperature T_{N} scales as $\sim J^2\rho(\epsilon_{\mathrm{F}})$ while T_{K} scales as in Eq. 2.22. For low couplings, the RKKY interaction dominates and the system orders magnetically. As the coupling is increased the RKKY interaction is enhanced but not as strongly as the Kondo interaction, which dominates at large J. Although T_{N} will increase initially, the effect of the Kondo interaction is to screen the local moments and suppress magnetic order. At a critical coupling J_{c}, T_{N} will be suppressed to zero at a quantum critical point (QCP) [120]. In many systems, a superconducting region is observed surrounding the QCP, where the Copper pairs consist of heavy quasiparticles and the superconductivity is believed to be mediated by spin fluctuations [13].

2.2 Superconductivity

2.2.1 Introduction to superconductivity

The key experimental signatures of superconductivity which motivated early studies were the loss of resistivity [1] and perfect diamagnetism [121]. In the case of the latter, not only will an applied field be unable to penetrate beyond the surface of superconducting material, but upon cooling through the superconducting transition temperature (T_{c}), magnetic flux is expelled from the bulk of the sample. In the absence of a thermodynamic or microscopic theory of the superconducting state, the electrodynamic properties are encapsulated by London equations given by

$$\mathbf{E} = \frac{m_{\mathrm{e}}}{n_s \mathrm{e}^2} \frac{\mathrm{d}\mathbf{J_s}}{\mathrm{dT}} \tag{2.23}$$

$$\nabla \times \mathbf{J_s} = -\frac{n_s \mathrm{e}^2}{m} \mathbf{B}, \tag{2.24}$$

where $\mathbf{E}$ and $\mathbf{B}$ are the electric field and the magnetic flux density, $\mathbf{J_s}$ is the supercurrent density and n_s is proportional to the superfluid density. The first equation describes a perfect conductor, since in the absence of an electric field, a finite current solution is permitted. Therefore electric fields are needed only to change the current and there are no dissipative processes. The utility of the second equation is generally found from substituting in Ampere's law for $\mathbf{J_s}$, which results in

$$\nabla^2 \mathbf{B} = \frac{\mathbf{B}}{\lambda_{\mathrm{L}}^2}, \tag{2.25}$$

where the London penetration depth is given by

$$\lambda_{\mathrm{L}}^2 = \frac{m_{\mathrm{e}} \mathrm{c}^2}{4\pi n_s \mathrm{e}^2}. \tag{2.26}$$

For a constant magnetic field applied to an infinite superconducting slab, the solution is a decaying exponential, with a decay constant λ_{L}. Therefore, apart from in a region at a depth of order $\sim \lambda_{\mathrm{L}}$ from the surface, magnetic fields are entirely excluded. This is related to the ability of supercurrents on the surface to screen the magnetic field and for larger superfluid densities n_s, magnetic fields are screened more effectively and the smaller λ_{L} is.

2.2.2 Phase transitions

Further progress can be made from considering the nature of the superconducting phase transition. The Ginzburg-Landau theory follows from the Landau theory of phase transitions for describing the change from an ordered to disordered system. For an ordered system, there is an order parameter (M) which is zero in the disordered phase but non-zero in the ordered phase. The state of a system must correspond to a minimum in the free energy F and at the critical temperature (T_{c}), the minimum in F changes from a disordered state with $M = 0$ to an ordered state with $M \neq 0$. In a second-order phase transition, the order parameter changes continuously at T_{c} so F can be expanded in even powers of M.

$$F = a(T - T_{\mathrm{c}})M^2 + bM^4 + ..., \tag{2.27}$$

where it has been assumed that M is spatially homogeneous, and a and $b > 0$. For $T > T_{\mathrm{c}}$, F is only minimized for $M = 0$ but for $T < T_{\mathrm{c}}$ there is a non-zero solution with

$$M^2 = \frac{a(T_{\mathrm{c}} - T)}{2b}. \tag{2.28}$$

Therefore upon cooling below the transition, M grows continuously from zero and $M \propto (T_{\mathrm{c}} - T)^{\frac{1}{2}}$. This is the expected behaviour of the (sublattice) magnetization in the mean field model of an (anti)ferromagnet close to a second order phase transition. In systems where the fluctuations can not be neglected, there may be a different temperature dependence but it will scale as $M \propto (T_{\mathrm{c}} - T)^{\beta}$. β is a critical exponent applicable for a wide range of phase transitions with the same dimensionality of the system and order parameter [109]. The first derivative of Eq. 2.27 is continuous at the phase transition but there is a discontinuity in the second derivative. Therefore a discontinuity will be observed at a second order transition in quantities dependent on the second derivative of the free energy, such as the specific heat. In the case of a first-order transition, F can not necessarily be expanded in powers of M, since there is no guarantee that the order parameter is small at the transition. However, if the order parameter is sufficiently small close to the transition, a first order transition can be described with

$$F = a(T - T_{\mathrm{c}})M^2 + bM^4 + cM^6 + ..., \tag{2.29}$$

where now $b < 0$ and $c > 0$. Again at high temperatures, the only minimum in the free energy occurs at $M = 0$. However now the minima at non-zero M do not grow

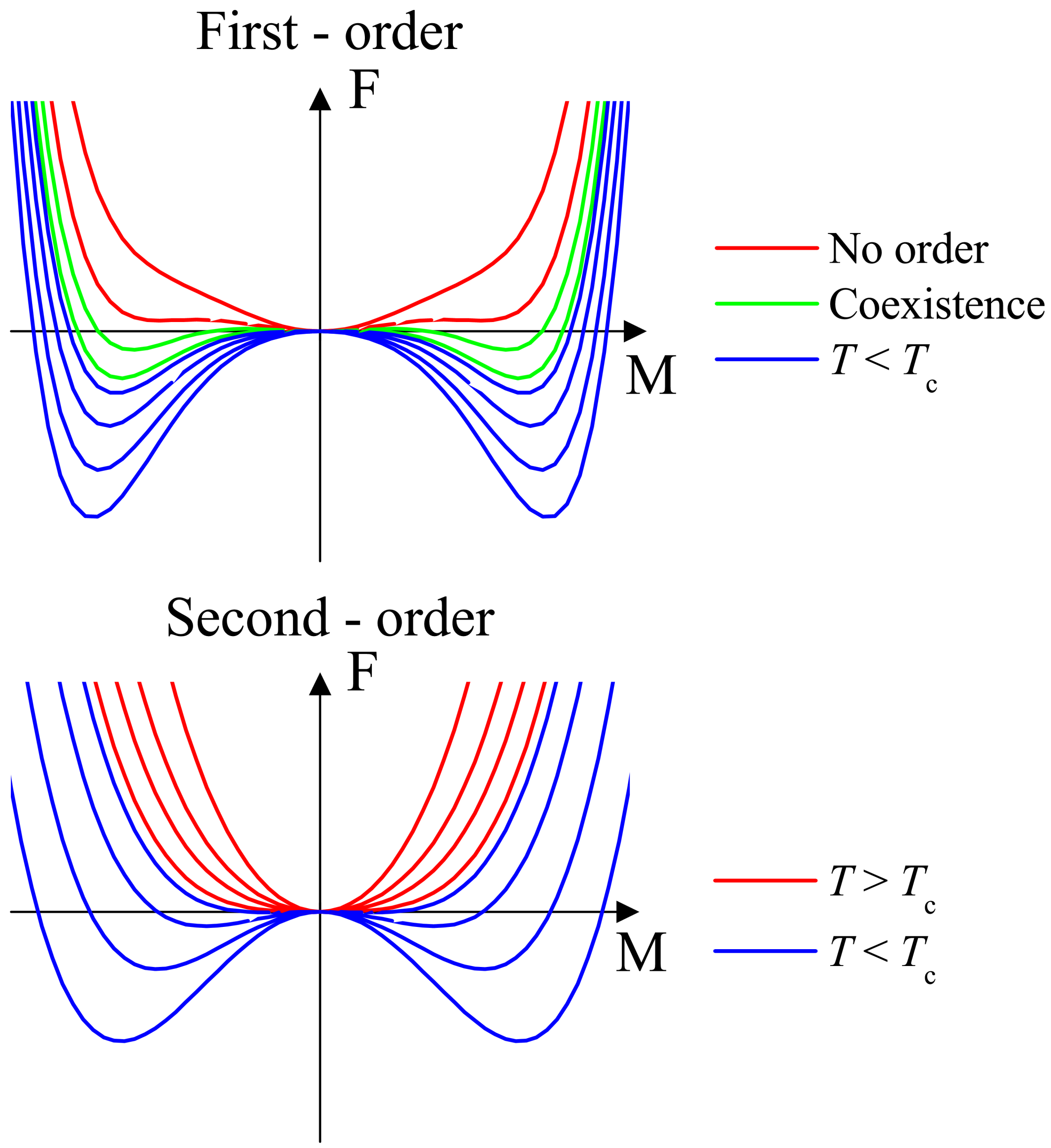

Figure 2.3: The top shows the free energy of the first order phase transition described by Eq. 2.29 while the bottom shows the free energy of the second order phase transition in Eq. 2.27. The red lines show curves where the only minimum is at $M = 0$ while the blue lines only have minima at $M \neq 0$. The green lines on the first order show curves with metastable states and there is coexistence between the ordered and disordered phases. In the second order plot, the minima emerge continuously from $M = 0$ while in the first order plot they emerge first at finite M.

continuously from zero and at the phase transition the order parameter jumps from zero to a finite value. Furthermore for the above model, if $B^2 > 3a(T - T_\mathrm{c})$ there are local minima for $M = 0$ and $M \neq 0$ and therefore in this temperature region there exist metastable states. This is the origin of superheating and supercooling phenomena, whereby the system does not necessarily sit in a global minimum of the free energy but in a metastable local minimum. The free energies for first and second order transitions are shown in Fig. 2.3. In the second-order plot, it can be seen that below T_c, the minima in the free energy start from $M = 0$ and move continuously away from the origin. For the first-order case, the minima initially emerge at finite M and there is a jump from $M = 0$ to a finite M. In the regions of coexistence shown in green, there exist local minima at both zero and non-zero M.

2.2.3 Ginzburg-Landau theory

Applying a similar principle to the superconducting transition, in Ginzburg-Landau theory a complex order parameter ψ is postulated. In addition to the terms in Eq. 2.27, the free energy also contains terms with the gradient of ψ as well as coupling to the magnetic field in the same way as a wave function. In this case the free energy density of the superconducting state f_s is given by [11]

$$f_\mathrm{s} = f_\mathrm{n} + \alpha|\psi|^2 + \frac{\beta}{2}|\psi|^4 + \frac{1}{2m}\left|\left(\frac{\hbar}{i}\nabla - \frac{2e}{c}\mathbf{A}\right)\psi\right|^2 + \frac{(\mathbf{B} - \mathbf{B}_\mathrm{app})^2}{2\mu_0}, \tag{2.30}$$

where f_n is the normal state free energy density, $\mathbf{B}$ is the total magnetic field, $\mathbf{B}_\mathrm{app}$ is the contribution from the external magnetic field and $\mathbf{A}$ is the magnetic vector potential. For a homogeneous solution, the gradient term disappears and a minimal solution can be found similar to Eq. 2.28. This can be substituted into Eq. 2.30 and it can be seen that there is a critical applied field $B_\mathrm{app} = B_\mathrm{c}$ above which the free energy of the Meissner state (with $B = 0$) is greater than f_n. Therefore, there is a phase transition from the superconducting to the normal state at B_c. This is the thermodynamic critical field and the temperature dependence is given by [122]

$$B_\mathrm{c}(T) = B_\mathrm{c}(0)\left[1 - \left(\frac{T}{T_\mathrm{c}}\right)^2\right]. \tag{2.31}$$

Two characteristic lengthscales emerge from Ginzburg-Landau theory. The first is the London penetration depth. If $|\psi|^2$ is identified as corresponding to the superfluid density, then an effective penetration depth (λ_{eff}) proportional to λ_{L} enters Ginzburg-Landau theory via Eq. 2.26. A relationship between n_s and the order parameter is expected, since n_s is a quantity which becomes non-zero only in the superconducting state. However, that does not mean that the order parameter is simply the density of superconducting electrons, since ψ is a complex number. The phase of the wave function is important for describing currents in the superconducting state. There is a second length scale, the Ginzburg-Landau coherence length ξ. This is the characteristic distance over which ψ varies. Both λ_{eff} and ξ are $\propto |\psi|^{-2}$ and therefore diverge approaching the superconducting transition temperature (T_{c}). The ratio $\kappa = \lambda_{\text{eff}}/\xi$ is the Ginzburg-Landau parameter and is almost temperature independent.

As discussed previously, the Meissner state with complete flux expulsion from the bulk was one of the key experimental signatures of superconductivity. However, the form of the free energy in Eq. 2.30 does not necessarily preclude the existence of a superconducting state with internal magnetic fields. At $B_{\text{app}} = B_{\text{c}}$, the energetic cost of maintaining the Meissner state is too great but for a non-zero $\mathbf{B}$, it may be that the superconducting state can remain energetically favourable, even for larger applied fields. Whether this is the case depends on the value of κ. For $\kappa < 1/\sqrt{2}$, the boundary energy between normal and superconducting states is positive. In this case, the reduction in energy from the increased penetration does not offset the energy cost of suppressing the order parameter in the boundary region. This describes a type-I superconductor. Upon applying a sufficiently large field, the samples undergoes a first order transition from the Meissner to the normal state. For a finite demagnetization factor [123], there is an intermediate state with macroscopic domains of normal and superconducting phases. The thickness of these domains depends on the sample thickness but the macroscopic nature reflects the energy cost of the normal-superconducting boundary region [11].

If the boundary energy is negative it may be expected that there would be no constraint to the normal-superconducting boundary area. However, as a result of the complex nature of ψ and the requirement that it is single valued throughout the sample, the flux threading a normal region must be a multiple of the magnetic flux quantum $\Phi_0 = 2.067833758 \times 10^{-15}$ Wb. For type-II superconductors, there is a Meissner state for applied fields less than the lower critical field given by

$$\mu_0 H_{\text{c1}}(T) = \frac{\Phi_0}{4\pi\lambda_{\text{eff}}^2}(\ln\kappa + \alpha(\kappa)), \tag{2.32}$$

where $\alpha(\kappa)$ is calculated numerically in Ref. [124]. Above this field, magnetic flux can penetrate into the sample via thin tubes and this is known as the mixed state. There is a core of normal material with an area of order $\sim \xi^2$ and the magnetic field penetrates into the surrounding superconducting region in a depth on the order of $\sim \lambda_{\mathrm{eff}}$. There is a repulsive force between flux lines and they arrange in the minimum energy configuration, which for an isotropic superconductor is a hexagonal flux line lattice [125, 126]. However once the applied fields reach the orbital upper critical field $B_{\mathrm{c2}}^{\mathrm{orb}}$, the cores of neighbouring flux lines overlap and the material is entirely in the normal state. $B_{\mathrm{c2}}^{\mathrm{orb}}$ is given by

$$B_{\mathrm{c2}}^{\mathrm{orb}} = \frac{\Phi_0}{2\pi\xi^2}. \tag{2.33}$$

$B_{\mathrm{c2}}^{\mathrm{orb}}$ can be related to the critical field with

$$B_{\mathrm{c2}}^{\mathrm{orb}} = \sqrt{2}\kappa B_{\mathrm{c}}, \tag{2.34}$$

which shows how the mixed state can remain energetically favourable in some type-II superconductors for applied fields considerably higher than B_{c}.

There is often interest in the magnetic properties of both type-I and type-II superconductors. This includes the average magnetization and the internal magnetic field distribution. The ideal magnetization as a function of field of type-I and II superconductors are shown in Fig. 2.4. For a type-I superconductor, it can be seen that in the absence of demagnetization effects, there is a discontinuity in the magnetization at H_{c}. This is the situation for a field applied parallel to the surface of an infinitely thin superconducting sheet. A real system has a finite demagnetization factor D. For for a uniform magnetization M, when

$$\mathbf{H} - D\mathbf{M} = \mathbf{H}_{\mathrm{c}}, \tag{2.35}$$

flux can penetrate the sample and the system enters the intermediate state. Since $\mathbf{M} = -\mathbf{H}$ for the Meissner state, this occurs when $(1 - D)H = H_{\mathrm{c}}$. The magnetic field probability distribution $P(B)$ of a type-I superconductor in the intermediate state is expected to have peaks at $B = 0$ for the regions in the Meissner state and at a field $B*$ corresponding to normal state domains. Evidently B^* must be greater than $\mu_0 H_{\mathrm{c}}$ if the material is in the normal state and the normal-superconducting boundaries are most stable if B^* is not much above the critical field [11]. The magnetization curves of an ideal type-I superconductor are reversible. This corresponds to the complete re-expulsion of flux upon reducing the field below H_{c}. However, real systems are often partially irreversible due to strain or inhomogeneities [11] but a region of re-entrant diamagnetism is often observed.

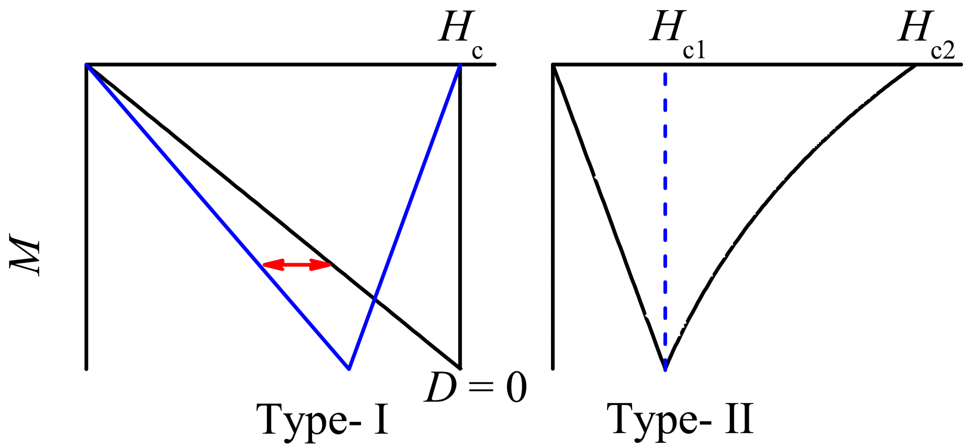

Figure 2.4: The magnetization against applied field for ideal type-I and type-II superconductors. The type-I curve is shown in black for $D = 0$ and in blue for a non-zero D, where the curve has been shifted by an amount DH indicated by the red arrow.

The magnetization against applied field is also shown for a type-II superconductor in Fig. 2.4. The magnetization is linear until H_{c1}, after which flux penetrates the sample until the magnetization reaches zero at H_{c2}. The field distribution of a hexagonal flux line lattice is shown in Fig. 2.5, which was obtained in Ref. [127] from numerically solving the Ginzburg-Landau equations. The spatial field distribution is shown on the right from Ref [128]. The former shows that the field distribution is mostly at fields lower than the applied field. The distribution is broad but has sharp cutoffs and well defined maximum and minimum fields. The maximum field corresponds to the vortex cores and the minimum field corresponds to a point equidistant between three cores. The peak in $P(B)$ corresponds to the saddle point. It is the maximal field on a line joining the two minima but a minimum on a perpendicular line joining two vortex cores. The saddle point splits into two or three peaks for non-hexagonal flux line lattices, since when the symmetry is lowered, the field at all the saddle point positions are no longer equivalent [129].

The field distribution is calculated for a range of applied fields and parameters using Ginzburg-Landau theory in Ref. [124]. The second moment ($\langle B^2 \rangle$) is calculated as a function of $b = B_{\text{app}}/B_{\text{c2}}$ for a range of κ. The results are shown in Fig. 2.6. Various approximate relationships for $\langle B^2 \rangle$ as a function of b, B_{c2}, κ and λ_{eff} are reported for different parameter regimes. Using Eq. 2.33, $\langle B^2 \rangle$ can be obtained for a given applied field with knowledge of only λ_{eff} and ξ. For small applied

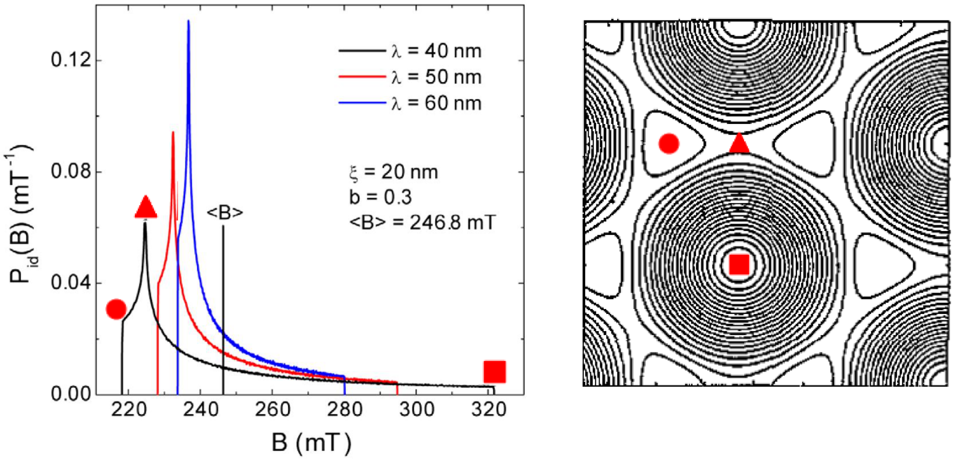

Figure 2.5: The left shows the field distribution of the mixed state of a type-II superconductor for three different values of the penetration depth, from Ref. [127]. The spatial field distribution for a hexagonal flux line lattice is shown on the right, from Ref. [128]. These have been modified to show the positions corresponding to the maximum, minimum and saddle points, which are marked with squares, circles and triangles respectively.

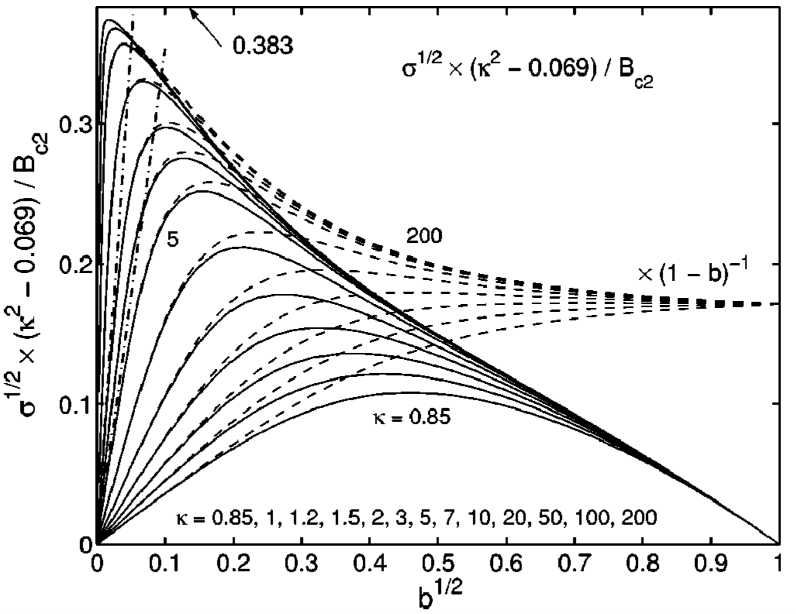

Figure 2.6: The second moment of the field distribution of a hexagonal flux line lattice for a range of κ from Ref. [124]. The square root of $\langle B^2\rangle$ is multiplied by a factor of $(\kappa^2 - 0.069)/B_{c2}$ and the dashed lines are multiplied by a factor of $(1-b)^{-1}$. The dashed lines all converge at $b = 1$ for all κ, following Eq. 2.37.

fields, $\langle B^2 \rangle$ increases approximately linearly with b before peaking at a maximum value, which shifts to lower b with increasing κ. For $\kappa > 50$, there is a very weak b dependence near the maximum and $\langle B^2 \rangle$ can be approximated as

$$\langle B^2 \rangle = 0.00371 \frac{\Phi_0^2}{\lambda_{\text{eff}}^4}. \tag{2.36}$$

A different approximation valid for higher values of b is given by

$$\langle B^2 \rangle = 7.52 \times 10^{-4} \frac{\Phi_0^2}{\lambda_{\text{eff}}^4} \frac{\kappa^4 (1-b)^2}{(\kappa^2 - 0.069)^2}. \tag{2.37}$$

This is a reasonable approximation for all κ in the range $0.25 < b < 1$. This can be seen from the dashed lines in Fig. 2.6 which all converge at $b = 1$ following the above expression. A more commonly used expression is

$$\langle B^2 \rangle = 0.02958 \frac{(1-b)^2}{\kappa^4} \left[1 + 1.21 \left(1 - \sqrt{b} \right)^3 \right]^2. \tag{2.38}$$

This is especially useful for studying many superconducting systems since it is valid across a large range of b, from around the point of the maximum to $b = 1$. However, this is only a good approximation for $\kappa > 5$ and is therefore unsuitable for studying systems close to the boundary of type-I and II behaviour. For these, it is generally necessary to use Eq. 2.37.

These results give some indication of the progress which can be made without resorting to a microscopic theory. This has been achieved by utilizing Landau theory with an order parameter that behaves as a complex valued wave function. On this basis, a wide range of superconducting properties can be deduced, including the existence of type-I and type-II superconductivity which depends only on the value of the dimensionless parameter κ. It has also been shown how Ginzburg-Landau theory can be used to quantitatively describe inhomogeneous systems, in this case the mixed state of a type-II superconductor. One caveat however is that Landau theory explicitly relies on the order parameter being small. It will therefore not necessarily be applicable away from the phase boundary, where this is not likely to be the case. The microscopic BCS theory is described in the next section. Soon after its proposal, it was shown that the Ginzburg-Landau equations can be derived from BCS theory in a temperature region close to T_c [130] and this provides a link between the phenomenological parameters in the Ginzburg-Landau free energy (Eq. 2.30) and the microscopic BCS parameters. This gives justification to the identification that $|\psi|^2$ is proportional to the superfluid density n_s [131]. As discussed further on, this allows the microscopic superfluid density to be related to the penetration depth, a measurable quantity.

2.2.4 BCS Theory and the superconducting energy gap

A successful microscopic theory of superconductivity requires a mechanism by which the ground state of a metal is not the normal state and therefore it is natural to look for means by which electrons in a free band can undergo a phase transition to an ordered state. It was a shown that if there is an arbitrarily attractive interaction between two electrons just above the Fermi level of a filled Fermi sea, then there exists a bound state between them [132]. The origin of the attractive interaction in conventional superconductivity is the electron-phonon interaction. There is an interaction between electrons arising from interactions with the lattice. In particular, upon considering the elastic process of an electron emitting a phonon which is subsequently absorbed by a second electron, it can be shown that there is an attractive interaction between electrons with an energy difference less than the phonon frequency [131]. Therefore in the simplest BCS models, there can be considered to be a constant attractive interaction within $\hbar\omega_{\mathrm{D}}$ of the Fermi surface, where ω_{D} is the Debye frequency, a characteristic maximum phonon frequency.

Some of the results of BCS theory can be summarised as follows [5, 6, 11]. The BCS wave function is given by

$$|\mathrm{BCS}>=\prod_{\mathbf{k}}(\mathrm{u}_{\mathbf{k}}+\mathrm{e}^{\mathrm{i}\theta}\mathrm{v}_{\mathbf{k}}\mathrm{c}^{\dagger}_{\mathbf{k}+\mathbf{s},\uparrow}\mathrm{c}^{\dagger}_{-\mathbf{k}+\mathbf{s},\downarrow})|0>, \tag{2.39}$$

where the normalization of the wave function requires that $u_{\mathbf{k}}^2 + v_{\mathbf{k}}^2 = 1$. The second term describes the creation of a pair of electrons with opposite crystal momenta $\mathbf{k}$ and $-\mathbf{k}$, a centre of mass momentum $2\hbar\mathbf{s}$ and opposite spins. These are Cooper pairs in the s-wave state. That is for an isotropic interaction, the lowest energy wave function is spatially symmetric. Therefore the Cooper pairs must have opposite spins, so that the overall pair wave function is antisymmetric under particle exchange. The quasiparticle excitation energy (E_k) is given by

$$E_k = \sqrt{\epsilon_{\mathbf{k}}^2 + \Delta_{\mathbf{k}}^2} \tag{2.40}$$

where $\epsilon_{\mathbf{k}}$ is the band energy measured from the chemical potential. The excitation spectrum is gapped with a k dependent energy gap $\Delta_{\mathbf{k}}$. This is found from self consistently solving the gap equation

$$\Delta_{\mathbf{k}} = -\sum_{\mathbf{k}'}(1-2f_{\mathbf{k}'})\frac{\Delta_{\mathbf{k}'}}{2E_{\mathbf{k}'}}V_{\mathbf{k}\mathbf{k}'}, \tag{2.41}$$

where f is the Fermi-Dirac function given by $f = (1 + e^{E/k_{\mathrm{B}}T})^{-1}$. $V_{\mathbf{k}\mathbf{k}'}$ is the

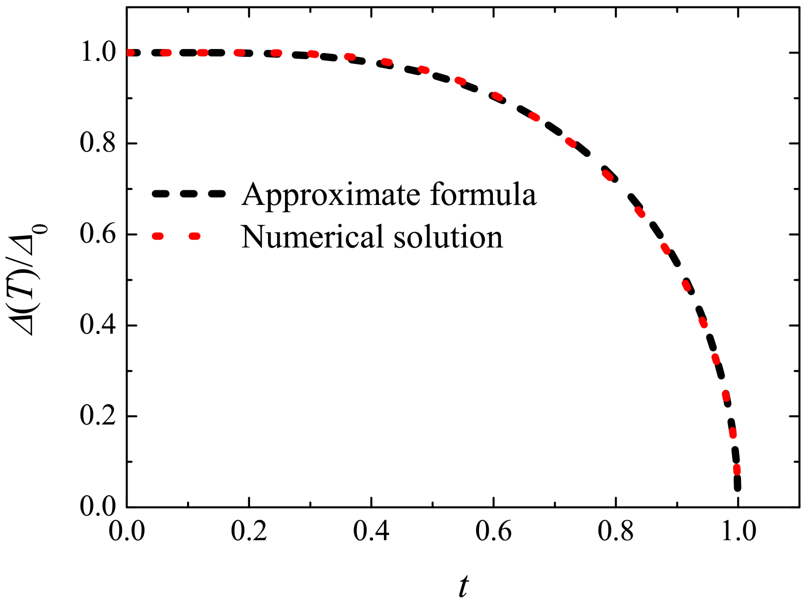

Figure 2.7: The temperature dependence of the BCS gap as a function of the reduced temperature $t = T/T_\mathrm{c}$. The approximate formula is Eq. 2.43 from Ref. [134], while the numerical solution is calculated following the procedure in Ref. [133].

matrix element for the interaction between electrons in the $\mathbf{k}$ and $\mathbf{k}'$ states. In isotropic weakly coupled BCS theory, there is an attractive potential $-V$ within $\hbar\omega_\mathrm{D}$ of the Fermi surface and $V = 0$ otherwise. In this case, the energy gap is $\mathbf{k}$ independent within this region and at $T = 0$ the magnitude of the gap (Δ_0) is given by

$$\Delta_0 = 1.764 k_\mathrm{B} T_\mathrm{c}. \tag{2.42}$$

Even with these approximations, an analytic solution can not be found for $T \neq 0$. A procedure for calculating $\Delta(T)$ numerically is given in Ref. [133]. Alternatively, an approximate formula, given in Ref. [134] is

$$\Delta(T) \;=\; 1.764 k_\mathrm{B} T_\mathrm{c} \tanh\left(1.82\left[1.018\left(\frac{T_\mathrm{c}}{T}-1\right)\right]^{0.51}\right). \tag{2.43}$$

The normalized temperature dependence of the gap is shown in Fig. 2.7. It can be seen that Eq. 2.43 is a good approximation to the BCS gap.

It is often desirable to calculate the gap function for superconductors with anisotropic gaps or for stronger couplings. Strictly speaking this requires finding a self consistent solution to Eq. 2.41 for an appropriate $V_{\mathbf{k}\mathbf{k}'}$. However, experimental data for these systems are often analyzed using the α-model of superconductivity [135, 136]. Within this model, the temperature dependence of the gap is the same as in weakly coupled, isotropic BCS theory as shown in Fig. 2.7. However, the factor of 1.764 in Eq. 2.7 is replaced by a variable α, so Δ_0 is given by

$$\Delta_0 = \alpha k_{\mathrm{B}} T_{\mathrm{c}}, \tag{2.44}$$

where $\alpha_{\mathrm{BCS}} = 1.764$ corresponds to BCS theory. $\alpha > \alpha_{\mathrm{BCS}}$ corresponds to moderate or strong electron-phonon coupling, while $\alpha < \alpha_{\mathrm{BCS}}$ can indicate an anisotropic superconducting gap [136]. The strength of the attractive interaction for BCS superconductors can be characterized by a dimensionless parameter known as the electron-phonon coupling parameter (λ_{ep}) [122]. This is equal to $N(E_{\mathrm{F}})V$, the product of density of states at the Fermi level and the attractive matrix element. The weak coupling limit is obtained from $\lambda_{\mathrm{ep}} \ll 1$ and superconductors with $\lambda_{\mathrm{ep}} < 0.5$ are weakly coupled, although there is not a universally accepted cut off. In strong coupling theory, the transition temperature is given by [137]

$$T_{\mathrm{c}} = \frac{\Theta_{\mathrm{D}}}{1.45} \exp\left[-\frac{1.04(1+\lambda_{\mathrm{ep}})}{\lambda_{\mathrm{ep}} - \mu(1+0.62\lambda_{\mathrm{ep}})}\right], \tag{2.45}$$

where Θ_{D} is the Debye temperature and μ^* is typically between 0.1 and 0.15, and arises due to Coulomb repulsion. This allows λ_{ep} to be estimated from readily measurable parameters. It also places important constraints on the transition temperatures of conventional BCS superconductors. Exceptionally large values of Θ_{D} and λ_{ep} are required to reproduce T_{c} of many cuprate superconductors, providing evidence for a pairing mechanism not mediated via the phonon-electron interaction.

So far the energy gap arising from BCS theory has been discussed. For an isotropic attractive potential, the Cooper pairs form an isotropic s-wave state with even parity ($l = 0$). This is a spin singlet state, since the spin component of the pairing wave function must be antisymmetric under particle exchange. However, other pairing mechanisms may favour pairing states with higher values of l, particularly when there are strong on-site Coulomb interactions. In p-wave superconductors, the Cooper pairs form odd parity states ($l = 1$) and therefore have a spin triplet configuration, where pairs consist of two electrons in an $S = 1$ state. In a spin triplet superconductor, the pairing state is specified by a vector $\mathbf{d}(\mathbf{k})$ and the gap is given by $\left|\mathbf{d}(\mathbf{k})\right|^2$ [138, 139]. The superconducting gap for triplet superconductors can either be isotropic or strongly anisotropic, becoming zero at certain points on the Fermi surface. These nodes can either be points or lines depending on the form of $\mathbf{d}(\mathbf{k})$. It is also possible for there to be non-unitary triplet states which break time reversal symmetry. In this case, the Cooper pairs are at least partially spin polarized and time reversal symmetry is broken in the superconducting state. There can also be spin singlet states with higher order pairing angular momenta. *d*-wave superconductors have even parity pairing $l = 2$ and therefore form spin singlets. This is believed to be the preferred pairing state for the cuprate superconductors which appear to have line nodes in the superconducting gap [27].

2.2.5 The gap structure of non-centrosymmetric superconductors

So far it has been assumed that the pairing states can be classified as either spin singlet or triplet. This is valid for centrosymmetric superconductors, where the orbital part of the pair wave functions have either even or odd parity. Since the overall wave function must be antisymmetric under particle exchange, the Cooper pairs must be either purely singlet or triplet. In non-centrosymmetric superconductors, parity is no longer a good quantum number [36] and in the presence of a finite antisymmetric spin-orbit coupling (ASOC), the pairing states can no longer be classified as singlet or triplet but an admixture of the two [140, 141]. In this case, the superconducting order parameter is given by [142]

$$\Delta(\mathbf{k}) = i(\psi + \mathbf{d}(\mathbf{k}) \cdot \sigma)\sigma_y, \tag{2.46}$$

where the first term in brackets is the singlet component and the second is the triplet. The effect of the ASOC is to split the spin degenerate conduction band into a pair of sheets. The resulting superconducting gaps are given by

$$\Delta_{\pm}(\mathbf{k}) = \psi \pm |\mathbf{d}(\mathbf{k})|. \tag{2.47}$$

Therefore the two gaps are given by the constructive and destructive interference of the singlet and triplet terms. It can be seen that if the triplet term is small, then the two gaps will be nodeless, near isotropic and similar in magnitude. The ASOC is characterized by a vector $\mathbf{g_k}$, which depends on the crystal and electronic structures. The Hamiltonian has a term of the form $\alpha_{\mathrm{SO}}\mathbf{g_k} \cdot \mathbf{S}$, where α_{SO} is the strength of the ASOC. For example in the case of $\mathrm{CePt_3Si}$ and $\mathrm{Ce}T\mathrm{X_3}$ with space groups $P4mm$ and $I4mm$, inversion symmetry is broken as a result of a lack of a mirror plane perpendicular to the c axis. The resulting ASOC is to the leading orders of the Rashba type, where $\mathscr{H}_{\mathrm{ASOC}} \propto (\mathbf{k} \times \mathbf{z})$, which corresponds to $\mathbf{g_k} = (k_y, -k_x, 0)$. As discussed in Sec. 1.1.1, a loss of inversion symmetry is in general detrimental to triplet pairing states but there exists a direction along which the triplet state is protected. This corresponds to when $\mathbf{d}(\mathbf{k}) \parallel \mathbf{g}_{\mathbf{k}}$ and for this structure such a $\mathbf{d}(\mathbf{k})$ can be found in the p-wave channel [45].

2.2.6 Thermodynamic properties of superconductors

Having discussed BCS theory and in particular the existence of a gap in the single particle excitation spectrum, thermodynamic properties in the superconducting state can be examined. The existence of a gap $\Delta_{\mathbf{k}}$ will significantly modify the density of states around the Fermi level which will therefore strongly affect many thermodynamic quantities. These will also be sensitive to the structure of the gap, particularly the presence of nodes. This is because nodal gap structures have a non-zero density of states all the way down to the Fermi level, which is not the case for fully gapped systems.

The electronic contribution to the specific heat of a normal state metal has a linear temperature dependence given by [143]

$$C_{\mathrm{el}} = \frac{\pi^2}{3} N(E_{\mathrm{F}}) k_{\mathrm{B}}^2 T, \tag{2.48}$$

which is just γT. The total specific heat at low temperatures, taking into account electronic and phonon contributions is then given by

$$C = \gamma T + \beta T^3, \tag{2.49}$$

where β is related to Θ_{D} by

$$\Theta_{\mathrm{D}} \; = \; (12\pi^4 N_{\mathrm{A}} n k_{\mathrm{B}}/5\beta)^{\frac{1}{3}}, \tag{2.50}$$

where n is the number of atoms per mole. A different expression is needed below T_{c}, which can be found from considering the entropy of the superconducting state given by [144]

$$\frac{S}{\gamma T_{\mathrm{c}}} \; = \; -\frac{6}{\pi^2}\frac{\Delta_0}{k_{\mathrm{B}} T_{\mathrm{c}}} \int_0^\infty [f \ln f + (1-f)\ln(1-f)] dy, \tag{2.51}$$

where f is the Fermi-Dirac function with $\mathrm{E} = \Delta_0\sqrt{y^2 + \delta(T)^2}$, where y is the energy of the normal state electrons and $\delta(T)$ is the temperature dependence of the superconducting gap. Both of these quantities have been normalized by Δ_0 which following the approach of the α-model is not necessarily fixed to the BCS value. The left hand side is in fact normalized to the normal state entropy at T_{c}. As discussed in Sec. 2.2.2, the first derivative of the free energy is continuous for a second order phase transition and therefore the left hand side will be equal to unity at the transition in zero-field. The electronic contribution to the specific heat is then given by

$$\frac{C_{\mathrm{sc}}}{\gamma T} = \frac{\mathrm{d(S/\gamma T_c)}}{\mathrm{dt}}. \tag{2.52}$$

The specific heat is discontinuous at the transition and the size of the jump in BCS theory is given by $\Delta C/\gamma T_{\mathrm{c}} = 1.426$ [11]. More generally within the α-model, the magnitude of the jump in the specific heat is proportional to α^2 and is therefore given by [136]

$$\frac{\Delta C}{\gamma T_{\mathrm{c}}} = 1.426\left(\frac{\alpha}{\alpha_{\mathrm{BCS}}}\right)^2. \tag{2.53}$$

The structure of the gap has the most significant effect at low temperatures. For a fully gapped superconductor, at $T << T_{\mathrm{c}}$, there are no states within $\sim k_{\mathrm{B}}T$ of the Fermi level and therefore there are no accessible states for electrons become excited to. As a result, the specific heat has an exponential dependence at low temperatures with $C \propto (\Delta_0/k_{\mathrm{B}}T)^{3/2}\mathrm{e}^{-(\Delta_0/k_{\mathrm{B}}T)}$ [145]. Nodal superconductors have accessible states for excitations at all temperatures and these low lying excitations will dominate the specific heat at low temperatures. In the case of line and point nodes in the energy gap, T^2 and T^3 dependencies in the specific heat are expected [138].

As discussed in Sec. 2.2.3, the difference between the free energy densities of the superconducting and normal states is related to the square of the thermodynamic critical field B_{c}. This can then be calculated by integrating the entropy difference between the normal and superconducting states or by twice integrating the difference in the specific heat using

$$\Delta f = \frac{B_{\mathrm{c}}^2(T)}{2\mu_0} = \int_{T_{\mathrm{c}}}^{T}\int_{T_{\mathrm{c}}}^{T'} \frac{C_{\mathrm{sc}} - C_{\mathrm{n}}}{T''} dT'' dT'. \tag{2.54}$$

The penetration depth is another quantity which depends on the structure of the energy gap. From Eq. 2.26, $\lambda_{\mathrm{L}}^{-2} \propto n_s$ and therefore the temperature dependence of $\lambda_{\mathrm{eff}}^{-2}$ will give information about the temperature dependence of the superfluid density. This can be modelled as [134]

$$\frac{\lambda_{\mathrm{eff}}^{-2}(T)}{\lambda_{\mathrm{eff}}^{-2}(0)} = 1 + \frac{1}{\pi}\int_0^{2\pi}\int_{\Delta(T)}^{\infty} \frac{\partial f}{\partial E} \frac{E dE d\phi}{\sqrt{E^2 - \Delta^2(T,\phi)}}, \tag{2.55}$$

where $\Delta(T,\phi)$ has an angular dependence for anisotropic gaps. Plots are shown in

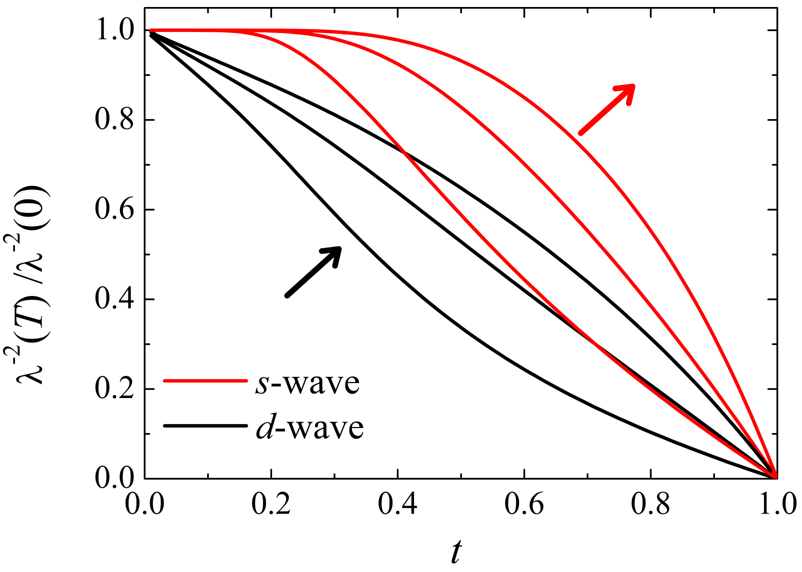

Figure 2.8: The temperature dependence of the penetration depth for an isotropic s-wave model and an anisotropic d-wave model with line nodes. The plots are shown for three values of Δ_0, one at the BCS value, and one above and below. The arrows indicate the direction of increasing Δ_0.

Fig. 2.8 for an s-wave fully isotropic model and a d-wave model with line nodes in the energy gap [146]. For the full gapped model, the penetration depth plateaus at low temperatures and the temperature at which this occurs increases with increasing gap size. This indicates that the superfluid density is constant at low temperatures. In a fully gapped system, there is a minimum pair breaking energy for the Cooper pairs at all points on the Fermi surface and if the thermal energy $k_{\mathrm{B}}T \ll \Delta_0$, then the thermal fluctuations are not energetic enough to deplete n_s, so it remains constant. For nodal superconductors, the thermal energy can always break pairs at some points on the Fermi surface and with increasing temperature, an increasing number of states are within $\sim k_{\mathrm{B}}T$ of the ground state and there is no plateau with constant n_s. At low temperature, there is a linear temperature dependence for $\lambda_{\mathrm{eff}}(T) - \lambda_{\mathrm{eff}}(0)$ in the presence of line nodes and a T^2 dependence for point nodes.

2.2.7 The clean and dirty limits

Having obtained a microscopic theory which can reproduce the phenomenological Ginzburg-Landau theory close to T_{c}, it is of interest to relate the characteristic length scales of this theory to microscopic properties. In particular, ξ was a characteristic length over which the order parameter ψ varied. Therefore it would be expected to be linked to a characteristic length of the extent of the Cooper pair wave function. This is the BCS coherence length (ξ_0) given by [11]

$$\xi_0 = \frac{\hbar v_{\mathrm{F}}}{\pi \Delta_0}, \tag{2.56}$$

where v_{F} is the Fermi velocity. Neglecting the elastic scattering of electrons from the lattice, this quantity is related to the coherence length in Ginzburg-Landau theory by $\xi \sim 0.74\xi_0$ [147]. This neglection is reasonable if the scattering rate is low and therefore the electrons have a long mean free path (l) between scattering events. The system is in this clean limit if $\xi_0 \ll l$. However, if the scattering rate is high, then ξ will be modified and in the dirty limit where $l \ll \xi_0$, $\xi \propto \sqrt{\xi_0 l}$. Therefore, strong elastic scattering reduces the effective coherence length from that expected from BCS theory. In the clean limit, λ_{eff} is given by $\lambda_{\mathrm{L}}/\sqrt{2}$. However, in the dirty limit

$$\lambda_{\mathrm{eff}} = \lambda_{\mathrm{L}} \sqrt{\frac{\xi_0}{1.33l}}. \tag{2.57}$$

The effect of strong scattering is to increase λ_{eff} and therefore reduce the effectiveness of the screening of magnetic fields from that expected from just considering the number of superconducting electrons. κ is now given by

$$\kappa = 0.96 \frac{\lambda_{\mathrm{L}}}{\xi_0}, \tag{2.58}$$

in the clean limit and

$$\kappa = 0.715 \frac{\lambda_{\mathrm{L}}}{l}, \tag{2.59}$$

in the dirty limit. In this case, κ is independent of ξ_0 but is instead inversely proportional to the mean free path.

2.2.8 Upper Critical Field

There are two pair-breaking mechanisms by which an applied field can destroy superconductivity in a type-II superconductor. The first is the orbital pair breaking, which occurs when there is significant overlap of vortex cores and the orbital upper critical field is given by Eq. 2.33. However, there is also the paramagnetic limiting effect. This can be understood by considering the effect of an applied magnetic field to a band of electrons [36]. This causes a splitting of the degenerate bands into spin-up and spin down bands and this lowers the energy of the system by an amount known as the Zeeman energys given by $\chi_{\mathrm{n}}H^2/2$, where χ_{n} is the normal state susceptibility, which is just the Pauli susceptibility for an electron gas. However, the spin susceptibility of the superconducting state (χ_{s}) is constrained by the nature of the pairing. Singlet Cooper pairs have opposite spins so if at $T = 0$ all the electrons on the Fermi surface are paired, then $\chi_{\mathrm{s}} = 0$. There is therefore an applied field for which there is a greater reduction in energy from the Zeeman energy then there is from the condensate energy, in which case the system will become normal. This is the Pauli paramagnetic limiting field (H_{P}) which is given by [36]

$$\mu_0 H_{\mathrm{P}} = \frac{\sqrt{2}\Delta_0}{g\mu_B\sqrt{\left(1-\chi_{\mathrm{s}}/\chi_{\mathrm{n}}\right)}}, \tag{2.60}$$

where $g = 2$ for free electrons. With the BCS theory value of Δ_0 from Eq. 2.42 and $\chi_{\mathrm{s}} = 0$ for an s-wave superconductor, the Clogston-Chandrasekhar limit is obtained [148] with $\mu_0 H_{\mathrm{P}} = 1.86T_{\mathrm{c}}$, where the coefficient has units of T/K. In the case of spin triplet superconductors, $\chi_{\mathrm{s}} = \chi_{\mathrm{n}}$ and there is no Pauli paramagnetic limiting. More complex pairing states can lead to anisotropic and intermediate values of χ_{s}, which will reduce but not entirely eliminate paramagnetic pair breaking.

The Werthamer-Helfand-Hohenberg (WHH) model analyzes B_{c2} within BCS theory in the dirty limit, taking into account both orbital and Pauli paramagnetic pair breaking effects [149]. The dirty limit will be appropriate in most cases where paramagnetic limiting is significant, since for many materials ξ_0 is large enough that $B_{\mathrm{c2}}^{\mathrm{orb}} \ll \mu_0 H_{\mathrm{P}}$ in the clean limit. In the dirty limit, ξ can be significantly reduced due to reduced l and therefore $B_{\mathrm{c2}}^{\mathrm{orb}}$ is large enough that Pauli paramagnetic limiting needs to be accounted for. A notable exception for this is in the heavy-fermion superconductors, where ξ_0 is much lower as a result of a greatly reduced v_{F} due to the large effective electronic masses. This is coupled with the fact that these systems are generally very clean, with large residual resistivity ratios. However, in the case of a BCS superconductor in the dirty limit, B_{c2} is found from solving

$$\begin{aligned} \ln\frac{1}{t} = &\left(\frac{1}{2}+\frac{i\lambda_{\mathrm{so}}}{4\delta}\right)\psi\left(\frac{1}{2}+\frac{h+0.5\lambda_{\mathrm{so}}+i\delta}{2t}\right) \\ &+\left(\frac{1}{2}-\frac{i\lambda_{\mathrm{so}}}{4\delta}\right)\psi\left(\frac{1}{2}+\frac{h+0.5\lambda_{\mathrm{so}}+-i\delta}{2t}\right)-\psi(0.5), \end{aligned} \tag{2.61}$$

where $\psi(x)$ is the digamma function, h is a dimensionless form of the upper critical field given by

$$h = \frac{4B_{\rm c2}}{\pi^2}\left(\frac{{\rm d}B_{\rm c2}}{{\rm d}t}\right)^{-1}_{t=1}, \tag{2.62}$$

and $\delta = \sqrt{(\alpha_M h)^2 - 0.25\lambda_{\rm so}^2}$. The two parameters which determine h are the Maki parameter α_M and the spin-orbit scattering parameter $\lambda_{\rm so}$. Since $\alpha_M = \sqrt{2}B_{\rm c2}^{\rm orb}/\mu_0 H_{\rm P}$, it is a measure of the relative influence of Pauli paramagnetic pair breaking compared to orbital limiting. $\alpha_M = 0$ corresponds to either the absence of paramagnetic limiting or when $B_{\rm c2}^{\rm orb} \ll \mu_0 H_{\rm P}$. In this limit, the upper critical field is given by

$$B_{\rm c2}^{\rm orb} \approx -0.693\left(\frac{{\rm d}B_{\rm c2}}{{\rm d}t}\right)_{t=1}. \tag{2.63}$$

The effect of increasing α_M is to increase the effect of paramagnetic pair limiting and therefore reduce the upper critical below the orbital value. $\lambda_{\rm so}$ characterizes the scattering rate for spin flip processes. The effect of spin flip scattering is to reduce the paramagnetic limiting effect. $\lambda_{\rm so}$ will not affect the upper critical field when $\alpha_M = 0$, but as $B_{\rm c2}$ is suppressed with increasing α_M, increasing $\lambda_{\rm so}$ will push it back towards the orbital value. The absolute values of $B_{\rm c2}$ within the WHH model can be obtained from Eq. 2.62 by determining the gradient of $B_{\rm c2}$ close to $T_{\rm c}$. Alternatively the gradient is related to α_M by

$$\alpha_M = 0.52758\left(\frac{{\rm d}B_{\rm c2}}{{\rm dT}}\right)_{T=T_{\rm c}}, \tag{2.64}$$

where the slope is given in units of T/K. Therefore, the WHH model allows the role of paramagnetic limiting to be examined. The absence or decrease in $H_{\rm P}$ can provide evidence for unconventional pairing symmetries. However, the WHH model is derived from one band, weak coupling BCS theory and it can be seen from Eq. 2.60 that $H_{\rm P}$ is likely to increase in a strongly coupled system. Furthermore, a sufficiently large $B_{\rm c2}^{\rm orb}$ is required to discern whether paramagnetic pair breaking effects have been suppressed.

2.3 Scattering theory

2.3.1 X-ray diffraction

X-ray diffraction is a powerful method of determining the structural properties of materials. It is observed in the coherent elastic scattering of x-rays from an ordered arrangement of atoms. The incoming x-rays have a wave vector $\mathbf{k_i}$ and $\mathbf{k_f}$ after scattering. For elastic scattering, $|\mathbf{k_i}| = |\mathbf{k_f}| = 2\pi/\lambda$ and the condition for constructive interference is

$$\mathbf{Q} = \mathbf{k_f} - \mathbf{k_i} = \mathbf{G}, \tag{2.65}$$

where $\mathbf{Q}$ is the scattering vector and $\mathbf{G}$ is a reciprocal lattice vector [143]. The reciprocal lattice corresponds to a Fourier transform of the real space lattice. Therefore information about the structure and orientation of crystal structure can be obtained from mapping the position and intensity of reciprocal lattice points. The diffraction condition can be visualized by considering the Ewald sphere construction shown in Fig. 2.9. Although shown in two dimensions, this is a sphere of radius $2\pi/\lambda$ where $\mathbf{k_i}$ touches one of the reciprocal lattice points. The condition for diffraction is that the point on the sphere touched by $\mathbf{k_f}$ is also a reciprocal lattice point, in which case the diffraction condition in Eq. 2.65 holds.

For measurements of single crystals with a monochromatic source, reciprocal space must be systematically measured by rotating the relative orientations of $\mathbf{k_i}$, $\mathbf{k_f}$ and the crystal. However, it is also possible to use the Laue method, whereby the x-ray beam has a wide range of wavelengths and there are a continuum of Ewald spheres with different radii. In this case, a large number of reflections will meet the diffraction condition for one of the constituent wavelengths and therefore if an area detector is used, many reflections can be recorded simultaneously. The diffraction pattern is sensitive to the orientation of the lattice and therefore from comparing simulated and observed patterns, the orientation of a single crystal relative to the incident beam can be deduced.

Rather than using single crystals, the diffraction from finely ground polycrystalline samples are often measured. Powdered material is used to ensure that the crystallites are randomly orientated and that there is no preferred direction. The scattering is measured as a function of the scattering angle 2θ and from considering the geometry of Fig. 2.9, the condition for diffraction becomes

$$\lambda = 2d_{hkl}\mathrm{sin}\theta, \tag{2.66}$$

where $d_{hkl} = 2\pi/|\mathbf{G}|$ for a reciprocal lattice vector $\mathbf{G} = (h\mathbf{a}* \; k\mathbf{b}* \; l\mathbf{c}*)$, and $\mathbf{a}*, \mathbf{b}*$ and $\mathbf{c}*$ are the basis vectors of the reciprocal lattice. Powder diffraction data is commonly fitted using the Rietveld method. This involves simulating the diffraction pattern for a specified crystal structure with a set of variable parameters. These include properties of the crystal structure such as lattice parameters, atomic positions and site occupancies. Additional variables can also be considered such as peak profile parameters, Debye-Waller factors, background terms and preferred orienta-

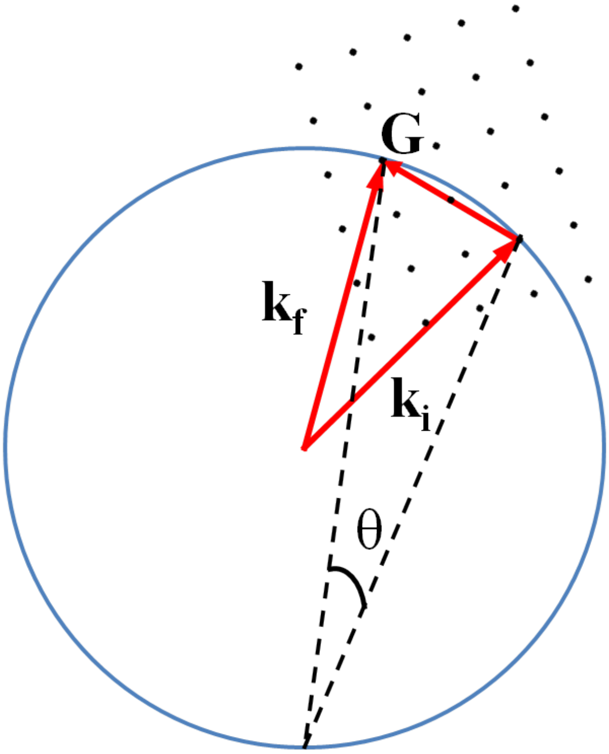

Figure 2.9: A diagram of the Ewald sphere when the condition for diffraction is met. The points correspond to points of the reciprocal lattice and therefore a vector joining two points is a reciprocal lattice vector. The condition in Eq. 2.65 holds since the points where $\mathbf{k_i}$ and $\mathbf{k_f}$ touch the sphere coincide with reciprocal lattice points.

tions. These are fitted so that the difference between the observed and simulated patterns are minimized. The absence of peaks in the observed pattern which appear in the simulated pattern may indicate an incorrect starting structure, although weak peaks may be too faint to be observed. The presence of peaks not predicted by the simulated pattern may indicate the presence of impurity phases. If these can be identified, multiple phases can be refined and the impurity fraction can be estimated. Significant discrepancies in intensities can indicate an additional effect that the model pattern does not correctly account for. There are several parameters for measuring the quality of a refinement and comparing different structural models [150]. The two used in this work are the weighted profile factor (R_{wp}) and the Bragg factor (R_{Bragg}). These are given by

$$R_{\text{wp}} = \left(\frac{\sum\limits_i w_i \left(y_{ci} - y_{oi}\right)^2}{\sum\limits_i w_i y_{ci}^2} \right)^{\frac{1}{2}}, \tag{2.67}$$

$$R_{\text{Bragg}} = \frac{\sum\limits_{hkl} \left| I_{c,hkl} - I_{o,hkl} \right|}{\sum\limits_{hkl} I_{o,hkl}}. \tag{2.68}$$

y_{ci} and y_{oi} are the calculated and observed intensities respectively at each point with a weight w_i inversely proportional to the square statistical uncertainty. $I_{c,hkl}$ and $I_{o,hkl}$ are the calculated and observed intensities for the peaks of the model. Both quantities are frequently expressed as percentages. R_{wp} is commonly used, as it gives the quality of fit for the whole model and can be related to the reduced χ^2. A poorer value of R_{wp} will be obtained if there are unindexed impurity peaks. This is less likely to be the case for R_{Bragg}, which only compares how well the peaks of the structural model are fitted. However, R_{Bragg} can not readily be related to statistical quantities [150]. R_{Bragg} can also be used to measure the quality of refinements of single crystal measurements and can also be used to get an indication of the quality of one component of a structure. For example, in the case of refining a model for neutron diffraction data with a crystal and magnetic structure, R_{Mag} can be defined which is given by Eq. 2.68 but only summed over the magnetic reflections.

Although aspects of x-ray diffraction have been discussed in this section, many of the above concepts can also be applied to neutron scattering measurements, which are discussed in the following section. There are several software packages for carrying out Rietveld refinements. In this work, TOPAS [151] has been used for refinements of x-ray diffraction data while the General Structure Analysis System

(GSAS) [152] and FullProf [153] have been used for neutron diffraction data.

2.3.2 Neutron scattering

Several properties of the neutron make it a useful probe of condensed matter systems. Owing to the nature of wave-particle duality, a particle of momentum p has a wavelength $\lambda = h/p$, where h is Planck's constant. The neutron has a mass of $m_n = 1.675 \times 10^{-27}$ kg and thermal neutrons with an energy of 300 K have a wavelength of 1.8 Å, which is comparable to the size of the lattice parameters of many crystalline solids. The neutron is a spin $\frac{1}{2}$ particle with a magnetic moment of $-1.913\ \mu_n$, where μ_n is the nuclear magneton. This compares to $\sim 2\ \mu_B$ for a free electron and since $\mu_n/\mu_B \sim (m_e/m_n)$, the nuclear magnetic moment is around 1000 times smaller than that of a free electron. It is therefore possible to study condensed matter systems from both the scattering of neutrons from nuclei and the magnetic moments of unpaired electrons.

2.3.3 Neutron diffraction

Neutrons are scattered by interactions with atomic nuclei. These are extremely short range nuclear forces and a neutron is symmetrically scattered from a nucleus. Unlike x-rays which scatter from the charge density of the electron clouds, neutrons are scattered from an extremely localized scatterer. The scattering length b characterizes the scattering strength of an individual nucleus. It is not only isotope dependent but if there is a nuclear spin, b depends on whether the neutron and nuclear spins align or antialign. A total cross section σ_{tot} can be defined which is the ratio of the total number of neutrons scattered per second and the incident neutron flux [154], and is given by $\sigma_{\text{tot}} = 4\pi b^2$. Although it is generally a very good assumption that neutrons scatter symmetrically, a strong angular dependence in the scattering from samples is often observed. These are coherence effects which arise from spatial correlations between scatterers. The angular dependence is given by the differential cross section, which is the ratio of the number of neutrons scattered per second through a solid angle $\mathrm{d}\Omega$ and the incident flux through $\mathrm{d}\Omega$. For elastic scattering from a crystalline material, this can be found by considering the scattering from a periodic array of atoms with a random distribution of scattering lengths b_j at a position $\mathbf{r_j}$. This takes into account the variation in scattering length from different isotopes and nuclear spin orientations. There is also factor of $\mathrm{e}^{i\mathbf{Q}\cdot\mathbf{r_j}}$, where $\mathbf{Q}$ by convention has the opposite sign to Eq. 2.65, which takes into account the phase relationship of waves scattered from different sites. From summing over pairs of sites, the differential cross section is given by [154]

$$\frac{\mathrm{d}\sigma}{\mathrm{d}\Omega} = \sum_{j,j'} \langle b \rangle^2 \mathrm{e}^{i\mathbf{Q}\cdot(\mathbf{r_j}-\mathbf{r_{j'}})} + \sum_{j} \left(\langle b^2 \rangle - \langle b \rangle^2 \right). \tag{2.69}$$

The first term has a $\mathbf{Q}$ dependence and describes coherent scattering. For a crystalline lattice, this is only non-zero when the Bragg condition for constructive interference (Eq. 2.65) holds and therefore this describes neutron diffraction. The strength of the coherent scattering is given by $b_{\mathrm{coh}} = \langle b \rangle^2$, which is the mean scattering length of the nuclei. The second term has no angular dependence and therefore describes incoherent scattering. The strength of the incoherent scattering is given by $b_{\mathrm{inc}} = \sqrt{\langle b^2 \rangle - \langle b \rangle^2}$, which is the standard deviation of the scattering amplitudes of the sample. In materials with a large average range of b, the incoherent background will be large.

Diffraction experiments can therefore be carried out with neutrons to measure the structure of materials as described in Sec. 2.3.1. There are advantages and disadvantages of using x-rays and neutrons in diffraction experiments. Neutrons are weakly interacting and scatter from the bulk of a material, whereas x-rays are strongly interacting and so do not usually penetrate beyond the surface. The scattering intensities of x-rays depends on the charge density of the electron clouds and therefore increases monotonically with the atomic number Z. As a result, the x-ray scattering from a structure is dominated by heavy elements and the position of light atoms may be difficult to measure. Furthermore, atoms of similar atomic number will have very similar scattering intensities, making it difficult to distinguish between them. However, neutron scattering lengths are dependent on complex nuclear processes and are not systematic in Z. Atoms with similar Z may scatter neutrons by dramatically different amounts, allowing for their role in crystal structures to be distinguished. Neutron scattering will not be suitable for measuring all compounds. There is also a finite probability that a nuclei will absorb rather than scatter a neutron. For example, naturally occurring gadolinium has a thermal absorption cross section ~ 275 times as large as the scattering cross section. In this case, the scattering will be extremely difficult to measure unless less absorbing isotopes are used. Neutron scattering measurements are also often more resource intensive, since large scale facilities are required to safely produce the requisite number of neutrons. This is in contrast to x-rays, where many diffraction experiments can be performed on small scale instruments. Also, the weak interaction of neutrons means that larger samples are required which may not be obtainable. X-ray diffraction measurements often only requires very small samples, particularly if high intensity synchrotron sources are used.

2.3.4 Diffraction from magnetic structures

As discussed previously, the neutron has a magnetic moment and can be scattered from the moment of unpaired electrons. Therefore, diffraction will also result from the periodic arrangements of magnetic moments as well as periodic nuclear arrangements. A magnetic differential cross section similar to Eq. 2.69 can be defined with b_j replaced by a magnetic scattering length. There are two important differences to the case of nuclear scattering. Firstly, the scattering of neutrons from a nucleus is spherically symmetric. However, there is an angular distribution to the magnetic scattering and the magnitude depends on the relative orientations of the magnetic moment and $\mathbf{Q}$. In particular, the magnitude of the scattering depends on the component of the moment perpendicular to the scattering vector and no magnetic scattering is observed when the two are parallel. A second difference is that while nuclei can be treated as point-like particles, the finite size of the scatterer for electron orbitals must be taken into account. This is done by the multiplication of a magnetic form factor ($F(\mathbf{Q})$) which can be approximated using the method of P.J. Brown in Ref. [155]. The form factors of Ce and Mn ions are shown in Fig. 2.10. The form factor drops more rapidly for the Mn than the Ce ions. This reflects the fact that cerium contains unpaired $4f$ rather than $3d$ electrons, which are more localized and therefore the effective size of the scatterers are smaller.

The origins of long range magnetic order are discussed in Sec. 2.1.3 and in this section there will be an overview of using neutron diffraction to study the resulting magnetic structures. A periodic magnetic structure will have a repeating unit called the magnetic unit cell which will in general not be equal to the unit cell of the lattice. The periodicity of the magnetic cell can be described by a propagation vector $\mathbf{k}$. The modulation of the magnetic moment is given by [156]

$$\mathbf{m_j} = \mathbf{\Psi_j} \mathrm{e}^{-2\pi \mathbf{k}\cdot\mathbf{r}}, \tag{2.70}$$

where $\mathbf{r}$ is in units of lattice spacings and $\mathbf{\Psi_j}$ is a vector which describes the magnetic moment at the origin in terms of projections of the magnetic moment along the crystallographic axes. For example, $\mathbf{\Psi_j} = (0, 0, 1)$ describes a magnetic moment pointing along the c axis. More generally, $\mathbf{\Psi_j}$ can be expressed as the sum of several basis vectors with a particular weighting. It can be seen from the above equation that when $\mathbf{k}\cdot\mathbf{r}$ is equal to an integer, $\mathbf{m_j}$ is unchanged from the position at the origin and this therefore defines the periodicity of the magnetic unit cell. So for

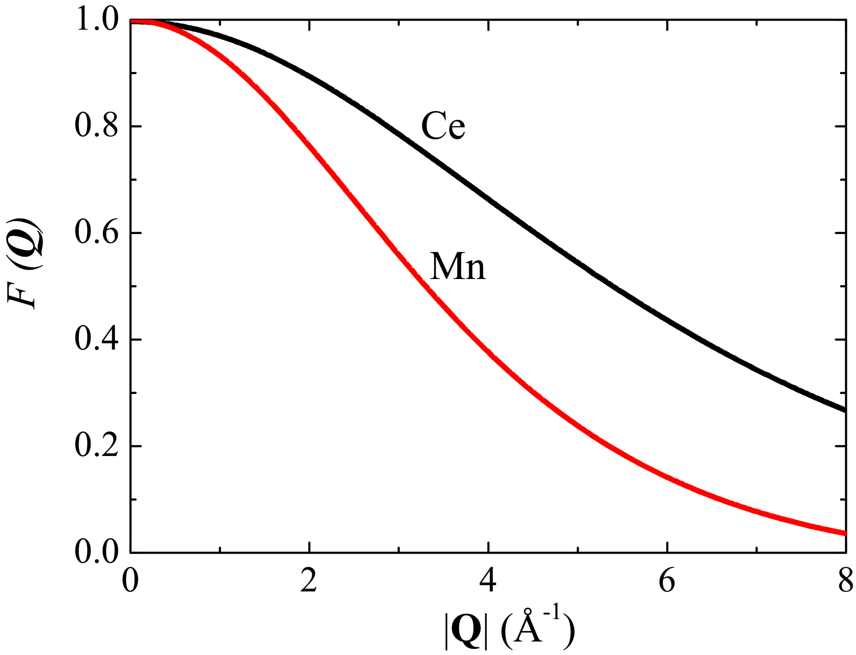

Figure 2.10: The magnetic form factors of cerium and manganese ions, calculated from Ref. [155]. For the manganese ion it has been assumed that $g_J = 2$.

$\mathbf{k} = (0, 0, \frac{1}{2})$, $\mathbf{k} \cdot \mathbf{r}$ is an integer for $\mathbf{r} = (0, 0, 2n)$ and the magnetic unit cell is now twice as long as the nuclear cell along the c axis. For a primitive cell this describes an antiferromagnetic structure with alternating equal moments. Since the periodicity of the magnetic lattice is different to the crystal lattice, additional magnetic Bragg peaks are observed at $(hkl) \pm \mathbf{k}$, where (hkl) corresponds to an allowed nuclear reflection. For $\mathbf{k} = 0$, there is no change in the moment for any translations and this corresponds to a ferromagnetic structure. In this case, there is an increase in the intensity of the nuclear reflections.

From indexing the positions of magnetic reflections, the magnetic propagation vector(s) can be deduced. However, for a particular propagation vector there may be a wide range of possible magnetic structures. Magnetic representation theory allows for the number of possible magnetic structures to be reduced. The results are based on group theoretical arguments described in Ref. [156]. A given crystal structure has an associated space group G_0 [155]. This is the group of symmetry operations which leave the crystal structure unchanged. For a given propagation vector, the little group G_k is the subgroup of G_0 which also leaves $\mathbf{k}$ invariant. Within the Landau theory of second order of phase transitions (Sec. 2.2.2), the basis vectors which make up $\mathbf{\Psi_j}$ in Eq. 2.70 must all correspond to one of the irreducible representations of G_k. This can significantly reduce the number of possible magnetic structures which need to be tested against experimental data. For example, in Sec. 4.4 a propagation vector of $\mathbf{k} = (0, 0, \frac{1}{2})$ is observed at 2 K in neutron diffraction measurements of CeCoGe$_3$. The software package SARAh [157] was used to find the irreducible representations of G_k and the corresponding basis vectors. This analysis showed that the magnetic structure can correspond to two possible irreducible representations, one of which is one dimensional, labelled Γ_2^1 and the other is two dimensional, labelled Γ_5^2. For the Γ_2^1 representation, the only associated basis vector points along the c axis while the Γ_5^2 representation contains basis vectors pointing along a and b. Therefore, provided the magnetic structure corresponds to only one representation, the allowed magnetic structures either have the moments pointing along the c axis or in the ab plane.

2.3.5 Inelastic neutron scattering

Neutron diffraction corresponds to coherent, elastic scattering. The cross section given by Eq. 2.69 is summed across all energies and this is usually taken as the elastic cross section, since the elastic component is generally much larger than the inelastic. The inelastic scattering can also be studied and this gives information about excitations of the system. Once again, the scattering can be split into coherent and incoherent components. The coherent partial differential cross section for N scatterers is given by [158]

$$\left(\frac{\mathrm{d}^2\sigma}{\mathrm{d}\Omega\mathrm{d}E_\mathrm{f}}\right)_{\mathrm{coh}} = N\langle b\rangle^2\frac{k_f}{k_i}S(\mathbf{Q},\omega). \tag{2.71}$$

$S(\mathbf{Q},\omega)$ is the scattering function which describes the scattering intensity as a function of both the momentum transfer $\mathbf{Q}$ and energy transfer $\hbar\omega = E_\mathrm{i} - E_\mathrm{f}$. A similar expression can be found for the incoherent cross section but with the prefactor from the right hand side of Eq. 2.69. The coherent inelastic scattering gives information about collective excitations of the system. In the case of nuclear scattering, these correspond to phonons which are quantized excitations corresponding to collective modes of the lattice.

There can be several origins of magnetic excitations. Transitions between CEF levels (see Sec. 2.1.2) can be probed directly. Due to the dipole selection rules, transitions are only allowed between levels where $\Delta m_J = \pm 1$. From an analysis of the energy dependence of the magnetic scattering integrated over $\mathbf{Q}$, the CEF Hamiltonian in Eq. 2.4 can be solved and the values of B_m^n obtained. Spin wave excitations in the magnetically ordered state can also be studied. The dispersion curves for these excitations can be mapped out, which gives information about the exchange interactions between magnetic ions. Inelastic neutron scattering is also used to study the Kondo effect in materials (Sec. 2.1.4). In many Kondo systems, broad magnetic quasielastic scattering is observed. That is a peak of magnetic scattering centred at $\omega = 0$ but with a Lorentzian linewidth (half width at half maximum) Γ broader than the elastic resolution of the instrument. Γ often scales with temperature according to a power law but extrapolates to a zero temperature value $\Gamma(0) \sim k_{\mathrm{B}}T_{\mathrm{K}}$ [159]. The magnetic scattering integrated over $\mathbf{Q}$ is fitted with

$$S_{\mathrm{mag}} = \frac{\hbar\omega}{1 - \exp\left(-\hbar\omega/k_{\mathrm{B}}T\right)} \frac{A\Gamma}{\Gamma^2 + (\hbar\omega)^2}, \tag{2.72}$$

where A is a constant. The left hand fraction is necessary to satisfy detailed balance. A linear temperature dependence is predicted when the thermal energy is much less than the first CEF excitation [160]. However a $\sqrt{T}$ [161] dependence and temperature independent [162] behaviour are also sometimes observed. In systems where the f electrons remain sufficiently localized, excitations due to CEF levels are still observed but these are broadened due to hybridization with the conduction electrons. For systems with a stronger Kondo coupling in the intermediate valence regime, CEF levels are not present and a broad peak in the magnetic scattering is observed at non-zero ω at low temperatures.

When analyzing the magnetic scattering, it is often useful to have knowledge of S_{mag} in absolute units (typically mb/sr meV formula unit). This requires both a means of obtaining $S(\mathbf{Q},\omega)$ in absolute units and a method of isolating the magnetic contribution. The former is done by normalizing the spectra to a standard vanadium sample. Vanadium is used because it has an incoherent cross section of 5.08 b but a coherent cross section of just 0.02 b and therefore the elastic scattering is very nearly angularly independent. The magnetic contribution is obtained by subtracting an estimate of the phonon contribution, often from measuring the scattering of non-magnetic analogues. Ideally these will be isostructural to the magnetic compound of interest and contain atoms of a similar atomic weight. Once the scattering of the non-magnetic compound ($S^{\mathrm{ph}}(\mathbf{Q},\omega)$) is obtained, one method of obtaining the magnetic contribution is to use

$$S_{\mathrm{mag}}(\mathbf{Q},\omega) = S(\mathbf{Q},\omega) - \alpha S^{\mathrm{ph}}(\mathbf{Q},\omega), \tag{2.73}$$

where α is the ratio of the coherent scattering cross sections of the magnetic and non-magnetic compounds. This is expression is often able to satisfactorily subtract the phonon scattering [163]. However, particularly when there are differences between the phonon energies of the two compounds, Eq. 2.73 does not adequately remove the phonon contribution. In this case, there is another method for obtaining estimated integrated cuts of S_{mag}. Firstly, cuts of $S(\mathbf{Q},\omega)$ and $S_{\mathrm{ph}}(\mathbf{Q},\omega)$ are made by integrating over low $|\mathbf{Q}|$ (S_{lQ}) and high $|\mathbf{Q}|$ (S_{hQ}) regions for the magnetic and non-magnetic compounds respectively. It is then assumed that the phonon contributions for the two compounds have the same $|\mathbf{Q}|$ dependence and that the magnetic contribution to S_{hQ} is negligible. This is likely to be the case, since phonon scattering increases with $|\mathbf{Q}|$, while the magnetic scattering falls due to $F(\mathbf{Q})$. In this case, the magnetic contribution is given by

$$S_{\mathrm{mag}} = S_{\mathrm{lQ}} - \frac{S_{\mathrm{lQ}}^{\mathrm{ph}}}{S_{\mathrm{hQ}}^{\mathrm{ph}}} S_{\mathrm{hQ}}. \tag{2.74}$$

This will be non-zero if there is additional scattering at low $|\mathbf{Q}|$ and is less sensitive to the absolute positions of the phonon peaks.

Chapter 3

Experimental techniques

3.1 Sample preparation

3.1.1 Polycrystalline samples

Polycrystalline samples were produced either using a Centorr tri-arc or a Cyberstar tetra-arc furnace. The constituent materials were placed on a water cooled copper hearth. With the tri-arc furnace, the sample chamber was evacuated several times with a rotary pump and flushed with argon before the samples were melted under a positive pressure of argon. For the tetra-arc furnace, the chamber was also flushed several times with argon before being evacuated with a turbo pump and the melting was carried out under a partial pressure of argon. The chamber of the tetra-arc furnace is displayed in Fig. 3.1. For both furnaces, tungsten electrodes are linked to a DC welding power supply and upon striking them against the hearth, an arc of current is created between the tip of the electrode and the hearth which can be used to melt the materials. Samples were flipped and remelted several times to improve homogeneity. The as-cast samples were subsequently sealed in evacuated quartz tubes and annealed in a box furnace to improve homogeneity and phase purity. Typically the samples were annealed at 900°C for two weeks.

3.1.2 Single crystals

Single crystals of $\mathrm{CeCoGe_3}$ were produced using the flux method [164], following the procedure outlined in Ref. [60]. Polycrystalline $\mathrm{CeCoGe_3}$ and the flux material bismuth (in a molar ratio of $\sim 1:20$) were placed in an alumina crucible, which was sealed inside an evacuated quartz tube. The quartz tube was necked in the middle where a metallic gauze was fixed. The tube was placed in an upright position in a box furnace. The tube was heated from room temperature to 1050°C at a

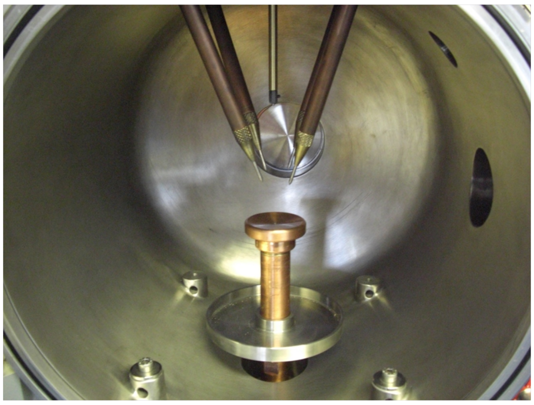

Figure 3.1: Photograph of the sample chamber of the Cyberstar tetra-arc furnace.

rate of 60°C/h. It was kept at this temperature for 24 hours before being slowly cooled at 1°C/h until it reached 650°C. At this temperature $CeCoGe_3$ has solidified but the bismuth is still liquid since it has a melting point of 271°C [165]. The tube was removed at this temperature, the liquid bismuth was drained and single crystals were obtained. Excess bismuth was removed by washing the crystals with a solution of 1 : 1 nitric acid (70%) and water. The flux method can be used to obtain crystals of materials which do not melt congruently, so may not be obtainable by other methods. However, the crystals are often not as large as those grown using the optical floating zone or Czochralski methods. There is also the possibility of there either being macroscopic regions of flux becoming embedded in crystals or substitution of the flux material for elements in the desired phase. These can be particularly problematic when measuring resistivity, since it can be difficult to discern whether a superconducting signal originates from the bulk material or surface regions of flux.

3.2 Magnetization

Magnetization measurements were made using a Quantum Design Magnetic Property Measurement System (MPMS) [166]. This is a magnetometer which utilizes a superconducting quantum interference device (SQUID) to make sensitive magnetization measurements. The system consists of a probe mounted in a dewar of helium-4, surrounded by a jacket filled with liquid nitrogen. For measurements between 1.8 and 400 K, samples are mounted inside a straw attached to a sample rod which is inserted vertically into the probe. The measurement system is illustrated in

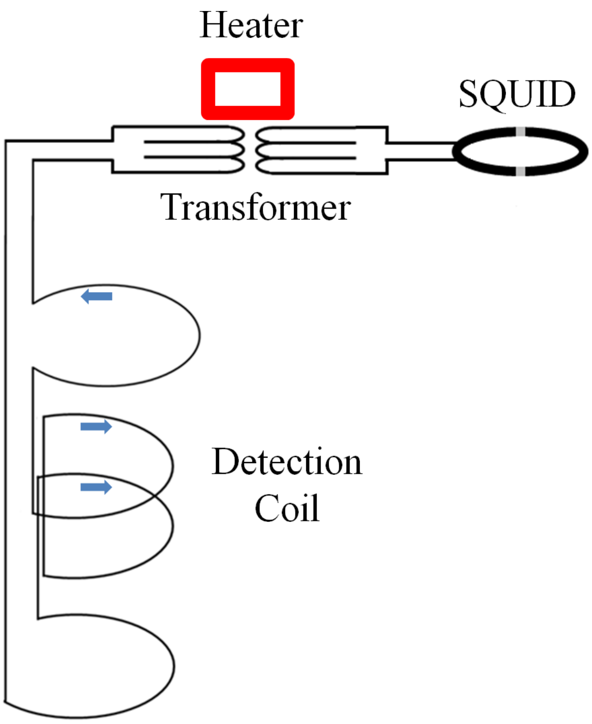

Figure 3.2: A schematic diagram of the detection system for the MPMS SQUID magnetometer. The circuit is made of superconducting wire which is kept in the superconducting state, except when the heater is engaged. The diagram was adapted from Ref. [166]

Fig. 3.2, where the sample is moved through a pair of superconducting coils, inducing supercurrents. A typical measurement consists of measuring 32 points across a scan length of 4 cm. The change in current at each step is converted by the SQUID to a voltage extremely accurately. The output voltage as a function of position is fitted with a model of the response to a dipole field. After calibration with a sample of known magnetic susceptibility, the absolute magnetization of an unknown sample can be obtained. The heater in the circuit shown in the diagram periodically drives the coil and SQUID into the normal state between measurements, which serves to remove the otherwise persistent currents in the system. Measurements can be performed in applied fields up to 7 T.

Magnetization measurements between 0.48 and 1.8 K were made using an iQuantum ^{3}He insert [167]. The sample rod is enclosed in a thin pipe which is inserted into the sample space of the MPMS. A closed system is formed between the pipe and the external ^{3}He tank. This operates in 'one shot' mode whereby the

^{3}He is condensed at the bottom of the pipe and the system is cooled to the base temperature. The magnetization as a function of temperature can be measured by warming the system from the base temperature, or alternatively measurements as a function of field can be performed by holding the sample space at a fixed temperature. Once the liquid ^{3}He has evaporated, it returns to the gas tank of the system and further measurements require the gas to be recondensed.

3.3 Resistivity

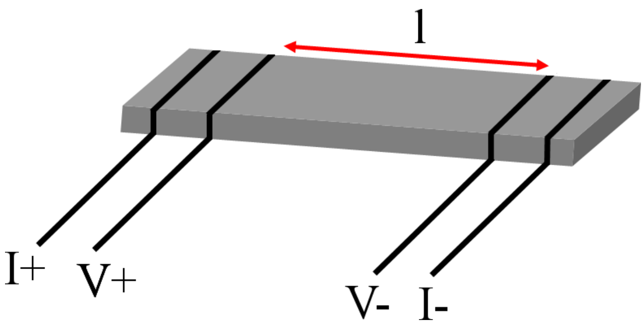

Figure 3.3: A schematic diagram of the sample for a four probe resistivity measurement, where l is the distance between the two voltage wires.

The resistivity was measured using the four-probe method with a Quantum Design Physical Properties Measurement System (PPMS). Measurements were either performed down to 1.8 K, or to 0.4 K using a ^{3}He insert. Magnetic fields up to 9 T were applied during the measurements. The samples were cut into bar shaped pieces and four silver wires, 0.05 mm in diameter were attached to the surface using DuPont 4929N silver paste as illustrated in Fig. 3.3. Either a direct or alternating current passes between the two outer wires, while the voltage is measured across a distance l between the two inner contacts and the resistivity (ρ) is calculated from the resistance (R) and the cross sectional area (A) by

$$\rho = \frac{RA}{l}. \tag{3.1}$$

3.4 Specific heat

The specific heat was measured in a Quantum Design PPMS between 1.8 and 400 K, or down to 0.4 K with a ^{3}He insert. Measurements were performed in applied fields of up to 9 T. The measurements were performed using the relaxation method, whereby the sample is mounted on a platform which is suspended by wires attached to a copper heat sink held at a constant temperature [168]. The samples were prepared with at least one polished face, which is mounted on the stage using Apiezon N or H grease to ensure a good thermal contact. The platform is made of sapphire and a heater and thermometer are attached to the underside. The wires allow both an electrical connection to these puck components and also create a thermal link between the otherwise isolated platform and the heat sink. The measurement is performed by switching on the heater to heat the platform before turning it off, with the platform temperature being measured during the heating and cooling stages. The relaxation of the platform temperature can either be fitted with a single or pair of exponential functions. The latter corresponds to a two-tau model, where there is an imperfect thermal contact between the platform and sample. In this case, there will be a fast relaxation process due to the fact that the stage initially equilibrates quickly with the thermal bath, while for the sample this is a slower process. To accurately measure the specific heat of the sample, addenda measurements of the stage and grease are made and the sample heat capacity is obtained from subtracting the heat capacity of the addenda from the total.

3.5 Neutron scattering

The theory of neutron scattering is described in Sec. 2.3.2. In this section aspects of neutron production and instrumentation are outlined. Neutron scattering facilities can either be classified as reactor or spallation sources. In this work, neutron scattering measurements have either been carried out at the Institut Laue-Langevin in Grenoble, France or at the ISIS pulsed neutron source at the Rutherford Appleton Laboratory, Didcot, UK.

The Institut Laue-Langevin (ILL) is a reactor source. A neutron flux of 1.5×10^{15} s^{-1} is produced by a water cooled reactor fuelled by enriched uranium. As well as the moderating effect of the cooling water, there is an additional heavy water moderator which decelerates the neutrons produced by fission reactions. The result is a distribution of neutron wavelengths which peaks at 1.2 Å(∼660 K) [154]. There is also a hot graphite moderator at 2400 K for producing higher energy neutrons and two liquid hydrogen moderators at 25 K for lower energies. Neutron scattering instruments are either located in the reactor hall or in one of two guide halls located at a further distance.

The ISIS pulsed neutron and muon source is a spallation source. Neutrons are produced by colliding pulses of protons with a tungsten target. H^- ions are accelerated in a linear accelerator to 70 MeV before being injected into a circular synchrotron. The ions are stripped of their electrons upon entering the synchrotron and are accelerated to energies of 800 MeV. Pulses of protons are extracted and four out of five pulses are directed to target station 1, while the remaining pulse is directed to target station 2. Each target station contains a target made of tungsten clad with tantalum and fast neutrons are produced upon collisions with the proton pulses. The high energy neutrons are slowed by various moderators. Both target stations have water moderators but target station 1 has additional moderators consisting of liquid methane at 110 K and hydrogen at 20 K while target station 2 has a 40 K solid methane moderator and one consisting of liquid hydrogen at 17 K.

3.5.1 Single crystal neutron diffraction

A diagram of the single crystal neutron diffractometer D10 at the ILL is shown in Fig. 3.4. Neutrons of a single energy are selected with the use of either a pyrolytic graphite or copper monochromator. In this work, the graphite monochromator was used to select an incident wavelength of 2.36 Å. D10 can be operated in four circle mode, where the sample sits in a Eulerian cradle where it can be rotated about three axes while the detector is rotated about one. To reduce the background signal, the instrument can be operated with an energy analyzer. In this case, the scattered neutrons are measured with a single ^{3}He detector after passing through vertically focussed pyrolytic graphite. This ensures that only neutrons with the same wavelength as the incident beam are detected. However, due to the physical dimensions of the analyzer, the angular coverage is reduced when it is used. With knowledge of both the neutron energy and angle of scattering, the momentum transfer can be deduced [154].

3.5.2 Inelastic neutron scattering

To perform inelastic neutron scattering measurements, it is necessary to have knowledge of the energy of both incident and scattered neutrons. This can be obtained either by using the triple-axis or time-of-flight techniques. With a triple-axis spectrometer, both the initial and final energies are selected using a crystal analyzer. However, all the inelastic neutron scattering instruments used in this work are time-of-flight spectrometers. For direct geometry spectrometers, the initial energy of a neutron pulse is selected and the energy of the scattered neutrons are deduced from the time taken for them to reach the detectors. In the case of indirect geometry spectrometers, the initial pulse is not monochromated but the scattered beam is passed

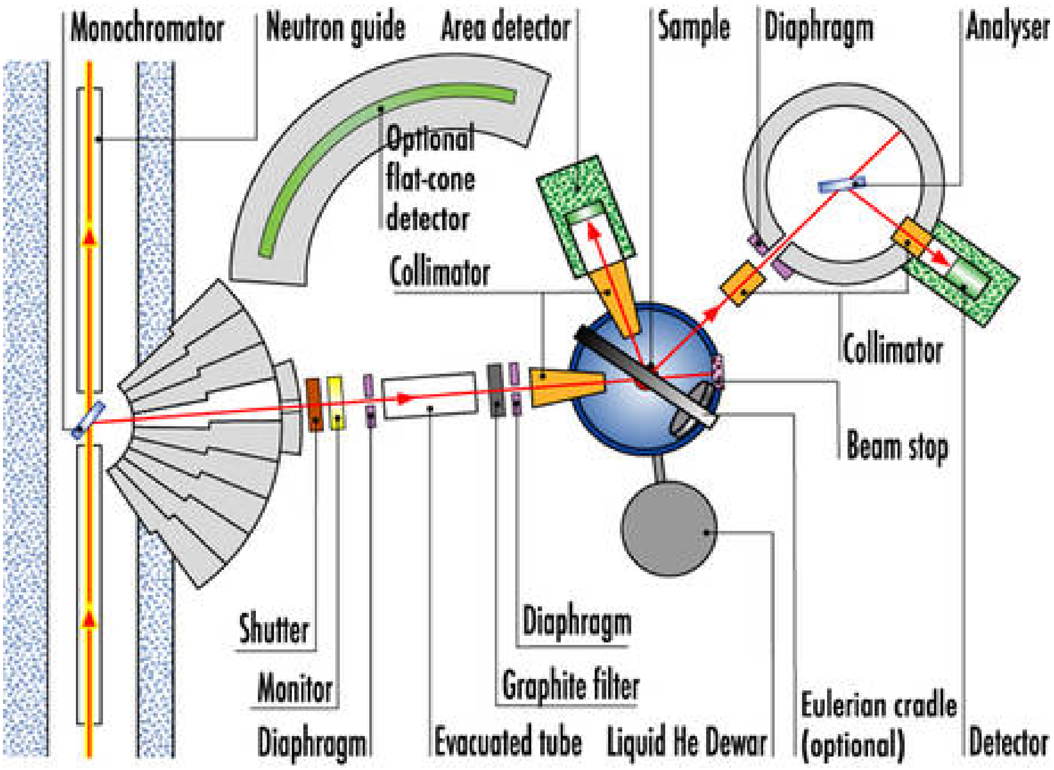

Figure 3.4: The layout of the D10 single crystal neutron diffractometer. Taken from Ref. [169].

through an analyzer so that neutrons of a single energy reach the detectors. At a neutron source such as ISIS, the time of flight instruments can exploit the pulsed structure of the neutron beam, whereas time-of-flight instruments at continuous sources require that the incident neutron beam is split into discrete pulses.

The IN6 spectrometer at the ILL is shown in Fig. 3.5. The white beam of neutrons enters the triple monochromator where up to three incident energies can be selected using crystals of pyrolytic graphite. Higher energy neutrons from higher order reflections are then removed by the beryllium filter. The beam is split into discrete pulses using a Fermi chopper. This is a large drum, rotating about an axis perpendicular to the neutron beam. It consists of alternating sheets of aluminium of gadolinium and therefore only neutrons traveling along the direction of the aluminium can pass through the chopper and a continuous beam will be split into a discrete one. The scattered neutrons are detected at a bank of ^{3}He detectors which covers a scattering angle of 10 to 115°. From the time taken for the scattered

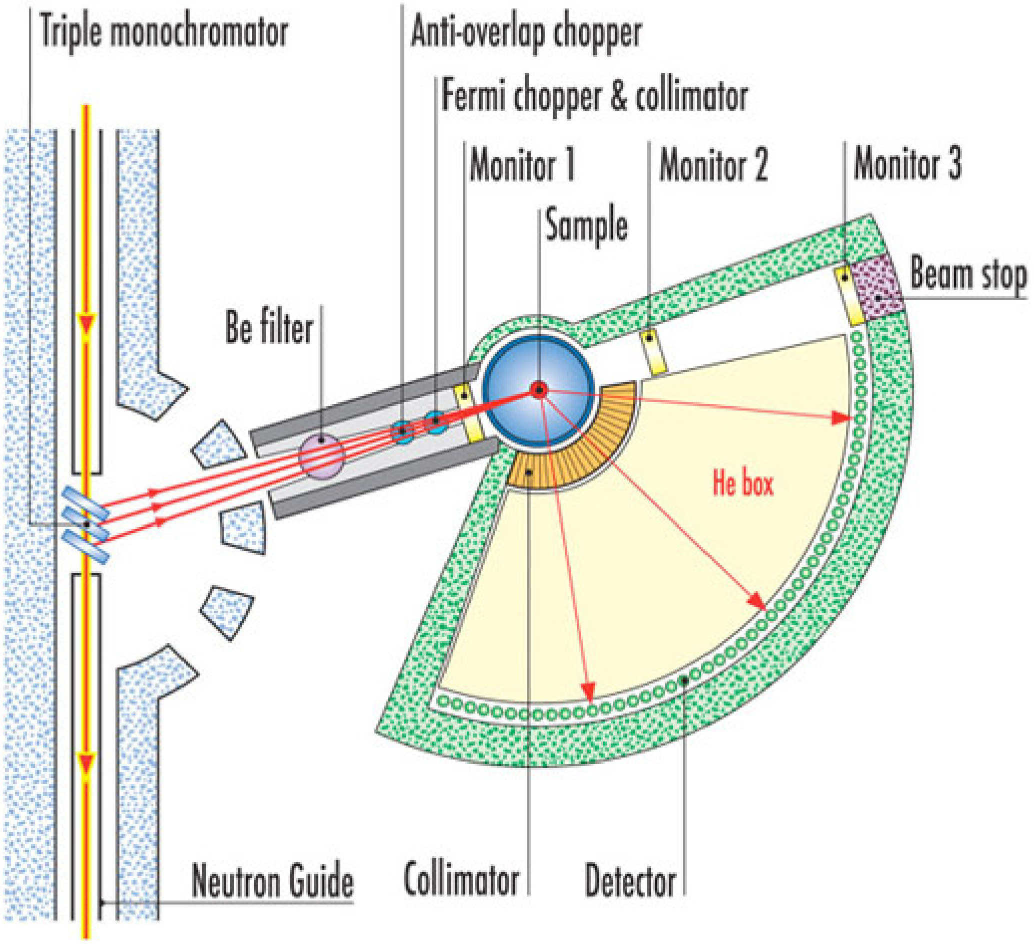

Figure 3.5: The layout of the IN6 inelastic neutron spectrometer. Taken from Ref. [170].

neutrons to reach the detector at a particular angle, $S(\mathbf{Q},\omega)$ can be measured.

3.6 Muon spin rotation/relaxation

Muon spin rotation and relaxation are two techniques, both denoted by μSR, whereby spin polarized, positive muons (μ^+) are implanted into materials and the magnetic field distribution at the muon stopping site is deduced from the directional dependence of the positrons emitted from μ^+ decay. The muon is one of the elementary particles of the standard model of particle physics and is a second generation lepton, where the electron is the corresponding first generation particle. Like the electron, the muon is a spin $\frac{1}{2}$ particle but due to having a larger mass of approximately 11% of that of the proton, the magnetic moment is considerably smaller, just $\sim 0.005\ \mu_{\mathrm{B}}$.

Positive muons are produced by the decay of positive pions. At the ISIS pulsed neutron and muon source, these are produced by colliding pulses of protons with a graphite target. As described in the previous section, pulses of accelerated protons are extracted from a synchrotron and directed towards one of two target stations. Before reaching target station 1, the protons pass through a graphite target and pions are produced via the collision of protons by [171]

$$\mathrm{p} + \mathrm{p} \rightarrow \pi^{+} + \mathrm{p} + \mathrm{n}. \tag{3.2}$$

A proton colliding with a neutron can also produce π^{+} particles but in this case two neutrons are produced. The pion is unstable and quickly decays to produce a muon and a muon-neutrino by

$$\pi^{+} \rightarrow \mu^{+} + \nu_{\mu}. \tag{3.3}$$

If the pion is at rest, the muons produced will be 100% spin polarized antiparallel to the direction of travel of the muon beam [172]. It is therefore possible to produce a beam of nearly entirely spin polarized muons, which are implanted into the samples at the instrument. The implanted muons are rapidly decelerated by electrostatic interactions so that they come to rest in the material, while the polarization of the moments remains unchanged. Muons decay with a half life of 2.2 μs by

$$\mu^{+} \rightarrow \mathrm{e}^{+} + \nu_{\mathrm{e}} + \bar{\nu_{\mu}}. \tag{3.4}$$

It is the positron emitted from this decay which is detected in a μSR experiment. The positron is emitted preferentially in the direction of the muon spin and this can be used to study the magnetic field at the muon stopping site. The angular dependence of the emitted positron direction is given by

$$N(\theta) \propto 1 + a\mathrm{cos}\theta, \tag{3.5}$$

where $N(\theta)$ is the number of positrons emitted at an angle θ to the muon spin. The parameter a measures the strength of the asymmetry and $a \sim 0$ for low positron energies, $a \sim 1$ at high energies and $a = \frac{1}{3}$ is obtained integrating over all energies. The configuration of a μSR experiment is shown in Fig. 3.6. The two detectors in blue are shown in the forward (F) and backward (B) positions relative to the sample. In the longitudinal field configuration, a magnetic field is applied parallel

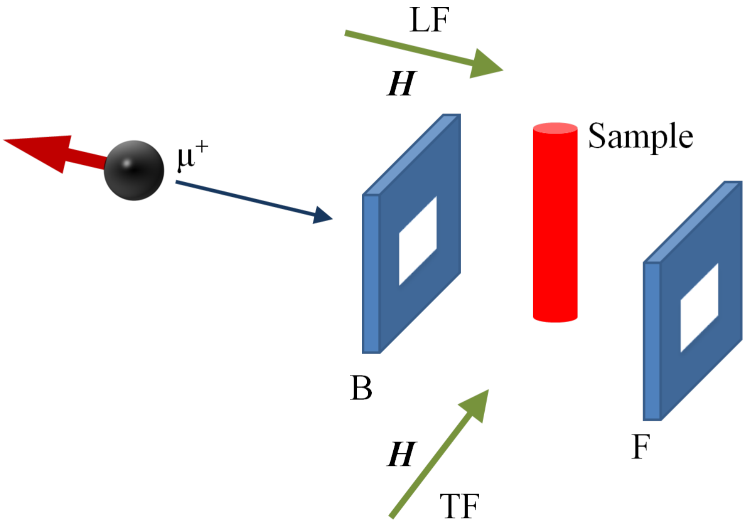

Figure 3.6: A typical geometry of a μSR experiment. Two detectors are shown in blue in the forward (F) and backward (B) positions relative to the sample. The direction of the applied field (**H**) is shown for the longitudinal field (LF) and the transverse field (TF) configurations.

to the direction of the muon beam, whereas it is perpendicular in the transverse field configuration. Although the detectors are shown in the forward and backward positions, for transverse field measurements they can be positioned along any axis perpendicular to the applied transverse field. Typically in a μSR experiment, the asymmetry as a function of time is measured, which is calculated by

$$A(t) = \frac{N_B - \alpha N_F}{N_B + \alpha N_F}, \tag{3.6}$$

where N_F and N_B are the number of counts in the forward and backward positions, and α is a calibration constant. Using $\alpha = 1$ for an ideal pair of detectors and substituting in Eq. 3.5 with $a = \frac{1}{3}$, a maximum asymmetry of $\frac{1}{3}$ is obtained for fully polarized muons. The maximum asymmetry on a real instrument will be less than this. If there is a magnetic field at the muon stopping site, the muon spin will precess about it and $A(t)$ will therefore be sensitive to the magnitude, distribution and dynamics of the magnetic field. This is described in much greater deal in Refs. [172, 173] but some results for situations applicable in this work will now be given.

Firstly, a distribution of static fields can be considered. This is applicable to many materials, since muons are sensitive to nuclear magnetic moments. Although these are not entirely static, the fluctuation rate is slower than the muon life time and therefore this is a valid approximation. In the case of a random Gaussian field distribution, the asymmetry is given by [173]

$$A(t) = A\left[\frac{1}{3} + \frac{2}{3}(1 - \sigma^2 t^2)\exp\left(-\frac{\sigma^2 \mathrm{t}^2}{2}\right)\right], \tag{3.7}$$

where the Gaussian width of the field distribution is given by σ/γ_μ and $\gamma_\mu/2\pi = 135.53$ MHz T^{-1} is the gyromagnetic ratio of the muon.

The relaxation of the asymmetry in the presence of fluctuating moments can also be considered. In the limit of fast fluctuations the relaxation is given by [172]

$$A(t) = A\mathrm{e}^{-\Lambda t}, \tag{3.8}$$

where Λ is the fluctuation rate. In a transverse field, the magnetic moment of the muon precesses, leading to oscillations in the asymmetry. A transverse field at the muon site may arise from an applied field or an ordered arrangement of magnetic moments, leading to all the muons at a particular site precessing about the same field. If all muons experienced an identical field then the asymmetry would be described by a sinusoidal function but for a finite field distribution, the asymmetry will also depolarize. The asymmetry can be modelled as a sum of n Gaussian distributions

$$A(t) = \sum_{i=1}^{n} A_i \cos(\gamma_\mu B_i t + \phi) e^{-(\sigma_i t)^2/2}, \tag{3.9}$$

where the field distribution for the ith component is centred on B_i and has a Gaussian width σ_i/γ_μ. In the case of a magnetically ordered material each field corresponds to a unique muon stopping site. For a superconductor in a transverse field, the field distribution of the flux line lattice (Fig. 2.5) can be modelled by summing multiple Gaussians [127]. The first and second moments of the overall distribution are then given by

$$\langle B \rangle = \sum_{i=1}^{n} \frac{A_i B_i}{A_{\mathrm{tot}}} \tag{3.10}$$

$$\langle B^2 \rangle = \sum_{i=1}^{n} \frac{A_i}{A_{\mathrm{tot}}} [(\sigma_i/\gamma_\mu)^2 + (B_i - \langle B \rangle)^2], \tag{3.11}$$

where A_{tot} is the total asymmetry given by

$$A_{\text{tot}} = \sum_{i=1}^{n} A_i. \tag{3.12}$$

Chapter 4

$CeCoGe_3$

4.1 Introduction

$CeCoGe_3$ is a member of the $CeTX_3$ (T = transition metal, X = Si or Ge) series of compounds which crystallize in the non-centrosymmetric, tetragonal $BaNiSn_3$ type structure (space group $I4mm$). Like the isostructural $CeRhSi_3$, $CeIrSi_3$ and $CeIrGe_3$, $CeCoGe_3$ orders magnetically at ambient pressure and displays pressure-induced superconductivity. At ambient pressure $CeCoGe_3$ orders antiferromagnetically, with three magnetic phases ($T_{N1} = 21$ K, $T_{N2} = 12$ K, $T_{N3} = 8$ K) [174, 60]. This is the highest reported ordering temperature for this series of compounds.

Initial measurements on polycrystalline samples had reported two magnetic transitions, at 21 and 18.5 K from specific heat measurements while only the former transition was observed in resistivity measurements. However, the successful growth of single crystals allowed the magnetic properties of $CeCoGe_3$ to be clarified more clearly. Unlike $CeRhSi_3$ and $CeIrSi_3$, the authors of Ref. [60] were unable to grow single crystals of $CeCoGe_3$ using the Czochralski method, suggesting this was due to incongruent melting of the compound. Single crystals were successfully grown using a bismuth flux, yielding plate like single crystals with faces perpendicular to [001]. Their measurements of the resistivity and magnetic susceptibility of these crystals in zero-field revealed the presence of three transitions. The existence of three magnetic phases was further supported by the observation of three sharp metamagnetic transitions in measurements of magnetization against applied field for $H \parallel [001]$ at 1.3 K, while the magnetization is linear up to 7 T for $H \parallel [100]$. The field-temperature phase diagram was constructed and is shown in Fig. 4.1. In between the transitions, the magnetization does not sharply increase with applied field. H_{c3} corresponds to the transition between the ordered and paramagnetic

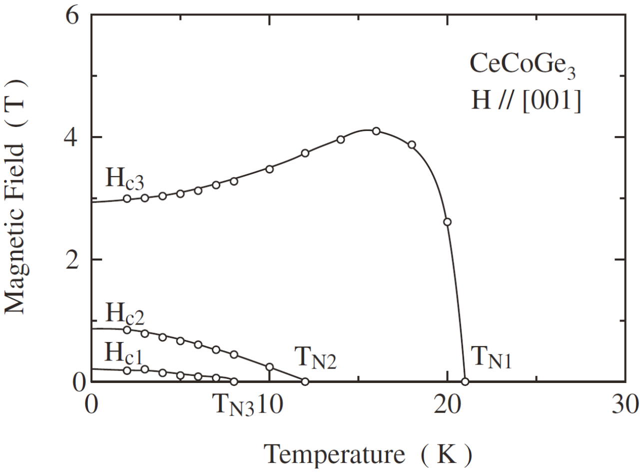

Figure 4.1: The field-temperature phase diagram of CeCoGe$_3$ from Ref. [60]. T_{N1}, T_{N2} and T_{N3} are the transition temperatures observed in zero-field.

states, while H_{c1} and H_{c2} are transitions between the ordered phases. Taking the value of the saturation magnetization (M_{s}) as 0.42 μ_{B}/Ce, the metamagnetic steps are observed at $M_{\mathrm{s}}/4$, $M_{\mathrm{s}}/3$ and M_{s}. The magnetic susceptibility below the ordering temperature is highly anisotropic with an easy axis along [001]. Below T_{N1} there is a sharp increase in χ which peaks at $T_{\mathrm{N2}} = 12$ K. Upon decreasing the temperature further, there is a shoulder until $T_{\mathrm{N3}} = 8$ K, below which χ drops sharply.

The explanation offered for this behaviour is that the cerium moments magnetically order along the c axis. Below T_{N3}, simple antiferromagnetic order is observed with the cerium moments alternating in an up-down configuration. Such a configuration has zero net magnetic moment at $T = 0$ and this explains the sharp drop in χ for $H \parallel [001]$ at low temperatures. The dramatic increase of χ for $T_{\mathrm{N3}} < T < T_{\mathrm{N1}}$ indicates a ground state with a net magnetization. It was suggested that the simplest spin structure consistent with the observations would be a three-up, one-down configuration for $T_{\mathrm{N3}} < T < T_{\mathrm{N2}}$ and a two-up, one-down configuration for $T_{\mathrm{N2}} < T < T_{\mathrm{N1}}$. A two-up, one-down arrangement is clearly compatible with a plateau at $M_{\mathrm{s}}/3$, since one in every three cerium spins make a net contribution to the magnetization. However, a three-up, one-down configuration would give a plateau at $M_{\mathrm{s}}/2$. In fact, the simplest configuration for a plateau at $M_{\mathrm{s}}/4$ is a three-up, five-down arrangement. In this model, the spins are strongly constrained to lie along the c axis and the transitions between magnetic phases just correspond to a change in structure resulting from flipping a certain number of spins.

A crystal electric field (CEF) scheme was also suggested, from measurements of χ with $H \parallel [001]$ and $H \parallel [100]$. Based on the observed magnetization above H_{c3} of around 0.4 μ_B/Ce, the ground state doublet of the split $J = \frac{5}{2}$ multiplet was taken to be $\left|\pm\frac{1}{2}\right\rangle$. A CEF scheme with $B_2^0 = 3$ K, $B_4^0 = -1$ K and $B_4^4 = = 0$ K was suggested, which gives such a ground state and this was shown to give reasonable agreement to the observed data allowing for finite molecular field parameters and temperature independent susceptibilities. The predicted level splittings from the ground state to the other two doublets of the multiplet are 9.8 and 27.3 meV.

Neutron diffraction experiments on CeCoGe$_3$ have been reported on both single crystal [175] and polycrystalline samples [176]. The single crystal neutron diffraction measurements at 2.9 K revealed a two component magnetic structure with a dominant component $\mathbf{k}_1 = (0,0,\frac{1}{2})$ and a weaker one $\mathbf{k}_2 = (0,0,\frac{3}{4})$. The ground state moment was deduced to be 0.5(1) μ_B/Ce in agreement with the magnetic measurements. The presence of the $\mathbf{k}_1$ component was also observed in the powder neutron diffraction experiments.

There has also been considerable interest in the properties of CeCoGe$_3$ under pressure. This has been studied both under applied hydrostatic pressure [49, 177, 178] or by applying chemical pressure in the CeCoGe$_{3-x}$Si$_x$ system [179, 180, 181, 182, 183]. The substitution of silicon for germanium compresses the lattice and therefore acts as an effective pressure. It has been of particular interest to study the proximity of the system to superconductivity and quantum criticality and compare this to other compounds in the CeTX_3 series. An initial study of the CeCoGe$_{3-x}$Si$_x$ system identified three regimes of behaviour; an antiferromagnetic region for $0 \leq x \leq 1$, a quantum critical region for $1 < x < 1.5$ and an intermediate valence region for $1.5 \leq x \leq 3$ [179]. Specific heat and magnetization measurements show that the ordering temperature (T_N) decreases with increasing x. At around $x \approx 1.2$, the transition is no longer observed and magnetic order has been suppressed. Measurements of the specific heat show that the low temperature values of C/T reach a maximum at $x = 1.25$. This corresponds to the maximum value of γ occurring at this concentration and indicates that the system is in the heavy-fermion state. Non-Fermi liquid behaviour for $x = 1.1, 1.25$ and 1.5 is deduced from the observation of a temperature range where there is a $\ln(T)$ dependence of C/T. The resistivity also shows a linear temperature dependence at low temperatures which is another indication of NFL behaviour. The region around this quantum critical point was measured with μSR [183]. These show that around $x = 1.2$, there is short range ordering of cerium moments with a low ordering temperature of 0.86 K and a greatly reduced magnetic moment of ~ 0.01 μ_B/Ce. It is also demonstrated that at these concentrations, $\sim 36\%$ of the Ce ions are

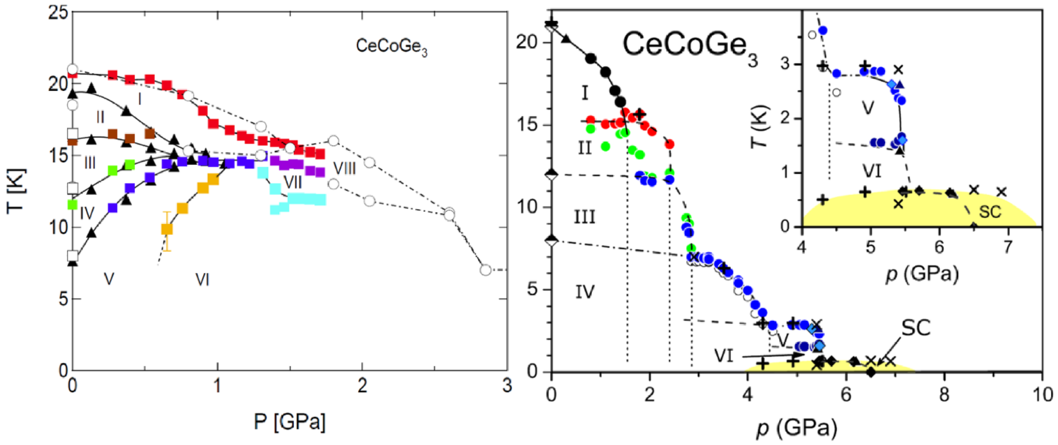

Figure 4.2: The temperature-pressure phase diagrams of CeCoGe$_3$. The low pressure phase diagram on the left is from Ref. [178] and the high pressure phase diagram on the right is from Ref. [177]. The low pressure phase diagram was constructed from measurements of polycrystalline samples, whereas single crystals were used for the high pressure measurements.

paramagnetic. This is associated with Ce ions which have a different local environment, either due to site vacancies or site disorder. This inhomogeneous magnetic phase indicates the possible importance of the degree of disorder in determining the properties around the critical region, which may be important for explaining the difference between applying hydrostatic and chemical pressure. Crucially, no evidence for superconductivity was observed in the critical region down to 30 mK, despite this being a region where strong spin fluctuations are expected to be present [179].

Upon further increasing x, the low temperature enhancement of C/T is reduced and for $x \geq 2.0$, a maximum is observed in the magnetic susceptibility. This is evidence for the system being in the intermediate valence state and T_{K} was deduced from the temperature where the susceptibility reaches a maximum, indicating $T_{\mathrm{K}} \sim 900$ K for $x = 3.0$. The change in the system towards an intermediate valence state is also observed in resonant inverse photoemission spectroscopy measurements (RIPES) [180]. RIPES spectra measured at the Ce-$N_{4,5}$ edge show two peaks labelled f^1 and f^2. These represent the weights of the $4f^0$ and $4f^1$ states of Ce respectively. The relative magnitude of the f^1 peak is greatest at the lowest temperatures and greatest values of x. These results give support to the fact that the localized $4f$ electron becomes itinerant at higher concentrations due to the Kondo interaction, with the local moment characteristics being recovered at sufficiently high temperatures.

Measurements of the magnetic properties of CeCoGe_3 under hydrostatic pressure have also been made on polycrystalline [178] and single crystal [177] samples. The resulting complex magnetic phase diagrams are shown in Fig. 4.2. The phase diagram measured on polycrystalline samples indicates the presence of five phases at ambient pressure. The transitions between the phases labelled III and IV and IV and V in the left of Fig. 4.2 correspond to the transitions at T_{N2} and T_{N3} reported in single crystals [60]. However two further transitions are reported to lie between T_{N1} and T_{N2}. Under an applied pressure all the transitions below T_{N1} move closer together until they merge to around 15 K for $p \sim 1$ GPa. At this pressure there is a downward step in T_{N1} and three further low temperature phases are reported up to 2 GPa. The high pressure phase diagram from measurements of the specific heat of single crystals is shown on the right of Fig. 4.2. The phases labelled I, III and IV correspond to the three magnetic phases reported in Ref. [60]. At $p = 0.8$ GPa, an additional transition is observed at 15.3 K. The temperature of this transition initially remains constant with increasing pressure, whereas T_{N1} is suppressed until it meets the pressure induced phase at 1.5 GPa. The transition temperature of this phase is suppressed as the pressure is increased further and it merges with T_{N2} at around 2.4 GPa and with T_{N3} at around 2.9 GPa. After this series of step-like decreases in T_{N} , there is a more gradual dome like suppression of the ordering temperature up until 4.4 GPa. The transition temperature of the new magnetic phase which emerges at this pressure remains relatively constant at about 2.8 K until around $p_{\text{c}} = 5.5$ GPa, where it sharply decreases and magnetic order is suppressed.

These results show that CeCoGe_3 has a complicated temperature-pressure phase diagram with several competing phases. The results also indicate several changes in magnetic structure between ambient pressure and p_{c}. Much like the results for the $\text{CeCoGe}_{3-x}\text{Si}_x$ system, the ordering temperature is reduced in temperature until magnetic order is fully suppressed at a quantum critical point. However, a major difference from the doped system is that under applied hydrostatic pressure, superconductivity is observed in resistivity measurements at $p = 4.3$ GPa and is still present at 7.1 GPa [49, 104, 184]. Evidence for bulk superconductivity was only observed in the specific heat in a narrower pressure range, up to 6.1 GPa [177]. The most novel feature of the superconducting state is the large, anisotropic values of H_{c2}, in common with the other isostructural HFSC. At $p = 7.1$ GPa, where the superconducting transition is at $T_{\text{c}} = 0.64$ K, H_{c2} is estimated to be 3.1 T for $H \parallel [100]$ and 24 T for $H \parallel [001]$ [184]. This strongly suggests an absence of Pauli paramagnetic limiting for $H \parallel [001]$. Whether the Pauli paramagnetic limit is exceeded for $H \parallel [100]$ depends on the magnitude of the superconducting gap and therefore the strength of the superconducting coupling.

There are therefore similarities between CeCoGe$_3$ and the pressure-induced HFSC CeRhSi$_3$, CeIrSi$_3$ and CeIrGe$_3$. The behaviour under chemical and hydrostatic pressures can be qualitatively described by the Doniach phase diagram with the competition between the RKKY interaction and the Kondo effect. A superconducting dome emerges around the point where the magnetic phase transition is suppressed by an applied hydrostatic pressure but not in silicon substituted samples. However, there are still several properties of the magnetic states of CeCoGe$_3$ at ambient pressure to be clarified. In this work polycrystalline and single crystal samples of CeCoGe$_3$ were studied at ambient pressure using magnetic susceptibility, INS, single crystal neutron diffraction and μSR. Zero-field μSR measurements confirm the onset of long range magnetic order at T_{N1} and the magnetic propagation vector in all three magnetic phases is determined using single crystal neutron diffraction. The INS measurements on polycrystalline samples allow the transitions between the CEF levels to be directly probed and an alternative CEF scheme is proposed, compatible with both magnetic susceptibility and INS data. INS measurements are also used to probe the low energy magnetic scattering which gives further information about the magnetic states for $T < T_{\mathrm{N1}}$ and the Kondo interaction for $T > T_{\mathrm{N1}}$. As well as further clarifying the physical properties of the magnetic states, information is deduced about the degree of hybridization in CeCoGe$_3$ and therefore the proximity of the system to quantum criticality.

It should be noted for the rest of this chapter and in subsequent chapters, the CGS system of electromagnetic units have been used.

4.2 Sample preparation and structural characterization

Polycrystalline samples of CeCoGe$_3$ and the non-magnetic LaCoGe$_3$ were produced by arc-melting stoichiometric quantities of the constituent elements (Ce : 99.9%, La : 99.9%, Co : 99.95%, Ge : 99.999%) in an argon atmosphere on a water cooled copper hearth. The resulting boules were flipped and remelted to improve homogeneity and were wrapped in tantalum foil and annealed at 900°C for a week under a dynamic vacuum, better than 10^{-6} Torr.

Powder x-ray diffraction measurements were perfomed using a Panalytical X-Pert Pro diffractometer and the resulting patterns are shown in Fig. 4.3. The crystal structure was refined using the Rietveld method using the TOPAS software [151]. One extraneous peak at 28.2° was identified in CeCoGe$_3$ which could not

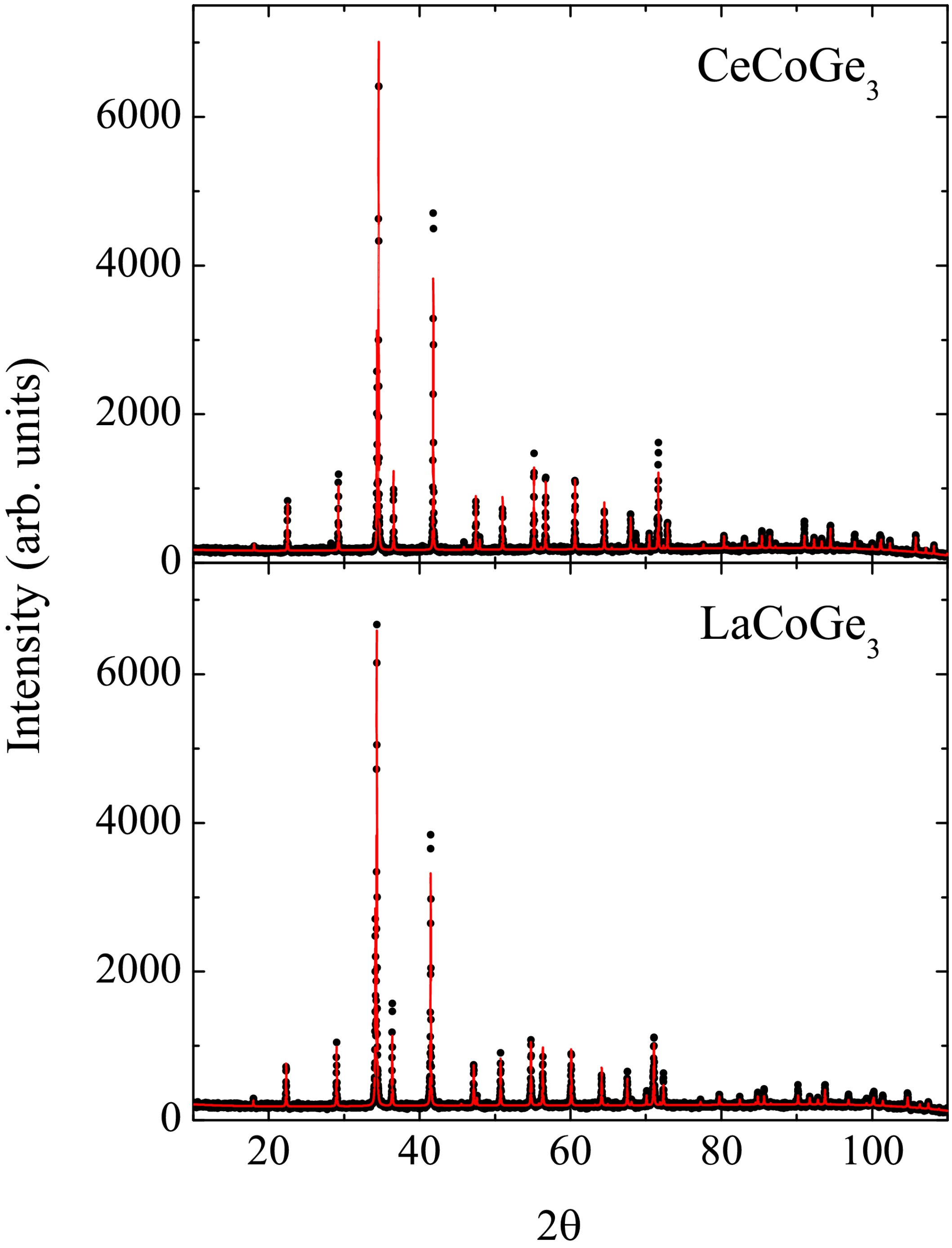

Figure 4.3: Powder x-ray diffraction measurements of CeCoGe$_3$ and LaCoGe$_3$ measured using a Panalytical X-Pert Pro diffractometer. The solid lines show the Rietveld refinements performed using TOPAS. The results are given in Table 4.1.

Table 4.1: Results of the refinements of powder x-ray diffraction measurements on CeCoGe$_3$ and LaCoGe$_3$. The lattice parameters, weighted profile factor (R_{wp}) and the atomic positions are shown.

	CeCoGe$_3$	LaCoGe$_3$		
a (Å)	4.32042(4)	4.35083(7)		
c (Å)	9.83484(11)	9.87155(2)		
R_{wp}(%)	10.33	8.86		
	Site	x	y	z
Ce	2a	0	0	0
Co	2a	0	0	0.666(7)
Ge1	2a	0	0	0.4281(6)
Ge2	4b	0	0.5	0.7578(5)
La	2a	0	0	0
Co	2a	0	0	0.6628(7)
Ge1	2a	0	0	0.4285(6)
Ge2	4b	0	0.5	0.7556(5)

be indexed to any reflections for the BaNiSn$_3$ structure while no extraneous peaks were observed for LaCoGe$_3$. The peak in the CeCoGe$_3$ plot likely corresponds to an impurity phase but as this peak had $\sim$ 1% of the intensity of the maximum sample peak, this implies the samples are very nearly single phase.

The results of the Rietveld refinement are shown in Table 4.1, where the site occupancies have been fixed to 100%. Due to the lack of symmetry along the c axis, the $z = 0$ position could be arbitrarily chosen and therefore was taken to be the position of the cerium atom. The lattice parameters are in good agreement with those obtained in Ref. [174]. The nearest neighbour distances for cerium are 4.32042(4) Å for Ce - Ce, 3.28(7) Å for Ce - Co and 3.1358(13) Å for Ce - Ge.

Single crystals of CeCoGe$_3$ were grown following the flux method described in Ref. [60], as described in Sec. 3.1.2. An image of several crystals is shown in Fig. 4.4. The typical dimensions of a large crystal were 6 × 2 × 1 mm. An x-ray Laue image taken with the beam perpendicular to the largest face is shown on the right of Fig. 4.5. On the left is a simulated Laue image along the [001] direction. This confirms that the crystals are high quality and the large face is perpendicular to [001]. In particular, the high symmetry point at the centre of the Laue image has four-fold rotational symmetry and the only four-fold symmetric axis of the crystal is along [001]. The composition was checked using EDAX and the average atomic composition measured on nine sites was 20.7(2)% Ce, 19.0(2)% Co and 60.3(2)% Ge.

Figure 4.4: Photograph of several $CeCoGe_3$ crystals obtained using a flux method. A ruler is shown for scale where one division is equal to 1 mm.

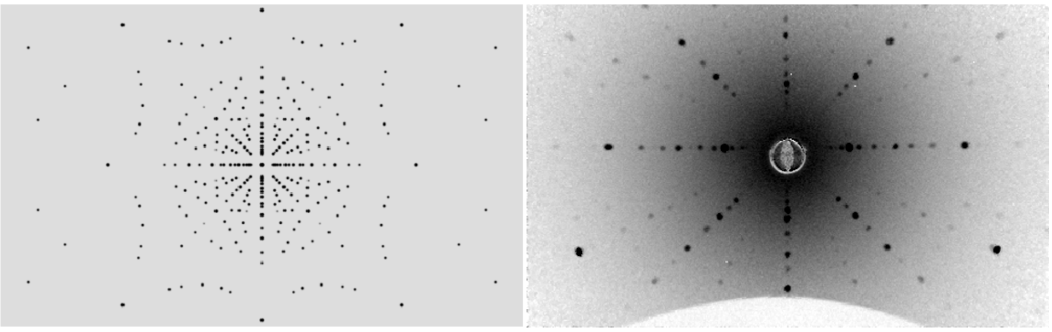

Figure 4.5: On the left is the simulated Laue image along [001] for $CeCoGe_3$. On the right is the x-ray Laue image of a plate shaped single crystal of $CeCoGe_3$ taken perpendicular to the face.

4.3 μSR measurements

The nature of the magnetic ordering of $CeCoGe_3$ was studied using zero and longitudinal field μSR. Polycrystalline $CeCoGe_3$ was mounted on a silver plate and was cooled in a standard cryostat down to 1.4 K. The experiment was performed on the MuSR spectrometer at ISIS and the detectors were arranged in the longitudinal configuration.

Zero-field μSR spectra at six temperatures are shown in Fig. 4.6. In the range 13 K $\leq T \leq$ 20 K, the spectra display oscillations in the asymmetry. Above 20 K and below 13 K oscillations are not observed and the asymmetry monotonically decreases. As shown in the bottom two panels, there is a sharp drop in the initial asymmetry between 21 and 20 K. These results indicate that $CeCoGe_3$ has long-range magnetic order below 21 K. The muons are implanted and precess about the

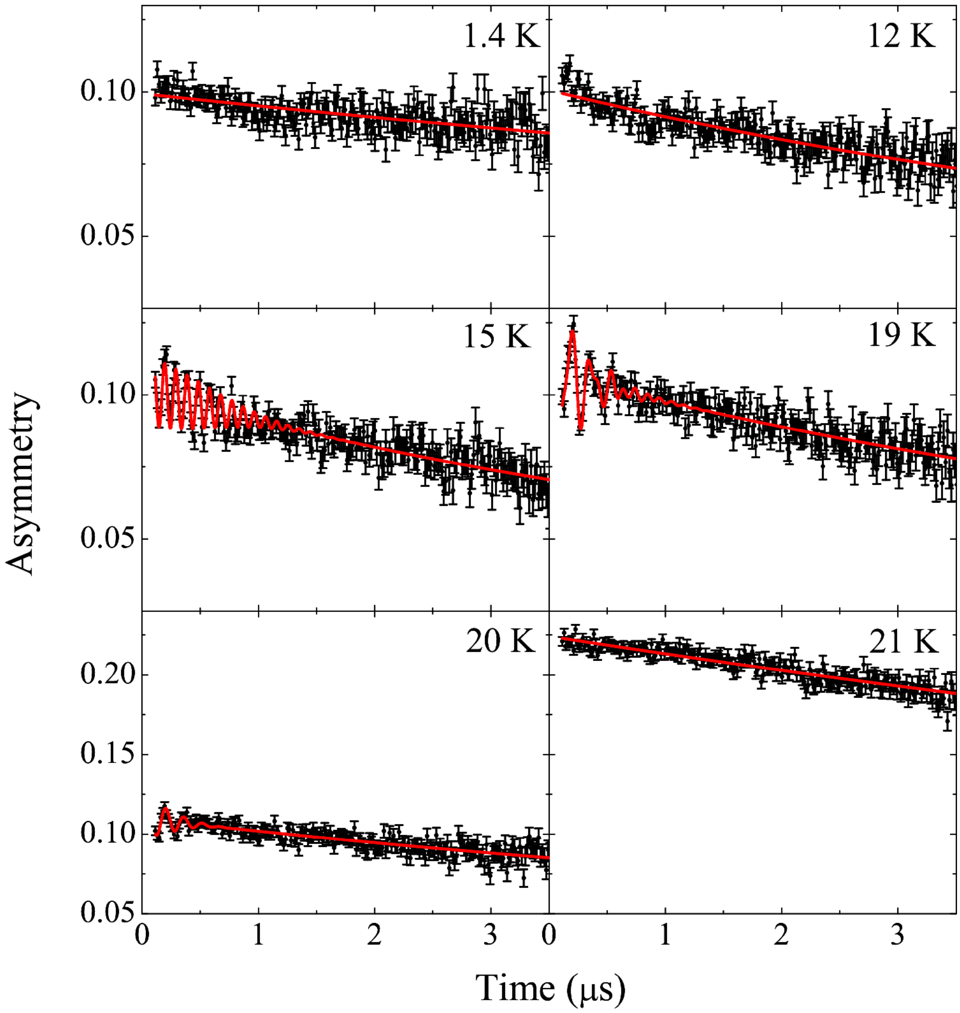

Figure 4.6: μSR spectra of polycrystalline $CeCoGe_3$ measured at six temperatures. At 19 K two frequencies were observed whereas one was observed at 15 and 20 K and none are present at 1.4, 13 or 21 K. The solid lines show the fits described in the text.

local field at the muon site. In the case of a perfect periodic arrangement of spins, the muons at a given position in the magnetic lattice experience a single field and the resulting asymmetry would consist of a single undamped oscillation. In a real system there will be a finite variance in the field distribution at the muon site and therefore the signal is a decaying oscillation. Assuming a random orientation of grains in a polycrystalline sample, $\frac{2}{3}$ of the implanted muons contribute towards the oscillatory component upon the onset of magnetic order so there is a drop in initial asymmetry. Therefore T_{N1} lies between 20 and 21 K.

The spectra were fitted with

$$G_z(t) = \sum_{i=1}^{n} A_i \cos(\gamma_\mu B_i t + \phi) e^{-\frac{(\sigma_i t)^2}{2}} + A_0 e^{-\Lambda t} + A_{\mathrm{bg}}, \tag{4.1}$$

which is the sum of an oscillating transverse component (Eq. 3.9), a fluctuating longitudinal component (Eq. 3.8) and a background term. With A_{bg} fixed at 0.03089, the spectra were fitted with $n = 2$ at 19 K and $n = 1$ for the remaining oscillatory spectra. Below 13 K and above 20 K, the spectra were just fitted with the last two terms. The observation of two frequencies at 19 K indicates there are at least two muon stopping sites in the magnetic unit cell. Two stopping sites in the lattice were identified in the μSR studies of CeCoGe$_{3-x}$Si$_x$ [183], but in that instance the second muon site was attributed to a disordered region where there was an interchange between Co and Ge. However, even if there is only one stopping site in the crystal lattice, there may be more than one distinct site in the magnetic lattice [172].

The temperature dependence of Λ and the internal fields are shown in Fig. 4.7. The sharp increase in Λ at T_{N1} indicates a transition between the paramagnetic and the ordered states. However, Λ smoothly decreases in the ordered state and anomalies are not observed at T_{N2} and T_{N3}. It shall be seen in the following section that these transitions correspond to a rearrangement of spins and change in magnetic structure. These results indicate that these rearrangements are not accompanied by a sharply increased spin fluctuation rate. The temperature dependence of the internal fields are shown in Fig. 4.7(b). The field observed at 20 K is larger than the lower of the fields observed at 19 K and is therefore associated with the higher field B_2. If the magnetic field at the muon site is taken to be proportional to the magnetic moment of the cerium atom, the temperature dependence of the order parameter can be obtained. The temperature dependence of B_1 was fitted with

$$B(T) = B(0) \left[1 - \left(\frac{T}{T_N} \right)^{\alpha} \right]^{\beta}. \tag{4.2}$$

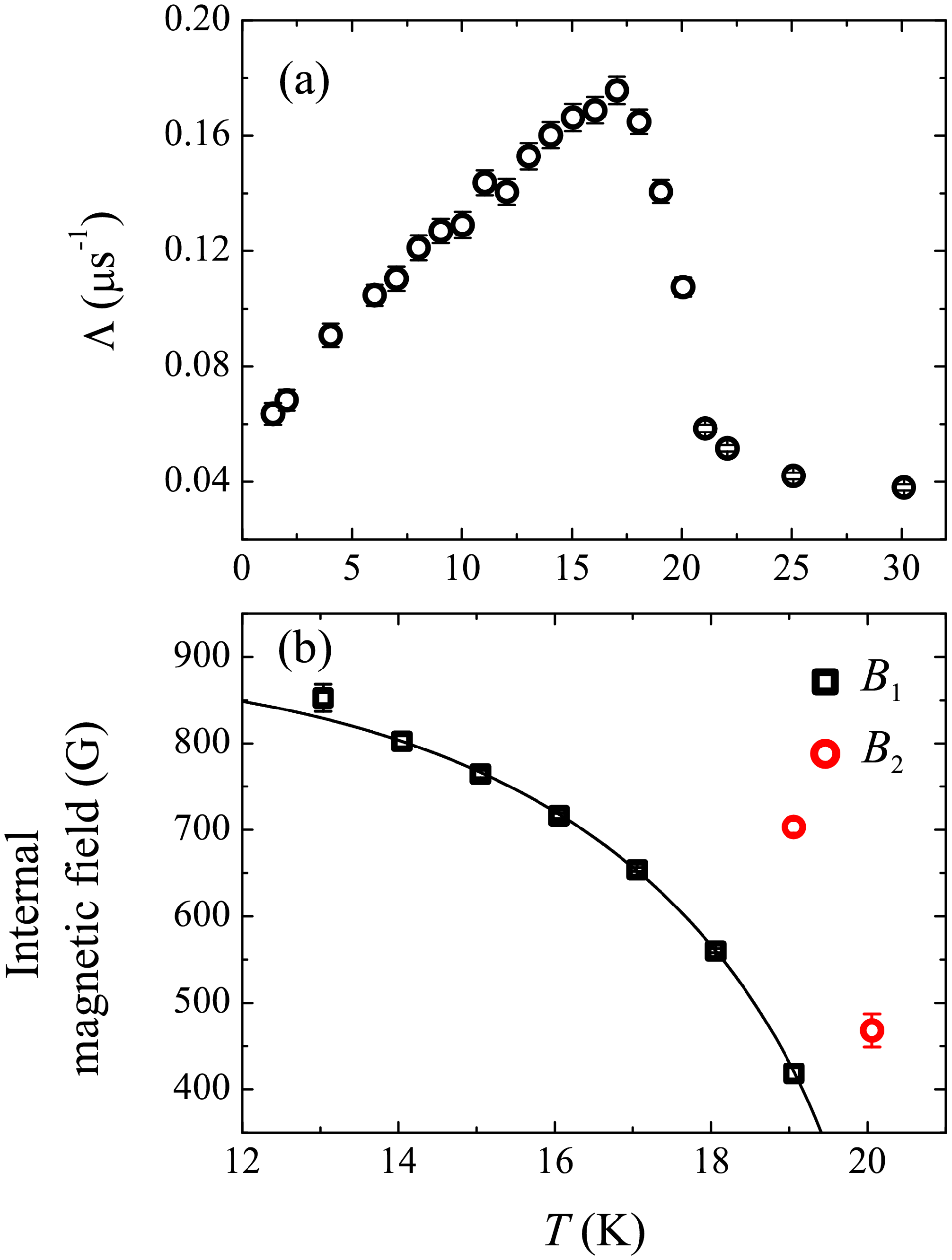

Figure 4.7: (a) The temperature dependence of the muon depolarization rate. (b) The temperature dependence of the internal fields at the muon stopping site, from the oscillation frequencies observed in zero-field μSR spectra. The solid line shows a fit of B_1 to Eq. 4.2 as described in the text.

This expression is an empirical interpolation between Bloch's law at low temperatures and critical behaviour at T_N [185]. With β fixed at 0.5 for a mean field magnet [109], values of $B(0) = 889(16)$ G, $\alpha = 4.7(4)$ and $T_\mathrm{N} = 20.12(8)$ K were obtained. A good fit with $\beta = 0.5$ means the observations are consistent with that of a mean field magnet. With a large value of α, there is a significant deviation from a $(1 - c(T/T_\mathrm{N})^2)$ dependence at low temperatures [186] and this could be due to a gap in the magnon dispersion [187]. The data could also be fitted with $\beta = 0.367$ and 0.326 for a 3D Heisenberg and Ising model respectively [109]. Fits with both these parameters gave $T_\mathrm{N} < 20$ K and poor fits were obtained for $T_\mathrm{N} > 20$ K. As discussed previously, the observation of oscillations at 20 K constrains $T_\mathrm{N} > 20$ K, so the data are incompatible with these models. Furthermore, Fig. 4.8 shows the magnetic moments obtained from magnetic refinements at 2 and 14 K, as described in Sec. 4.4. The solid lines show fits to the three models, with α and T_N fixed to the values from the μSR fits and $B(0)$ was the only free parameter. The fitted curves and values of χ^2 show that only the mean free model is in agreement with the neutron diffraction data. This also supports the applicability of the fit in Fig. 4.7 at low temperatures, even though the μSR data only goes down to 13 K.

The dependence of the asymmetry on the longitudinal applied field is shown in Fig. 4.9. The asymmetry has been normalized so that it is equal to one when it reaches the full asymmetry of the MuSR spectrometer. At this point, the muon is fully polarized in the forward direction and is fully decoupled from its local environment. As expected for a polycrystalline magnet, the asymmetry is equal to $\frac{1}{3}$ in zero-field. The data were fitted with

$$A(b) = \frac{3}{4} - \frac{1}{4b^2} + \frac{(b^2-1)^2}{8b^3}\ln\left|\frac{\mathrm{b}+1}{\mathrm{b}-1}\right|, \tag{4.3}$$

where $b = B_\mathrm{app}/B_1$ is the ratio of the applied field to the internal field at the muon stopping site [188]. $B_1 = 1080(40)$ G was obtained which is slightly higher that the value of 889(16) G obtained from the mean field model. However the magnetic structure at 1.4 K is different to the structure in the region where Equation 4.2 was fitted.

4.4 Single crystal neutron diffraction

Single crystal neutron diffraction measurements were carried out on the D10 diffractometer in the paramagnetic state as well as the three ordered phases. In a previous single crystal neutron diffraction study, the coexistence of two magnetic propaga-

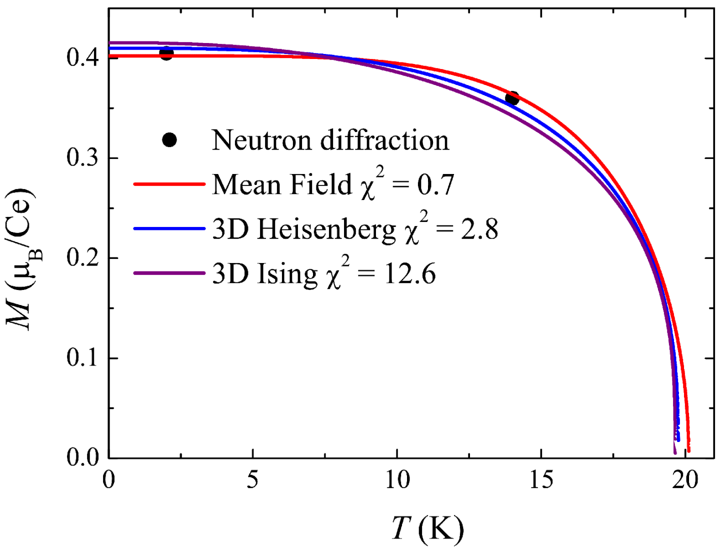

Figure 4.8: The solid lines show three models of the temperature dependence of the order parameter and the magnitudes of the cerium moment obtained from the refinements at 2 and 14 K described in Sec. 4.4. The fits were made to Eq. 4.2 with β fixed the value for a given model and α and T_{N} fixed to the values obtained from fitting B_1 in Fig. 4.7.

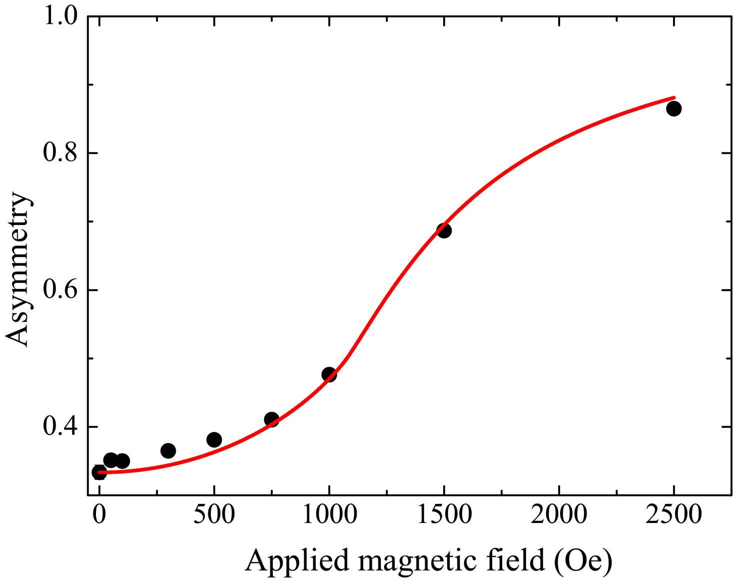

Figure 4.9: The dependence of the asymmetry on the applied longitudinal field at 1.4 K. The asymmetry has been normalized so that it equals unity at the full asymmetry of the spectrometer. The solid line shows a fit to Eq. 4.3.

tion vectors was reported with the observation of the $(10\frac{1}{2})$ and $(10\frac{1}{4})$ reflections at 2.9 K [175]. The aim of the measurements presented in this section is to study the temperature dependence of the magnetic structure and to characterize the nature of the magnetic ordering up to T_{N1}.

A plate like sample was glued on an aluminium pin and cooled in a helium-flow cryostat to temperatures down to 2 K. Details of the instrument are described in Sec. 3.5.1. The incident neutron wavelength was 2.36 Å which was selected using a pyrolytic graphic monochromator. Scattered neutrons passed through a vertically focused pyrolytic graphite analyzer and were detected with a single ^{3}He detector.

Scans across $(10l)$ are shown in Fig. 4.10 at 30, 14, 10 and 2 K. These show that below 20 K, additional peaks are observed for non-integer l. Since no peaks are observed in this range at 30 K, this indicates the onset of antiferromagnetic ordering below T_{N1}. At 2 K there is an additional peak at $(10\frac{1}{2})$, which shifts to $(10\frac{3}{8})$ at 10 K and $(10\frac{1}{3})$ at 14 K. Further scans were taken from 22 to 3 K in 1 K increments to check the temperature dependence of the magnetic propagation vector. Peaks were observed at $l = \frac{1}{2}$ for $T \leq T_{\mathrm{N3}}$, $l = \frac{3}{8}$ for $T_{\mathrm{N3}} \leq T \leq T_{\mathrm{N2}}$ and $l = \frac{1}{3}$ for $T_{\mathrm{N2}} < T < T_{\mathrm{N1}}$. This confirms that the transitions at T_{N2} and T_{N3} correspond to a change in the magnetic propagation vector and therefore a change in magnetic structure. The (100) reflection is forbidden in the body-centered structure so the propagation vectors are $\mathbf{k} = (0,0,\frac{1}{2})$ below T_{N3}, $\mathbf{k} = (0,0,\frac{5}{8})$ for $T_{\mathrm{N3}} \leq T < T_{\mathrm{N2}}$, and $\mathbf{k} = (0,0,\frac{2}{3})$ for $T_{\mathrm{N2}} < T < T_{\mathrm{N1}}$. The $\mathbf{k} = (0,0,\frac{1}{2})$ propagation vector at 2 K is in agreement with the dominant propagation vector reported for this phase in Ref. [175]. However, the weaker peak reported at $l = \frac{1}{4}$ is not observed at 2 K and there is no evidence in any of these measurements for a two $\mathbf{k}$ structure. As shown in Fig. 4.11, peaks are observed at $l = \frac{3}{8}$ and at $l = \frac{1}{2}$ at 8 K. This indicates that there is a coexistence of two magnetic phases, which suggests a first order transition at T_{N3}. The peak at $l = \frac{3}{8}$ has a much larger intensity indicating that T_{N3} is below 8 K. No coexistence of phases is observed at T_{N2}, but it is not possible to conclude the order of the transition from this alone.

The existence of ferrimagnetic phases were deduced for measurements of polycrystalline samples in Ref [174] at 3 K. Although a different phase diagram is proposed, the existence of a region with a ferrimagnetic phase is suggested upon either increasing the field or temperature from the zero-field low temperature antiferromagnetic state. To look for evidence of a ferromagnetic component, the temperature dependence of the intensity of the (110) reflection was measured. This was selected because the structural peak has a relatively low intensity. Of all the exper-

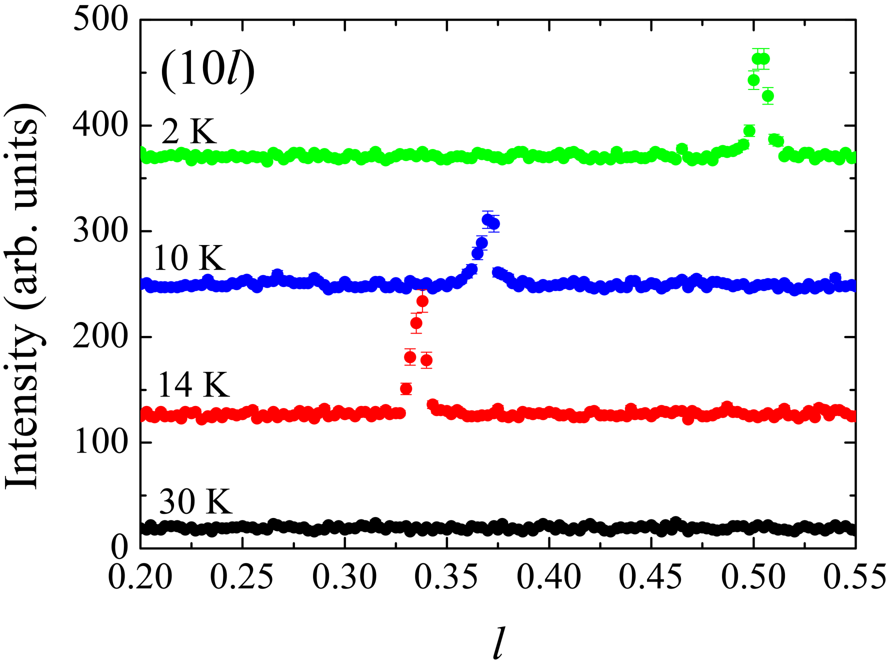

Figure 4.10: Elastic scans of a single crystal of $CeCoGe_3$ across (10l) at four temperatures. Above T_N at 30 K, no peak is observed.

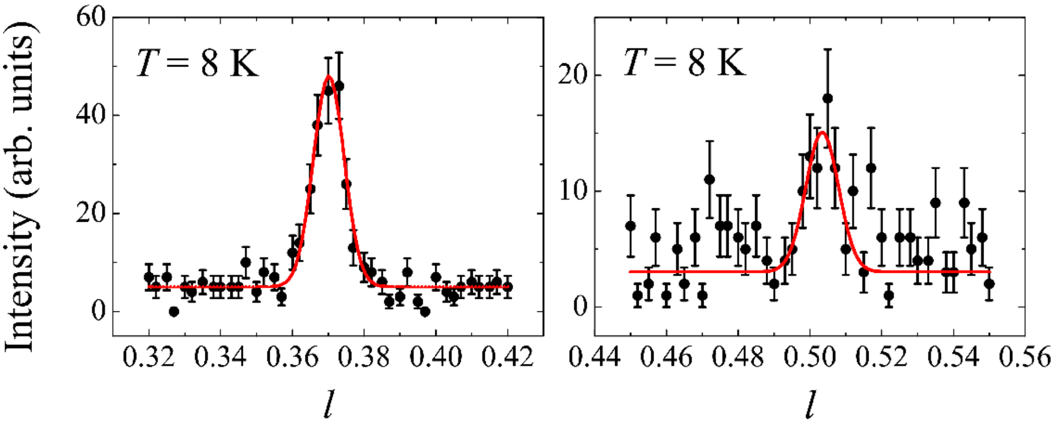

Figure 4.11: Elastic scans of $CeCoGe_3$ across (10l) at 8 K. There is a coexistence between the peaks at $l = \frac{3}{8}$ and at $l = \frac{1}{2}$.

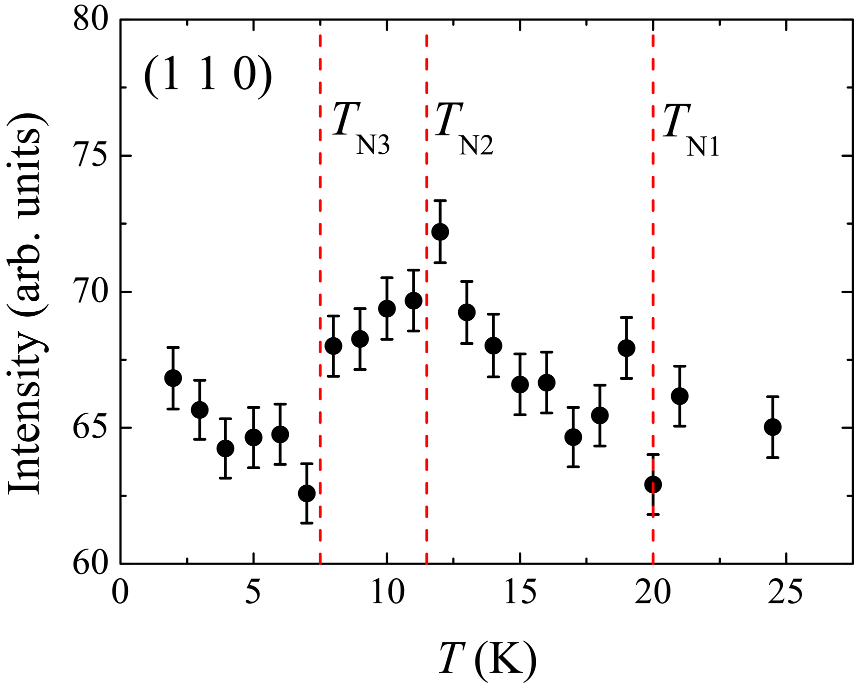

Figure 4.12: The integrated intensity of the (110) reflection as a function of temperature. The vertical dashed lines show the three transition temperatures and there is an increased intensity between T_{N1} and T_{N3}.

imentally accessible, allowed structural reflections measured at 35 K, this reflection had the smallest integrated intensity. In addition, (110) corresponds to a low value of $|\mathbf{Q}|$, so the intensity of the magnetic scattering will not have dropped off significantly as a result of the magnetic form factor. The temperature dependence of the integrated intensity of the (110) reflection is displayed in Fig. 4.12. The intensity begins to increase below T_{N1} and reaches a maximum at T_{N2}. Below this, the intensity decreases and below T_{N3} the intensity is similar to that observed above T_{N1}. This is evidence for a ferromagnetic component for $T_{\text{N3}} < T < T_{\text{N1}}$, in addition to antiferromagnetic order.

Having identified three distinct magnetic phases, further data were collected to solve the magnetic structure and to measure the magnitude and direction of the cerium magnetic moments. At 35 K, the experimentally accessible nuclear reflections (hkl) were measured, excluding those forbidden by the crystal symmetry. In each magnetic phase, reflections at $(hkl) \pm \mathbf{k}$ were measured. A total of 104 magnetic reflections were measured at 2 and 14 K whereas 57 were measured at 10 K. Reflections were not at observed at $(00l) \pm \mathbf{k}$ in any phase, indicating that the mo-

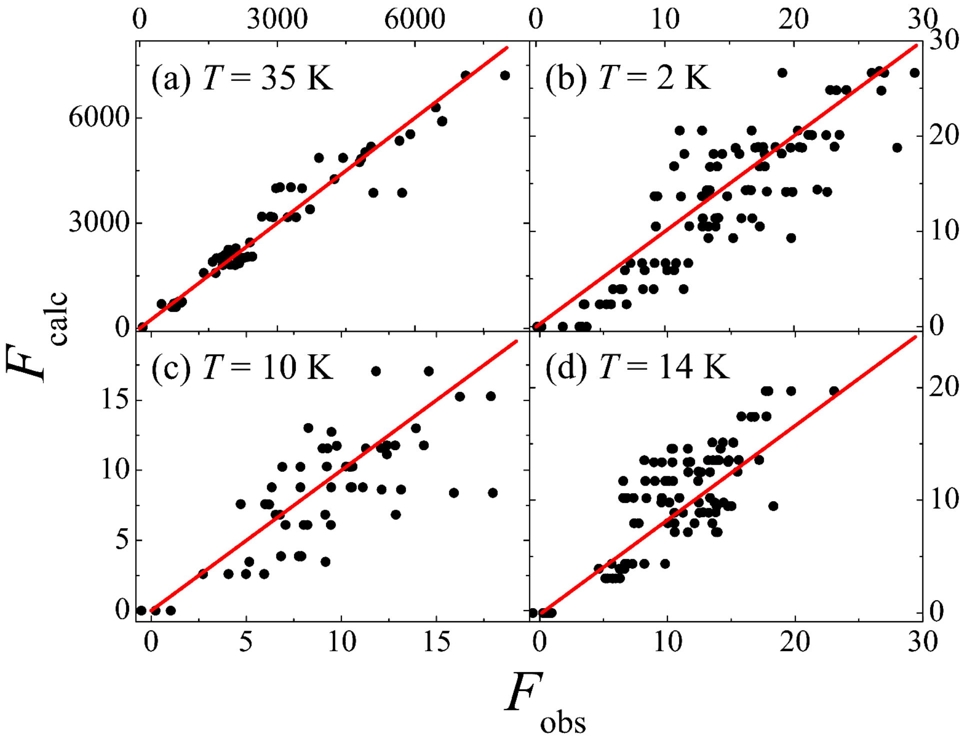

Figure 4.13: The calculated against the observed values of the structure factor (F_{hkl}) for the refinements of (a) the crystal structure at 35 K, (b)-(d) the magnetic structures at 2, 10 and 14 K. The solid lines show where $F_{\mathrm{calc}} = F_{\mathrm{obs}}$.

ments point along the c axis in all three phases. A symmetry analysis of the possible magnetic structures was carried out using SARAh [157]. This analysis shows that there is only one irreducible representation of G_k with moments along the c axis for all the propagation vectors. The crystal and magnetic structures were fitted using FullProf [153]. Scale factors and extinction parameters were fixed from the results of the structural refinement and therefore there was only one free parameter in the refinement of the magnetic phases. This corresponds to the magnetic moment on the cerium atoms, although it is always possible to introduce a global phase ϕ to a magnetic structure while leaving the diffraction pattern unchanged. The values of R_{Bragg} were 10.9% for the crystal structure refinement at 35 K and 21.5, 24.3 and 22% for the magnetic structure refinements at 2, 10 and 14 K respectively. Plots of the structure factors, F_{calc} against F_{obs} are shown in Fig. 4.13. The solid lines show where the two are equal and represents the position of the points for a perfect fit. Although ϕ can not be directly determined from diffraction measurements, selecting $\phi = \pi/4$ gives an equal moment on each Ce of 0.405(5) μ_{B}. This has a two-up two-down spin configuration along the c axis and is displayed in Fig. 4.14(c). As previously discussed, a ferromagnetic component is observed between T_{N1} and T_{N3}. With $\phi = 0$ at 14 K, the structure consists of an up moment of 0.485(6) μ_{B}/Ce followed by two down moments of 0.243(3) μ_{B}/Ce. The addition of a ferromagnetic component of -0.125 μ_{B}/Ce gives an equal moment, two-up one-down structure of 0.360(6) μ_{B}/Ce. This is displayed in Fig. 4.14(a) and such a structure is consistent with a magnetization plateau at $M_{\mathrm{s}}/3$ reported in Ref. [60]. For the phase at 10 K with $\mathbf{k} = (0,0,\frac{5}{8})$, a combination of ϕ and ferromagnetic component that gives an equal moment solution could not be found. This indicates that the structure in this phase has unequal magnetic moments. The antiferromagnetic component with $\phi = 0$ is shown in Fig. 4.14(b). However there is also a ferromagnetic moment in this phase, the magnitude of which can not be reliably determined from unpolarized measurements of a single nuclear reflection.

4.5 Inelastic neutron scattering

In the previous section, the magnetic structure of the three magnetic phases of CeCoGe$_3$ was studied with neutron diffraction and an ordered moment of 0.405 μ_{B}/Ce was deduced at 2 K. A straightforward explanation for this low moment would be a CEF scheme where the ground state doublet of the $J = \frac{5}{2}$ multiplet consists of the $|\pm\frac{1}{2}\rangle$ states, which has a c axis moment of $g_J m_J = 0.429$ μ_{B}/Ce as suggested in Ref. [60]. To test this proposed CEF scheme and to measure the magnetic scattering both in the ordered state below T_{N1} and the quasielastic scattering in the paramagnetic state due to the Kondo effect, INS measurements were carried out on polycrystalline CeCoGe$_3$ using the MARI and MERLIN spectrometers at ISIS.

INS Measurements were carried out on polycrystalline CeCoGe$_3$ and LaCoGe$_3$. LaCoGe$_3$ does not magnetically order [174] and is isostructural to CeCoGe$_3$. It was therefore used to estimate the phonon contribution. The samples were wrapped in Al foil, placed in an Al can and cooled to 4 K in a closed cycle refrigerator. Measurements were made on MARI with $E_{\mathrm{i}} = 10$ and 40 meV selected with a Fermi chopper. Colour plots of the INS intensity in absolute units, measured with $E_{\mathrm{i}} = 40$ meV are shown in Figs. 4.15(a) and 4.15(b) for CeCoGe$_3$ at 4 and 25 K respectively and in Fig. 4.15(c) for LaCoGe$_3$ at 5 K. The CeCoGe$_3$ measurements in both the magnetically ordered and paramagnetic states show two inelastic excitations at around 19 and 28 meV, with significant intensity at low $|\mathbf{Q}|$. These excitations are absent in the scattering of LaCoGe$_3$, indicating a magnetic origin. These account for the two

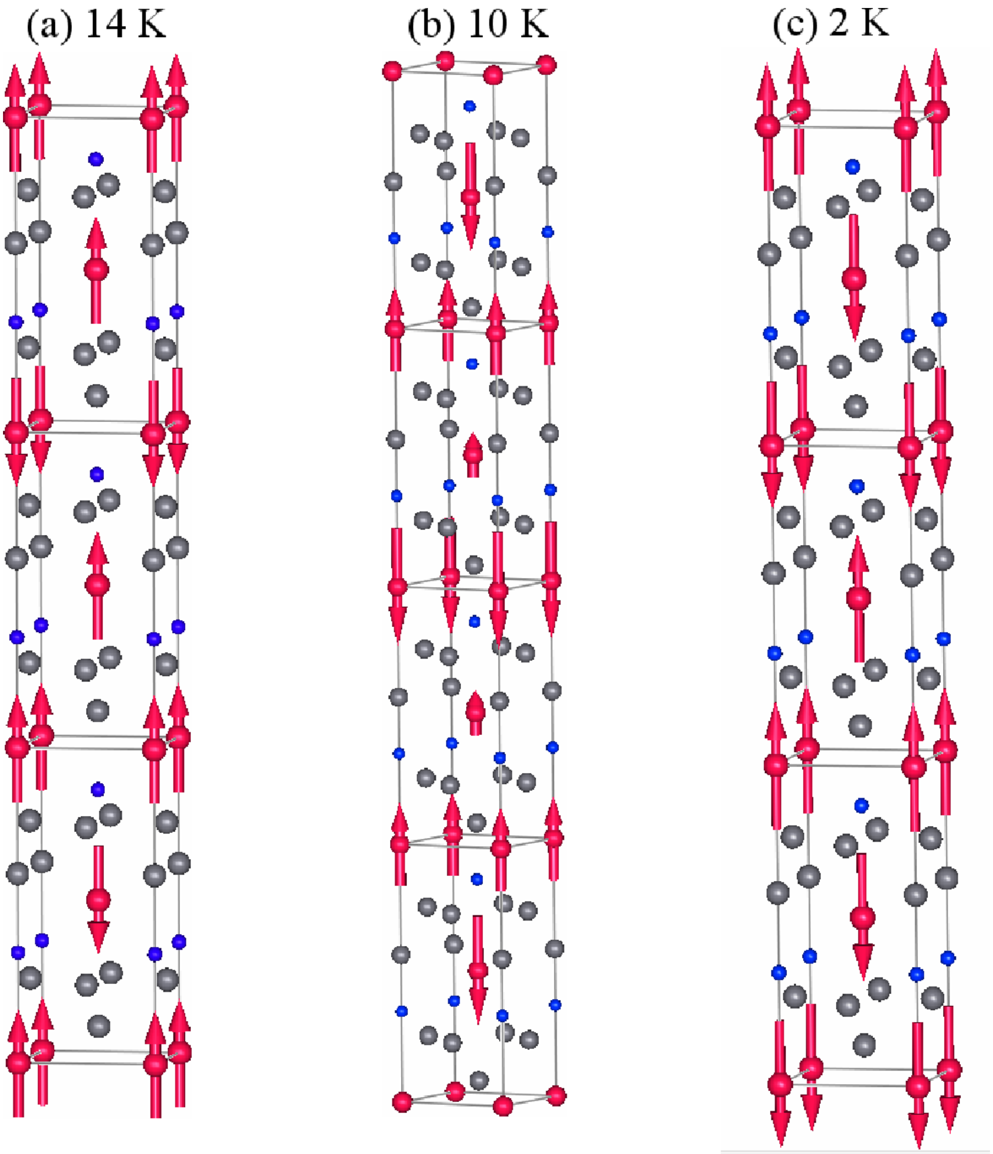

Figure 4.14: The crystal and magnetic structures of $CeCoGe_3$ with Ce atoms in red, Co atoms in blue and Ge atoms in grey. The arrows depict the magnetic moments on the Ce atoms. (a) shows the magnetic structure at 14 K consisting of an antiferromagnetic component with $\phi = 0$ with a ferromagnetic component adjusted to give an equal moment, two-up one-down structure. (b) shows the antiferromagnetic component at 10 K with $\phi = 0$. One half of the magnetic unit cell is displayed. (c) shows the magnetic structure at 2 K with $\phi = \pi/4$, to give an equal moment two-up two down structure.

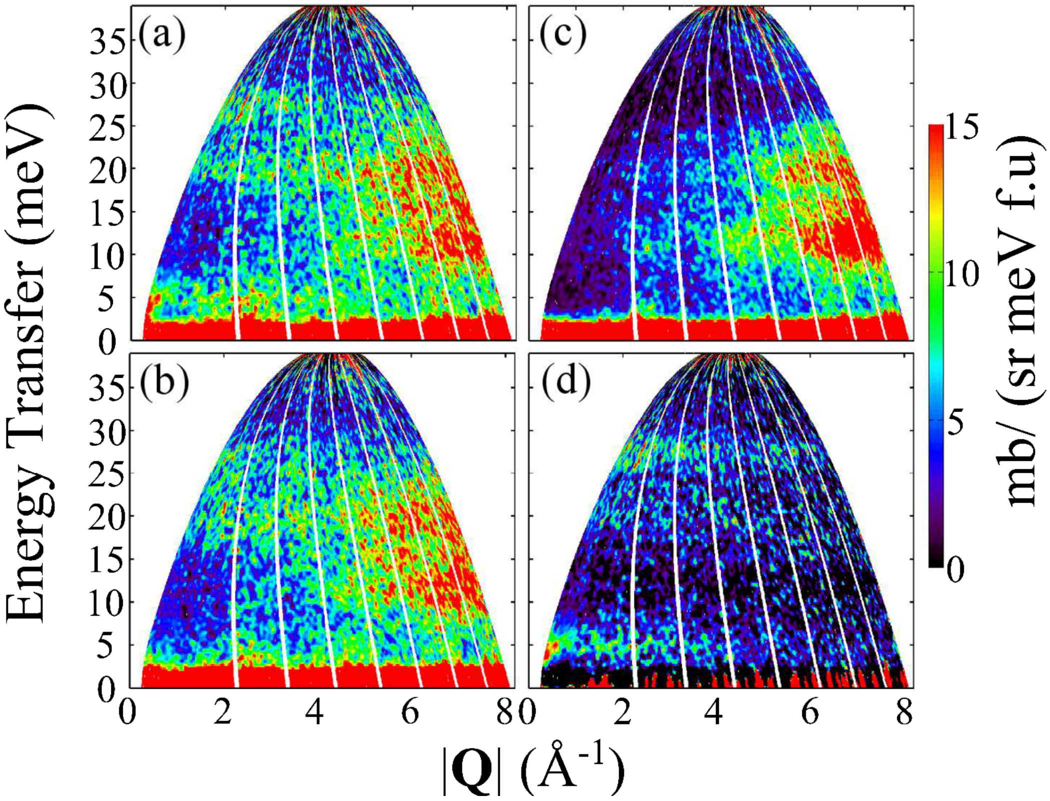

Figure 4.15: Colour plots of the INS intensity measured on MARI with $E_\mathrm{i} = 40$ meV for (a) CeCoGe$_3$ at 4 K, (b) CeCoGe$_3$ at 25 K and (c) LaCoGe$_3$ at 5 K. (d) shows the magnetic scattering of CeCoGe$_3$ at 4 K after subtracting an estimate of the phonon contribution as described in the text.

excited CEF doublets of the $J = \frac{5}{2}$ multiplet. Furthermore, additional magnetic scattering is observed at lower energy transfers in $CeCoGe_3$. A different $|\mathbf{Q}|$ dependence of the low energy magnetic scattering is observed, with a relatively weak dependence at 25 K but with clear features in the dispersion at 4 K. The scattering at 4 K is due to spin waves in the ordered state while the scattering at 25 K is quasielastic scattering due to the Kondo effect. Although an antiferromagnetic spin wave like dispersion might be expected to be observed at 4 K, this can not be resolved due to the measurements being performed on a polycrystalline sample. In this case, the spin waves will be anisotropic and since all orientations will be measured, a sharp dispersion will not be observed. There is also significant amounts of scattering observed at higher $|\mathbf{Q}|$ in Figs. 4.15(a)-(c) which is from phonons. Fig. 4.15(d) shows the magnetic scattering obtained from subtracting the scattering of $LaCoGe_3$ at 5 K from $CeCoGe_3$ at 4 K using Eq. 2.73 with $\alpha = 0.9$, the ratio of the neutron scattering cross sections of $CeCoGe_3$ and $LaCoGe_3$. This has mostly removed the high $|\mathbf{Q}|$ phonon scattering. The two CEF levels can be readily resolved as well as the magnetic scattering at lower energies. Further analysis was carried out from making cuts of the data by integrating across a range of $|\mathbf{Q}|$. Cuts of low energy INS measurements are first discussed followed by the high energy measurements.

4.5.1 Low energy inelastic neutron scattering

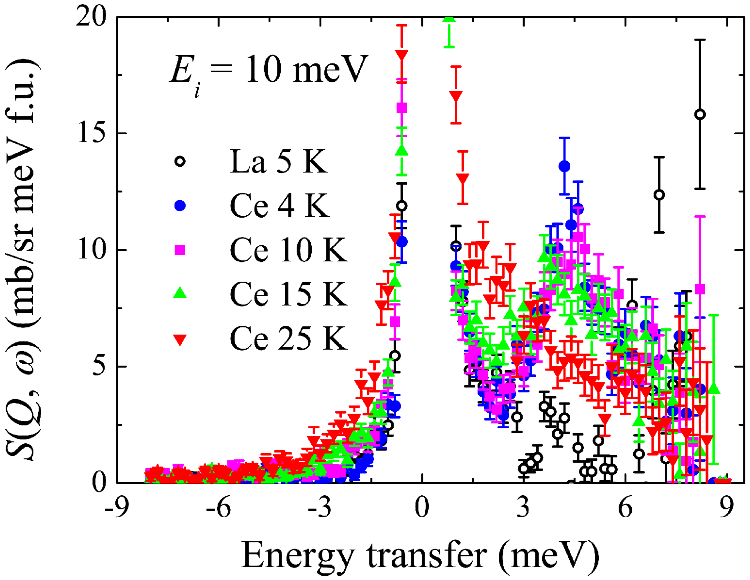

Figure 4.16: Cuts of $S(\mathbf{Q},\omega)$ with $E_\mathrm{i} = 10$ meV for $CeCoGe_3$ and $LaCoGe_3$, integrated across $|\mathbf{Q}|$ from 0-2 Å^{-1}.

Fig. 4.16 shows cuts of $S(\mathbf{Q},\omega)$ of $CeCoGe_3$ for E_i = 10 meV. The cuts are integrated from 0-2 Å^{-1}. The lack of inelastic scattering from $LaCoGe_3$ shows there are no phonon excitations at energy transfers less than 10 meV and the scattering observed in $CeCoGe_3$ has a magnetic origin. The cuts at 4 and 10 K show a well defined peak at 4.5 meV due to spin wave excitations and this is the energy scale of the zone boundary magnons. Very little difference is observed in the magnetic scattering crossing T_N3. However at 15 K, the magnon peak weakens and broadens, as if some of the spectral weight has shifted from the magnon to quasielastic scattering. Above T_N1 the peak is no longer observed and there is broad quasielastic scattering.

To study the temperature dependence of the quasielastic scattering above T_N1, further measurements were made on the MERLIN spectrometer with E_i = 15 meV. This is shown for six temperatures in Fig. 4.17. Clear evidence of quasielastic scattering is observed since the central peak is broader than the elastic resolution of the instrument and it becomes increasingly asymmetrical with temperature. The data were fitted using Eq. 2.72 and the temperature dependence of the half width at half maximum is shown in Fig. 4.18. A linear fit was made to Γ up to 150 K and $\Gamma(0) = 1.0(3)$ meV was obtained. From this $T_\mathrm{K} = 11(3)$ K is estimated. At 190 K there is a significant deviation from linear behaviour. A $T^{\frac{1}{2}}$ dependence could also be fitted to the data as has been observed in other heavy fermion systems [161, 189]. But this gives a negative $\Gamma(0)$ for which there is not a clear physical interpretation. At 190 K the value of Γ is unchanged from that at 140 K. A linear dependence is predicted as long as the separation of the first excited doublet is sufficiently greater than the thermal energy [160]. The first CEF level is at 19 meV (220 K), which may explain the change in the temperature dependence.

4.5.2 High energy inelastic neutron scattering

Cuts were made of $S(\mathbf{Q},\omega)$ by integrating across $|\mathbf{Q}|$ and are shown for E_i = 40 meV in Fig. 4.19. The low $|\mathbf{Q}|$ cuts are from integrating from 0-3 Å^{-1} and the high $|\mathbf{Q}|$ from 5-8 Å^{-1}. The high $|\mathbf{Q}|$ measurements of $LaCoGe_3$ show two peaks at around 12 and 20 meV which are also present in the high $|\mathbf{Q}|$ $CeCoGe_3$ data. The peak at 12 meV is almost entirely absent in the low $|\mathbf{Q}|$ measurements while a peak is observed at around 20 meV in the low $|\mathbf{Q}|$ measurements of $CeCoGe_3$ but not $LaCoGe_3$. The peak at 12 meV is more intense in $LaCoGe_3$ while they are approximately equal at 20 meV. This supports the presence of peaks due to phonons at 12 and 20 meV in both compounds with an increased scattering intensity with increasing $|\mathbf{Q}|$. However, there is extra scattering at 20 meV for both low and high

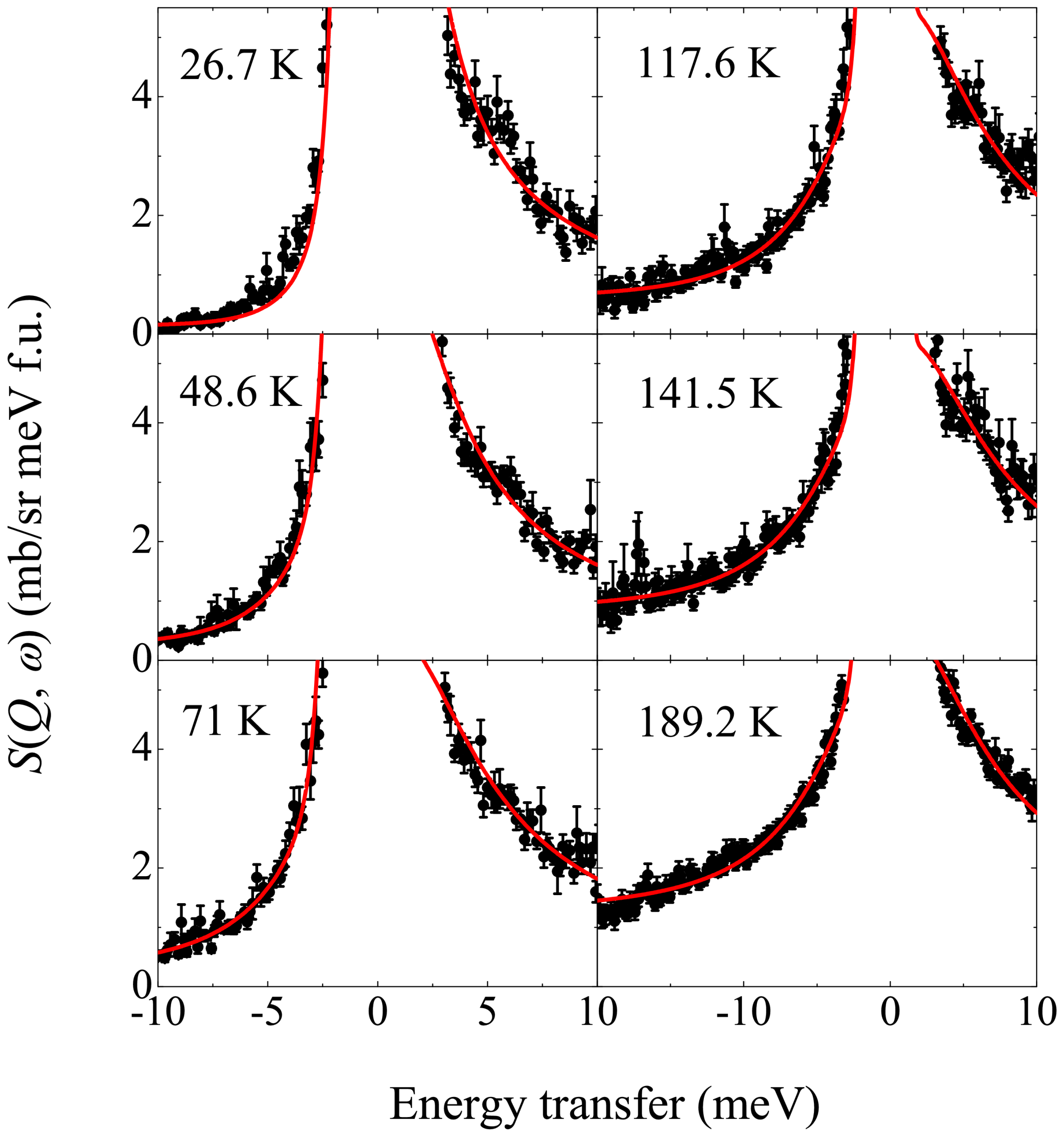

Figure 4.17: Cuts of $S(\mathbf{Q},\omega)$ for $CeCoGe_3$ with E_i = 15 meV measured on the MERLIN spectrometer. The solid lines show fits to the elastic line and a Lorentzian quasielastic component.

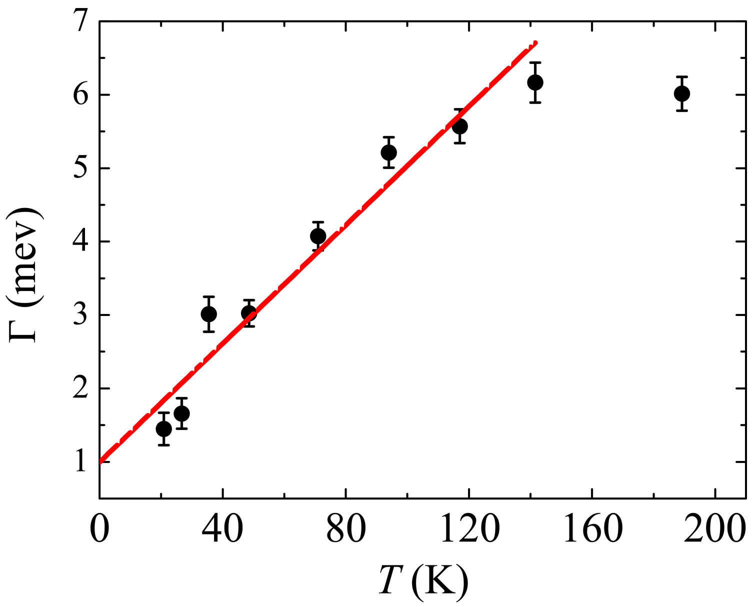

Figure 4.18: The temperature dependence of the quasielastic linewidth (half width at half maximum) of $CeCoGe_3$ measured on the MERLIN spectrometer. A linear fit has been made to the data up to 150 K.

$|\mathbf{Q}|$ cuts of $CeCoGe_3$, consistent with the presence of a CEF level at this energy transfer. At ∼28 meV there is an additional peak at low $|\mathbf{Q}|$ for $CeCoGe_3$ but not for the other cuts. The scattering of $CeCoGe_3$ is greater at this energy than $LaCoGe_3$ and the low $|\mathbf{Q}|$ intensity is greater than the high $|\mathbf{Q}|$, indicating a second CEF level at around 28 meV.

Having established the presence of two CEF excitations at low temperatures, cuts of $S_{\mathrm{mag}}(\mathbf{Q},\omega)$ were made for $E_{\mathrm{i}} = 40$ (Fig. 4.20) and 10 meV (Fig. 4.21). The data were analyzed with a CEF Hamiltonian for a Ce^{3+} ion in a tetragonal crystal field (Eq. 2.5), as described in Sec. 2.1.2. A CEF scheme was sought which was compatible with both magnetic susceptibility and INS data. B_0^2 was estimated using Eq. 2.16 for isotropic exchange interactions and using the values for the Curie-Weiss temperatures [60], $B_0^2 = -0.376$ meV was estimated. In particular, a negative B_0^2 is expected since $\theta_{ab} < \theta_c$. A simultaneous fit was made to S_{mag} above T_{N1}. Initially B_0^2 was fixed but was allowed to vary in the final fit. Good fits to the data are obtained, as shown by the solid lines in Figs. 4.20(b)-(d) and 4.21(b).

As discussed previously, at 4 K an extra peak is observed in the cut of S_{mag} at 4.5 meV. This was accounted for within the CEF model with the addition of an internal magnetic field. This was carried out by adding a term $-g_J\mu_{\mathrm{B}}\mathbf{B}\cdot\mathbf{J}$

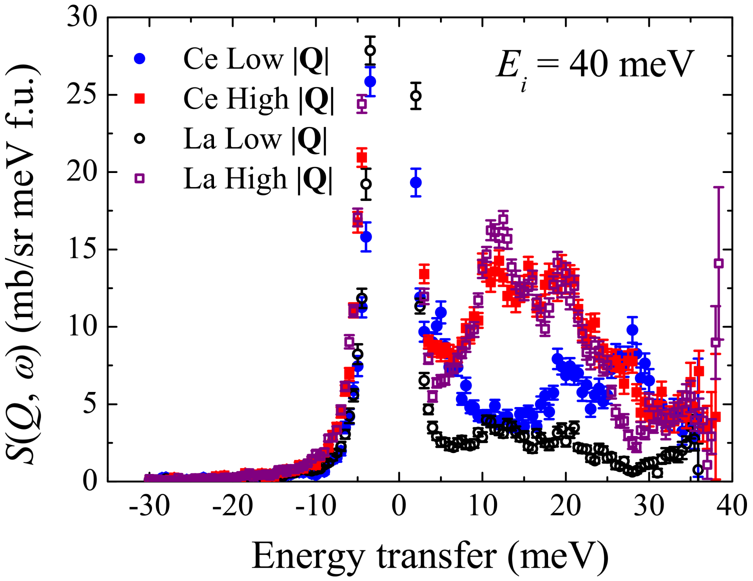

Figure 4.19: Cuts of $S(\mathbf{Q},\omega)$ with E_i =40 meV of CeCoGe$_3$ at 4 K and LaCoGe$_3$ at 5 K from integrating across $|\mathbf{Q}|$. The integration was from 0-3 Å^{-1} for low $|\mathbf{Q}|$ and from 5-8 Å^{-1} for high $|\mathbf{Q}|$.

to the Hamiltonian $\mathscr{H}_\mathrm{CEF}$ in Eq. 2.5. In the presence of a magnetic field, time reversal symmetry is broken and the states of the ground state doublet are no longer degenerate, leading to an additional peak in S_mag. Since the magnetic moments lie along the c axis, S_mag was fitted with a finite internal field $\mathbf{B}$ = (0,0,B_z), with B_4^0 and B_4^4 also being varied. Small changes in CEF parameters are allowed below T_N either due to small changes in the lattice parameters or due to the contribution of conduction electrons to the CEF [190][191]. Figs. 4.20(a) and 4.21(a) show that B_z = 340(20) kG gives a good fit to the data.

The inverse magnetic susceptibility of CeCoGe$_3$ single crystals for $H \parallel c$ and $H \parallel ab$ are shown in Fig. 4.22. Fits were made to Eqs. 2.14 and 2.15 with the CEF parameters fixed from the fitted INS data. Molecular-field parameters and temperature independent susceptibilities were allowed to vary and the resulting fit is shown by the solid lines which shows reasonably good agreement. Similar CEF parameters were obtained from simultaneously fitting the INS data at 25 K and the magnetic susceptibility data. The results from fitting the data at 4 and 25 K are shown in Table 4.2.

The corresponding wave functions above T_N1 are

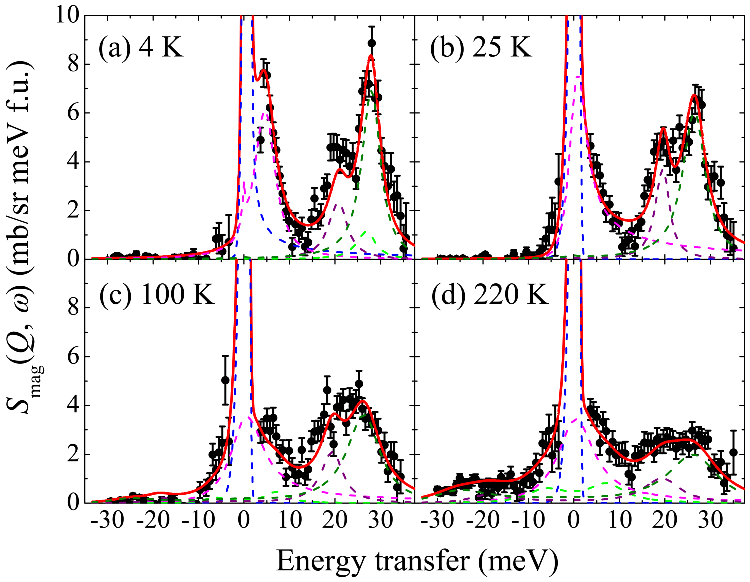

Figure 4.20: $S_{\mathrm{mag}}(\mathbf{Q}, \omega)$ of CeCoGe$_3$ with E_{i} =40 meV at (a) 4 K, (b) 25 K, (c) 100 K and (d) 220 K. The subtraction was made following Eq. 2.73. The solid line shows a fit to a CEF model described in the text and the dashed lines show the fit components.

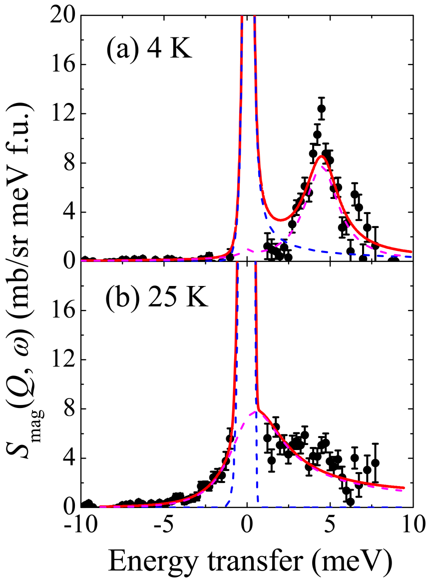

Figure 4.21: $S_{\mathrm{mag}}(\mathbf{Q}, \omega)$ of CeCoGe$_3$ with E_{i} = 10 meV at (a) 4 K and (b) 25 K. The subtraction was made following Eq. 2.73. The solid line shows a fit to a CEF model described in the text and the dashed lines show the fit components.

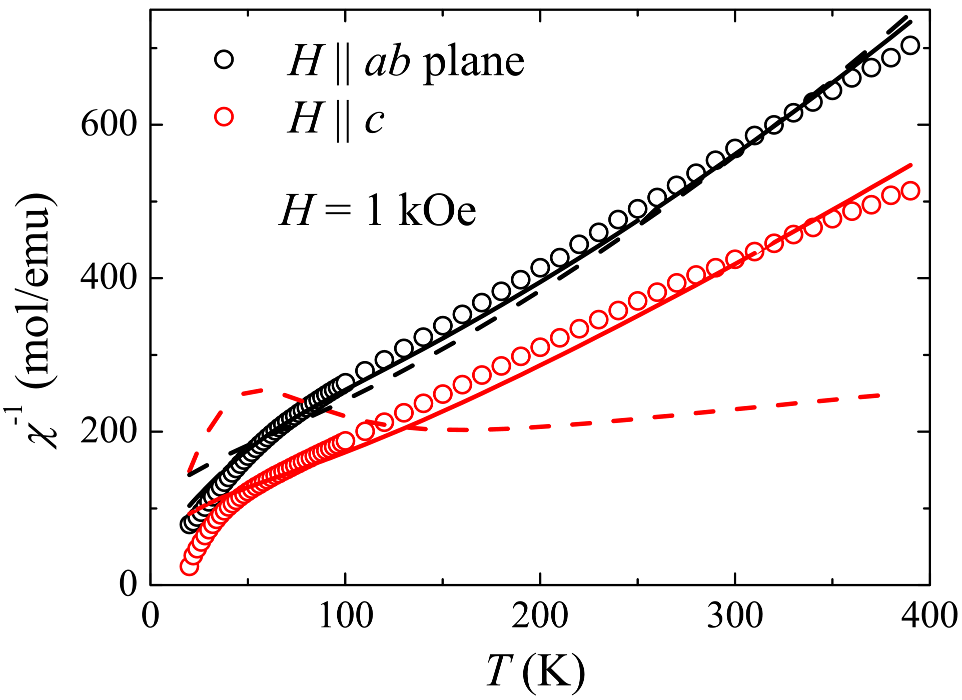

Figure 4.22: The inverse magnetic susceptibility for single crystals of $\mathrm{CeCoGe_3}$ between 20 and 390 K in an applied field of 1 kOe. The solid lines show a fit to a CEF model described in the text. The dashed lines show the best fit to a model with the $\left|\pm\frac{1}{2}\right\rangle$ ground state, with CEF parameters which can be fitted to the INS data

$$|\psi_1^{\pm}\rangle = 0.8185\left|\pm\frac{5}{2}\right\rangle - 0.5745\left|\mp\frac{3}{2}\right\rangle, \tag{4.4}$$

$$|\psi_2^{\pm}\rangle = \left|\pm\frac{1}{2}\right\rangle, \tag{4.5}$$

$$|\psi_3^{\pm}\rangle = 0.8185\left|\pm\frac{3}{2}\right\rangle + 0.5745\left|\mp\frac{5}{2}\right\rangle.$$

ψ_1 is the ground state wave function, ψ_2 is the first excited doublet at 19.3 meV and ψ_3 is at 26.4 meV. The ground state moments were evaluated using Eq. 2.11. $\langle\mu_z\rangle$ and $\langle\mu_x\rangle$ are calculated to be 1.01 μ_B and 0.9 μ_B. A calculation of the magnetocrystalline anisotropy energy for this CEF model using Eq. 2.10 gives $K_1 = 4.9$ meV,

Table 4.2: Results from fitting INS and magnetic susceptibility data to a CEF model at 4 and 25 K. The CEF parameters, quasi-elastic and CEF linewidths, molecular-field parameters and temperature independent susceptibilities are shown.

	4 K	25 K
B_2^0 meV	-0.61	$-0.61(4)$
B_4^0 meV	$-0.013(3)$	$-0.007(2)$
B_4^4 meV	0.412(8)	0.463(8)
Γ_{QES} (meV)	–	1.9(3)
Γ_{ψ_2} (meV)	2.5(2)	1.6(3)
Γ_{ψ_3} (meV)	2.3(2)	2.9(3)
λ_{ab} (mole/emu)	–	-40.9
λ_c(mole/emu)	–	-52.0
χ_0^{ab} ($\times 10^{-3}$ emu/mol)	–	-0.404
χ_0^c ($\times 10^{-3}$ emu/mol)	–	-1.936

so the moment is predicted to lie along the c axis.

The CEF model predicts a ground state moment of 1.01 μ_{B}/Ce whereas as previously discussed, the observed ordered moment is 0.405 μ_{B}. This suggests that the moment is significantly reduced compared to that predicted from a single ion CEF model. This is a markedly different conclusion to the one that would be drawn if the ground state doublet was $\left|\pm\frac{1}{2}\right\rangle$, where there would be no significant moment reduction. Therefore, the possibility of there being a set of CEF parameters which gives this ground state and is compatible with the data should be considered further. Reasonable agreement with magnetic susceptibility data was found in Ref. [60] for such a scheme. This is despite the proposed scheme having B_2^0 ∼0.3 meV when a negative value would be expected from Eq. 2.16. However, the excited doublets are expected to be at 9.8 and 27.3 meV which are clearly incompatible with the INS data. A CEF scheme was found that was compatible with such a ground state with a larger positive value of B_2^0 ∼1.1 meV. The best fit to the magnetic susceptibility for this set of CEF parameters is shown by the dashed lines in Fig. 4.22. Reasonable agreement is obtained for $H \parallel ab$ although the fit is worse than the one shown by the solid black line. However there is very poor agreement for $H \parallel c$, demonstrating that this model is incompatible with the susceptibility data. Furthermore the pronounced hump in χ^{-1} at low temperatures for $H \parallel c$ is not observed in the data. A hump is also present in the model in Ref. [60], albeit in a less pronounced form and has also been observed in other compounds with such a ground state doublet [192]. However it is absent in $CeCoGe_3$, which is further evidence that this is not the ground state doublet. Therefore only one CEF model was found to fit the magnetic susceptibility and INS data and this indicates a reduced cerium moment in $CeCoGe_3$.

4.6 Discussion and summary

$CeCoGe_3$ has been studied using μSR, single crystal neutron diffraction, magnetic susceptibility and powder inelastic neutron scattering. Single crystals grown by the flux method were measured using single crystal neutron diffraction in zero-field and the magnetic propagation vector is observed to change at each transition with $\mathbf{k} = (0,0,\frac{1}{2})$ for $T < T_{\mathrm{N3}}$, $\mathbf{k} = (0,0,\frac{5}{8})$ for $T_{\mathrm{N3}} \leq T < T_{\mathrm{N2}}$, and $\mathbf{k} = (0,0,\frac{2}{3})$ for $T_{\mathrm{N2}} < T < T_{\mathrm{N1}}$. A ferromagnetic component is also inferred between T_{N3} and T_{N1} from an increase in the intensity of the (110) reflection in this region. The results indicate the that the moments align along the c axis in all three phases and are compatible with an equal moment, two-up, two down structure below T_{N3} and two-up one down between T_{N2} and T_{N1}. For these equal moment solutions, magnetic refinements give moments of 0.405(5) μ_{B}/Ce at 2 K and no equal moment structure could be deduced for the middle phase. This indicates a solution with unequal moments. Such spin-density wave type structures can arise in systems with competing interactions [116]. Further information about the structure in this phase would require a measurement of the magnitude of the ferromagnetic moment, which could be found by performing polarized neutron diffraction measurements. The $\mathbf{k} = (0,0,\frac{1}{2})$ propagation vector agrees with the dominant component observed in Ref. [175], but no evidence was found for the weaker $\mathbf{k} = (0,0,\frac{3}{4})$. This shows that there appears to be sample dependence for single crystals, even though both samples were synthesized using the same method. This suggests that $CeCoGe_3$ has many competing magnetic phases and small variations in the crystal structure, site ordering or stoichiometry may promote different ground states.

The observation of a sharp drop in asymmetry, increase in the fluctuation rate and oscillations of the asymmetry in zero-field μSR spectra confirm the onset of long range magnetic order between 21 and 20 K. The internal fields were deduced from the frequency of the oscillations and the data were fitted with a model of the order parameter. The value of β may give information about the dimensionality of the system and order parameter [109]. The fact that the moments in all phases order along the c axis and sharp metamagnetic transitions are observed in the c axis susceptibility may suggest that the system is best described by an Ising model. The role of dimensionality is a very important topic in heavy-fermion superconductivity, with the higher superconducting T_c in CeTIn$_5$ often being ascribed to a quasi-two-dimensional electronic structure [13]. The CeTX_3 superconducting states have lower values of T_c and in this would be further supported by a model with $\beta = 0.326$ for a three-dimensional Ising model. However, the only model which fitted the data was $\beta = 0.5$ for the mean field case, which does not reveal the universality class of the phase transition. This mean field model was also consistent with the size of the magnetic moments deduced from refinements of the neutron diffraction data at 2 and 14 K.

INS measurements were used to measure the CEF scheme as well the temperature dependence of low energy magnetic scattering. It is of particular use to compare the response to other CeTX_3 compounds. INS measurements have previously been made on CeRhGe$_3$ [162] and CeRhSi$_3$ [56]. At 2 and 10 K a well defined peak in cuts of $S_{\mathrm{mag}}(\mathbf{Q}, \omega)$ at 4.5 meV gives the energy of the zone boundary magnons. In CeRhGe$_3$ a peak was observed at 3 meV and it orders at $T_{\mathrm{N1}} = 14.5$ K. Both the peak energy and T_{N1} scale similarly between CeRhGe$_3$ and CeCoGe$_3$ and the higher values in the case of the latter indicate stronger intersite exchange interactions. Possible evidence is seen for a second low energy peak in CeRhGe$_3$ which may be evidence for anisotropic dispersions. However no evidence for a second peak is observed in CeCoGe$_3$. Further characterization of the spin-waves and in particular anisotropic properties would be greatly aided by INS measurements of single crystals. T_{K} deduced from the zero temperature width of the quasielastic linewidth was similar in both compounds, being 11(3) K in CeCoGe$_3$ and 12.6(3) CeRhGe$_3$. However Γ is linear with temperature up to 140 K in CeCoGe$_3$ while it is nearly temperature independent above 20 K in CeRhGe$_3$. Although the first excited CEF doublet is at a lower level in the latter ($\sim$87 K), it is not clear that this entirely explains the difference in the temperature dependence at low temperatures.

From fitting single crystal magnetic susceptibility and INS data, a CEF scheme for CeCoGe$_3$ has been proposed for the splitting of the $J = \frac{5}{2}$ multiplet. The ground state is an admixture of $\left|\pm\frac{5}{2}\right\rangle$ and $\left|\mp\frac{3}{2}\right\rangle$ states and schemes with a $\left|\pm\frac{1}{2}\right\rangle$ ground state are not compatible with the data. A similar ground state was proposed for CeRhGe$_3$, although the largest component was $\left|\pm\frac{3}{2}\right\rangle$ rather than $\left|\pm\frac{5}{2}\right\rangle$. In both cases a sizeable B_4^4 leads to this mixing. B_2^0 is negative for CeCoGe$_3$ but positive for CeRhGe$_3$.

The predicted moment is 1.01 μ_{B}/Ce along the c axis and therefore the direction of the observed moment is correctly predicted but the magnitude is reduced compared to that predicted from the CEF model. In both CeRhGe$_3$ and CeRhSi$_3$

the moment is predicted to lie in the *ab* plane. This is correct for $\mathrm{CeRhSi_3}$ but for $\mathrm{CeRhGe_3}$, the change in orientation was ascribed to two-ion anisotropic exchange interactions. These are not necessary to account for the moment direction $\mathrm{CeCoGe_3}$, but the presence of a similar anisotropic exchange would further increase the energy cost of deviations of the moment from the c axis and may explain the strong Ising like behaviour observed in the magnetic phases.

The significant moment reduction is evidence for hybridization of the cerium $4f$ and conduction electrons and there is partial screening of the moments. In the case of $\mathrm{CeRhGe_3}$, a similar moment aligned along the c axis is observed through neutron diffraction measurements but this is in agreement with the predicted $\langle\mu_z\rangle$. However, the moment reduction of $\mathrm{CeCoGe_3}$ is not as great as in $\mathrm{CeRhSi_3}$, where the CEF model predicts a moment of 0.92 μ_B/Ce but 0.12 μ_B/Ce is observed in neutron diffraction measurements [53]. A similar trend is observed in the linewidths of the CEF excitations. As shown in Table 4.2, the linewidths at 25 K were 1.6(3) and 2.9(3) meV for transitions from the ground state to ψ_2 and ψ_3. The corresponding values for $\mathrm{CeRhGe_3}$ were 1.4(2) and 2.2(3) meV and therefore the excitation to ψ_3 is broader in $\mathrm{CeCoGe_3}$. However the CEF excitations were broader still in $\mathrm{CeRhSi_3}$, where 3.9(2) and 9.2(4) meV are obtained [193]. These results indicate that $\mathrm{CeCoGe_3}$ displays a degree of hybridization in between that of $\mathrm{CeRhGe_3}$ and $\mathrm{CeRhSi_3}$. This agrees with $\mathrm{CeRhSi_3}$ being closer to quantum criticality, becoming superconducting at 1.2 GPa and $\mathrm{CeRhGe_3}$ being further away, not displaying superconductivity up to 8.0 GPa.

Chapter 5

Ce$\boldsymbol{T}$X$_3$

5.1 Introduction

In the previous chapter, ground state properties of the antiferromagnetic, pressure induced superconductor CeCoGe$_3$ were reported. The magnetic structure was characterized using single crystal neutron diffraction and a CEF scheme was deduced from inelastic neutron scattering measurements. These results indicate that the observed ordered moment is reduced, compared to that predicted from ground state doublet. As discussed in Sec. 1.1.1, a range of ground state behaviours are observed in CeTX_3 series, many of which have not been fully characterized. In this section, inelastic neutron scattering measurements of CePdSi$_3$, CePtSi$_3$ and CeRuSi$_3$ are reported. CePdSi$_3$ and CePtSi$_3$ both order antiferromagnetically at low temperatures. CePdSi$_3$ was reported to exhibit two magnetic transitions at 5.2 and 3 K from specific heat measurements of polycrystalline samples, although an anomaly at the lower transition is not observed in resistivity measurements [65]. CePtSi$_3$ orders at T_{N1} = 4.8 K and undergoes a subsequent transition at T_{N2} = 2.4 K [64]. Measurements of single crystals grown by the flux method indicate that [100] is the magnetic easy axis and an ordered moment of 1.15 μ_{B}/Ce is deduced from the value of the saturation magnetization. In this chapter, both high and low energy inelastic neutron scattering measurements are reported for polycrystalline samples of CePdSi$_3$, while low energy measurements are reported for CePtSi$_3$. In the latter, spin wave excitations are observed below the ordering temperature and quasielastic scattering above, while the CEF excitations are observed in the high energy measurements.

Not all of the CeTX_3 compounds have magnetically ordered ground states. Single crystals of CeRuSi$_3$ have previously been grown using the Czochralski method and it has been reported to be non-magnetic with a broad peak in the magnetic susceptibility at around 150 K [194]. It has therefore been considered to be an intermediate valence compound, where the Kondo interaction is sufficiently strong that the system does not magnetically order [36]. In this section, magnetic susceptibility, specific heat and inelastic neutron scattering measurements are reported for polycrystalline $\mathrm{CeRuSi_3}$. This allows the magnetic response to be compared to systems where the $4f$ electrons appear to have a more localized nature.

5.2 $\mathrm{CeRuSi_3}$

5.2.1 Sample preparation and structural characterization

Polycrystalline samples of $\mathrm{CeRuSi_3}$ and the non-magnetic $\mathrm{LaRuSi_3}$ were produced by arc-melting stoichiometric quantities of the constituent elements (Ce : 99.9%, La : 99.9%, Ru : 99.99%, Si : 99.999%) in an argon atmosphere on a water cooled copper hearth. The samples were flipped and remelted several times before being wrapped in tantalum foil, sealed in an evacuated quartz tube and annealed at 900°C for two weeks. Powder x-ray diffraction measurements were carried out using a Bruker D5005 diffractometer. Rietveld refinements were carried out using the TOPAS software [151] and the fitted patterns are shown in Fig. 5.1. Several extraneous peaks are observed in both compounds which can not be indexed to any reflections for the $\mathrm{BaNiSn_3}$ structure. The largest of these peaks for the $\mathrm{CeRuSi_3}$ pattern is at 25.4° which has an intensity $\sim 4\%$ of the largest sample peak.

The results of the Rietveld refinements are given in Table 5.1. The lattice parameters are in good agreement with the previously reported values [195]. There is also reasonably good agreement for the atomic positions. However, it can be seen in Fig. 5.1 that the intensity of the (004) reflection at 36.0° is significantly underestimated in both patterns. If a z position on the Si1 site of ~ 0.42 from Ref. [195] is used rather than the fitted value of ~ 0.40, then this discrepancy is greatly reduced. More generally it should be noted that the Bruker D5005 diffractometer has a lower angular resolution than the Panalytical X-Pert Pro diffractometer used in Sec. 4.2. Higher resolution x-ray diffraction measurements may be required to accurately determine the atomic positions.

5.2.2 Magnetic susceptibility

The magnetic susceptibility of $\mathrm{CeRuSi_3}$ in an applied field of 10 kOe is shown in Fig. 5.2. The two main features are a broad peak at around 150 K and a sharp increase in the susceptibility at low temperatures. Magnetic susceptibility measure-

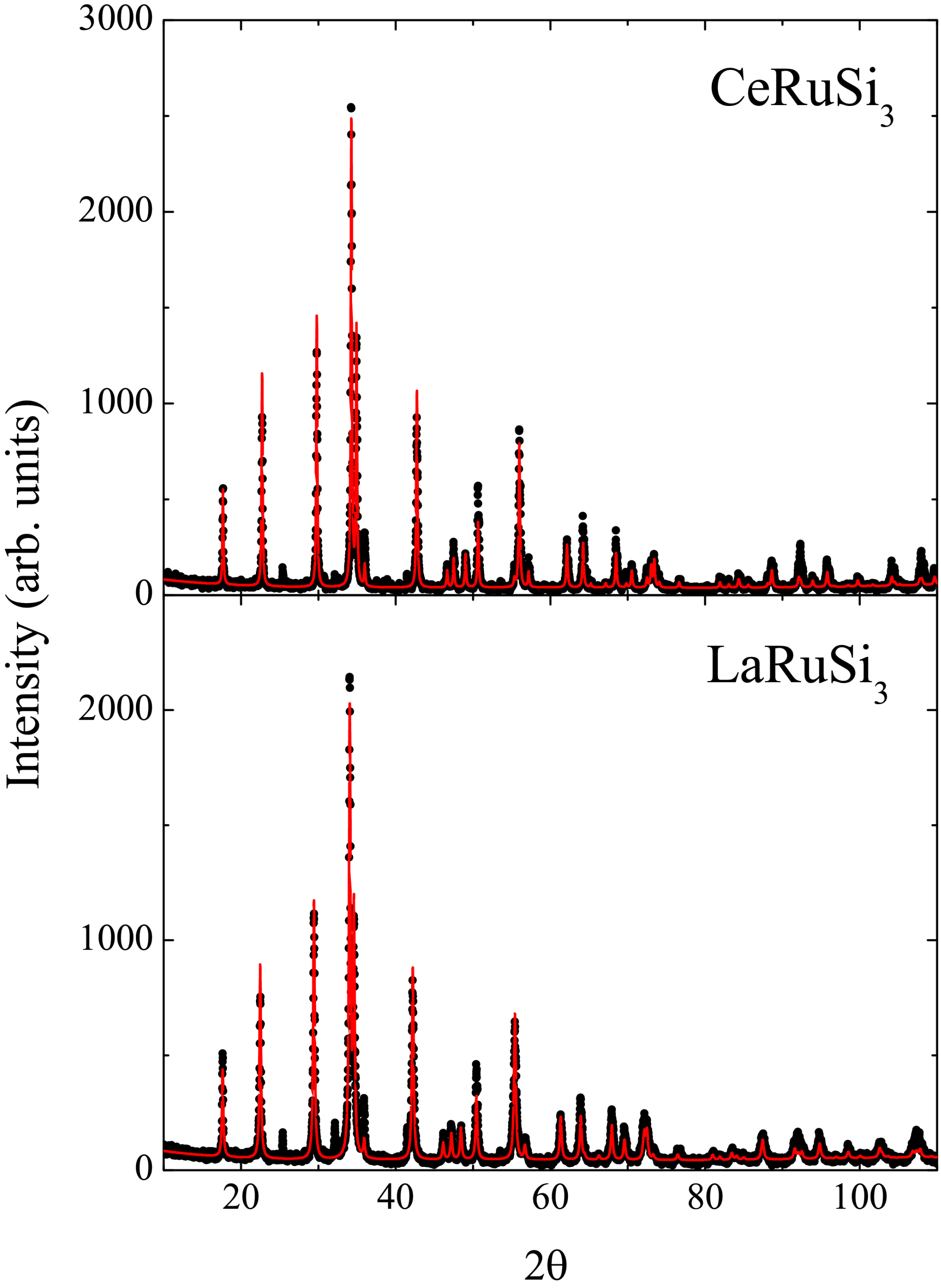

Figure 5.1: Powder x-ray diffraction measurements of CeRuSi$_3$ and LaRuSi$_3$ measured using a Bruker D5005 diffractometer. The solid lines show the Rietveld refinements performed using TOPAS. The results are given in Table 5.1.

Table 5.1: Results of the refinements of powder x-ray diffraction measurements on $CeRuSi_3$ and $LaRuSi_3$. The lattice parameters, weighted profile factor (R_{wp}) and the atomic positions are shown.

	$CeRuSi_3$	$LaRuSi_3$		
a (Å)	4.2106(2)	4.2597(3)		
c (Å)	9.9204(7)	9.9382(9)		
R_{wp}(%)	24.2	21.4		
	Site	x	y	z
Ce	2a	0	0	0
Ru	2a	0	0	0.6528(5)
Si1	2a	0	0	0.403(2)
Si2	4b	0	0.5	0.762(1)
La	2a	0	0	0
Ru	2a	0	0	0.6513(5)
Si1	2a	0	0	0.398(2)
Si2	4b	0	0.5	0.761(1)

ments of single crystals in Ref. [194] also show the broad peak at higher temperatures. However, although there is a slight upturn at low temperatures, it is far smaller than that observed in this polycrystalline sample, which suggests that this mainly originates from paramagnetic impurities. Although these may constitute a relatively small fraction of the sample, in the absence of a Curie like susceptibility from the main phase, such a contribution from an impurity may dominate at low temperatures.

5.2.3 Inelastic neutron scattering

Inelastic neutron scattering measurements on polycrystalline $CeRuSi_3$ and $LaRuSi_3$ were performed on the MERLIN spectrometer at ISIS. The samples were wrapped in Al foil and cooled to 7 K in a closed cycle refrigerator. Measurements were made at 7 and 300 K with $E_i = 30$, 100 and 200 meV selected via a Fermi chopper. Colour plots of the INS intensity in absolute units for $E_i = 200$ meV are shown in Fig. 5.3. Figures 5.3 (a) and (b) show the low temperature scattering of $CeRuSi_3$ and $LaRuSi_3$ respectively. Extra scattering at low $|\mathbf{Q}|$ can be identified in the $CeRuSi_3$ plot. Although this is most intense at around 50 meV, it extends up close to 100 meV whereas the scattering is negligible for $LaRuSi_3$ at these energies, apart from at high momentum transfers. The scattering of $LaRuSi_3$ at 300 K (Fig. 5.3(d)) is similar to

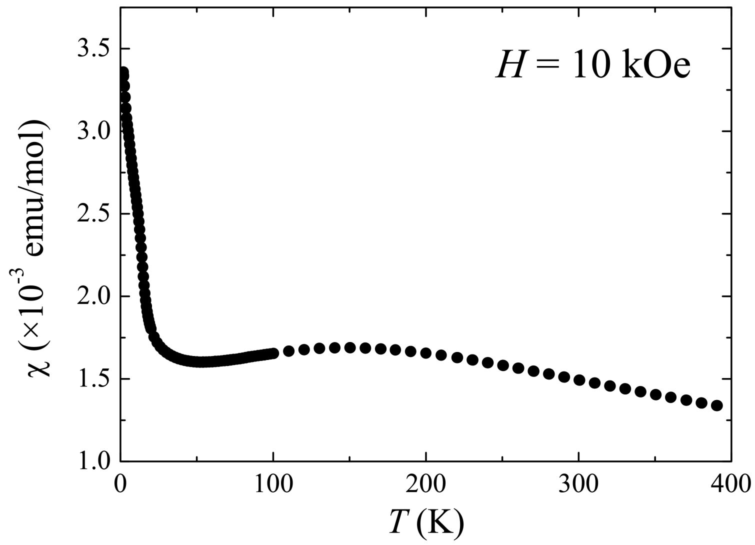

Figure 5.2: Magnetic susceptibility of $\mathrm{CeRuSi_3}$ as a function of temperature in an applied field of 10 kOe.

that observed at low temperatures. However, although magnetic scattering can still be identified in the measurements of $\mathrm{CeRuSi_3}$ at 300 K (Fig. 5.3(c)), it has shifted to lower energies. The low $|\mathbf{Q}|$ scattering is significantly reduced above 50 meV, suggesting a change in behaviour with increasing temperature.

Cuts of $S(\mathbf{Q},\omega)$ were made by integrating across low and high values of $|\mathbf{Q}|$. These are shown for $E_{\mathrm{i}} = 30$ and 100 meV in Fig. 5.4. The low $|\mathbf{Q}|$ cuts were integrated from 0-3 Å^{-1} for $E_{\mathrm{i}} = 30$ meV and 0-5 Å^{-1} for $E_{\mathrm{i}} = 100$ meV, while the high $|\mathbf{Q}|$ cuts were integrated from 4-7 Å^{-1} for $E_{\mathrm{i}} = 30$ meV and 8-13 Å^{-1} for $E_{\mathrm{i}} = 100$ meV. For energy transfers less than 60 meV, the high $|\mathbf{Q}|$ scattering is significantly stronger than that for low $|\mathbf{Q}|$ in both compounds, indicating the dominance of phonon scattering at these energies, whereas above 60 meV very little phonon scattering is seen within this range of momentum transfers. Three peaks from phonons can be identified in the plot with $E_{\mathrm{i}} = 100$ meV. The two higher energy peaks occur in the same position for both compounds but the lowest energy peak is at lower energies in $\mathrm{CeRuSi_3}$ compared to $\mathrm{LaRuSi_3}$. Clear evidence for magnetic scattering in $\mathrm{CeRuSi_3}$ is observed in both plots. For $E_{\mathrm{i}} = 30$ meV, the low $|\mathbf{Q}|$ scattering of $\mathrm{CeRuSi_3}$ is larger than that of $\mathrm{LaRuSi_3}$ for energy transfers greater than 16 meV, despite similar scattering at high $|\mathbf{Q}|$. For $E_{\mathrm{i}} = 100$ meV, while the high $|\mathbf{Q}|$ scattering is similar for both compounds at energies greater than 20 meV, the

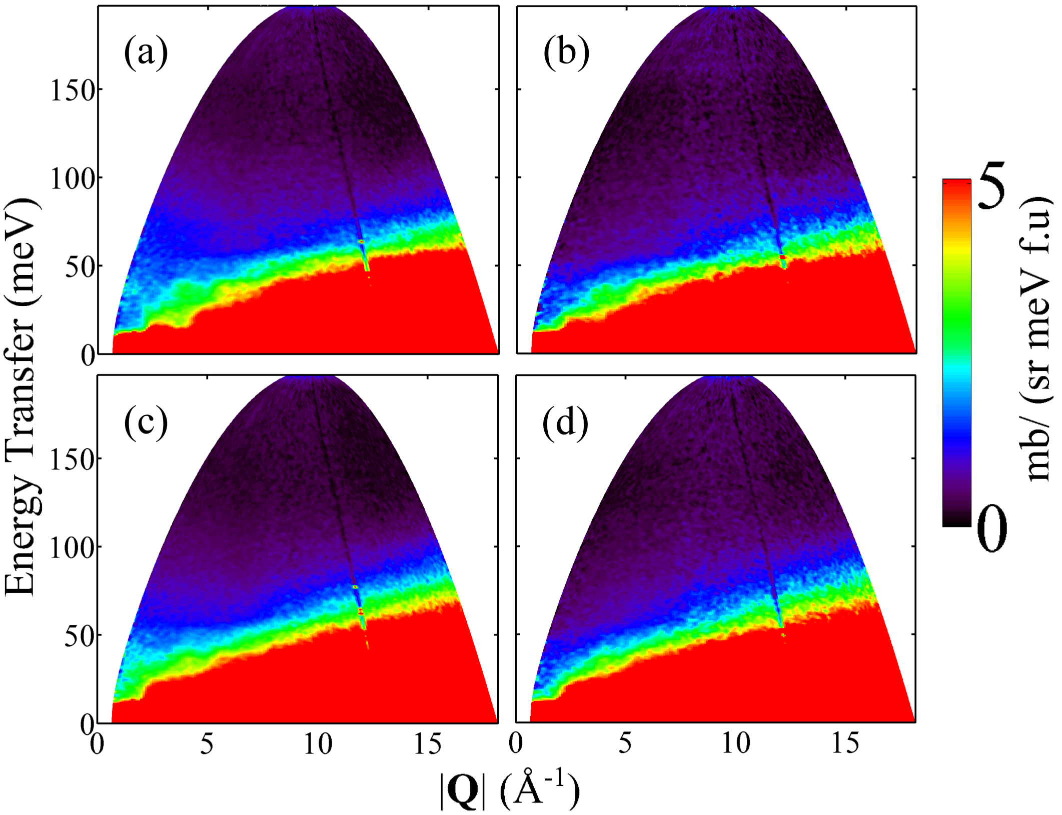

Figure 5.3: Colour plots of the INS intensity measured on MERLIN with E_i = 200 meV for (a) CeRuSi$_3$ at 7 K, (b) LaRuSi$_3$ at 7 K, (c) CeRuSi$_3$ at 300 K. (d) LaRuSi$_3$ at 300 K.

low $|\mathbf{Q}|$ scattering is consistently larger for $\mathrm{CeRuSi_3}$. Above 60 meV, where very little phonon scattering is observed, the low $|\mathbf{Q}|$ scattering of $\mathrm{CeRuSi_3}$ is greater than the high $|\mathbf{Q}|$. This is all evidence for the presence of magnetic scattering above 20 meV, up to energy transfers of just under 100 meV. This is quite different to the magnetic scattering observed from CEF levels, where it is relatively well localized to the energies of the excited doublets.

It is therefore desirable to estimate the magnetic scattering by subtracting an estimate of the phonon contribution. A direct subtraction using Eq. 2.73 does not provide a good estimate. An inadequate subtraction might be expected in the region of the phonon peak at around 20 meV, since the peak position is different for the two compounds. In fact, all three phonon peaks observed for $E_\mathrm{i} = 100$ meV are still clearly visible after making such a subtraction. As a result, S_mag was estimated using Eq. 2.74. This is shown at 7 and 300 K for $E_\mathrm{i} = 30$ meV in Fig. 5.5. At 300 K broad quasielastic scattering is observed. However, at 7 K the magnetic scattering is greatly reduced, with S_mag remaining nearly flat across energy transfers up to 30 meV. The value is small but larger than that observed for negative energy transfers. It would be of interest to determine whether the magnetic scattering is entirely absent at low energies and therefore if the excitation spectrum can be said to be entirely gapped as has been observed in several other heavy fermion compounds [196]. The finite value may be the result of inaccuracies in the subtraction of the phonon scattering, small quantities of magnetic scattering from cerium-based impurity phases or the presence of low energy magnetic scattering in $\mathrm{CeRuSi_3}$. It should be noted that in Fig. 5.4, the low $|\mathbf{Q}|$ scattering of $\mathrm{CeRuSi_3}$ exceeds that of $\mathrm{LaRuSi_3}$ above around 16 meV, while the high $|\mathbf{Q}|$ scattering of the two compounds are similar in this region.

Figure 5.6 displays estimates of the magnetic scattering at 7 K for $E_\mathrm{i} = 100$ and 200 meV. For $E_\mathrm{i} = 200$ meV, a broad peak in the magnetic scattering is observed. The data were fitted with a single Lorentzian convoluted with the resolution function of the instrument. A peak centre of (58.5 ± 1.4) meV with a Lorentzian linewidth of (31.5 ± 1.1) meV was obtained. This is considerably broader then the widths generally observed for CEF excitations. The single peak appears to account well for the magnetic scattering and any further structure in the data can not be resolved. The magnetic scattering for $E_\mathrm{i} = 100$ meV is also broad, with a maximum at around 60 meV. However, additional structure in the magnetic scattering can be observed at lower energy transfers. Further maxima are observed at around 32 and 45 meV. The feature at 32 meV appears particularly sharp and narrow compared to the rest of the magnetic scattering. The data were fitted with two Lorentzian functions and data in

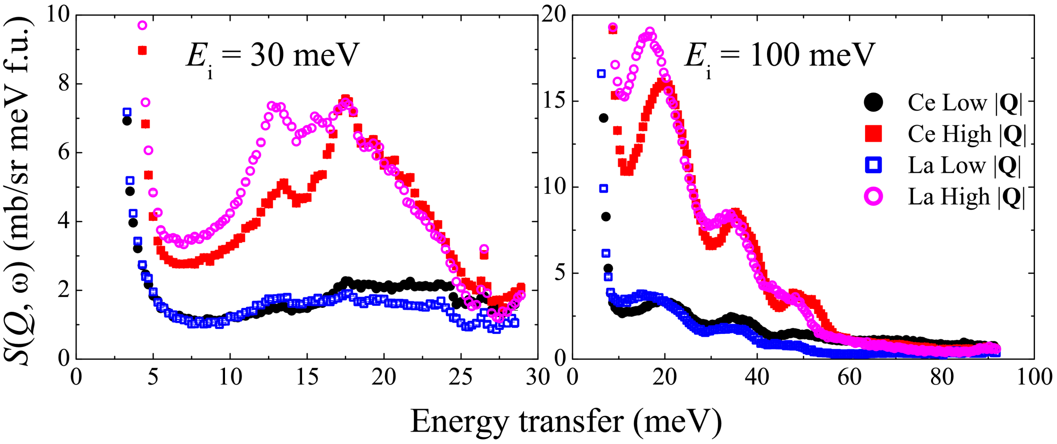

Figure 5.4: Cuts of $S(\mathbf{Q}, \omega)$ with $E_\mathrm{i} = 30$ and 100 meV of CeRuSi$_3$ at 7 K and LaRuSi$_3$ at 7 K from integrating across $|\mathbf{Q}|$. For $E_\mathrm{i} = 30$ meV, the integration was from 0-3 Å^{-1} for low $|\mathbf{Q}|$ and from 4-7 Å^{-1} for high $|\mathbf{Q}|$ while for $E_\mathrm{i} = 100$ meV they were from 0-5 Å^{-1} and 8-13 Å^{-1}.

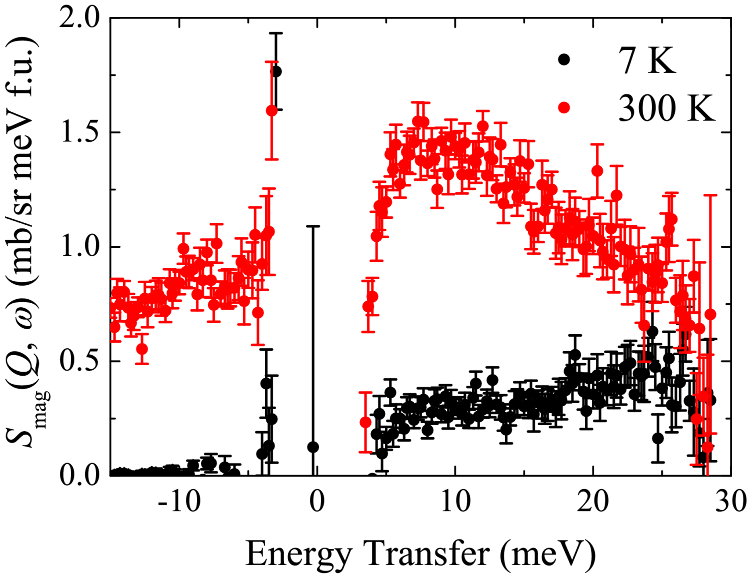

Figure 5.5: The magnetic scattering of CeRuSi$_3$ at 7 and 300 K for $E_\mathrm{i} = 30$ meV, estimated using Eq. 2.74.

the region of the sharp feature were excluded from the fit. Peak centres of 60(5) and 39(3) meV were obtained. This accounts well for the magnetic scattering apart from in the region excluded from the fit. The peak at 60 meV is approximately four times more intense and the centre position agrees with the fitted value for $E_\mathrm{i} = 200$ meV.

There are several other options for fitting the data. Firstly, a single peak could be fitted either across the whole region of magnetic scattering or excluding the narrow feature at around 32 meV. In both cases this was not a particularly good fit to the data and the peak position was significantly lower than that obtained for $E_\mathrm{i} = 200$ meV. This suggests that there are additional features in the magnetic scattering not accounted for by a single Lorentzian peak. Secondly, two peaks were fitted but not excluding the sharp feature. This did not particularly fit the magnetic scattering well between 40 and 60 meV and again the peak position of the higher peak did not agree with the $E_\mathrm{i} = 200$ meV data. The linewidth of the lower peak was significantly narrower confirming its localized nature compared to the magnetic scattering at higher energies.

It may be that there is a localized feature in the magnetic scattering of CeRuSi$_3$, which co-exists with the dominant broad scattering. Another possible origin for this feature could be the incorrect subtraction of the phonon scattering. In Fig. 5.4 there is a peak in the high $|\mathbf{Q}|$ scattering for both CeRuSi$_3$ and LaRuSi$_3$ at around 35 meV. However, the peak for CeRuSi$_3$ is stronger and more pronounced while the feature for LaRuSi$_3$ is flattened. This suggests differences in the phonon dispersion between the two compounds which may lead to an incorrect subtraction in this region. The feature could also be a CEF level from an impurity phase. As discussed in Sec. 5.2.1, the maximum magnitude of peaks in the powder x-ray diffraction measurements corresponding to the impurity phases was $\sim 4\%$ of the largest sample peak, although the structure of these compounds could not be identified. It may be that an impurity phase of this fraction is sufficient to cause a sharp peak to appear on top of the broad magnetic scattering, although such a compound would need to contain cerium atoms with localized $4f$ electrons.

The magnetic scattering at 300 K for $E_\mathrm{i} = 200$ meV is shown in Fig. 5.7. At this temperature, the magnetic scattering is centred on the elastic line but is considerably broader than the instrument resolution. This quasielastic scattering was fitted with Eq. 2.72 convoluted with the resolution of the instrument and a linewidth of $\Gamma = 30(3)$ meV is obtained. Therefore between 7 and 300 K the magnetic scattering changes from a maximum at finite energy transfers to broad quasielastic scattering. This is consistent with the shift in the magnetic scattering towards lower energy transfers observed in Fig. 5.3.

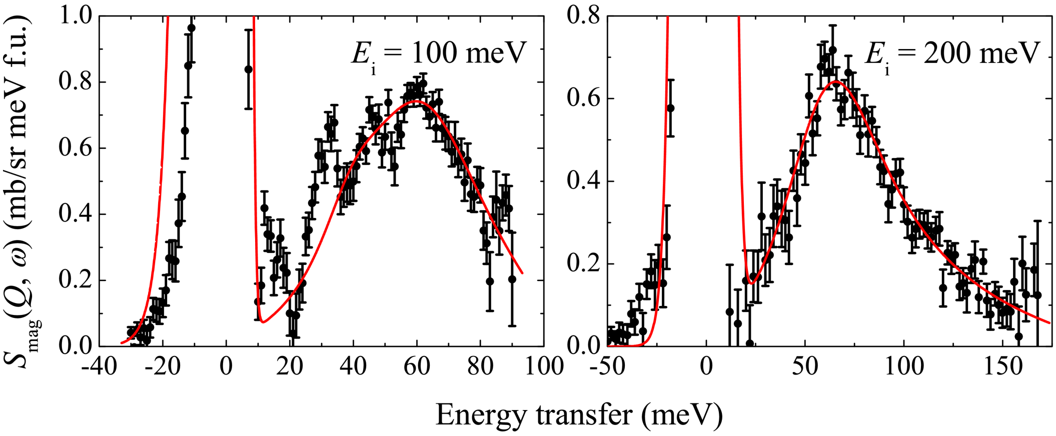

Figure 5.6: The magnetic scattering of CeRuSi$_3$ at 7 K for E_i = 100 and 200 meV, estimated using Eq. 2.74. The data has been fitted with a single Lorentzian function for E_i = 200 meV and two Lorentzian functions for E_i = 100 meV.

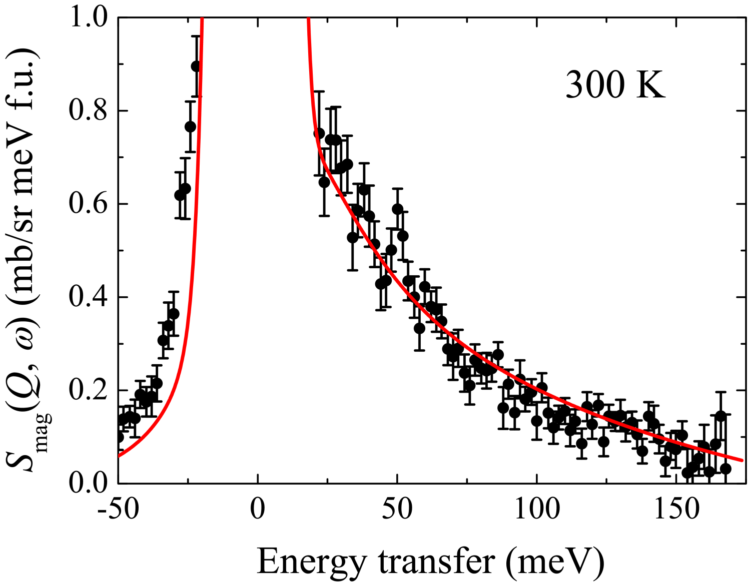

Figure 5.7: The magnetic scattering of CeRuSi$_3$ at 300 K for E_i = 200 meV, estimated using Eq. 2.74. The data has been fitted with Eq. 2.72 convoluted with the resolution of the instrument.

5.2.4 Specific heat

The specific heat of $CeRuSi_3$ and non-magnetic $LaRuSi_3$ are shown in Fig. 5.8. At low temperatures, C/T is finite in both compounds but is significantly larger in $CeRuSi_3$, indicating an enhanced value of γ. The inset shows C/T against T^2 and a linear fit to the data gives $\gamma = 62.5(1)$ mJ/mol K^2. The specific heat of $CeRuSi_3$ is consistently larger than that of $LaRuSi_3$, indicating the presence of a magnetic contribution. However, the difference in the values of C/T decreases with temperature, indicating that the enhanced value of γ does not persist at high temperatures. The temperature dependence of the specific heat of $LaRuSi_3$ is shown in Fig. 5.9. A linear fit to C/T against T^2 shown in the inset gives $\gamma = 6.5(1)$ mJ/mol K^2, suggesting an enhanced value of γ in $CeRuSi_3$ due to heavy fermion behaviour. The specific heat of $LaRuSi_3$ was fitted with a single Debye model [143] in addition to a γT contribution, with γ fixed from the fit in the inset with $\Theta_{\mathrm{D}} = 413(2)$ K being obtained. $\Theta_{\mathrm{D}} = 439$ K is calculated using Eq. 2.50 from the low temperature value of β but although the calculated specific heat agrees well with the data and high and low temperatures, there is poorer agreement at intermediate values.

It is therefore desirable to estimate the magnetic contribution to the specific heat (C_{mag}) by subtracting an estimate of the phonon contribution (C_{ph}). C_{ph} was estimated from the specific heat of $LaRuSi_3$ by two methods. Firstly, C_{ph}/T was estimated by subtracting $\gamma = 6.5(1)$ mJ/mol K^2 from C/T of $LaRuSi_3$. Secondly, it was calculated using the fitted value of Θ_{D}. Two estimates of C_{mag}/T are shown in Fig. 5.10. In principle it is necessary to correct C_{ph} for the difference in masses between $CeRuSi_3$ and $LaRuSi_3$. Following Ref. [197], this corresponds to scaling either the temperature axis or Θ_{D} by a factor of ~ 0.99, which has little effect on the results. In both plots there is a peak in C_{mag}/T at around 45 K, which is of greater intensity for the Debye subtraction. The dashed lines shows a fit to a phenomenological two level model often employed for heavy fermion compounds with a hybridization gap [198, 199], given by

$$C = R\left(\frac{\Delta E}{k_{\mathrm{B}}T}\right)^2 \frac{(2J+1)\mathrm{e}^{\Delta E/k_{\mathrm{B}}T}}{(2J+1+\mathrm{e}^{\Delta E/k_{\mathrm{B}}T})^2}, \tag{5.1}$$

where $J = \frac{5}{2}$ for a cerium ion and ΔE is the gap between the ground and excited states, with a fitted value of $\Delta E = 15.3(2)$ meV. The magnetic entropy obtained from integrating C_{mag}/T to 390 K is $\sim 1.1R\ln(6)$and $\sim 1.4R\ln(6)$ for the direct and Debye subtractions respectively. This of the same order as that expected for an atom with a six fold degenerate ground state.

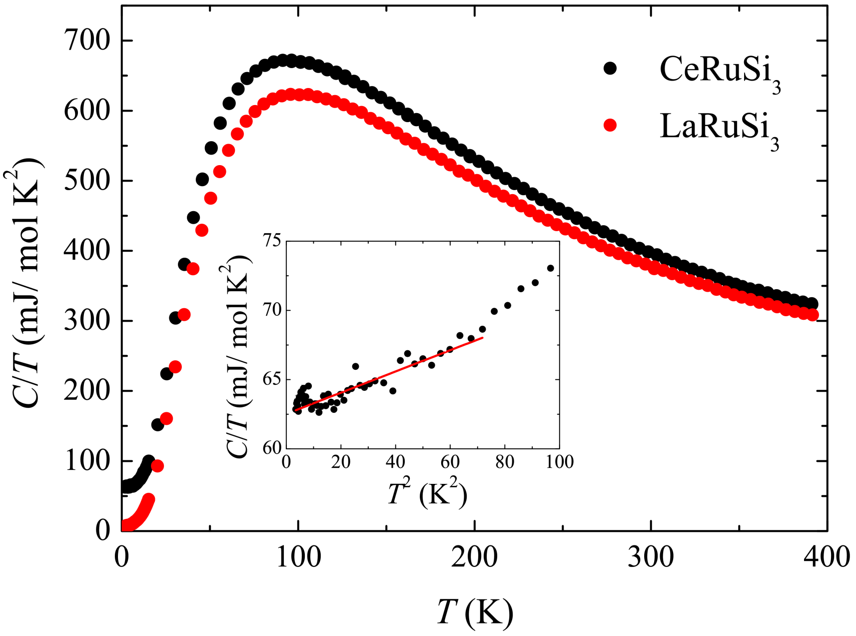

Figure 5.8: The temperature dependence of the specific heat of CeRuSi$_3$ and LaRuSi$_3$. The inset shows C/T against T^2 of CeRuSi$_3$ with a linear fit.

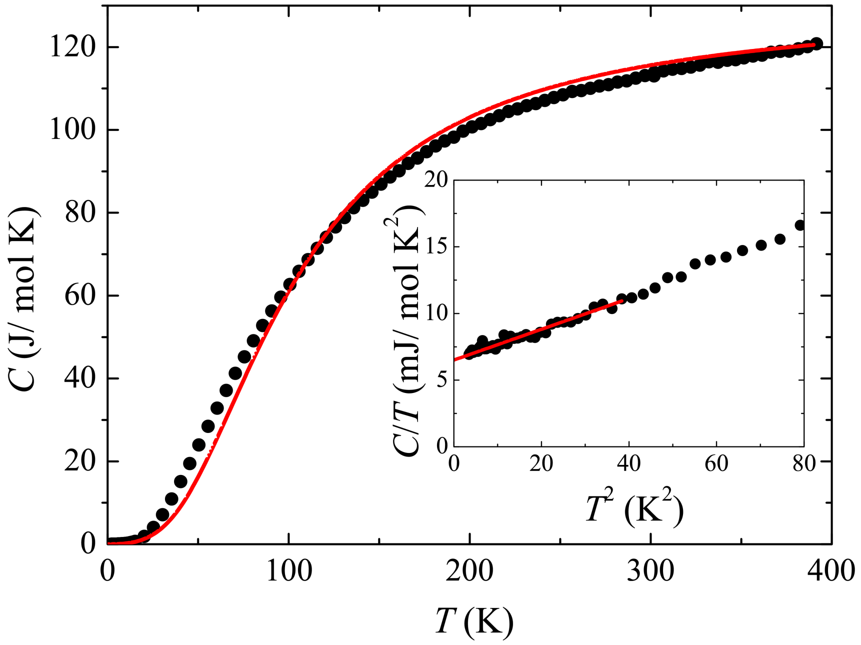

Figure 5.9: The specific heat of LaRuSi$_3$ fitted with electronic and phonon contributions, using the Debye model. C/T against T^2 of LaRuSi$_3$ with a linear fit is shown in the inset.

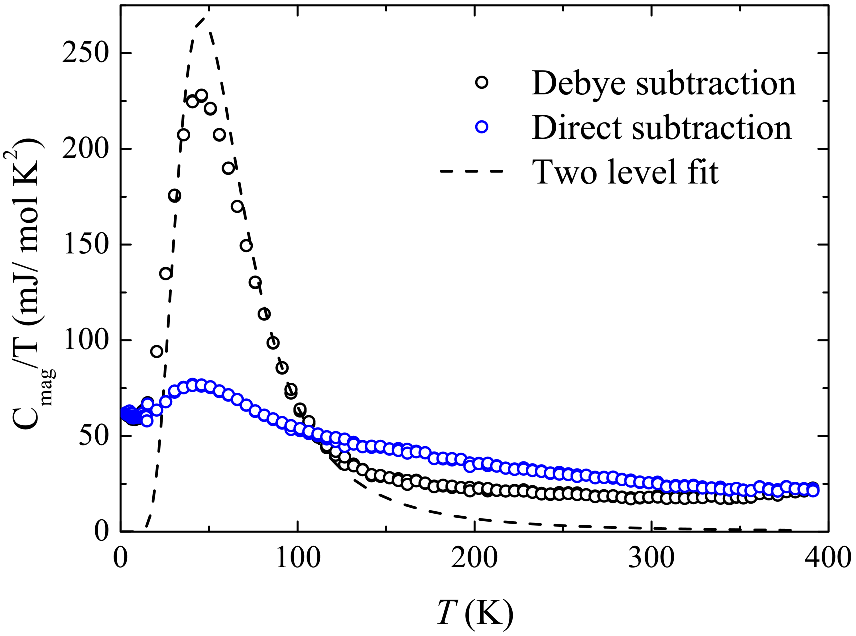

Figure 5.10: Two estimates of the magnetic contribution to the specific heat obtained from subtracting C_{ph}. The black circles show values calculated from calculating C_{ph} using the fitted Debye temperature of $LaRuSi_3$ while the blue circles were calculated from directly subtracting the $LaRuSi_3$ data. The dashed lines show a fit to a phenomenological two level model (Eq. 5.1).

5.2.5 Discussion and summary

Magnetic susceptibility, specific heat and neutron scattering measurements were performed on polycrystalline $CeRuSi_3$. The magnetic susceptibility displays a peak at around 150 K, whereas the estimate for the magnetic contribution to the specific heat peaks at a lower temperature of around 45 K. The peak in the magnetic susceptibility is in agreement with Ref. [194]. In intermediate valence compounds and those displaying a hybridization gap, the maximum of the magnetic susceptibility and C_{mag}/T often occur at similar temperatures. For example, $CeFe_4Sb_{12}$ displays a peak in the magnetic susceptibility at 140 K and the specific heat at 125 K [200], and similar agreement between the two is observed in the intermediate valence compound $CePd_3$ [201]. This may indicate the presence of more low lying excitations in $CeRuSi_3$ or alternatively the peak could be shifted to lower energies due to an incorrect phonon subtraction. It can be seen in Fig. 5.9 that the peak position corresponds to a region where the specific heat of both $CeRuSi_3$ and $LaRuSi_3$ are both rapidly rising and therefore C_{mag} will be sensitive to small mismatches in C_{ph}.

The low temperature specific heat gives a value of $\gamma = 62.5(1)$ mJ/mol K^2. This indicates an enhanced γ due to hybridization between $4f$ and conduction electrons. The value is larger than that observed in CeCoSi$_3$ of 37 mJ/mol K^2 and is similar to CeCoGe$_{0.75}$Si$_{2.25}$ [179]. This suggests that the hybridization strength is not as strong as in CeCoSi$_3$ and places CeRuSi$_3$ closer to quantum criticality.

The magnetic inelastic neutron response at 7 K peaks at finite energy transfers which shifts to a broad quasielastic response at 300 K. With $E_{\rm i} = 200$ meV the magnetic scattering is well described by a single Lorentzian peak centred at (58.5 ± 1.4) meV, whereas the response at $E_{\rm i} = 100$ meV reveals additional magnetic scattering at lower energies. The data were fitted with two Lorentzian peaks at 60(5) and 39(3) meV. Peaks in the magnetic response at finite energy transfers for heavy fermion compounds have often been interpreted as originating from energy gaps which open in the hybridized heavy bands of the Kondo lattice [196]. However, a peak in the magnetic inelastic neutron scattering can also arise in the Anderson impurity model (Eq. 2.21) [201, 202], where coherence effects are not taken into account. Below about 20 meV, the magnetic scattering is greatly reduced, if not entirely absent at low temperatures. Two particular features of the low temperature magnetic scattering are of particular interest. In Ref. [196], it was shown that for a wide range of heavy fermion compounds with a hybridization gap, the inelastic peak position corresponds to three times the temperature at which the magnetic susceptibility reaches a maximum. Exceptions to this rule are URu$_2$Sn$_2$, CePd$_3$ and CeNi where the peak position is anomalously high and YbAl$_2$, where it is anomalously low. Secondly, two peaks in the magnetic scattering are not commonly observed, with CeOs$_4$Sb$_{12}$ [203] being another example. The magnetic scattering of CeRuSi$_3$ also shows at least two peaks, with one corresponding to ~ 450 K in agreement with the aforementioned relation. The dominant peak at around 60 meV corresponds to ~ 700 K, which is significantly larger. The peak at lower energies of CeOs$_4$Sb$_{12}$ also agrees with the relation. However, in this compound the lower peak is of greater intensity whereas the higher energy peak is stronger in CeRuSi$_3$.

An additional narrower peak in the magnetic scattering is also observed at around 32 meV. While this may arise from an incorrectly subtracted phonon peak or an impurity CEF level, it may also be a a weaker localized magnetic excitation that is coexistent with a stronger broader peak. Such behaviour has been observed in YbAl$_3$, where there is a broad peak at 44 meV and a narrow one at 34 meV [204]. The substitution of Lu for Yb weakens the periodicity of the Kondo lattice which suppresses the localized excitation but not the broader one, indicating the former arises due to the coherence of the Kondo lattice. Subsequently, the $|\mathbf{Q}|$ dependence of the magnetic scattering of $YbAl_3$ has been examined using single crystals [205]. It would therefore be desirable to perform inelastic neutron scattering measurements on single crystals of $CeRuSi_3$, both to clarify whether there is additional structure in the magnetic scattering and whether there is a $|\mathbf{Q}|$ dependence arising from coherence effects. Since the low temperature magnetic scattering is often interpreted as corresponding to transitions between heavy, hybridized bands, these measurements may give information about their structure and anisotropy.

5.3 $CePdSi_3$

5.3.1 Sample preparation and structural characterization

Polycrystalline samples of $CePdSi_3$ were produced by arc-melting stoichiometric quantities of the constituent elements in an argon atmosphere on a water cooled copper hearth. The samples were flipped and remelted several times. The $CePdSi_3$ sample measured in this section was annealed for 18 days at at 950°C under a dynamic vacuum, better than 10^{-6} Torr. Powder x-ray diffraction measurements were carried out using a Bruker D5005 diffractometer. Rietveld refinements were carried out using the TOPAS software [151] and the fitted patterns are shown in Fig. 5.11. Several unfitted peaks are observed due to the presence of impurity phases. The largest unfitted peak is at around 34.2°, which is around $\sim 6\%$ of the largest sample peak. However, the relative magnitude is difficult to estimate due to the proximity of the two peaks. The results of the Rietveld refinement are shown in Table 5.2. The lattice parameters are similar to those reported in Ref. [65].

5.3.2 High energy inelastic neutron scattering

Inelastic neutron scattering measurements on polycrystalline $CePdSi_3$ and $LaPdSi_3$ were performed on the MERLIN spectrometer at ISIS. The samples were wrapped in Al foil and cooled to 5 K in a closed cycle refrigerator. Measurements were made down to 5 K with $E_{\mathrm{i}} = 15$ and 60 meV, selected via a Fermi chopper. Colour plots of the inelastic neutron scattering intensity are shown for $E_{\mathrm{i}} = 15$ meV in Fig. 5.12. A strong excitation is observed in the plot for $CePdSi_3$ (Fig. 5.12(a)) which is not observed for $LaPdSi_3$ (Fig. 5.12(b)). This is most intense at low $\mathbf{Q}$, indicating the excitation is magnetic in origin and is a CEF excitation centred at around 5 meV. The lack of any significant intensity in the $LaPdSi_3$ plot for the full range of momentum transfers suggests that phonon scattering is much weaker than the magnetic scattering from the CEF at these energies.

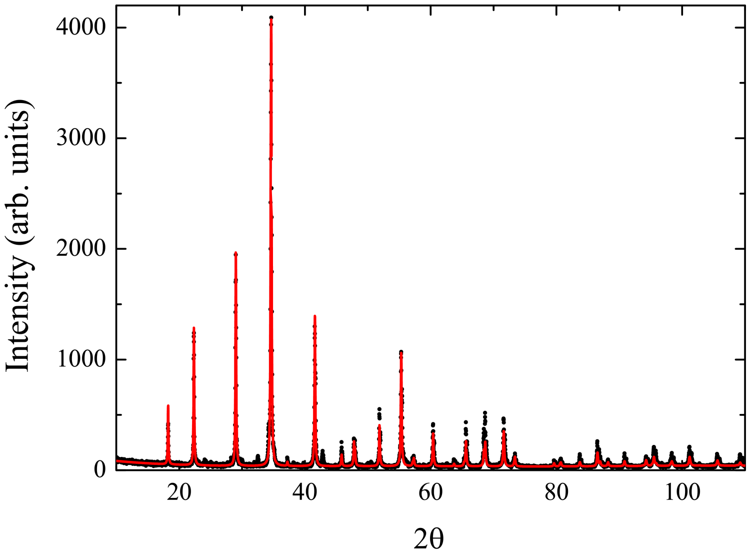

Figure 5.11: Powder x-ray diffraction measurements of $CePdSi_3$ measured using a Panalytical X-Pert Pro diffractometer. The solid lines show the Rietveld refinements performed using TOPAS. The results are given in Table 5.2.

Table 5.2: Results of the refinements of powder x-ray diffraction measurements on $CePdSi_3$. The lattice parameters, weighted profile factor (R_{wp}) and the atomic positions are shown.

	$CePdSi_3$			
a (Å)	4.3206(4)			
c (Å)	9.6089(5)			
R_{wp}(%)	25.0			
	Site	x	y	z
Ce	2a	0	0	0
Pd	2a	0	0	0.6448(6)
Si1	2a	0	0	0.371(2)
Si2	4b	0	0.5	0.775(1)

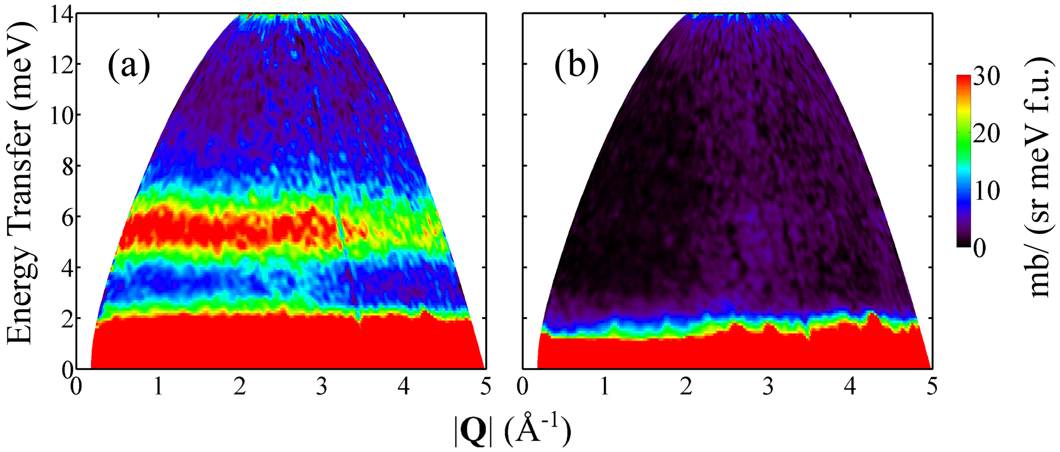

Figure 5.12: Colour plots of the INS intensity measured on MERLIN with E_i = 15 meV for (a) CePdSi$_3$ at 5.4 K and (b) LaPdSi$_3$ at 5 K.

Colour plots for E_i = 60 meV are shown for CePdSi$_3$ at 5 and 75 K in Fig. 5.13 (a) and (c) and for LaPdSi$_3$ at 5.4 and 75 K in Fig. 5.13 (b) and (d) respectively. Unlike the measurements with E_i = 15 meV, the intensity scale has not been normalized to absolute units. In the CePdSi$_3$ plots there is a narrow strip of scattering at low **Q** which is absent in the LaPdSi$_3$ measurements. This is shown more closely in Fig. 5.14, where the scattering is shown for energy transfers between 20 and 40 meV. This indicates the presence of a second CEF excitation with a significantly weaker intensity at around 31 meV. Also in the plots displayed in Fig. 5.13, a region of scattering is observed at around 20 meV, centred at momentum transfers of $\sim$ 3 Å. The intensity of this scattering increases between 5.4 and 75 K. It should be noted that scattering is also observed in this region for LaPdSi$_3$. However, the scattering is weaker below 4 Å and does not appear to peak at an intermediate **Q**.

Cuts of the intensity were made by integrating across low and high values of $|\mathbf{Q}|$. These are shown at two temperatures in Fig. 5.15. The low $|\mathbf{Q}|$ cuts were integrated from 0-4 Å^{-1}, while the high $|\mathbf{Q}|$ cuts were integrated from 4-7 Å^{-1}. The low $|\mathbf{Q}|$ scattering of CePdSi$_3$ shows a strong peak at around 5.5 meV, which is absent in the other plots, indicating the presence of a CEF excitation. At around 31 meV, where a weak CEF excitation was identified from Fig. 5.14, there is a small bump in the low $|\mathbf{Q}|$ scattering of CePdSi$_3$ which is absent in the other plots. The intensity of the peak is weaker at 75 K than 5.4 K. It should be noted there is also a phonon peak at slightly lower energies, which can be identified in all four plots. The high and low $|\mathbf{Q}|$ scattering of LaPdSi$_3$ shows a peak at around 14 meV,

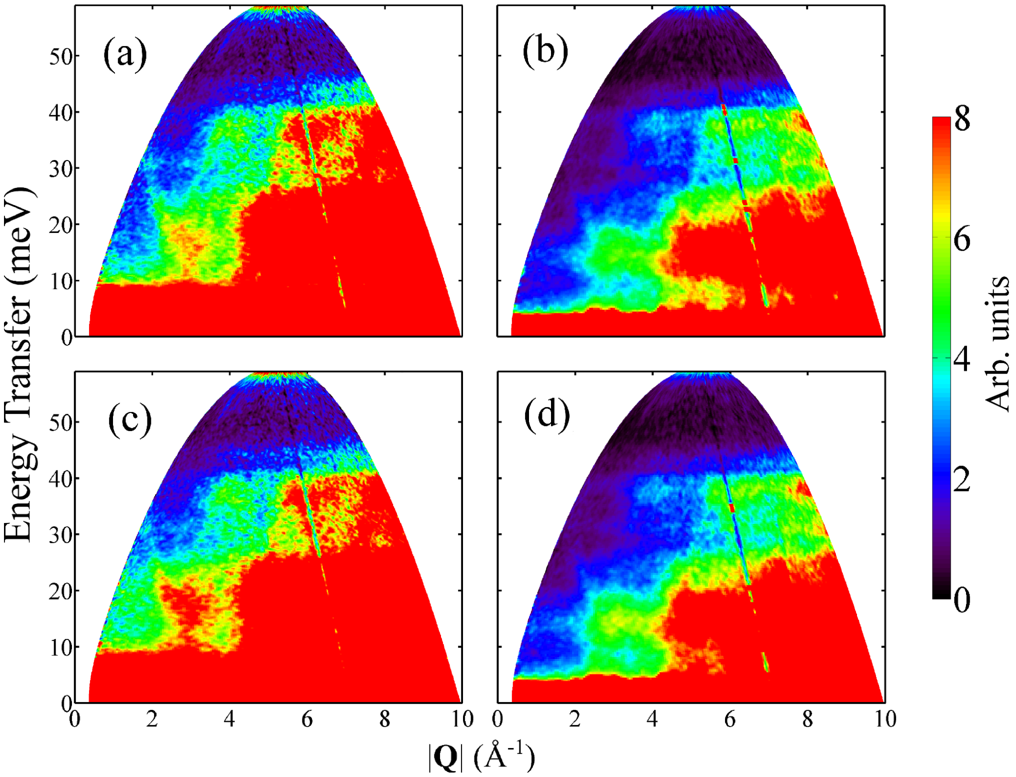

Figure 5.13: Colour plots of the INS intensity measured on MERLIN with E_i = 60 meV for (a) $CePdSi_3$ at 5 K, (b) $LaPdSi_3$ at 5.4 K, (c) $CePdSi_3$ at 75 K and (d) $LaPdSi_3$ at 75 K.

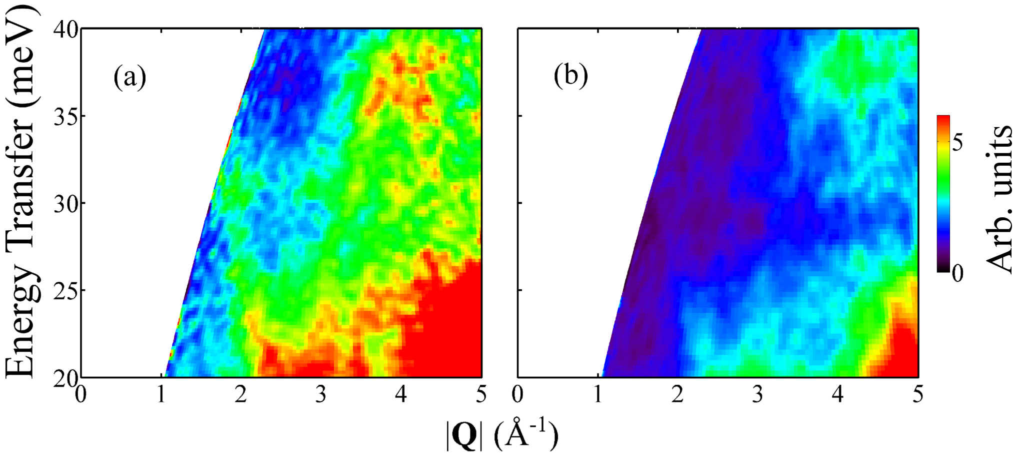

Figure 5.14: Colour plots of the INS intensity measured on MERLIN for energy transfers between 20 and 40 meV with E_i = 60 meV for (a) $CePdSi_3$ at 5 K and (b) $LaPdSi_3$ at 5.4 K.

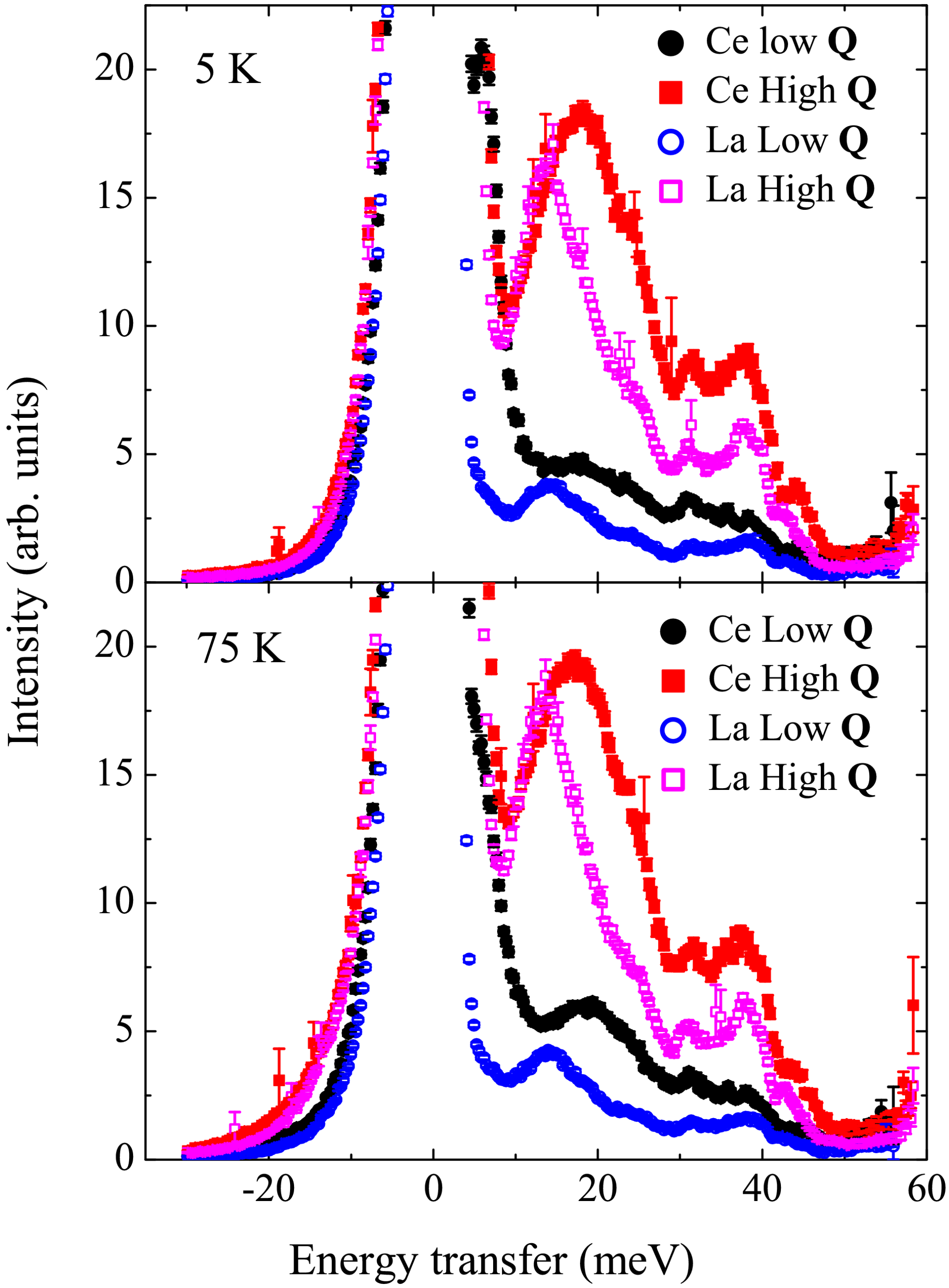

Figure 5.15: Cuts of the INS intensity with $E_{\mathrm{i}} = 60$ meV of $\mathrm{CePdSi_3}$ at 5 K and $\mathrm{LaPdSi_3}$ at 5.4 K (top) and at 75 K (bottom), from integrating across $|\mathbf{Q}|$. The integration was from 0-4 Å^{-1} for low $|\mathbf{Q}|$ and from 6-10 Å^{-1} for high $|\mathbf{Q}|$.

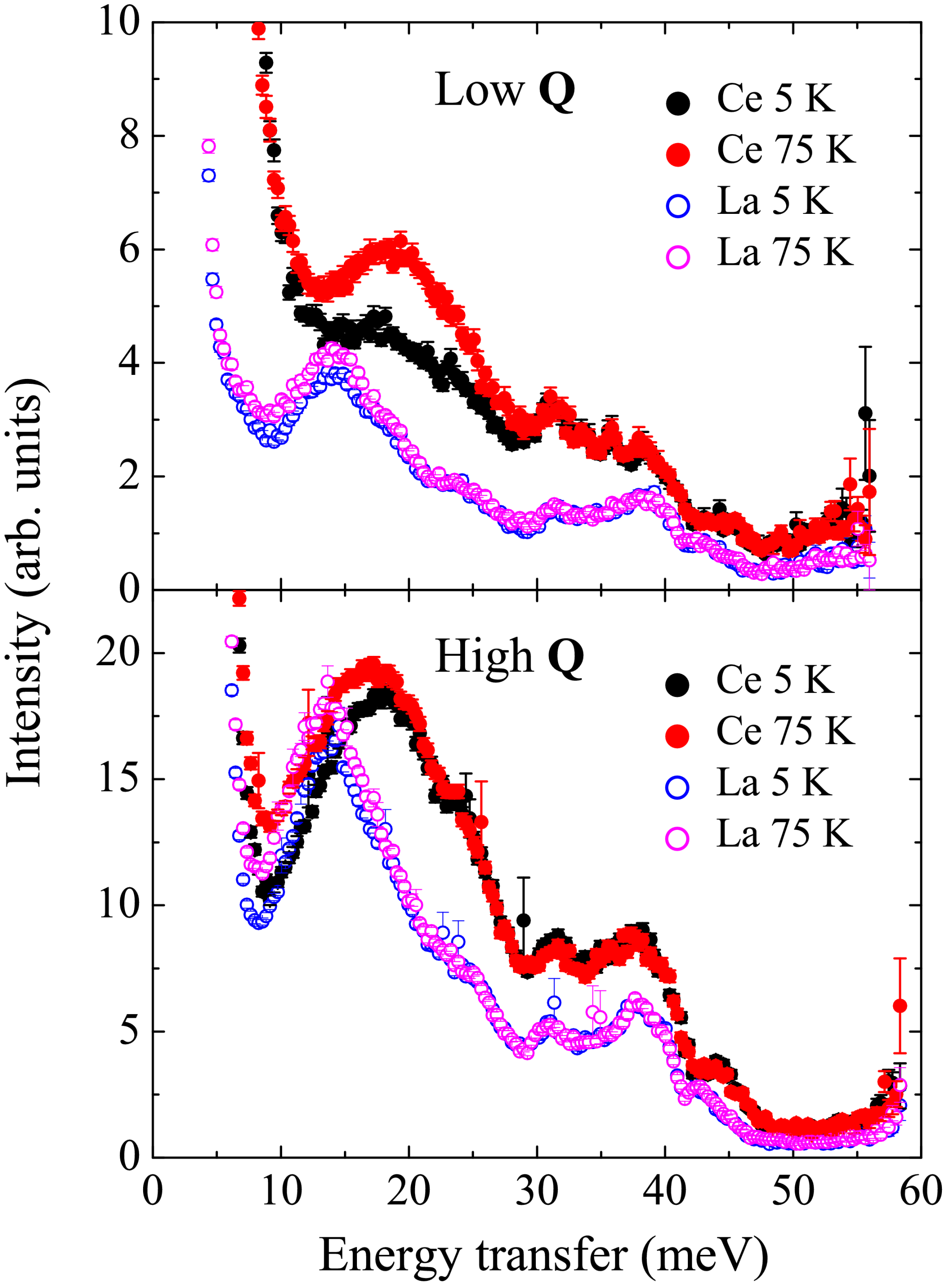

Figure 5.16: Cuts of the INS intensity with $E_{\mathrm{i}} = 60$ meV of $CePdSi_3$ at 5 K and $LaPdSi_3$ at 5.4 K, and at 75 K, from integrating across $|\mathbf{Q}|$. The integration was from 0-4 Å^{-1} for low $|\mathbf{Q}|$ (top) and from 6-10 Å^{-1} for high $|\mathbf{Q}|$ (bottom).

resulting from phonon scattering. The corresponding peak in $CePdSi_3$ is shifted to higher energies and is considerably broader. The scattering in this region of $LaPdSi_3$ appears to change little between 5 and 75 K and similarly there is little change in the high $|\mathbf{Q}|$ scattering of $CePdSi_3$. However, the low $|\mathbf{Q}|$ scattering of $CePdSi_3$ displays a broad shoulder at 5 K but at 75 K this sharpens and increases in intensity. The anomalous temperature dependence of this excitation is displayed more clearly in Fig. 5.16, where there is little change in the intensity between 5 and 75 K, apart from in the low $|\mathbf{Q}|$ scattering of $CePdSi_3$ in a region from around 13 to 24 meV.

The magnetic scattering of $CePdSi_3$ was estimated using Eq. 2.74. The estimates at four temperatures for $E_{\rm i} = 60$ meV are shown in Fig. 5.17. At 5 K, two peaks are observed at around 6 and 31 meV corresponding to the CEF excitations. At this temperature, no magnetic scattering is observed at intermediate energies corresponding to additional excitation. However, at 75, 150 and 250 K additional magnetic scattering is observed, centred at around 21 meV. This reflects the strong increase in the low $|\mathbf{Q}|$ scattering of $CePdSi_3$ at these temperatures as discussed previously. It might be expected that at 75 K an additional excitation would be observed for the transition between the first and second excited doublets, since the thermal energy would be approximately equal to the energy of the first excited state. Since the intensity between the ground state and the second excited state is weak, it is likely that the ground state doublet either consists of the $|\pm\frac{1}{2}>$ states or predominantly the $|\pm\frac{5}{2}>$ states. In this case, the first excited doublet would mainly consist of the $|\pm\frac{3}{2}>$ states and the intensity of the excited transition would be strong. However, at energy transfers of around 27 meV, the difference between the first and second excited doublets, there is no evidence for such a transition. The same is true for the scattering at 150 and 250 K. These results suggest that this excitation is neither purely phonon scattering nor does it correspond to an excited CEF transition.

5.3.3 Low energy inelastic neutron scattering of $CePdSi_3$ and $CePtSi_3$

In the previous section, inelastic neutron scattering measurements of $CePdSi_3$ on the MERLIN spectrometer were reported. While the existence of quasielastic scattering could be inferred from these measurements, a greater resolution and smaller elastic width are required to resolve its magnitude. In this section, low energy inelastic neutron scattering measurements are reported on $CePdSi_3$ and isostructural $CePtSi_3$. Both compounds order magnetically at low temperatures and the scattering above and below and $T_{\rm N}$ are compared.

Low energy measurements of $CePdSi_3$ were performed on the IRIS instrument

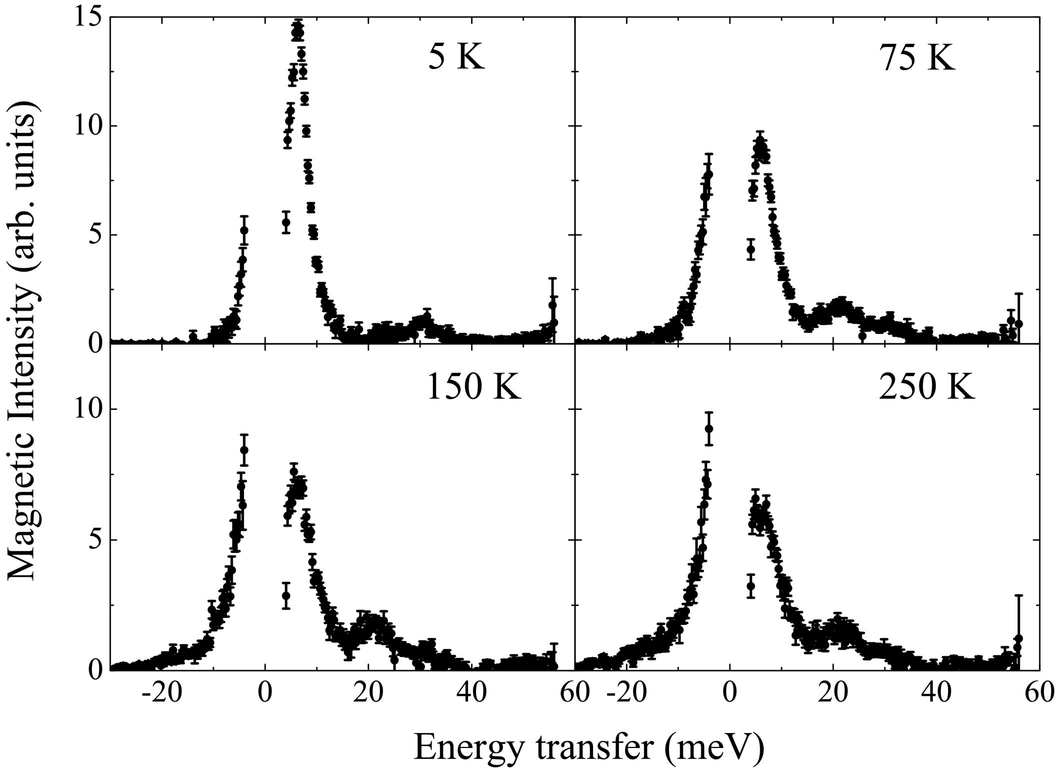

Figure 5.17: Estimates of the magnetic scattering of CePdSi$_3$ at several temperatures, obtained using Eq. 2.74.

at ISIS [206]. Unlike the other inelastic neutron scattering instruments described in this work, IRIS is configured in the indirect geometry. Rather than the incident neutron energy being fixed, a white neutron beam is incident on the sample and the scattered neutrons pass through a graphite analyzer, so that neutrons of a single energy are detected. In these measurements, the (002) reflection of a pyrolytic graphite analyzer was used. With a chopper frequency of 25 Hz selected, energy transfers from 0.6 to 3.5 meV could be measured with a full width at half maximum of the elastic line of 17.5 μeV. Polycrystalline samples of CePdSi$_3$ were wrapped in Al foil and cooled in an Orange cryostat to 1.5 K.

The scattering as a function of energy transfer is shown for several temperatures down to 1.5 K in Fig. 5.18. At 1.5 K, there is a peak in the scattering at inelastic positions, while at 7 K broad quasielastic scattering is observed which is considerably wider than the elastic resolution of the instrument. The width of the quasielastic scattering broadens with temperature and at 120 K and 200 K, the scattering is nearly flat as a function of energy transfer. Measurements performed

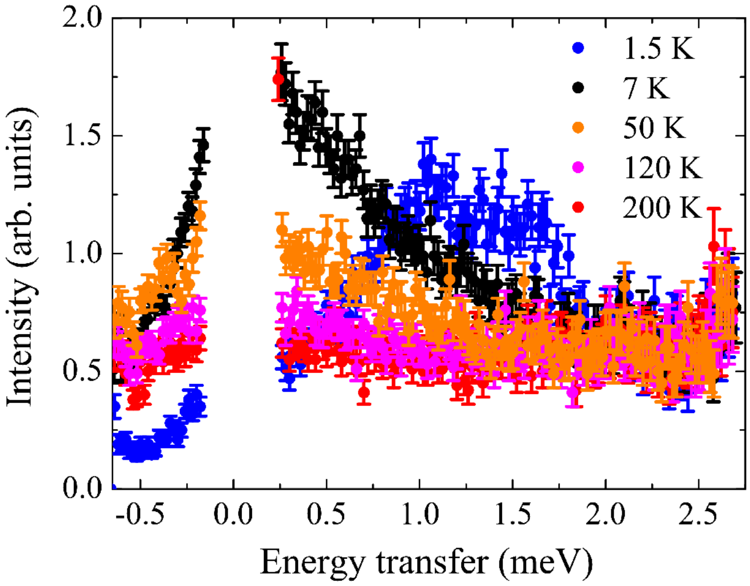

Figure 5.18: Inelastic neutron scattering measurements of $CePdSi_3$ at several temperatures measured on the IRIS spectrometer.

on the MERLIN spectrometer with E_i = 15 meV (not shown), show that at high temperatures the quasielastic scattering merges with the first CEF excitation at around 5.5 meV. The quasielastic scattering was fitted using Eq. 2.72, with a small constant background fixed at all temperatures. Some of the fitted curves are displayed in Fig. 5.19. Measurements performed at 120, 200 and 250 K could not be adequately fitted, since the quasielastic width is too large for the energy window of the instrument. Upon entering the magnetically ordered state, a peak is observed in the scattering as a result of spin wave excitations. Inspection of the scattering suggests that a two peak structure may be present. The data were fitted to a single and pair of Lorentzian functions. The single function is centred at 1.21(1) meV while the pair of peaks are centred at 1.00(2) and 1.53(3) meV. While a reasonable fit is obtained with a single peak, the peak centre appears to be shifted across from the position of maximum scattering. This suggests that two peaks are required to account for the low temperature scattering. The temperature dependence of Γ is shown in Fig. 5.20. A linear fit to the data is displayed and $\Gamma(0) = 0.52(2)$ meV was obtained, giving $T_K = 6.0(2)$ K. This is of a similar order to the ordering temperature $T_{N1} = 5.2$ K.

Low energy measurements of $CePtSi_3$ and $LaPtSi_3$ were performed on the IN6 spectrometer at the ILL. Powdered polycrystalline material was placed in a 1 mm thick, disc shaped sample holder and cooled to 1.5 K in an Orange cryostat.

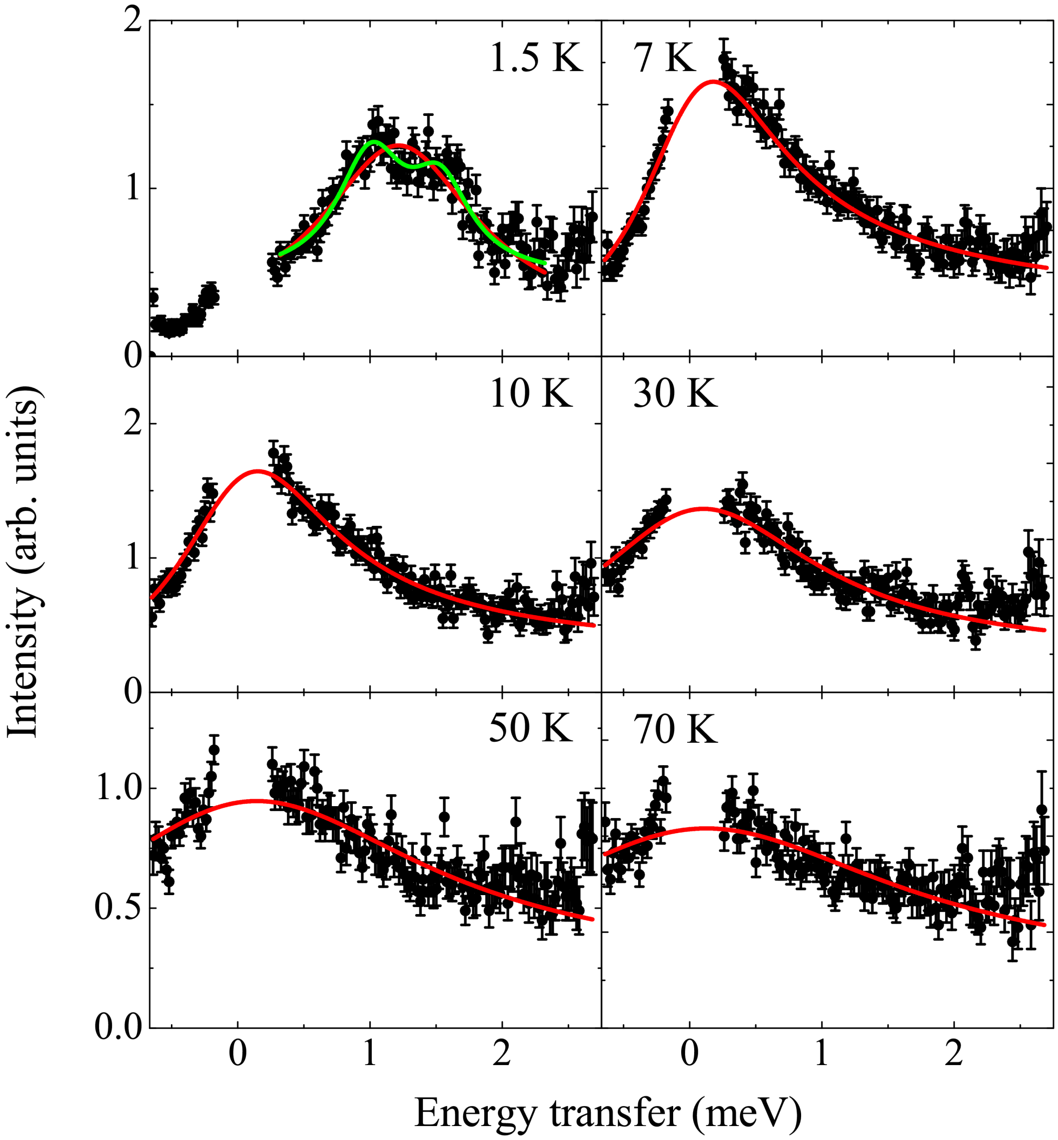

Figure 5.19: Inelastic neutron scattering of $CePdSi_3$ measured on the IRIS spectrometer. The solid lines show fits to a Lorentzian quasielastic component with the exception of the data measured at 1.5 K, where fits with one and two Lorentzian peaks centred on inelastic positions are shown.

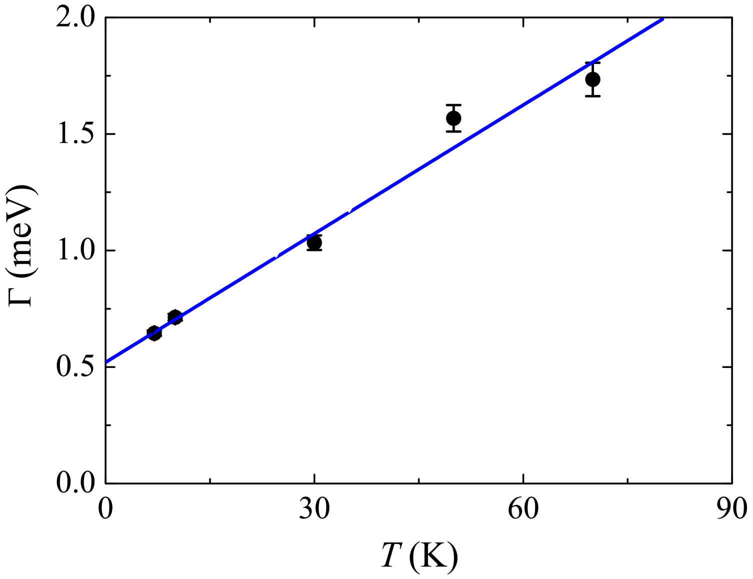

Figure 5.20: The temperature dependence of the quasielastic linewidth (half width at half maximum) of $CePdSi_3$ measured on the IRIS spectrometer. A linear fit has been made to the data.

An incident energy of 3.1 meV was selected using a pyrolytic graphite monochromator. Cuts of the scattering were made integrating from 0.5 to 1.9 Å and these are displayed for $CePtSi_3$ at several temperatures and $LaPtSi_3$ at 1.5 K in Fig. 5.21. At 1.5 K, below T_{N2} , there is maximum in the scattering at inelastic positions while above T_{N1} , the scattering centred on the elastic line is clearly broader than that of $LaPtSi_3$. This indicates the presence of quasielastic scattering above the ordering temperature. At 4 K, between T_{N1} and T_{N2}, a broadened elastic line is observed but there is still a shoulder close to the position of the inelastic peak observed at 1.5 K. This suggests the presence of both quasielastic scattering and a peak associated with the spin wave excitation.

The magnetic scattering was estimated by directly subtracting the scattering of $LaPtSi_3$ and is displayed for six temperatures in Fig. 5.22. As with $CePdSi_3$, either one or two Lorentzian functions were fitted to the scattering at 1.5 K. A peak centre of 1.14(1) meV was obtained for a single Lorentzian while 0.92(4) and 1.55(7) meV were obtained for a pair of peaks. The measurements above T_{N1} were fitted using Eq. 2.72. The temperature dependence of Γ is shown in Fig. 5.23. A linear fit was made to the data giving $\Gamma(0) = 0.479(4)$ meV and therefore $T_{\mathrm{K}} = 5.56(5)$ K. This is both very similar to T_{N1} and T_{K} of $CePdSi_3$.

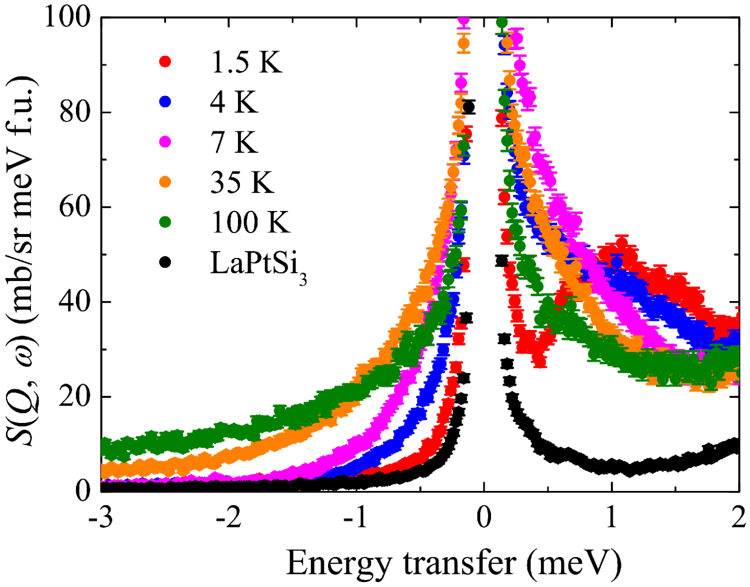

Figure 5.21: Cuts of $S(\mathbf{Q}, \omega)$ of CePtSi$_3$ and LaPtSi$_3$ with E_i = 3.1 meV, measured on the IN6 spectrometer.

5.3.4 Discussion and summary

Inelastic scattering measurements have been performed on CePdSi$_3$ and CePtSi$_3$. High energy measurements of CePdSi$_3$ and LaPdSi$_3$ measured on the MERLIN spectrometer with E_i = 15 and 60 meV reveal the presence of two CEF excitations at around 5.5 and 31 meV. The intensity of the lower excitation is very strong while the excitation to the second excited doublet is particularly weak. A possible explanation for a small transitition amplitude is that the transitions between the two states are largely forbidden. If the ground state consists of the $|\pm\frac{1}{2}>$ states and the excited doublet the $|\pm\frac{5}{2}>$ states or vice versa, then there would be $\Delta m_J = \pm 2$ between the levels and no scattering intensity would be observed. Therefore a small amplitude indicates that the pair of doublets mostly consist of these levels with a small mixing of the $|\pm\frac{5}{2}>$ and $|\mp\frac{3}{2}>$ states. However, this would suggest that the first excited doublet would predominantly consist of $|\pm\frac{3}{2}>$ states and therefore at 75 K a strong excited CEF transition would be expected to be observed. No such excited state is observed and instead at 75 K the low $|\mathbf{Q}|$ scattering strongly increases in a broad region from around 13 to 24 meV while the high $|\mathbf{Q}|$ behaviour is largely identical. This is not expected for either phonon scattering or that from a CEF. In the isostructural compound CeCuAl$_3$, three magnetic excitations were observed at 4.7 K [207]. Two of these were ascribed to CEF excitations while it was

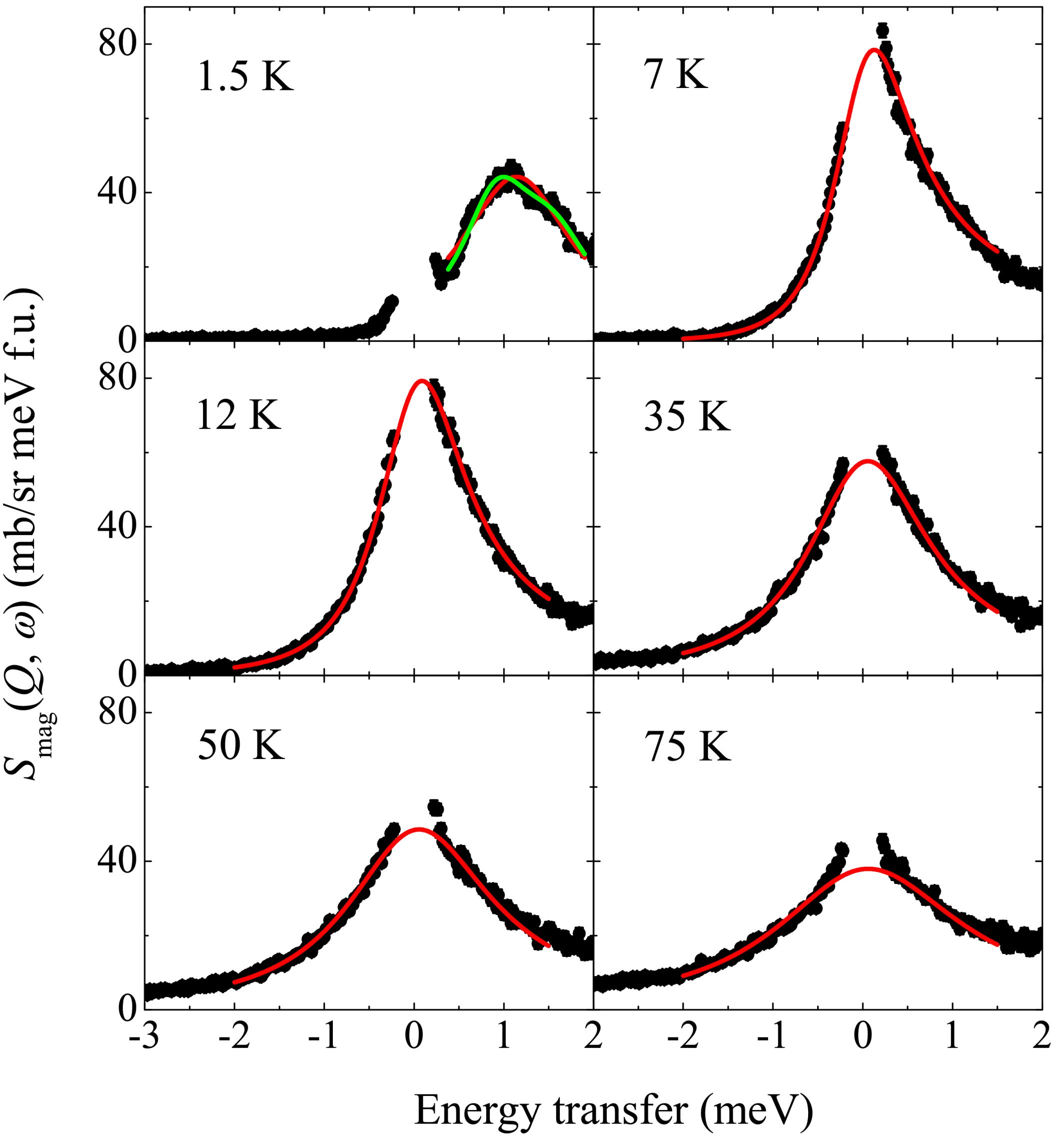

Figure 5.22: Cuts of the magnetic scattering of CePtSi_3 with $E_\text{i} = 3.1$ meV measured on the IN6 spectrometer, with a direct subtraction of the scattering of LaPtSi_3. The solid lines show fits to a Lorentzian quasielastic component with the exception of the data measured at 1.5 K, where one and two Lorentzian functions have been fitted.

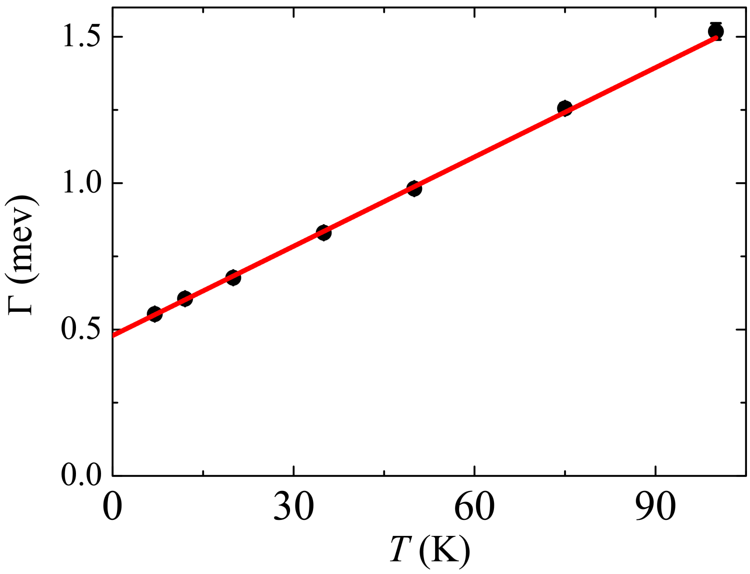

Figure 5.23: The temperature dependence of the quasielastic linewidth (half width at half maximum) of $CePtSi_3$ measured on the IN6 spectrometer. A linear fit has been made to the data.

proposed that the third excitation arises from coupling between phonons and a CEF level. In this instance the magnetic scattering could be fitted using a Hamiltonian which is the sum of Eq. 2.5, a phonon term and a term which couples phonons to the CEF levels. It would be of interest to determine if the measurements of $CePdSi_3$ can be accounted for with such a model although unlike $CeCuAl_3$, the additional scattering is not observed at low temperatures but in $CeCuAl_3$ it is. Since the anomalous excitation is diffuse and appears to have an unusual $|\mathbf{Q}|$ dependence, measurements of single crystals may be useful in determining its nature.

Low energy inelastic neutron scattering measurements were performed on $CePdSi_3$ and $CePtSi_3$ using the IRIS and IN6 spectrometers respectively. Both measurements below the ordering temperature reveal a peak corresponding to spin wave excitations and quasielastic scattering in the paramagnetic state. Interestingly a double peak structure may be present in the spin wave excitations of both compounds which may result from anisotropic magnetic exchanges. Above T_{N1} a linear temperature dependence of Γ is observed up to at least 100 K in $CePtSi_3$ and 70 K in $CePdSi_3$. This despite the first CEF excitation being at around 53 K in the former [64] and 64 K in the latter. This is different to the behaviour observed in $CeCoGe_3$ and $CeRhGe_3$, as discussed in Sec. 4.5.1. Kondo temperatures of $T_{\mathrm{K}} = 6.0(2)$ and 5.56(5) K were obtained for $CePtSi_3$ and $CePdSi_3$ respectively.

This is very similar to the ordering temperature for both compounds and indicates that the coupling between conduction and f electrons is weaker than in $\mathrm{CeRhSi_3}$, $\mathrm{CeIrSi_3}$, $\mathrm{CeCoGe_3}$ and $\mathrm{CeRhGe_3}$. This suggests that neither $\mathrm{CePtSi_3}$ nor $\mathrm{CePdSi_3}$ are good candidates for becoming superconducting at readily accessible pressures and in the case of $\mathrm{CePtSi_3}$, this is supported by the fact that T_{N} is almost pressure independent up to at least 8 GPa [66]. This further supports the observation that the transition metal group gives a greater indication of the hybridization strength of the $\mathrm{Ce}TX_3$ compounds than the period.

Chapter 6

LaTSi$_3$

6.1 Introduction

In the preceding two sections, ground state properties of several compounds in the CeTX_3 series of compounds at ambient pressures are reported. As discussed in Sec. 1.1.1, there are significant experimental and theoretical difficulties in understanding the superconducting states of heavy fermion non-centrosymmetric superconductors. Therefore there has been considerable research efforts towards characterizing weakly correlated, non-centrosymmetric superconductors, where the effects of inversion symmetry breaking may be more readily discerned. This is the subject of the next two chapters.

In this chapter, the superconducting properties of non-centrosymmetric LaPdSi$_3$ and LaPtSi$_3$ are reported. Both compounds crystallize in the BaNiSn$_3$ type structure, isostructural to the non-centrosymmetric CeTX_3 compounds. LaPdSi$_3$ was previously reported to be a superconductor with $T_{\mathrm{c}} = 2.6$ K [65]. Apart from reporting a jump in the specific heat at the transition of $\Delta C/\gamma T_{\mathrm{c}} = 1.16$, the remaining superconducting properties have not been clarified. LaPtSi$_3$ has previously been measured as a non-magnetic analogue, where it was reported to be non-superconducting down to 2 K [208]. In this chapter, it is reported that LaPtSi$_3$ is a superconductor with $T_{\mathrm{c}} = 1.52(6)$ K. Magnetization, specific heat, resistivity and μSR measurements are reported for the superconducting states for both compounds.

6.2 $LaPdSi_3$

6.2.1 Sample preparation and structural characterization

Polycrystalline samples of $LaPdSi_3$ were produced by arc-melting stoichiometric quantities of the constituent elements in an argon atmosphere on a water cooled copper hearth. The samples were flipped and remelted several times before being wrapped in tantalum foil, sealed in an evacuated quartz tube and annealed at 900°C for two weeks. Powder x-ray diffraction measurements were performed at room temperature using a Panalytical X-Pert Pro diffractometer and are shown in Fig. 6.1. A Rietveld refinement was carried out using TOPAS and the results are displayed in Table. 6.1.

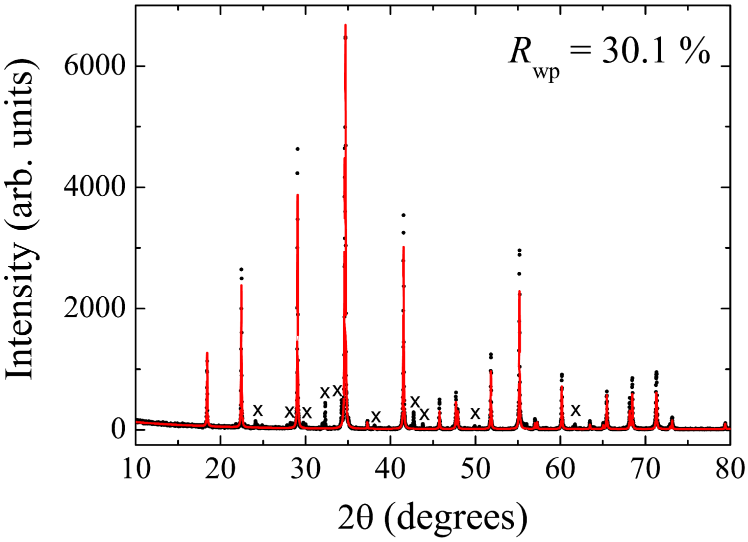

Figure 6.1: Powder x-ray diffraction measurements of $LaPdSi_3$ measured using a Panalytical X-Pert Pro diffractometer. The solid lines show the Rietveld refinements performed using TOPAS and the crosses indicate impurity peaks. The results are displayed in Table 6.1.

The values of the lattice parameters are in good agreement with those given in Ref. [65]. Several peaks corresponding to impurity phases are indicated by the crosses in Fig. 6.1. The first and third most intense peaks corresponding to a secondary phase in $LaPdSi_3$ are consistent with an impurity phase of $LaSi_2$, with the orthorhombic α-$GdSi_2$ structure and a weight fraction smaller than 5%.

Table 6.1: Results of the refinements of powder x-ray diffraction measurements on $LaPdSi_3$. The lattice parameters, weighted profile factor (R_{wp}) and the atomic positions are shown.

	$LaPdSi_3$			
a (Å)	4.3542(4)			
c (Å)	9.6642(12)			
R_{wp}(%)	30.1			
	Site	x	y	z
La	2a	0	0	0
Pd	2a	0	0	0.6437(11)
Si1	2a	0	0	0.374(4)
Si2	4b	0	0.5	0.778(3)

6.2.2 Magnetization and resistivity measurements

The magnetic susceptibility of $LaPdSi_3$ as a function of temperature in an applied field of 10 Oe is shown in Fig. 6.2(a). A sharp superconducting transition is observed at 2.6 K. An estimate of the demagnetization factor was made by approximating the sample as a rectangular prism using Ref. [123]. The zero-field cooled (ZFC) curve reaches $4\pi\chi = -1.03$ at 1.8 K, where χ is in cgs units. This indicates complete flux expulsion and bulk superconductivity in the sample. A magnetization loop measured at 2 K is shown in Fig. 6.2(b). The sample was ZFC, before the magnetization as a function of applied field was measured from 0 to 100 Oe, 100 to -100 Oe and -100 to 100 Oe as indicated by the arrows. A calculation of χ using the low field value of $\frac{dM}{dH}$ of the virgin curve gives $4\pi\chi \sim -1$, again indicating bulk superconductivity. At an applied field of 80 Oe, there is an abrupt change in the gradient of the magnetization and a loss of diamagnetism which suggests that superconductivity has been suppressed. Upon reducing the field from 100 to below 80 Oe, the magnetization is reversible down to about 70 Oe. There is a partial recovery of diamagnetism as magnetic flux is expelled from the sample. This is different behaviour to the magnetization curves typically observed in type-II superconductors [11] but has been observed in type-I materials. In an ideal type-I superconductor, a jump in the magnetization is expected at H_c (Fig. 2.4) but this is not observed due to demagnetization effects.

The temperature dependence of the resistivity between 0.4 and 3 K in fields up to 400 Oe are shown in Fig. 6.3. In the normal state, the resistivity reaches a constant value at low temperatures of $\rho_0 \sim 3.9$ $\mu\Omega$-cm. A sharp superconducting

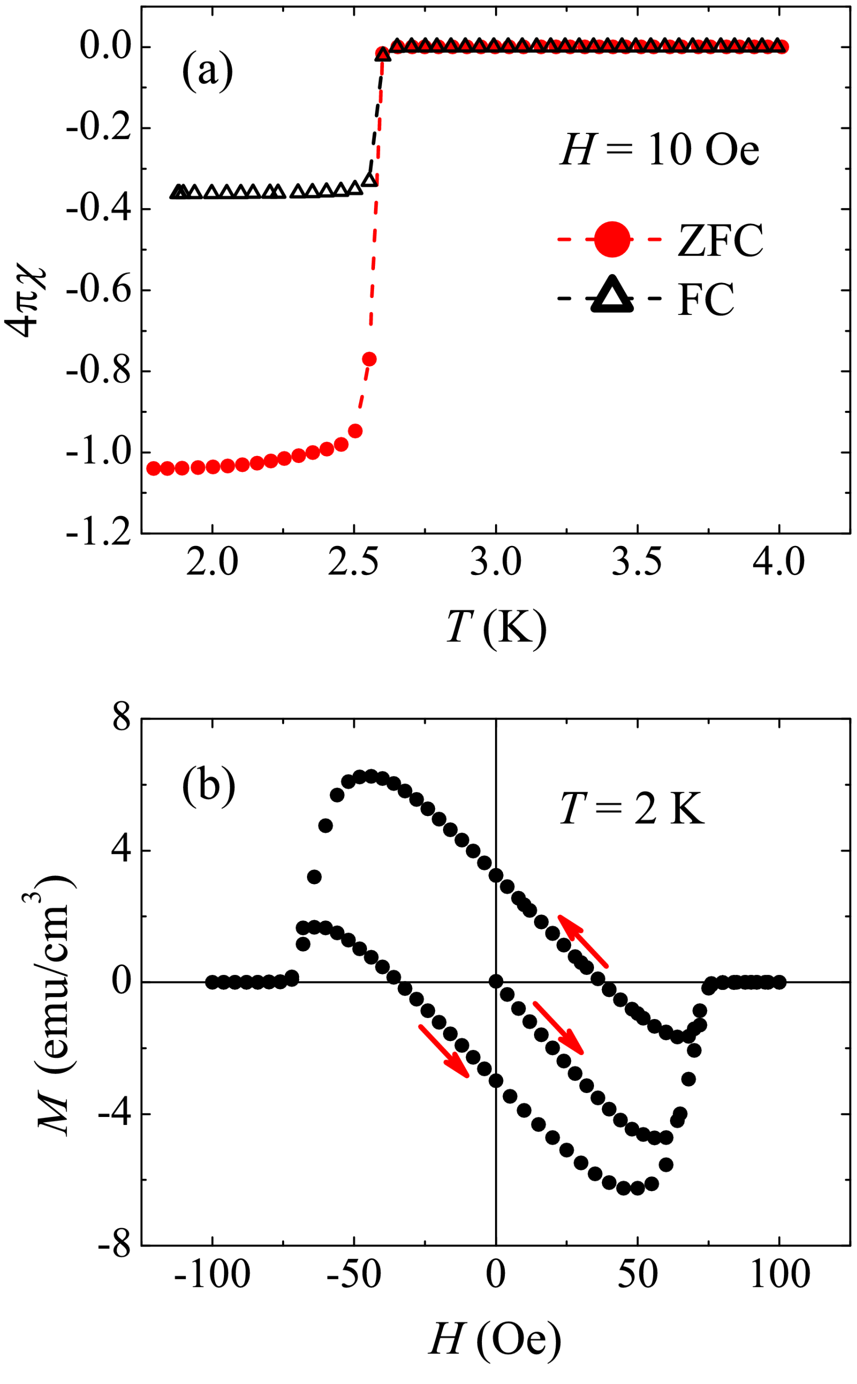

Figure 6.2: (a) Magnetic susceptibility of $LaPdSi_3$ as a function of temperature in an applied field of 10 Oe. Zero-field cooled (ZFC) and field-cooled (FC) measurements are displayed. (b) Magnetization of $LaPdSi_3$ as a function of applied field at 2 K.

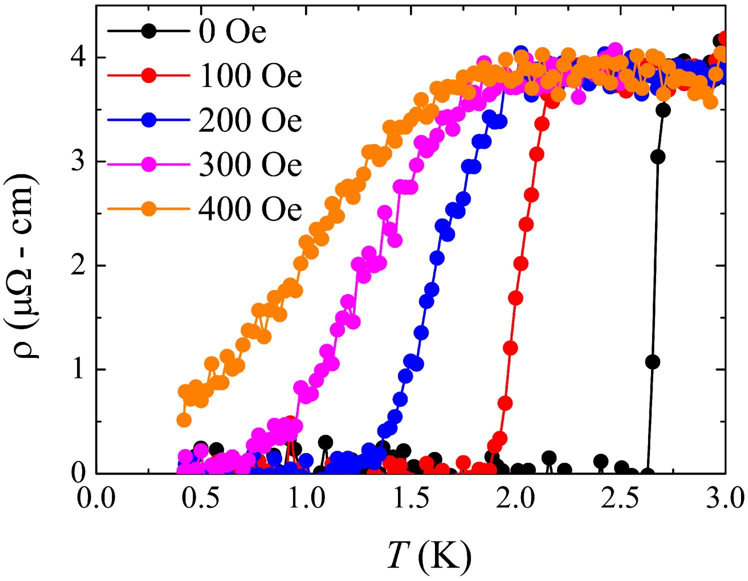

Figure 6.3: Temperature dependence of the resistivity of $LaPdSi_3$ in applied fields up to 400 Oe.

transition is observed in zero-field which onsets at $T_c^{\rm onset} = 2.70(3)$ K and reaches zero resistivity at $T_c^{\rm zero} = 2.63(3)$ K. In an applied magnetic field, $T_c^{\rm zero}$ is rapidly suppressed, whereas there is relatively little change in $T_c^{\rm onset}$. As a result, there is a significant broadening of the transition. When 400 Oe is applied, zero resistivity is not observed down to 0.4 K but $T_c^{\rm onset}$ is around 1.7 K.

6.2.3 Specific heat measurements

The specific heat in zero and applied fields up to 200 Oe are shown in Fig. 6.4(a). In zero-field, there is a jump in the specific heat, indicating the onset of bulk superconductivity. If the transition temperature is defined to be the midpoint of the transition, $T_c = 2.65(5)$ K is obtained. A fit to the normal state is shown by the dashed line using Eq. 2.49. The fitted values are $\gamma = 4.67(4)$ mJ/mol K^2 and $\beta = 0.155(5)$ mJ/mol K^4. Using Eq. 2.50 and Eq. 2.45, $\Theta_D = 397(4)$ K and $\lambda_{e-ph} = 0.51$ are obtained. This puts $LaPdSi_3$ in the weak coupling limit. T_c is suppressed by the application of a magnetic field and bulk superconductivity is not observed above 0.4 K in an applied field of 200 Oe. The shape of the transition is also dramatically different to that in zero-field. The transition sharpens and the jump is larger in fields up to 75 Oe. This suggests that there is a change from a jump to a divergence in the specific heat and therefore the transition is second order in zero-field but first order in an applied field. This is consistent with type-I superconductivity.

The temperature dependence of the electronic contribution to the specific heat is shown in Fig. 6.4(b), from subtracting βT^3 from the total specific heat. At 0.4 K, C_{el}/T starts to flatten but it is still offset from zero. This indicates a non-superconducting fraction, most likely resulting from the presence of impurity phases. The solid line shows a fit to an isotropic BCS model. The specific heat in the superconducting state was modelled using Eq. 2.51 and Eq. 2.52. To take into account the presence of a non-superconducting component, the superconducting entropy was scaled with a parameter a_{sc}, the superconducting fraction. Furthermore, although $\gamma = 4.67(4)$ mJ/mol K^2 is obtained in the normal state, if there is a significant impurity fraction the value of γ for the superconducting phase (γ_{sc}) may be different from the measured value in the normal state. The data were fitted with two free parameters, giving $a_{\mathrm{sc}}\gamma_{\mathrm{sc}} = 3.366(11)$ mJ/mol K^2 and $\alpha = 1.757(4)$ (Eq. 2.44). The value of α is very close to the BCS value of 1.764. If γ_{sc} is taken to be the fitted value in the normal state, $a_{\mathrm{sc}} = 0.72$ is obtained. Alternatively, using $a_{\mathrm{sc}} = 0.765$ from the estimate of the volume fraction from μSR measurements in Sec. 6.2.4, γ_{sc} is calculated to be 4.40(1) mJ/mol K^2. $\Delta C/\gamma T_{\mathrm{c}}$ is calculated to be 0.99 using the observed values but taking into account the fitted parameter $a_{\mathrm{sc}}\gamma_{\mathrm{sc}}$, the value is 1.37 which is closer to the BCS value. In Ref. [65], $\gamma = 5.4$ mJ/mol K^2 and $\Delta C/\gamma T_{\mathrm{c}} = 1.16$ are reported. The fact that these are different to the values reported here indicates the effect that the presence of impurity phases may have on the observed values of these parameters.

6.2.4 μSR measurements

μSR measurements of LaPdSi$_3$ in zero-field at 0.5 and 3 K are shown in Fig. 6.5. The data were fitted with a Kubo-Toyabe function (Eq. 3.7) multiplied with an exponential decay term (Eq. 3.8). At 3 K, $\sigma = 0.0692(14)$ μs^{-1} and $\Lambda = 0.012(2)$ μs^{-1} are obtained and $\sigma = 0.071(2)$ μs^{-1} and $\Lambda = 0.011(2)$ μs^{-1} are obtained at 0.5 K. Since there is no significant difference between the values in the normal and superconducting states, there is no evidence for spontaneous magnetic fields below T_{c} and the breaking of time reversal symmetry.

Transverse field μSR measurements were performed using the MuSR spectrometer, with the sample field cooled in applied fields up to 300 Oe down to temperatures of 50 mK using a dilution refrigerator. Additional measurements were made at 0.5 K in applied fields of 110, 140 and 160 Oe, where the sample was not cooled through the transition in the fields at which the sample was measured. Typically

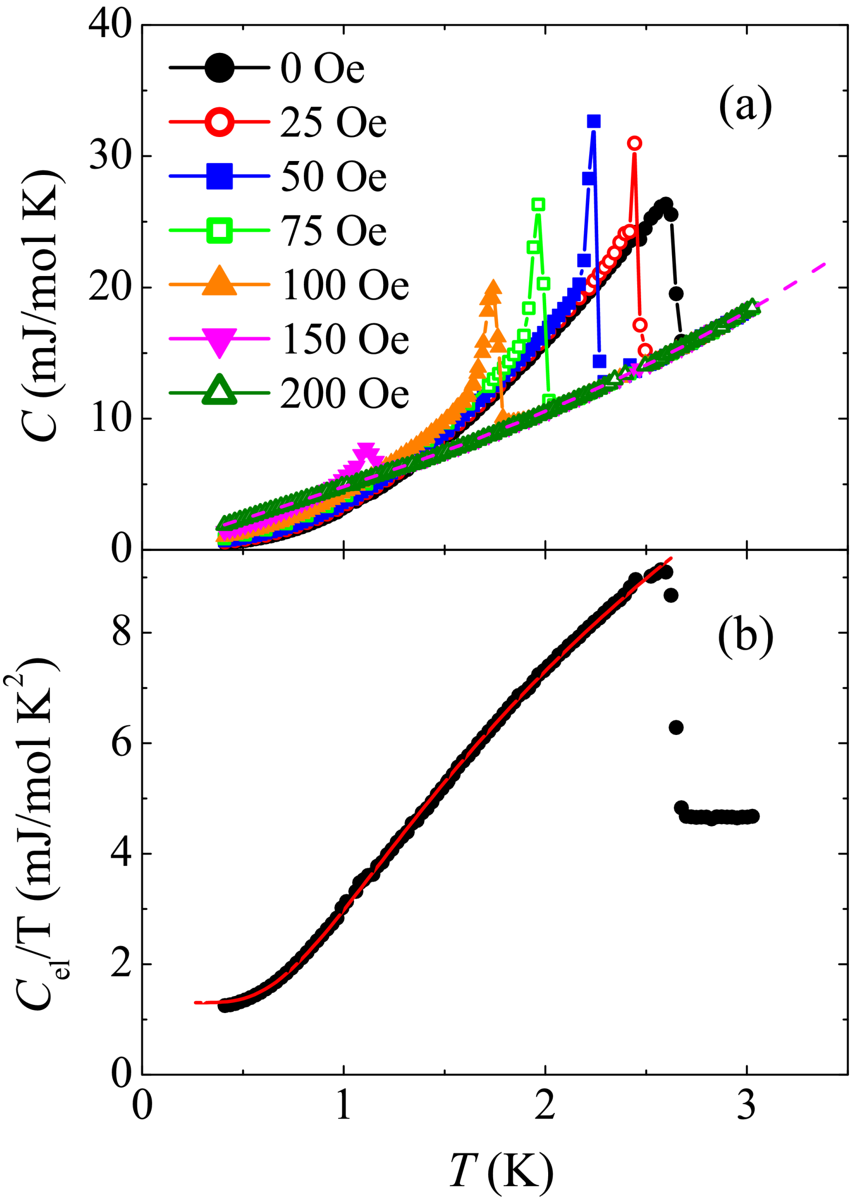

Figure 6.4: (a) Specific heat of $LaPdSi_3$ in zero and applied fields up to 200 Oe. The dashed line shows a fit to the normal state described in the text. (b) Electronic contribution to the specific heat in zero-field, obtained from subtracting an estimate of the phonon contribution. The solid line shows a fit to a BCS model described in the text.

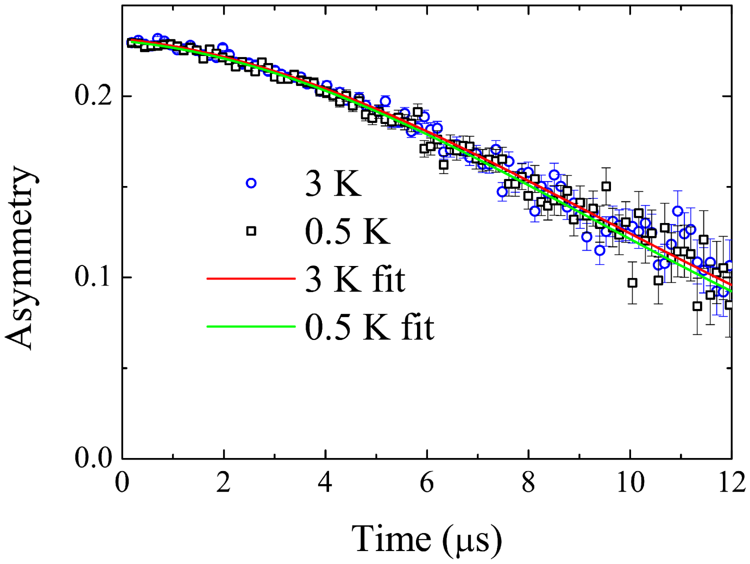

Figure 6.5: Zero-field μSR measurements of LaPdSi$_3$ measured at 0.5 and 3 K. The solid lines show fits to the Kubo-Toyabe function multiplied by an exponential decay.

when transverse μSR measurements are performed using the MuSR spectrometer, the 64 detectors are grouped into two sets, perpendicular to each other and the applied field. These are in the 'forward' and 'backward' positions along the axis of the muon beam and the 'top' and 'bottom' positions above and below. it. In these measurements, only the spectra calculated from the 'top' and 'bottom' detectors are displayed and analyzed.

Figures 6.6(a) and (c) show the μSR spectra measured in an applied transverse field of 150 Oe at 3 and 0.8 K, above and below T_c. There is a sharp increase in the depolarization rate and reduction in the initial asymmetry upon entering the superconducting state. The magnetic field probability distributions are shown by the maximum entropy spectra [209] in Figs. 6.6(b) and (d). At 3 K, a sharp peak is observed centred on 150 G. At 0.8 K this peak at the applied field has broadened and an additional peak is present at a field greater than the applied field. This peak appears asymmetric with a longer tail in the low field direction. The presence of an internal field greater than the applied field is further evidence for type-I superconductivity. For an applied field of $B < B_c$, demagnetization effects may mean that some regions of the superconductor have a field applied greater than B_c, in which case magnetic flux can penetrate the bulk of the sample. Muons implanted in these normal regions of the intermediate state will precess at a frequency corresponding

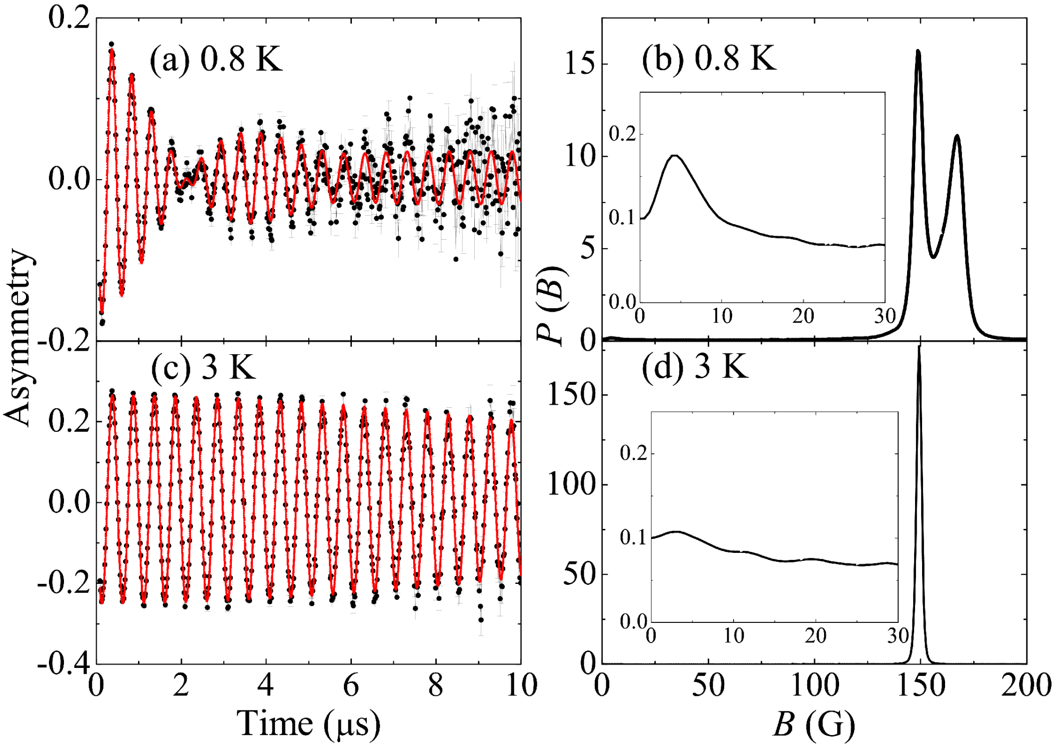

Figure 6.6: Transverse field μSR spectra of LaPdSi$_3$ at (a) 0.8 K and (c) 3 K for an applied field of 150 Oe. Panels (b) and (d) show the maximum entropy spectra for the respective temperatures. The insets show the maximum entropy spectra at low values of B.

to the field at the muon site which must be at least equal to B_c. Muons implanted in regions in the Meissner state, where magnetic flux is expelled will only be affected by nuclear moments. This accounts for the peak present at low fields in the inset of Fig. 6.6(b) but absent in the inset of Fig. 6.6(d). It can be seen that the low field peak at 0.8 K is considerably lower than the peak corresponding to the normal regions of the intermediate state. This is despite the fact that apart from regions of the $H - T$ phase diagram close to the phase boundary, the fraction of the sample in the Meissner state is not expected to be much smaller than that in the normal state. However, the effect of using the 'top' and 'bottom' detectors is to significantly reduce the signal from muons implanted in the Meissner regions. A muon implanted in a region with zero magnetic field will have its moment parallel to the muon beam and the resulting decay positron has an equally probability of being detected at one of the 'top' or 'bottom' detectors. Therefore, there will be no overall contribution to the asymmetry of this detector pairing. The effect of nuclear moments would be to introduce a Kubo-Toyabe term to the asymmetry of the forward and backward detectors as is observed in Fig. 6.5. This is mostly removed when using the top and bottom detectors and as a result, the drop in the initial asymmetry upon entering the superconducting state corresponds to the presence of regions from which magnetic flux is expelled.

The asymmetries were fitted using Eq. 3.9 with a constant background. Three oscillatory components were fitted with $B_2 = B_3$ and $\sigma_3 = 0$. This means there are two components with weights A_2 and A_3 precessing about the applied field, one with a decaying component and one without. The non-decaying component corresponds to muons implanted in the silver sample holder. In the initial fit, the weightings were all fitted freely but in the final fit A_2 and A_3 were fixed to 0.0528 and 0.0326 respectively. The former are likely to correspond to a non-superconducting fraction of the sample. By comparing A_2 to the initial asymmetry from the sample in the normal state of 0.225, the non-superconducting volume fraction is estimated to be 23.5 %. This is the origin of the estimate of $a_\mathrm{sc} = 0.765$ used in Sec. 6.2.3. The $n = 1$ component (A_1) corresponds to muons precessing about a field B_1 higher than the applied field. The temperature dependence of A_1 for several applied fields is shown in Fig. 6.7(a). For each field, the points appear to lie on a curve which is relatively flat at low temperatures but turns up sharply at higher temperatures. This indicates that upon approaching the phase boundary, there is a strong increase in the fraction of the intermediate state consisting of normal regions. Fig. 6.7(b) shows A_1 as a function of $B_\mathrm{app}/B_\mathrm{c}$, where B_c has been taken to be equal to B_1. Interestingly, whereas distinct curves were obtained for each field in Fig. 6.7(b), the

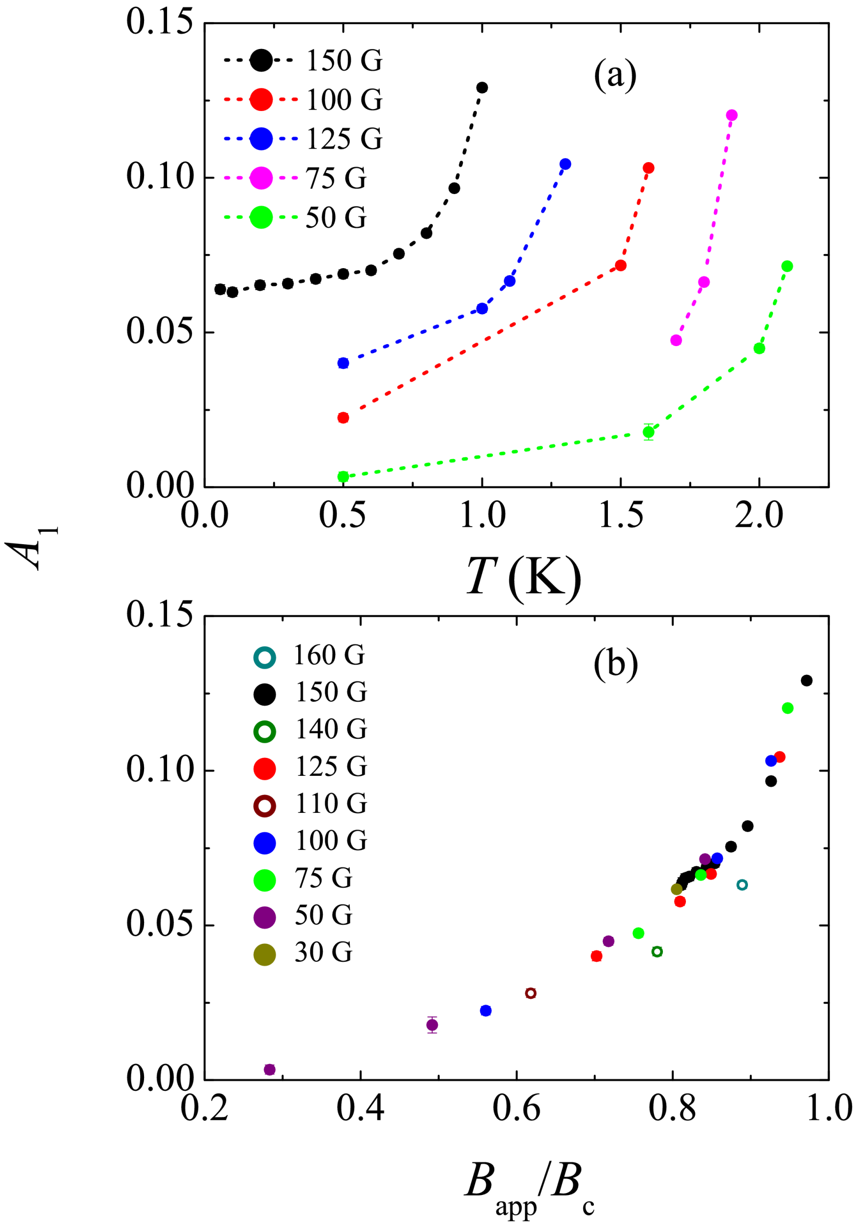

Figure 6.7: The weighting of the second oscillatory component of the fitted transverse μSR spectra of LaPdSi$_3$. This corresponds to the fraction of implanted muons precessing about a field higher than the applied field. A_2 is shown (a) as a function of temperature for several applied fields and (b) as a function of the ratio of the applied and critical fields. Filled circles indicate measurements where the sample was cooled through the transition in the field that it was subsequently measured in.

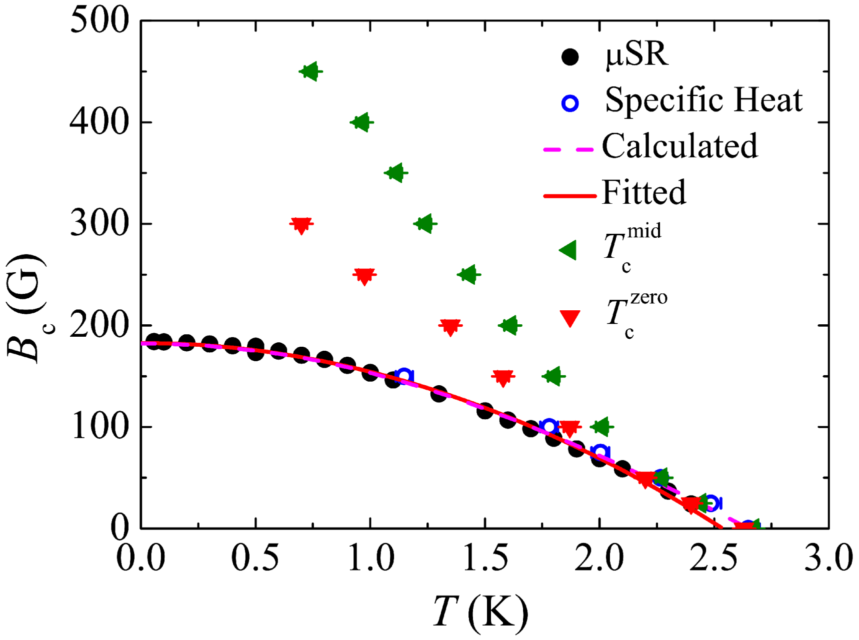

Figure 6.8: Temperature dependence of the critical field of LaPdSi$_3$ obtained from specific heat, μSR and resistivity measurements. The dashed lines show the calculated critical field using Eq. 2.54 whereas the solid lines show a fit to Eq. 2.31.

points collapse onto a single curve as a function of $B_{\mathrm{app}}/B_{\mathrm{c}}$. The only exceptions are two points where the measurements were not taken after field cooling. This suggests that the normal fraction of the intermediate state when the system is field-cooled is only a function of the ratio of the applied and critical fields. It also indicates that the normal fraction of the intermediate state can be sensitive to the field history of the system once the superconducting state has been entered, although the non-field cooled measurement taken in 110 Oe appears to lie on the curve.

The temperature dependence of B_{c} is shown in Fig. 6.8. Values are shown obtained from μSR and specific heat measurements as well as those from the mid-points of resistive transition and where $\rho = 0$. Specific heat and μSR are both bulk probes and there is good agreement between the values of B_{c}, whereas those from the resistivity are higher and display a different shape. The solid line shows a fit to the μSR data using Eq. 2.31, with $B_{\mathrm{c}}(0) = 182.7(7)$ G and $T_{\mathrm{c}} = 2.54(1)$ K. The dashed line shows a calculation of $B_{\mathrm{c}}(T)$ using Eq. 2.54 with $\gamma_{\mathrm{sc}} = 4.40$ mJ/mol K^2 and $\alpha = 1.757$ from Sec. 6.2.3. $B_{\mathrm{c}}(0) = 182.1$ G is calculated and there is good agreement between the two curves and the data.

6.3 $LaPtSi_3$

6.3.1 Sample preparation and structural characterization

Polycrystalline samples of $LaPtSi_3$ were produced by arc-melting stoichiometric quantities of the constituent elements in an argon atmosphere on a water cooled copper hearth. The samples were flipped and remelted several times before being wrapped in tantalum foil, sealed in an evacuated quartz tube and annealed at 900°C for two weeks. Powder neutron diffraction measurements were carried out using the General Materials Diffractometer (GEM) at ISIS [210]. Around 12 g of powdered $LaPtSi_3$ was placed in a thin walled cylindrical vanadium can, 6 mm in diameter. GEM utilizes the time-of-flight technique to collect the diffraction pattern in six banks of detectors, each at a fixed value of 2θ and distance from the sample. The banks are numbered one to six, corresponding to increasing values of 2θ. As a result, bank 1 has the poorest resolution but covers the largest range of d spacings while the opposite is true for bank 6, which is situated close to the backscattering position. Room temperature diffraction data for four of the banks is displayed in Fig. 6.9. The solid lines show the results of Rietveld refinements performed using GSAS [152]. The results of the refinements are shown in Table. 6.2. The values of the lattice parameters are close to those reported in Ref. [208]. The crosses show the position of unfitted peaks, corresponding to impurity phases. The relative magnitudes of these impurity peaks compared to those of the sample are smaller than those in $LaPdSi_3$ (Sec. 6.2.1). These peaks could not be indexed to any La-Pt-Si compounds in the 2013 ICDD Powder Diffraction File [211].

6.3.2 Magnetization and resistivity measurements

The magnetic susceptibility of $LaPtSi_3$ as a function of temperature in an applied field of 10 Oe is shown in Fig. 6.10(a), which displays a sharp superconducting transition at 1.58 K. After correcting for demagnetization effects after Ref. [123], $4\pi\chi = -1.05$ is obtained at 0.5 K, indicating complete flux expulsion. This demonstrates that $LaPtSi_3$ is a bulk superconductor. Figure 6.10(b) shows a magnetization loop measured at 0.5 K between ± 300 Oe. Unlike the abrupt change of gradient observed in the magnetization of $LaPdSi_3$ (Fig. 6.2(b)), the magnetization of $LaPtSi_3$ smoothly flattens with increasing field. This much more resembles the magnetization of a type-II superconductor shown in Fig. 2.4. Furthermore unlike $LaPdSi_3$, upon decreasing the field there is no reentrance of diamagnetism and the loop appears much more like that expected for a type-II superconductor in the presence of flux pinning [11].

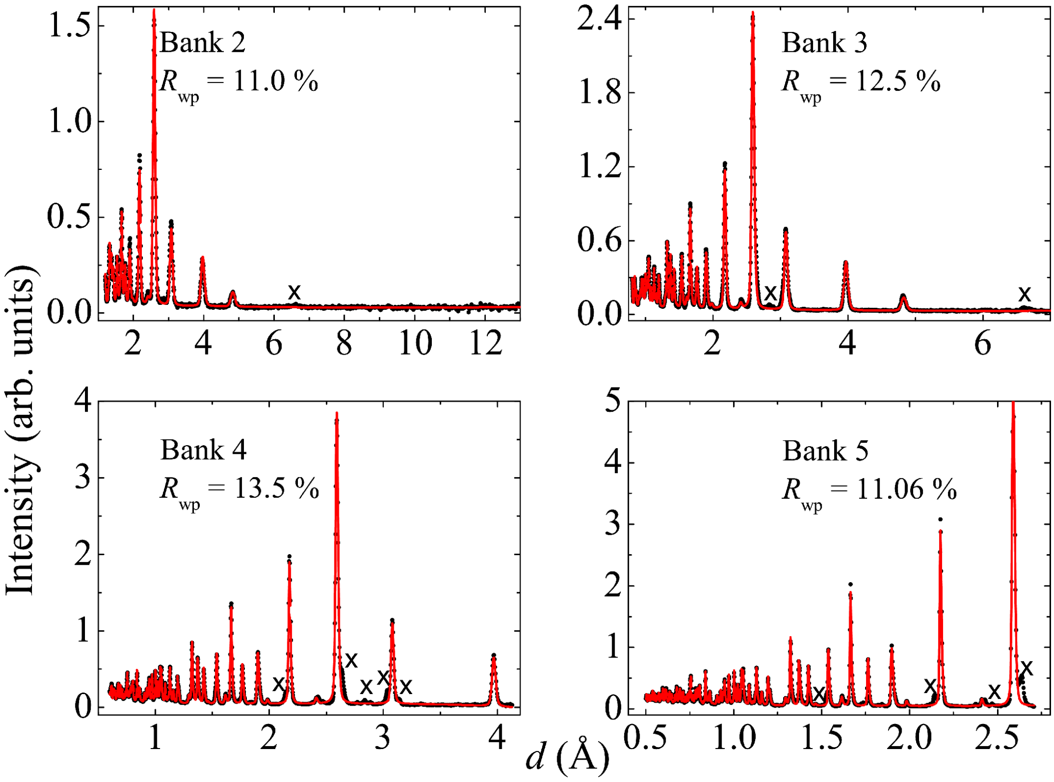

Figure 6.9: Powder neutron diffraction measurements of LaPtSi$_3$ measured on selected banks of the GEM diffractometer at ISIS. The solid lines show the Rietveld refinements performed using GSAS and the crosses indicate impurity peaks. The results are given in Table 6.2.

Table 6.2: Results of the refinements of powder neutron diffraction measurements of LaPtSi$_3$. The lattice parameters and atomic positions are shown. R_{wp} for selected banks are shown in Fig. 6.9.

	LaPtSi$_3$			
a (Å)	4.3474(2)			
c (Å)	9.6368(6)			
	Site	x	y	z
La	2a	0	0	0
Pd	2a	0	0	0.6498(2)
Si1	2a	0	0	0.3986(3)
Si2	4b	0	0.5	0.2622(3)

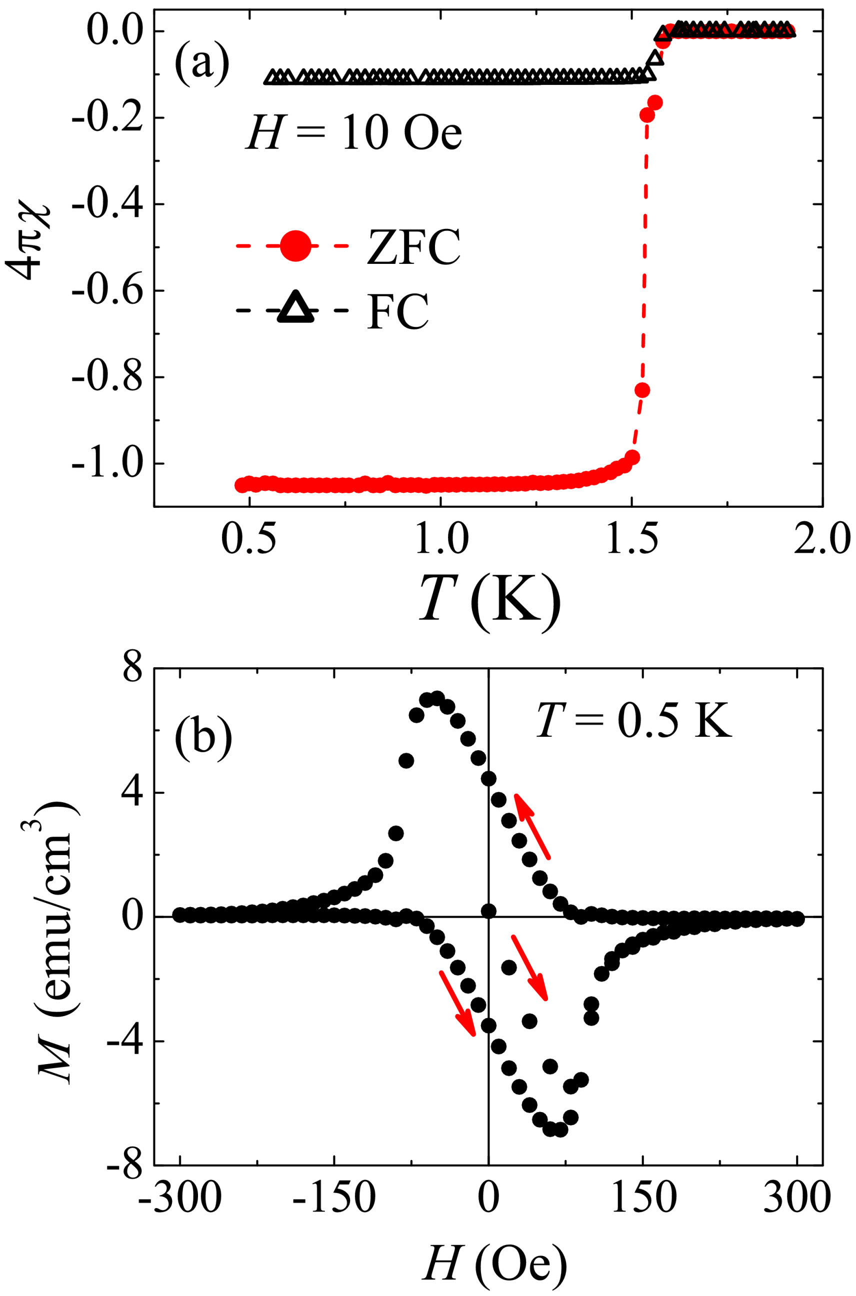

Figure 6.10: (a) Magnetic susceptibility against temperature for LaPtSi$_3$ in an applied field of 10 Oe. Zero-field cooled (ZFC) and field-cooled (FC) measurements are displayed. (b) Magnetization of LaPtSi$_3$ as a function of applied field at 0.5 K.

The temperature dependence of the resistivity as a function of field is shown in Fig. 6.11. The resistivity in the normal state flattens at low temperatures at around $\rho_0 \sim 24.5\ \mu\Omega$-cm. The transition in zero-field is sharp, with an onset at $T_{\mathrm{c}}^{\mathrm{onset}} = 1.58(2)$ K and zero resistivity at $T_{\mathrm{c}}^{\mathrm{zero}} = 1.43(2)$ K. As with LaPdSi$_3$, there is a significant broadening of the transition in field as $T_{\mathrm{c}}^{\mathrm{zero}}$ is suppressed much more rapidly than $T_{\mathrm{c}}^{\mathrm{onset}}$. In fact, the broadening is more significant than LaPdSi$_3$ and in an applied field of 500 Oe, $T_{\mathrm{c}}^{\mathrm{zero}}$ is less than 0.4 K but $T_{\mathrm{c}}^{\mathrm{onset}}$ is around 1.4 K. The relative robustness of $T_{\mathrm{c}}^{\mathrm{onset}}$ can be seen in the plot of resistivity against applied field at 0.4 K, shown in Fig. 6.12. As displayed in the inset, the resistivity is no longer zero in an applied field of $\mu_0 H \sim 0.05\ T$ but only reaches the normal state value at around 1.5 T. This robust superconducting component would only correspond to a small fraction of the sample, so a contribution from an impurity superconducting phase can not necessarily be excluded.

The upper critical fields obtained from $T_{\mathrm{c}}^{\mathrm{zero}}$ and the midpoint of the transition ($T_{\mathrm{c}}^{\mathrm{mid}}$) are shown in Fig. 6.13. Bulk values of B_{c2} obtained from μSR measurements (Sec. 6.3.4) are also displayed. The values obtained from $T_{\mathrm{c}}^{\mathrm{zero}}$ are slightly larger than those in the bulk but this is generally expected since resistivity measurements probe the surface superconductivity, which is expected to be more robust [11]. The solid line shows a fit to the WHH model using Eqs. 2.62 and 2.61. From fitting this, $\alpha_M = 0.0280(3)$ is obtained, indicating that orbital pair breaking is the dominant mechanism for destroying superconductivity. As discussed in Sec. 2.2.8, λ_{so} reduces the influence of the paramagnetic limiting effect, so has little effect on B_{c2} for low values of α_M. It was therefore fixed to zero when fitting. This is consistent with the fact that $B_{\mathrm{c2}}(0) = 526$ G was obtained from the model but $H_{\mathrm{P}} = 28.3$ kOe is calculated using Eq. 2.60 for a BCS superconductor. This indicates that B_{c2} deduced from $T_{\mathrm{c}}^{\mathrm{zero}}$ follows the expected BCS behaviour. However, those obtained from $T_{\mathrm{c}}^{\mathrm{mid}}$ show very different behaviour and there is a positive curvature of B_{c2} down to 0.4 K. This demonstrates the increasing broadening of the transition in field. The inset of Fig. 6.13 shows the critical field calculated using Eq. 2.54 and the results of the analysis of the specific heat in Sec. 6.3.3. The value $B_{\mathrm{c}}(0) = 104.3$ G is lower than that obtained for LaPdSi$_3$, due to the lower transition temperature of the compound.

6.3.3 Specific heat

The specific heat of LaPtSi$_3$ in zero and applied fields up to 1000 Oe are shown in Fig. 6.14(a). In zero field, there is a bulk superconducting transition with $T_{\mathrm{c}} = 1.52(6)$ K. The dashed line shows a fit to the normal state using Eq. 2.49 with

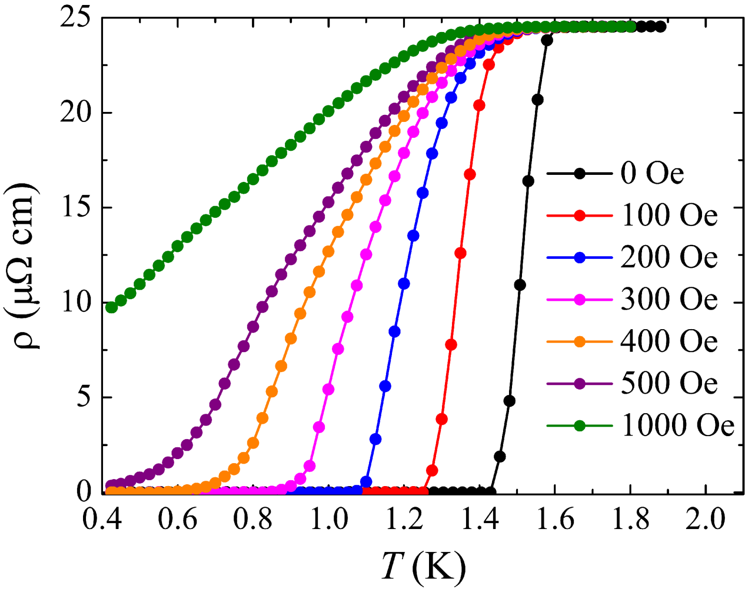

Figure 6.11: Temperature dependence of the resistivity of $LaPtSi_3$ in applied fields up to 1000 Oe.

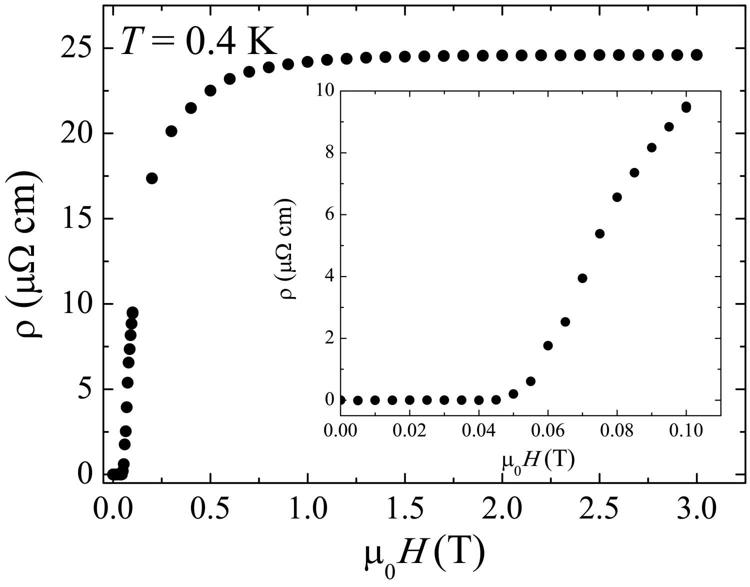

Figure 6.12: Field dependence of the resistivity of $LaPtSi_3$ at 0.4 K.

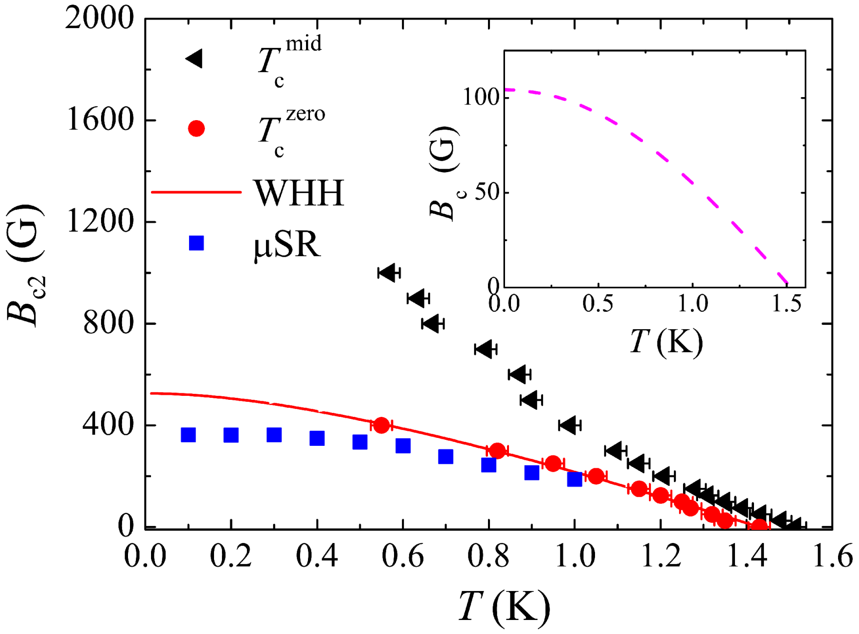

Figure 6.13: Temperature dependence of the upper critical field obtained from resistivity and μSR measurements. The solid line shows a fit made to the latter with a WHH model as described in the text. The blue points show the bulk values of B_{c2} obtained from μSR measurements as described in Sec. 6.3.4. A calculation of the critical field using equation 2.54 is shown in the inset.

$\gamma = 4.41(4)$ mJ/mol K^2 and $\beta = 0.238(5)$ mJ/mol K^4, giving $\Theta_D = 344(2)$ K (Eq. 2.50). Using this value of Θ_D with Eq. 2.45, $\lambda_{e-ph} = 0.47$ is obtained, putting LaPtSi$_3$ in the weak coupling limit. The in-field measurements show significant broadening compared to those taken in zero field, particularly with applied fields of 100 and 200 Oe. Furthermore, the jump in the specific heat at the transition is smaller than in zero-field, unlike the sharp in-field transitions observed in LaPdSi$_3$. This suggests that the transition is second-order in field, as expected for type-II superconductors. Although the superconducting transition is not apparent in the plot of the specific heat with an applied field of 1000 Oe, the inset of Fig. 6.14(b) shows that there is a deviation from linear behaviour in C/T against T^2 at around 1.1 K. This may correspond to a superconducting transition with a significantly reduced volume fraction.

The electronic contribution to the specific heat is shown in Fig. 6.14(b). The solid lines shows a fit to a BCS model (Eq. 2.51 and 2.52) with $a_{sc} = 0.93$ and $\alpha = 1.735(5)$. The larger value of a_{sc} and smaller offset indicate a larger

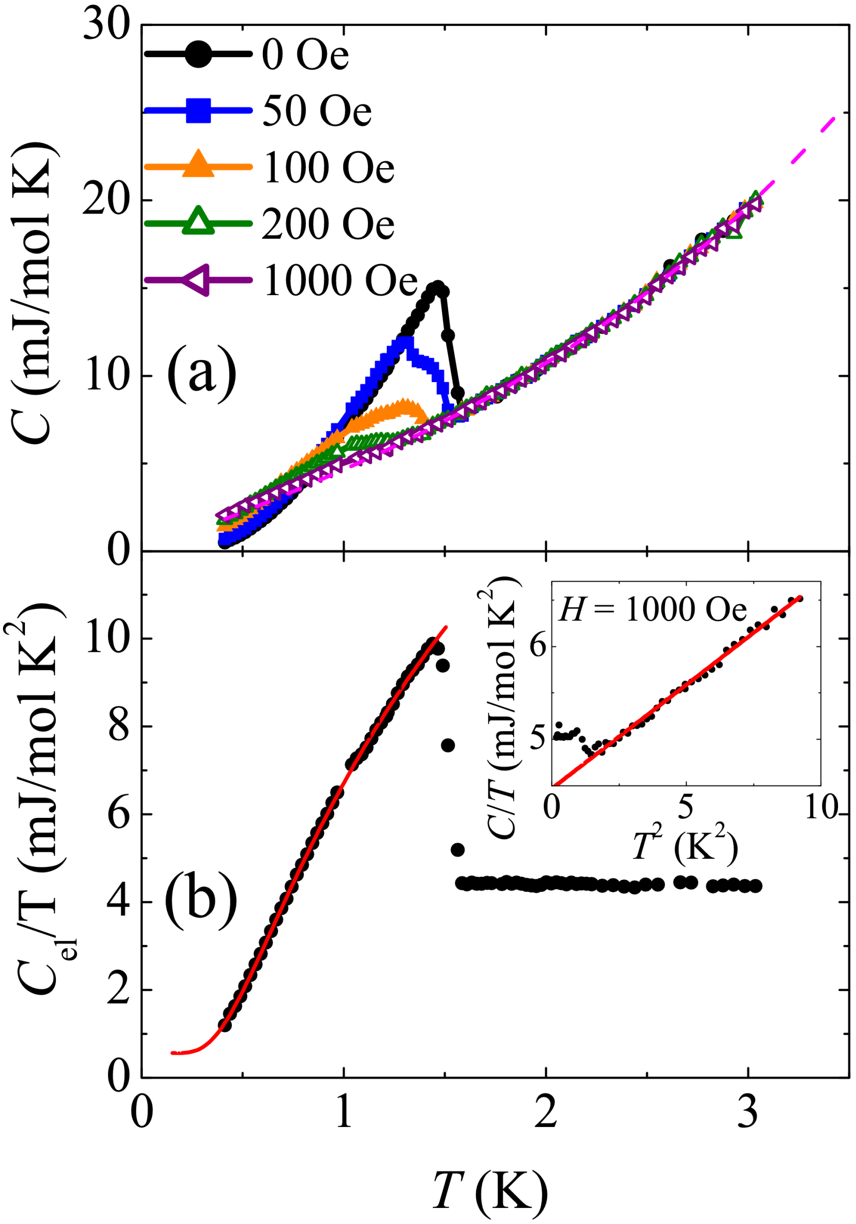

Figure 6.14: (a) Specific heat of $LaPtSi_3$ in zero and applied fields up to 1000 Oe. The dashed line shows a fit to the normal state described in the text. (b) Electronic contribution to the specific heat in zero-field, obtained from subtracting an estimate of the phonon contribution. The solid line shows a fit to a BCS model described in the text. The inset shows C/T against T^2 in an applied field of 1000 Oe.

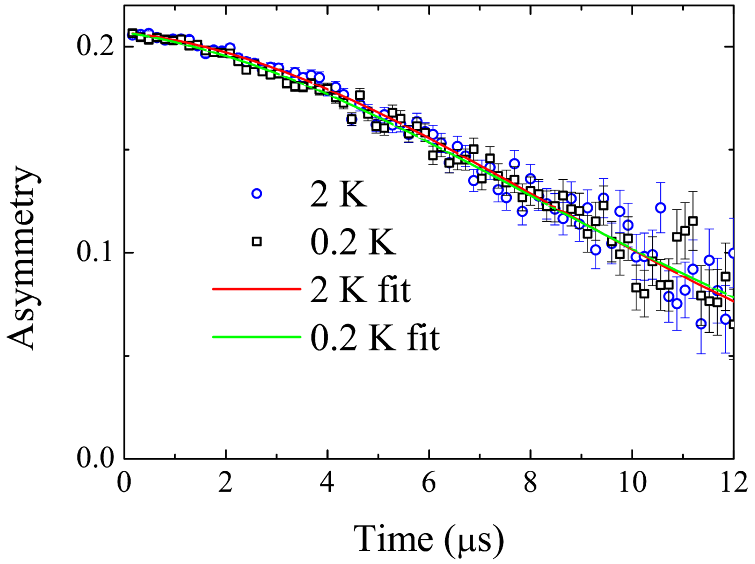

Figure 6.15: Zero-field μSR measurements of LaPdSi$_3$ measured at 0.2 and 2 K. The solid lines show fits to the Kubo-Toyabe function multiplied by an exponential decay.

superconducting fraction than in the LaPdSi$_3$ sample, which is consistent with the smaller impurity peaks observed in diffraction data. The observed jump in the specific heat is $\Delta C/\gamma T_c \sim 1.33$ and the BCS value of ~ 1.43 is obtained, taking into account the fitted value of a_{sc}. Along with α being close to the BCS value, this shows the data are compatible with an isotropic, BCS model. However, C/T has not flattened at 0.4 K and therefore the specific heat measurements are not able to confirm or rule out gapped behaviour.

6.3.4 μSR measurements

μSR measurements of LaPtSi$_3$ in zero-field at 0.2 and 2 K are shown in Fig. 6.15, fitted with a Kubo-Toyabe function multiplied with an exponential decay term (Eqs. 3.7 and 3.8). $\sigma = 0.079(1)\ \mu s^{-1}$ and $\Lambda = 0.013(2)\ \mu s^{-1}$ are obtained at 2 K and $\sigma = 0.078(2)\ \mu s^{-1}$ and $\Lambda = 0.014(2)\ \mu s^{-1}$ are obtained at 0.2 K. Therefore there is no evidence that TRS is broken in the superconducting state of LaPtSi$_3$.

Transverse field μSR measurements were carried out in several applied fields up to 400 Oe. The spectra at 0.1 and 2 K in an applied transverse field of 150 Oe are shown in Figs. 6.16(a) and 6.16(c) respectively. There is a significant increase

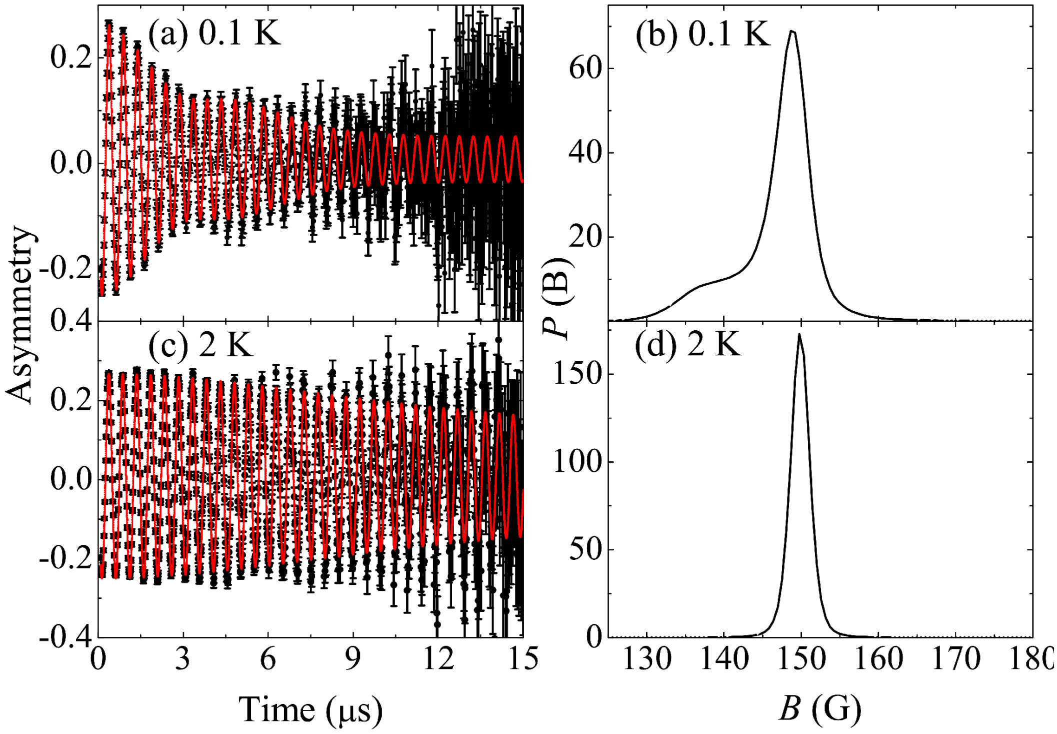

Figure 6.16: Transverse field μSR spectra of $LaPtSi_3$ at (a) 0.1 K and (c) 2 K for an applied field of 150 Oe. Panels (b) and (d) show the maximum entropy spectra for the respective temperatures.

in the depolarization upon entering the superconducting state, indicating the onset of bulk superconductivity. The corresponding maximum entropy spectra are shown in Figs. 6.16(b) and 6.16(d). In the normal state, the spectra show a peak in $P(B)$ centered around an applied field. In the superconducting state, the peak around the applied field broadens and an additional shoulder in the distribution is observed at lower fields. This is very different to the field distribution observed in the superconducting state of $LaPdSi_3$ (Fig. 6.6) and indicates bulk type-II superconductivity. This is the field distribution of the flux-line lattice in the mixed state, where most of the contribution to $P(B)$ is at fields less than the applied field. No significant increase in depolarization is observed in an applied field 400 Oe, indicating that bulk superconductivity has been suppressed.

The asymmetries were fitted using Eq. 3.9. Three oscillatory components were used apart from in a field of 300 Oe, where only two could be fitted. σ_3 was fixed to zero and this component corresponded to muons stopping in the silver sample holder. The first and second moments of the field distribution of the sample

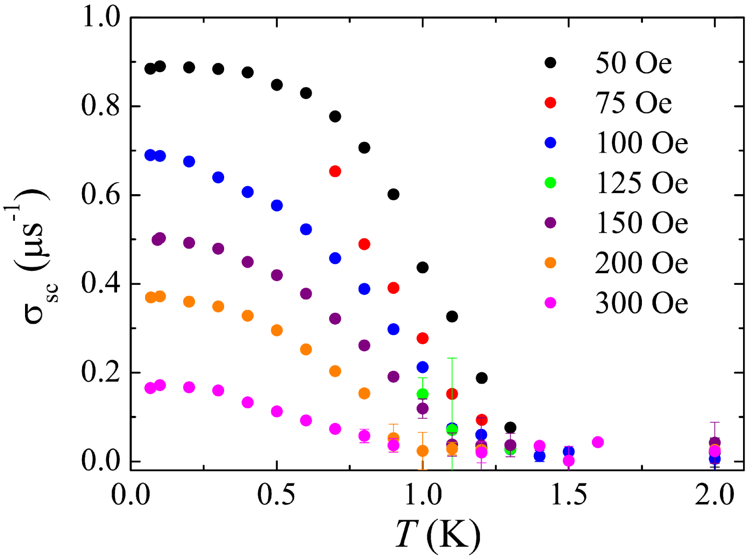

Figure 6.17: The temperature dependence of σ_{sc} for LaPtSi$_3$.

were calculated using Eqs. 3.10 and 3.11, where the component corresponding to muons implanted in the silver holder was not included in any of the summations. The superconducting contribution to the second moment ($\langle B^2\rangle_{\mathrm{sc}}$) was obtained from subtracting the value obtained in the normal state. The field dependence of $\langle B^2\rangle_{\mathrm{sc}}$ at a given temperature was fitted using Eq. 2.37 for $b > 0.25$. This was selected rather than the more commonly used Eq. 2.38 due to the value of $\kappa < 5$ obtained in Sec. 6.3.2. However, it should be noted that similar results were obtained using the latter expression. Equation 2.37 can be expressed in terms of two free parameters, λ_{eff} and B_{c2}. The temperature and field dependence of σ_{sc} are shown in Figs. 6.17 and 6.18, where $\sigma_{\mathrm{sc}} = \sqrt{\langle B^2\rangle_{\mathrm{sc}}/\gamma_\mu^2}$. The field dependence was fitted for temperatures between 0.1 and 1 K. The values of B_{c2} are shown in Fig. 6.13 and as discussed in Sec. 6.13, the bulk values are slightly lower than those deduced from $T_{\mathrm{c}}^{\mathrm{zero}}$ and $B_{\mathrm{c2}} = 360(10)$ G is obtained. This is consistent with the lack of bulk superconductivity in an applied field of 400 Oe.

The temperature dependence of λ_{eff} is shown in Fig. 6.19. The data were fitted using Eq. 2.55, with T_{c} fixed to 1.52 K from the analysis of the specific heat. The fit was made to an isotropic gap, so $\Delta(T,\phi) = \Delta(T)$ which is given by Eq. 2.43 but with a variable prefactor Δ_0. $\Delta_0 = 0.209(7)$ meV was obtained, giving $\Delta_0/k_{\mathrm{B}}T_{\mathrm{c}} = 1.60(8)$. This is slightly below the BCS value of 1.764 and the data are compatible with a fully gapped, weakly coupled superconductor. $\lambda_{\mathrm{eff}}(0) = 239(3)$ nm

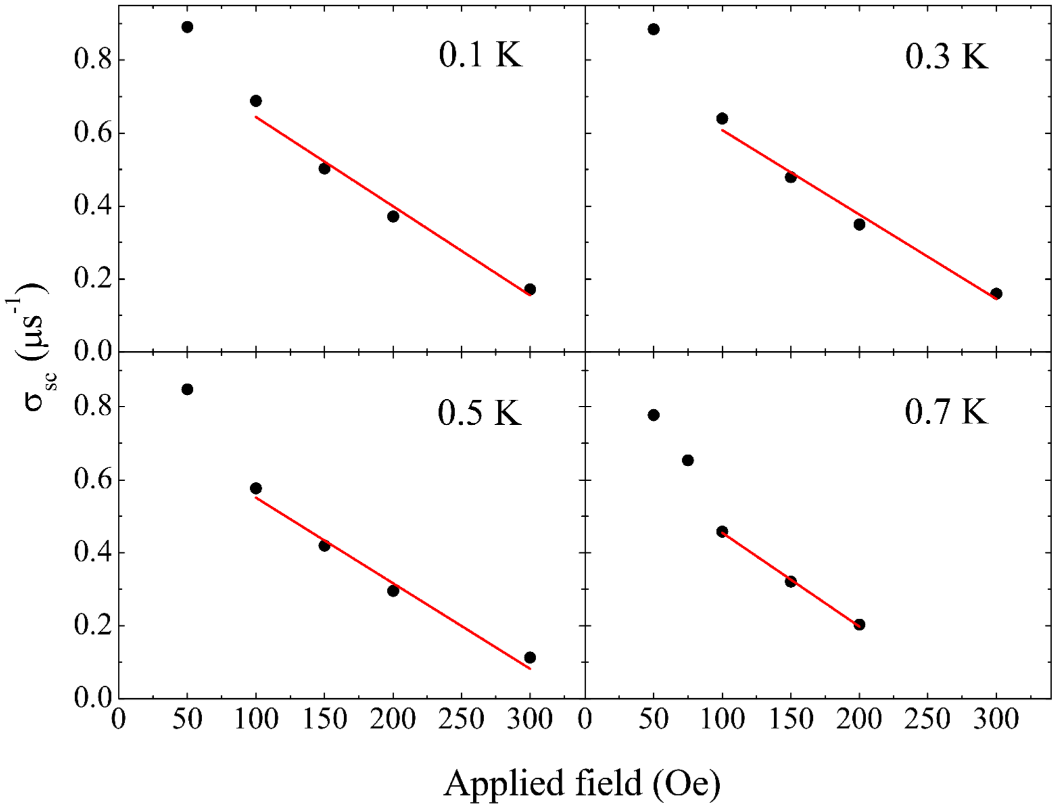

Figure 6.18: The field dependence of σ_{sc} for LaPtSi$_3$ at four temperatures. The solid lines show fits to Eq. 2.38 over the appropriate range of fields.

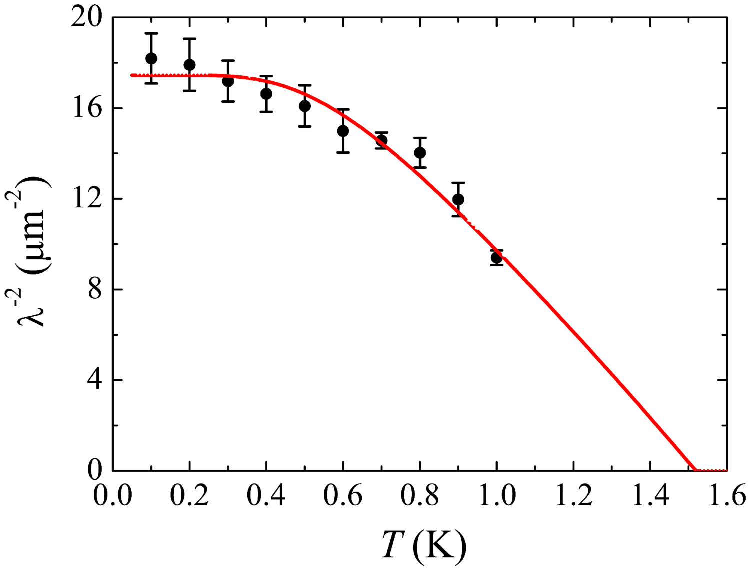

Figure 6.19: The temperature dependence of the effective penetration depth of LaPtSi$_3$. The solid line shows a fit made using Eq. 2.55

was also obtained and using $\xi = 96(1)$ nm from Eq. 2.33, $\kappa = 2.49(4)$ is calculated. Alternatively κ can be calculated using Eq. 2.34. Using $B_{\mathrm{c}}(0) = 104.3$ G from Sec. 6.3.2 and $B_{\mathrm{c2}} = 360(10)$ G, $\kappa = 2.44(7)$ is obtained. There is therefore agreement between the two values which both indicate that LaPtSi$_3$ is in the low κ regime.

6.4 Discussion and summary

The superconducting properties of two non-centrosymmetric superconductors with the BaNiSn$_3$ structure, LaPtSi$_3$ and LaPdSi$_3$ have been reported. Various superconducting parameters are shown in Table 6.3. Magnetization, specific heat and μSR measurements reveal that LaPdSi$_3$ is a bulk type-I superconductor. The specific heat measurements reveal that the superconducting transition is second-order in zero-field but first-order in an applied field, as expected for a type-I superconductor. μSR measurements confirm the presence of bulk type-I superconductivity. With an applied transverse field, a fraction of muons are implanted in an environment with a local magnetic field larger than the applied field. This is consistent with probing macroscopic normal regions of the intermediate state. The critical field (B_{c}) is deduced from the value of this field and is in excellent agreement with those mea-

Table 6.3: Superconducting parameters of $LaPdSi_3$ and $LaPtSi_3$.

	$LaPdSi_3$	$LaPtSi_3$
T_c (K)	2.65(5)	1.52(6)
λ_{e-ph}	0.51	0.47
Δ_0/k_BT_c	1.757(4)	1.735(5) - specific heat 1.60(8) - μSR
λ_{eff}(nm)		239(3)
ξ(nm)		96(1)
κ		2.49(4)
$B_c(0)$ (G)	182.1 - calculated 182.7 - μSR	104.3 - calculated
$B_{c2}(0)$ (G)		360(10) - μSR 526 - resistivity ($\rho = 0$)

sured from the specific heat measurements and $B_c(0) = 182.7(7)$ G is obtained from the analysis of the temperature dependence of $B_c(T)$, in excellent agreement with the calculated value of 182.1 G. This is slightly higher than that observed in the isostructural type-I superconductor $LaRhSi_3$, where $B_c(0) = 172.7$ G was observed [103].

In contrast to $LaPdSi_3$, magnetization, specific heat and μSR measurements reveal type-II superconductivity in $LaPtSi_3$. Specific heat measurements reveal that the superconducting transition is second-order in both zero and applied fields. μSR measurements are used to probe the field distribution of the mixed state and the temperature dependence of λ_{eff} and $B_{c2}(0)$ are obtained from the field dependence of the second moment of magnetization. Zero temperature values of $\lambda_{eff}(0) = 239(3)$ nm and $\xi(0) = 96(1)$ nm give $\kappa = 2.49(4)$, whereas 2.44(7) is obtained using Eq. 2.34. A similar value of $\kappa = 2.6$ is reported for $BaPtSi_3$ [100], while larger values of 8.3 and 11 were reported in $CaIrSi_3$ and $CaPtSi_3$ respectively [102]. It should be noted that the value for $BaPtSi_3$ was deduced from μSR measurements fitted with Eq. 2.38, while the latter were calculated using Eq. 2.34 with upper critical fields deduced from ac susceptibility measurements.

The effect of substituting Pt for Pd in the $LaTSi_3$ system is to increase κ and drive the system from type-I to type-II behaviour. It would be useful to determine whether the observed values of κ can be calculated or whether the trend from type-I to type-II can be reproduced. The calculation of κ requires knowledge of whether the system is in the clean or dirty limits. This depends on the relative magnitudes of ξ_0 and the mean free path l. ξ_0 can be calculated using Eq. 2.56. It is necessary to estimate v_F which can be calculated after Ref. [212] using

$$v_\mathrm{F} = \frac{2\pi^2\hbar^3}{m^{*2}V_\mathrm{cell}}N(E_\mathrm{F}), \tag{6.1}$$

where $m^* = m_\mathrm{e}(1 + \lambda_\mathrm{e-ph})$, V_cell is the unit cell volume and $N(E_\mathrm{F})$ is calculated from γ_sc using Eq. 2.48. The factor of two arises because there are two formula units per unit cell. Values of $v_\mathrm{F} = 8.3\times10^5$ and 7.8×10^5 ms^{-1} are calculated for LaPtSi$_3$ and LaPdSi$_3$ respectively. Using these, $\xi_0 = 762$ and 407 nm are calculated from Eq. 2.56. l can be obtained from the expression [212]

$$l = \frac{3\pi^2\hbar^3}{\rho_0}\left(\frac{1}{m^*\mathrm{e}v_\mathrm{F}}\right)^2. \tag{6.2}$$

For LaPtSi$_3$ and LaPdSi$_3$, $l = 4.5$ and 30.7 nm are obtained respectively. This suggests that $l \ll \xi_0$ for both compounds, placing them in the dirty limit. This justifies the use of Eq. 2.61 for evaluating the upper critical field of LaPtSi$_3$. Given that the systems are in the dirty limit, κ should be calculated using Eq. 2.59 rather than 2.58. This may also be expected due to the fact that κ is experimentally larger in LaPtSi$_3$ than in LaPdSi$_3$. However, LaPtSi$_3$ has a lower T_c and therefore a smaller Δ_0 so would be expected to have a smaller value of κ in the clean limit. λ_L can be estimated from calculating the plasma frequency (ω_p) using [212]

$$\omega_\mathrm{p}^2 = \frac{4m^{*2}\mathrm{e}^2v_\mathrm{F}^3}{3\pi\hbar^3} \tag{6.3}$$

$$\lambda_\mathrm{L} = \frac{\mathrm{c}}{\omega_\mathrm{p}}, \tag{6.4}$$

giving 32.6 nm for LaPtSi$_3$ and 34.7 nm for LaPdSi$_3$. Using Eq. 2.59, $\kappa = 5.2$ and 0.8 are estimated for the two compounds. The value of 5.2 for LaPtSi$_3$ is larger than the value of 2.49 deduced from μSR measurements and the value of 0.8 would imply that LaPdSi$_3$ is a type-II material. Therefore the values are too large for both materials. One source of error may be that in using ρ_0 to calculate l, it is assumed that the low temperature resistivity is determined entirely by the scattering rate of electrons in the bulk of the material, rather than there being significant contributions from dislocations and grain boundaries. If this is the case, the mean free path will be higher than that calculated using the observed ρ_0. This would be expected to be particularly true for polycrystalline samples and therefore it would be of interest to examine the resistivity of single crystals. A similar calculation for polycrystalline LaRhSi$_3$ did correctly predict type-I behaviour [103], but a lower value of $\rho_0 = 1.08\ \mu\Omega$-cm was obtained rather than 3.9 and 24.5 $\mu\Omega$-cm for $LaPdSi_3$ and $LaPtSi_3$ respectively. Even though this method does not correctly reproduce the observed values of κ, it does suggest that the change from type-I to type-II behaviour is due to a reduced electronic mean free path. This is unlike the clean limit calculation (Eq. 2.58), which fails to reproduce the trend of increasing κ. It is noted that both $LaRhSi_3$ [103] and $LaPdSi_3$ with a $4d$ transition metal are type-I while the reported type-II materials all contain $5d$ transition metals. It remains to be seen if it is a general feature of the NCS $RTSi_3$ compounds that those where T has a $4d$ outer shell are type-I and those with a $5d$ configuration are type-II.

The analysis of the specific heat of the compounds reveal that both are weakly coupled superconductors with $\lambda_{\mathrm{e-ph}}$ of around 0.5. The electronic contribution of the specific heat of both compounds was fitted with an isotropic s-wave model, with gap ratios of $\alpha = 1.757(4)$ and 1.735(5) obtained for $LaPdSi_3$ and $LaPtSi_3$ respectively. The electronic contribution of C/T for $LaPdSi_3$ (Fig. 6.4(b)) flattens at low temperatures and the value of α is very close to the BCS value of 1.764, indicating that the data are consistent with an isotropic, fully-gapped BCS superconductor. The specific heat $LaPtSi_3$ (Fig. 6.14) is only measured to $\sim T_{\mathrm{c}}/4$ which may not be low enough to observe the flattening out of the electronic contribution of C/T associated with fully gapped behaviour. However, the data above 0.4 K are compatible with an isotropic model with α being very close to the BCS value. μSR measurements were made down to 0.1 K, which should be sufficient to determine whether the system is gapped by examining whether $\lambda_{\mathrm{eff}}^{-2}$ reaches a constant level at low temperatures. As shown in Fig. 6.19, the data are consistent with an isotropic s-wave model with $\alpha = 1.60(8)$. It should be noted that although such a model is compatible with the data, there are a relatively small number of points with relatively large error bars. This reflects the need to model the field dependence of σ_{sc} which was fitted with two free parameters, B_{c2} and λ_{eff}. There is also a relatively large error in α which may also reflect the lack of points close to T_{c}, where an insufficient number of points were measured to fit the field dependence. It may also be desirable to model the two gap structure which is believed to arise in non-centrosymmetric superconductors from Eq 2.47, as observed in several compounds [95, 82, 105]. However, if the triplet component is small then not only will both gaps be fully gapped but also of similar magnitudes. Since a one gap model can fit the data well, the addition of two additional parameters in a two gap model would not be justified. Therefore, it would be desirable to perform more detailed and precise measurements of λ_{eff} across the full range of temperatures below T_{c}. This may be best performed using a tunnel diode oscillator. This technique does not require the measurement of the field dependence of the signal or modelling the field distribution of the flux line lattice, so may be most appropriate for extracting more precise measurements of the temperature dependence of the penetration depth.

The (upper) critical fields extracted from resistivity measurements of $\mathrm{LaPdSi_3}$ ($\mathrm{LaPtSi_3}$) are larger than the values obtained from the bulk. In the case of $\mathrm{LaPdSi_3}$, there is a pronounced difference in the shape of the temperature dependence of the critical field values deduced from $T_{\mathrm{c}}^{\mathrm{zero}}$ and $T_{\mathrm{c}}^{\mathrm{mid}}$, whereas for $\mathrm{LaPtSi_3}$ the values from $T_{\mathrm{c}}^{\mathrm{zero}}$ could be fitted to the WHH model but those from $T_{\mathrm{c}}^{\mathrm{mid}}$ have a positive curvature. A positive curvature in B_{c2} has been observed in some two-band superconductors [213], this has been reported close to T_{c} where it is not observed in $\mathrm{LaPtSi_3}$. Similar behaviour in the values of B_{c2} deduced from resistivity measurements has also been observed in $\mathrm{CaIrSi_3}$, $\mathrm{CaPtSi_3}$ [102] and $\mathrm{BaPtSi_3}$ [101]. In all these materials, a relatively sharp transition in zero field is observed which increasingly broadens in applied fields. The sharp zero field transition and lack of step like features in field means that it is unlikely that this robust superconducting fraction is from an impurity phase. Three further suggestions were offered for $\mathrm{CaIrSi_3}$ and $\mathrm{CaPtSi_3}$ in Ref. [102]. One possibility was that the upper critical field could be highly anisotropic with a narrow peak along one particular direction. It is not clear what the mechanism behind such an enhancement would be and the specific heats of both compounds were compatible with an isotropic gap. However, single crystals may be necessary to determine the presence of anisotropy. Pressure induced enhancement of the superconductivity at grain boundaries was also proposed but in Ref [214], the superconductivity of $\mathrm{CaIrSi_3}$ and $\mathrm{CaPtSi_3}$ was found to be suppressed with pressure. It was also suggested that there may be regions of defected material where l is much less than ξ_0. As discussed previously, both $\mathrm{LaPdSi_3}$ and $\mathrm{LaPtSi_3}$ appear to be in the dirty limit and therefore a variation in l in certain regions due to defects or site disorder may lead to different values of l and therefore κ. This may also explain the small increase in C/T of $\mathrm{LaPtSi_3}$ observed in an applied field of 1000 Oe in the inset of Fig. 6.14(b).

There is therefore considerable interest in studying single crystals of the weakly correlated superconductors in the $RT\mathrm{Si_3}$ series. The measurements of polycrystalline samples of $\mathrm{LaPdSi_3}$ and $\mathrm{LaPtSi_3}$ are consistent with both compounds being isotropic, s-wave superconductors. The study of single crystals would allow the anisotropy to be probed directly. Furthermore if the broadening in the resistivity is due to the presence of inhomogenous or defected regions the effect would be expected to be reduced or absent in high quality single crystals.

Chapter 7

$Nb_{0.18}Re_{0.82}$

7.1 Introduction

Superconductivity was reported in several compounds with the non-centrosymmetric α-Mn structure (space group $I\bar{4}3m$) in the 1960's [9, 10, 215], which are rich in rhenium or other heavy elements belonging to the sixth period of the periodic table. The Nb_xRe_{1-x} system forms homogeneously in the α-Mn structure across a wide compositional range ($0.13 < x < 0.38$) [216, 217]. The unit cell contains 58 atoms with four crystallographically distinct sites. Two of these have Wyckoff positions of $2a$ and $8c$ which are believed to be entirely occupied by niobium atoms, while the remaining two are labelled $24g$ and contain a distribution of niobium and rhenium [218]. Of the four sites, only the $2a$ site has an inversion centre and therefore the rhenium atoms are all in non-centrosymmetric positions. The crystal structure is displayed in Fig. 7.1, where both of the $24g$ sites are entirely occupied with rhenium atoms, corresponding to $x = 0.17$.

Although the lack of inversion symmetry does not appear to have been noted in the early studies, in light of recent interest in non-centrosymmetric superconductors, the properties of polycrystalline Nb_xRe_{1-x} have recently been reported [217, 219, 220]. These studies indicate that Nb_xRe_{1-x} displays an isotropic s-wave superconducting state. T_c ranges from around 8.8 K for $x = 0.18$ to around 3.5 K for $x = 0.38$. NMR measurements on $Nb_{0.17}Re_{0.83}$ indicate a value of α very close to the BCS value (Eq. 2.42), while Refs. [219] and [217] report a moderately enhanced gap in $Nb_{0.18}Re_{0.82}$. As discussed in Sec. 2.2.5, when the triplet component in non-centrosymmetric superconductors is small, the two gaps may be fully gapped and of a similar magnitude. Resolving the gap structure in these materials may require the measurement of single crystals.

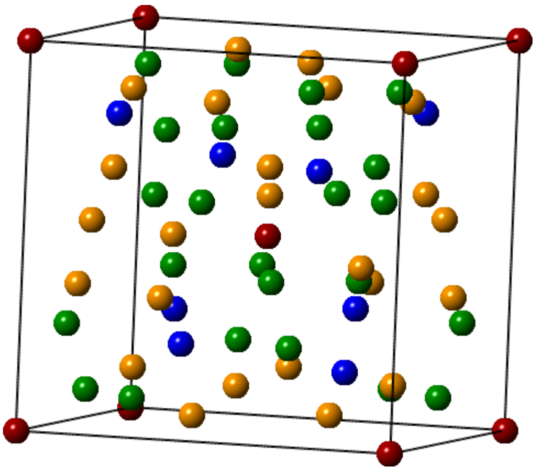

Figure 7.1: Crystal structure of $\mathrm{Nb}_x\mathrm{Re}_{1-x}$. Nb atoms belonging to the $2a$ and $8c$ sites are shown in blue and red respectively, while Re atoms occupying two $24g$ sites are shown in green and orange. This corresponds to $x = 0.17$.

In this chapter, measurements of single crystals of $\mathrm{Nb}_{0.18}\mathrm{Re}_{0.82}$ are reported. The composition with $x = 0.18$ was chosen due to this having the largest value of T_c [217]. Single crystals were grown using the floating zone technique, as described in Ref. [221]. The crystals were checked using x-ray Laue and aligned along the [100] direction. The superconducting properties were investigated using magnetic susceptibility, resistivity and specific heat measurements.

7.2 Magnetic susceptibility

The magnetic susceptibility of a single crystal of $\mathrm{Nb}_{0.18}\mathrm{Re}_{0.82}$ is shown in Fig. 7.2. The geometry of the aligned sample was such that the demagnetization factor could not be readily estimated. However, the inset shows the magnetic susceptibility of an unaligned piece with a more regular geometry, where the demagnetization factor was estimated from Ref. [123]. The fact that the zero field cooled curve reaches $4\pi\chi = -1.05$ at 2 K indicates complete flux expulsion from the sample. Therefore for the measurement of aligned sample, the demagnetization factor was adjusted so that $4\pi\chi = -1$ at 1.8 K. All the curves indicate an onset of superconductivity at around 8.8 K. The magnitude of the field cooled signal at low temperatures is larger than that reported in polycrystalline samples [219].

The magnetization as a function of field for low fields applied along [100] at several temperatures are shown in Fig. 7.3. The curves are initially linear with a

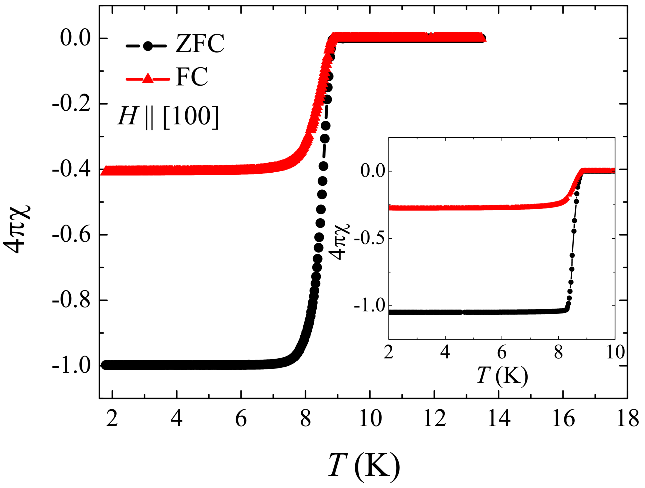

Figure 7.2: Temperature dependence of the magnetic susceptibility of a single crystal of $\mathrm{Nb}_{0.18}\mathrm{Re}_{0.82}$ in an applied field of 10 Oe. Zero-field cooled (ZFC) and field-cooled (FC) measurements are displayed. The inset shows the magnetic susceptibility of an unaligned piece with a regular geometry from which the demagnetization factor could be estimated.

gradient that indicates complete flux expulsion. When flux penetrates the sample, perfect diamagnetism is lost and the gradient decreases before the curves eventually turn up, as discussed in Sec. 2.2.3. On the right, the temperature dependence of H_{c1} is shown, obtained from the field at which the curves deviate from the initial slope. This field was scaled by a factor of $(1 - D)^{-1}$ to calculate H_{c1}. The data were fitted to Eq. 2.31 and $H_{\mathrm{c1}} = 55(2)$ Oe is obtained, in good agreement with Ref. [219].

A magnetization loop at 1.8 K is shown in Fig. 7.4. The main plot shows the magnetization between ±6.5 kOe while the inset shows it to ±50 kOe. For applied fields up to 50 kOe, a large diamagnetic signal is observed indicating that the system is still in the bulk superconducting state. However the magnetization becomes reversible in this region and remains so until around 5 kOe, when a hysteresis loop typical of a type-II superconductor opens. This indicates a significant weakening of the pinning in larger applied magnetic fields.

7.3 Resistivity and specific heat measurements

The resistivity of the single crystal of $\mathrm{Nb}_{0.18}\mathrm{Re}_{0.82}$ in fields up to 90 kOe applied along [100] are shown in Fig. 7.5. In zero-field, there is a sharp onset of supercon-

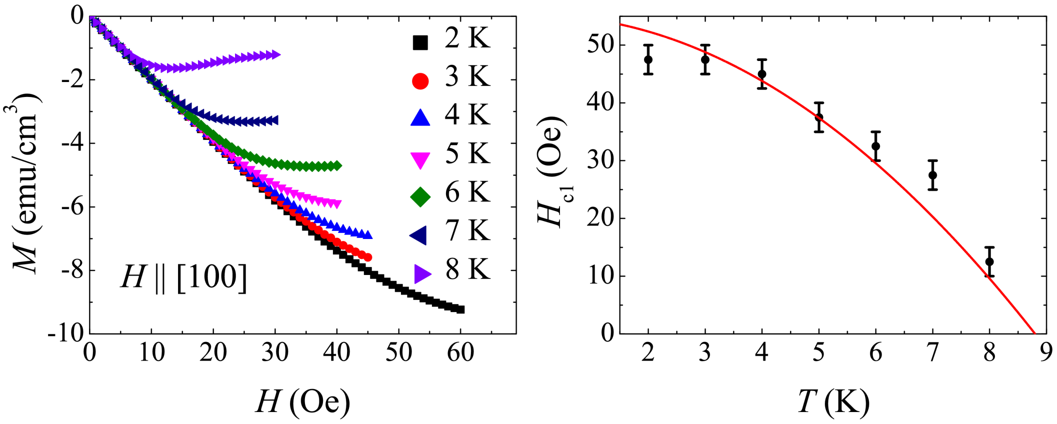

Figure 7.3: The left shows the magnetization as a function of field of a single crystal of $Nb_{0.18}Re_{0.82}$. Lower critical fields as a function of temperature are shown on the right, corrected with a demagnetization factor.

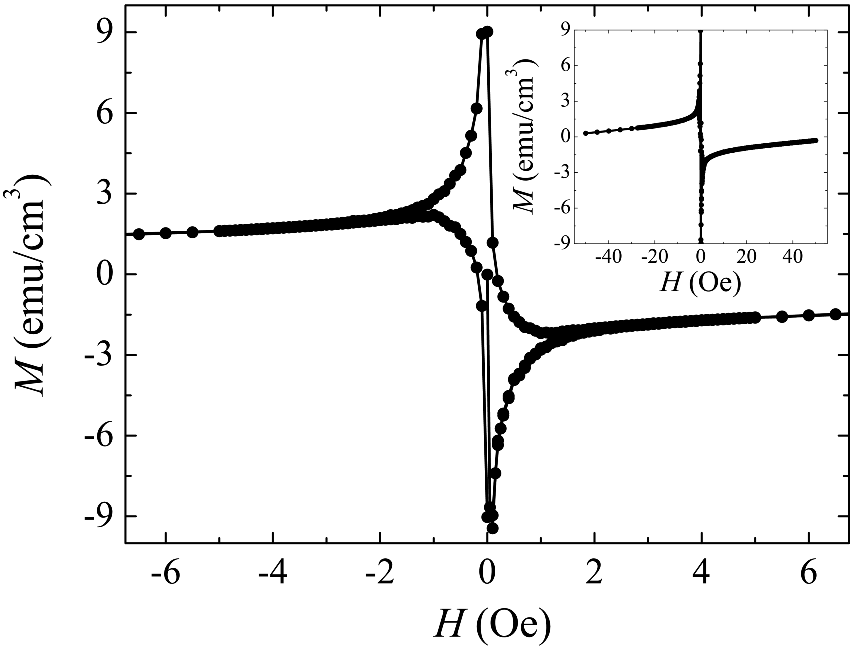

Figure 7.4: Magnetization as a function of applied field for a single crystal of $Nb_{0.18}Re_{0.82}$ at 1.8 K. The inset shows the measurements up to ±50 kOe

ductivity at 8.85 K, in good agreement with the magnetic susceptibility data. The transition is relatively sharp in zero-field apart from a distinct step feature with a width of about 0.05 K, beginning at 8.74 K. The resistivity of this plateau is at approximately 30% of the normal state value. Below this, the resistivity again sharply drops and zero resistivity is observed at around 8.6 K. Since T_c is very sensitive to the stoichiometry, this may reflect the presence of two regions with small compositional differences. For low applied fields, the step feature appears less distinct as the transition broadens. However, at large applied fields, an additional kink emerges which is strongest in the applied field of 90 kOe. This is observed at a different position to the previously discussed feature, occurring at around 80% of the normal state resistivity. It may be that there is a second step at low fields but this was not resolved due to the sharpness of the transition near the onset.

The upper critical field was estimated from the temperature of the onset of superconductivity ($T_\mathrm{c}^\mathrm{onset}$). This was performed by linearly extrapolating above and below the transition and $T_\mathrm{c}^\mathrm{onset}$ was taken as the point at which these lines intersect. The upper critical field for fields along [100] are shown in Fig. 7.6. The data were analyzed with the WHH model in the dirty limit. The dashed line shows a calculation of the WHH model with $\alpha_M = 0$. From Eq. 2.60, $H_\mathrm{P} = 164.6$ kOe for a BCS gap or 177.6 kOe using the gap from Ref. [217] are calculated. Therefore if the data were compatible with $\alpha_M = 0$, it may indicate an absence or significant suppression of Pauli paramagnetic limiting. The dashed curve was calculated using Eqs. 2.61 and 2.62 with $\alpha_M = 0$ and $B_\mathrm{c2}(0)$ is solely determined by the orbital limiting field (Eq. 2.63) of 169 kG. However, it can be seen that while there is good agreement with the values close to T_c, the observed values become increasingly lower than the dashed curve with decreasing temperature. This indicates that Pauli paramagnetic limiting is not absent in $\mathrm{Nb_{0.18}Re_{0.82}}$. The data could be fitted with a non-zero α_M and λ_so using Eqs. 2.61 and 2.64 and $\alpha_M = 1.51(2)$, and $\lambda_\mathrm{so} = 2.2(6)$ are obtained. This compares to the calculated value of $\alpha_M = 1.45$ obtained from the previously calculated values of $B_\mathrm{c2}^\mathrm{orb}$ and H_P. From the fitted curve, $B_\mathrm{c2}(0) = 148.4$ kG is calculated.

The specific heat of the $\mathrm{Nb_{0.18}Re_{0.82}}$ crystal is shown in Fig 7.7 in zero field and an applied field of 90 kOe. A jump in the specific heat in zero field indicates the onset of bulk superconductivity with $T_\mathrm{c} = 8.8$ K. In an applied field of 90 kOe, T_c is suppressed but a bulk superconducting transition is still observed indicating the robustness of the bulk superconductivity. C/T against T^2 is shown in the inset. Linear behaviour is not observed in the zero field data above T_c but could be fitted to the 90 kOe data from 5.8 to 8.8 K, giving $\gamma = 5.40(6)$ mJ/mol K^2

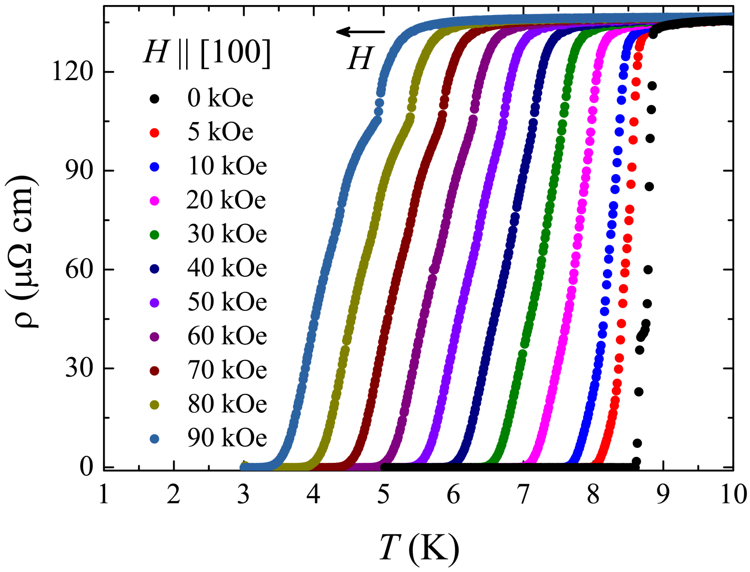

Figure 7.5: Resistivity against temperature of a single crystal of $\mathrm{Nb}_{0.18}\mathrm{Re}_{0.82}$ across the superconducting transition in applied fields up to 90 kOe along [100].

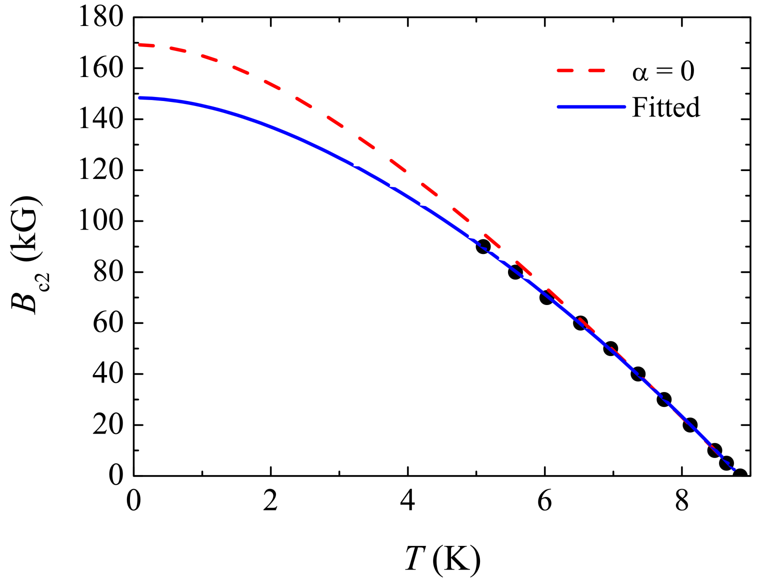

Figure 7.6: Temperature dependence of the upper critical field of a single crystal of $\mathrm{Nb}_{0.18}\mathrm{Re}_{0.82}$ for fields applied along [100]. The values were obtained from the onset of the resistive transition. The dashed line shows a calculation of B_{c2} using the WHH model with $\alpha_M = 0$, while the solid line shows a fit with non-zero α_M and λ_{so}.

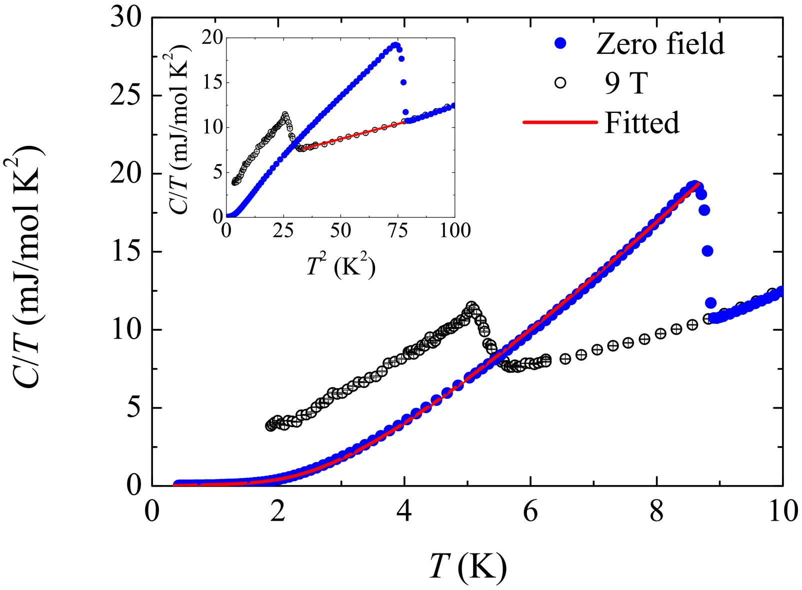

Figure 7.7: Temperature dependence of the specific heat of a single crystal of $Nb_{0.18}Re_{0.82}$ in zero field and an applied field of 90 kOe. The red curve shows a fit to a single gap, BCS model. The inset shows C/T against T^2 with a linear fit to the 90 kOe data in the normal state.

and $\beta = 0.0668(13)$ mJ/mol K^4. The solid curve shows a fit to the specific heat with an isotropic, one gap model. The electronic contribution to the specific heat was calculated using Eqs. 2.51 and 2.52. The β value was fixed from the fit to the 90 kOe data but γ was allowed to vary. Fitted values of $\gamma = 4.94(2)$ mJ/mol K^2 and $\alpha = 2.054(8)$ are obtained. A small constant background term of 0.015 was also fitted, which corresponds to a non-superconducting fraction of around 0.3 %. The jump in the specific heat at the transition is estimated to be $\Delta C = 82.53$ mJ/mol K, from which $\Delta C/\gamma T_c$ is calculated to be 1.91 and 1.75 for $\gamma = 4.94$ and 5.40 mJ/mol K^2 respectively. Using Eq. 2.53, α would be estimated to be 2.04 or 1.84 respectively. The former is close to the fitted value and slightly larger than that reported in Ref. [217].

7.4 Discussion and summary

The superconducting properties of a single crystal of $Nb_{0.18}Re_{0.82}$ have been characterized using magnetization, resistivity and specific heat measurements. Magnetic susceptibility measurements reveal the onset of bulk superconductivity at 8.8 K. The temperature dependence of H_{c1} was measured from low field magnetization data and

$H_{c1}(0) = 55(2)$ Oe was obtained. Magnetization loops as a function of field at 1.8 K, up to 50 kOe reveal that the magnetization becomes reversible above 5 kOe. This only corresponds to $\sim 4\%$ of the estimated value of B_{c2} at this temperature. This suggests that there is significantly weaker pinning of flux lines at higher fields. Similar behaviour was observed in the isostructural non-centrosymmetric phase of Re_3W, whereas the magnetization of the centrosymmetric phase only becomes reversible at higher fields [98].

The resistivity in zero-field shows a superconducting transition which onsets at around 8.85 K. Although the transition is relatively sharp, a step-like feature is observed. In field, the transitions broaden and the prominence of this feature is reduced. Under applied magnetic fields, an additional 'kink' is also observed which becomes more prominent at high fields. It may be that both these features arise from small inhomogeneities in the composition but it is not clear why one becomes more prominent and the other less prominent with increasing field. The temperature dependence of the upper critical field was obtained from the onset of the resistive transition. A calculation of the orbital limiting field overestimates B_{c2} at lower temperatures, indicating that Pauli paramagnetic limiting is not absent or greatly reduced. The data were fitted to the WHH model in the dirty limit and $\alpha_M = 1.51(2)$, and $\lambda_{so} = 2.2(6)$ were fitted, giving $B_{c2} = 148.4$ kG. A good fit could not be obtained with $\lambda_{so} = 0$, suggesting that the reduction of the Pauli limiting field due to spin-orbit scattering needs to be accounted for. However, the maximum field which could be applied was 90 kOe, which means that T_c could only be suppressed to $\sim$60% of the zero-field value. To more accurately determine the role of Pauli paramagnetic limiting and the applicability of the WHH model, it would be necessary to perform measurements in larger magnetic fields.

The specific heat was fitted with single gap BCS model. One difficulty is in accurately determining the normal state contribution of the specific heat. For example in Ref [217], C_{ph} was fitted with two higher order terms while in Ref. [219] linear behaviour was reported in C/T against T^2 up to temperatures of 50 K. In this work, linear behaviour was not observed in zero field measurements and as such C_{ph} was estimated from a linear fit to data in 90 kOe. γ was allowed to vary in the final fits of specific heat in the superconducting state, to allow for the possibility of an in field enhancement. A reasonable fit was obtained for one gap with $\alpha = 2.054(8)$, slightly larger than the value of 1.93 found in Ref [217]. Both values are consistent with moderately enhanced electron-phonon coupling. The fitted values of γ are 5.40 mJ/mol K^2 for the normal state in 90 kOe and 4.94 mJ/mol K^2 was fitted for the superconducting state, indicating a small enhancement.

It may be expected that a two gap structure would be present in noncentrosymmetric superconductors from Eq. 2.47, where the triplet component is sufficiently small that both gaps are fully gapped. Attempts were made to freely fit the data to a two gap model but a meaningful two band fit could not be obtained. However, point contact spectroscopy measurements of our single crystals indicate the presence of two superconducting gaps. An advantage of these measurements is that the presence of an additional gap is determined from fitting spectra at a given temperature, rather than from fitting the temperature dependence of a thermodynamic quantity. The two band model used to analyze the specific heat contained the sum of two terms from Eq. 2.52, each weighted by a fraction. Such a model neglects any interactions between the separate bands but has been successfully used to analyze several two gap systems [213]. Additional analysis is currently underway to look for a gap structure compatible with both specific heat and point contact spectroscopy measurements.

Chapter 8

Summary and conclusions

Non-centrosymmetric superconductors have been the subject of intense research due to the possibility of mixed parity pairing, where the superconducting state is not purely spin singlet or triplet but an admixture of the two. There has been particular focus on cerium based non-centrosymmetric superconductors such as the CeTX_3 (T = transition metal, X = Si or Ge) series where unconventional superconductivity has been observed in some compounds under pressure. In this work, examples of two approaches for understanding the behaviour of these compounds are given.

Firstly, ground state properties of the CeTX_3 compounds have been examined at ambient pressure. In chapter 4, μSR and inelastic neutron scattering measurements of polycrystalline CeCoGe$_3$, and neutron diffraction and magnetic susceptibility measurements were made on single crystals. CeCoGe$_3$ orders antiferromagnetically at T_{N1} = 21 K with two further transitions at T_{N2} = 12 K, T_{N3} = 8 K and becomes superconducting for $p >$ 5.5 GPa, a higher pressure than for the isostructural CeRhSi$_3$ and CeIrSi$_3$. The appearance of oscillations of the asymmetry in the μSR spectra indicate the onset of long range order in CeCoGe$_3$ between 20 and 21 K. Oscillations were observed down to 13 K and the temperature dependence of the internal field was fitted with a mean field model.

The magnetic structure in the three magnetic phases of CeCoGe$_3$ was clarified using single crystal neutron diffraction measurements. Propagation vectors of $\mathbf{k}$ = (0,0,$\frac{1}{2}$) below T_{N3}, $\mathbf{k}$ = (0,0,$\frac{5}{8}$) for $T_{\mathrm{N3}} \leq T < T_{\mathrm{N2}}$, and $\mathbf{k}$ = (0,0,$\frac{2}{3}$) for $T_{\mathrm{N2}} < T < T_{\mathrm{N1}}$ were deduced. An increase in intensity of the (110) reflection between T_{N1} and T_{N3} indicate a ferromagnetic component in these phases. The neutron diffraction data are compatible with an equal moment, two-up, two-down structure for $T < T_{\mathrm{N3}}$ and a two-up, one-down structure for $T_{\mathrm{N2}} < T < T_{\mathrm{N1}}$, with the magnetic moments lying along the c axis in all three phases.

INS measurements were used to study the CEF as well as the temperature dependence of the quasielastic scattering. A CEF scheme was found which was compatible with both the INS and magnetic susceptibility data. Previously a CEF scheme was suggested for $\mathrm{CeCoGe_3}$, with the ground state doublet consisting of the $|\pm\frac{1}{2}>$ states [60]. The INS data are incompatible with this scheme and our proposed CEF scheme has a ground state which is an admixture of $\left|\pm\frac{5}{2}\right\rangle$ and $\left|\mp\frac{3}{2}\right\rangle$ states and the magnetic moment is predicted to be 1.01 μ_{B}/Ce along c. However, the refined moment at 2 K is only 0.405(5) μ_{B}/Ce and this is evidence for a reduced ordered moment due to the Kondo effect. This is compared with $\mathrm{CeRhGe_3}$, where there is agreement between the predicted and observed moments [162] and with $\mathrm{CeRhSi_3}$, where there is a greater moment reduction. This suggests that the hybridization strength of $\mathrm{CeCoGe_3}$ is between that of $\mathrm{CeRhSi_3}$, which becomes superconducting for $p > 1.2$ GPa and $\mathrm{CeRhGe_3}$, which does not become superconducting up to 8 GPa, which is supported by comparing the linewidths of the CEF excitations. The Kondo temperature was estimated to be $T_{\mathrm{K}} = 11(3)$ K from the zero temperature value of the quasielastic linewidth.

In chapter 5, INS measurements are reported for $\mathrm{CePtSi_3}$, $\mathrm{CePdSi_3}$ and $\mathrm{CeRuSi_3}$. $\mathrm{CePtSi_3}$ and $\mathrm{CePdSi_3}$ both order antiferromagnetically and were studied using low energy INS. $\mathrm{CePdSi_3}$ has previously been reported to exhibit two magnetic transitions at 5.2 and 3 K from specific heat measurements [65], while magnetization, specific heat and resistivity measurements have been performed on $\mathrm{CePtSi_3}$. In this work, a linear dependence of the quasielastic linewidth was observed for both compounds and $T_{\mathrm{K}} = 6.0(2)$ and 5.56(5) K were obtained for $\mathrm{CePtSi_3}$ and $\mathrm{CePdSi_3}$ respectively. Higher energy INS measurements of $\mathrm{CePdSi_3}$ were performed and CEF levels were identified at around 5.5 and 31 meV. An unusual temperature dependence is also observed in the scattering of $\mathrm{CePdSi_3}$ in a broad region from about 13 to 24 meV. Between 5 and 75 K, there is very little change in the high $|\mathbf{Q}|$ scattering of $\mathrm{CePdSi_3}$ or the scattering of non-magnetic $\mathrm{LaPdSi_3}$. However, the low $|\mathbf{Q}|$ scattering of $\mathrm{CePdSi_3}$ significantly increases in this region and the origin of this behaviour is not clear.

$\mathrm{CeRuSi_3}$ is non-magnetic and the hybridization between the conduction and f electrons is believed to be sufficiently strong that magnetic order is entirely suppressed. Single crystals have previously been grown using the Czochralski method and the magnetic susceptibility displays a broad peak at around 150 K [194]. In this work, INS measurements of $\mathrm{CeRuSi_3}$ are also reported. At low temperatures, a maximum in the magnetic scattering is observed at inelastic positions which shifts to quasielastic scattering at 300 K. This behaviour is commonly observed in intermediate valence compounds. The magnetic scattering for $E_{\mathrm{i}} = 200$ meV could be well fitted with a Lorentzian function centred at (58.5 ± 1.4) meV with a linewidth of (31.9 ± 1.3) meV. The size of this hybridization gap relative to temperature of the peak in the magnetic susceptibility is larger than that observed in many heavy fermion compounds [196]. Interestingly, the data with $E_{\mathrm{i}} = 100$ meV displays evidence of additional structure to the magnetic scattering. The estimate of the magnetic scattering displays additional maxima at around 40 and 32 meV, with the latter feature being particularly narrow. Confirmation of additional structure would be particularly interesting as this may reflect the structure of the heavy hybridized bands believed to arise in Kondo lattice systems. There would be particular interest in studying the INS response of single crystals to confirm the presence of additional structure of the magnetic scattering and to characterize any $|\mathbf{Q}|$ dependence.

These results give some indication of the use of characterizing the ground states of compounds in the CeTSi$_3$ system at ambient pressure. Even though none of the aforementioned compounds become superconducting at ambient pressure, these measurements can help characterize the position of the compounds in the Doniach phase diagram and their proximity to the superconducting dome and quantum criticality. This has previously been understood for several compounds by plotting T_{N} and γ against unit cell volume and relating this behaviour to that expected from the Doniach model [63] (reproduced in Fig. 1.5). As discussed in Sec. 1.1.1, this does not correctly account for several CeTX_3 compounds and does not give much information about the relationship between magnetic order and the Kondo effect. For instance, it is interesting that previous studies of CeCoGe$_3$ appeared entirely consistent with antiferromagnetism with an entirely localized cerium moment. However, our INS measurements indicate that at this position of the phase diagram, there is a significant reduction in the ground state moment and broadening of the CEF levels due to the Kondo effect. It would be of interest to fully compare the INS response of CeCoGe$_3$ to that of CeRhSi$_3$ and CeIrSi$_3$, which are closer to quantum criticality and display incommensurate spin density wave magnetic structures.

A second approach towards understanding the superconducting behaviour of cerium based NCS is to study NCS without strong electronic correlations. The advantage of this approach is that the superconducting states of many of these systems are both easier to access and the effects of strong electronic correlations need not be taken into account. Although the mixing of singlet and triplet states should occur generically in NCS, the measurements of many weakly correlated NCS are consistent with single gap, s-wave BCS superconductivity. This is the case for both the measurements of LaPdSi$_3$ and LaPtSi$_3$ in chapter 6, and a single crystal of $\mathrm{Nb_{0.18}Re_{0.82}}$ in chapter 7. In the case of $\mathrm{Nb_{0.18}Re_{0.82}}$, the upper critical field is consistent with the WHH model in the presence of Pauli paramagnetic limiting, while the specific heat was fitted with an isotropic, single gapped model with a moderately enhanced gap ratio of $\alpha = 2.054(8)$. The results are similar those from polycrystalline samples, but the availability of single crystals means that a broader range of techniques such as point contact spectroscopy and small angle neutron scattering can be performed.

$\mathrm{LaPdSi_3}$ and $\mathrm{LaPtSi_3}$ are both NCS isostructural to the $\mathrm{Ce}TX_3$ compounds. Superconductivity had previously been reported in $\mathrm{LaPdSi_3}$, although the superconducting properties were not extensively characterized [65]. $\mathrm{LaPtSi_3}$ had been reported to be non-superconducting down to 2 K. In this work $\mathrm{LaPtSi_3}$ is reported to be a new superconductor with $T_\mathrm{c} = 1.52(6)$ K and the superconducting properties of both materials are investigated using magnetization, specific heat, resistivity and μSR measurements. The specific heat of both compounds are consistent with isotropic, s-wave superconductivity with an energy gap very close to that of weakly coupled BCS theory. A slightly smaller value of $\alpha = 1.60(8)$ is obtained from μSR measurements of $\mathrm{LaPtSi_3}$. Magnetic susceptibility, specific heat and μSR measurements reveal that $\mathrm{LaPdSi_3}$ is a type-I superconductor, while $\mathrm{LaPtSi_3}$ is a type-II material, with $\kappa = 2.49(4)$. Since both materials are believed to be dirty limit superconductors, this crossover from type-I to type-II may be driven by differences in the mean free path. Unlike the massive values observed in the isostructural cerium based compounds, the bulk upper critical field of $\mathrm{LaPtSi_3}$ is much lower than the Pauli limiting field, indicating the dominance of orbital pair breaking. The investigation of the properties of single crystals of single crystals of the weakly correlated $RT\mathrm{Si_3}$ superconductors would be desirable, both to directly look for evidence of anisotropy in the superconducting properties and because it would allow techniques such as point contact spectroscopy to be utilized.

Bibliography

[1] D. van Delft, Physica C **479**, 30 (2012).

[2] E. Maxwell, Phys. Rev. **78**, 477 (1950).

[3] C. A. Reynolds, B. Serin, W. H. Wright, and L. B. Nesbitt, Phys. Rev. **78**, 487 (1950).

[4] H. Fröhlich, Phys. Rev. **79**, 845 (1950).

[5] J. Bardeen, L. N. Cooper, and J. R. Schrieffer, Phys. Rev. **106**, 162 (1957).

[6] J. Bardeen, L. N. Cooper, and J. R. Schrieffer, Phys. Rev. **108**, 1175 (1957).

[7] G. K. Gaule, "Rules for the occurence of superconductivity among the elements, alloys and compounds," USAELRDL Technical Report 2329 (1963).

[8] D. Pines, Phys. Rev. **109**, 280 (1958).

[9] B. Matthias, V. Compton, and E. Corenzwit, J. Phys. Chem. Solids **19**, 130 (1961).

[10] R. Blaugher and J. Hulm, J. Phys. Chem. Solids **19**, 134 (1961).

[11] J. R. Waldram, *Superconductivity of Metals and Cuprates* (Institute of Physics Publishing, Bristol, 1996).

[12] F. Steglich, J. Aarts, C. D. Bredl, W. Lieke, D. Meschede, W. Franz, and H. Schäfer, Phys. Rev. Lett. **43**, 1892 (1979).

[13] F. Steglich, O. Stockert, S. Wirth, C. Geibel, H. Q. Yuan, S. Kirchner, and Q. Si, J. Phys.: Conf. Ser. **449**, 012028 (2013).

[14] M. R. Norman, ArXiv e-prints (2013), arXiv:1302.3176 .

[15] E. Bucher, J. P. Maita, G. W. Hull, R. C. Fulton, and A. S. Cooper, Phys. Rev. B **11**, 440 (1975).

[16] B. T. Matthias, C. W. Chu, E. Corenzwit, and D. Wohlleben, Proc. Natl. Acad. Sci. **64**, 459 (1969).

[17] F. Steglich, P. Gegenwart, C. Geibel, R. Helfrich, P. Hellmann, M. Lang, A. Link, R. Modler, G. Sparn, N. Büttgen, and A. Loidl, Physica B **223 - 224**, 1 (1996), proceedings of the International Conference on Strongly Correlated Electron Systems.

[18] G. M. Luke, A. Keren, K. Kojima, L. P. Le, B. J. Sternlieb, W. D. Wu, Y. J. Uemura, Y. Ōnuki, and T. Komatsubara, Phys. Rev. Lett. **73**, 1853 (1994).

[19] N. D. Mathur, F. M. Grosche, S. R. Julian, I. R. Walker, D. Freye, R. K. W. Haswelwimmer, and G. G. Lonzarich, Nature **394**, 39 (1998).

[20] A. J. Schofield, Physica Status Solidi B **247**, 563 (2010).

[21] H. Q. Yuan, F. M. Grosche, M. Deppe, C. Geibel, G. Sparn, and F. Steglich, Science **302**, 2104 (2003).

[22] J. Bednorz and K. Müller, Z. Phys. B **64**, 189 (1986).

[23] M. K. Wu, J. R. Ashburn, C. J. Torng, P. H. Hor, R. L. Meng, L. Gao, Z. J. Huang, Y. Q. Wang, and C. W. Chu, Phys. Rev. Lett. **58**, 908 (1987).

[24] A. Schilling, M. Cantoni, J. D. Guo, and H. R. Ott, Nature **363**, 56 (1993).

[25] L. Gao, Y. Y. Xue, F. Chen, Q. Xiong, R. L. Meng, D. Ramirez, C. W. Chu, J. H. Eggert, and H. K. Mao, Phys. Rev. B **50**, 4260 (1994).

[26] C. Petrovic, P. G. Pagliuso, M. F. Hundley, R. Movshovich, J. L. Sarrao, J. D. Thompson, Z. Fisk, and P. Monthoux, J. Phys. Condens. Matter **13**, L337 (2001).

[27] C. C. Tsuei and J. R. Kirtley, Rev. Mod. Phys. **72**, 969 (2000).

[28] Y. Kamihara, T. Watanabe, M. Hirano, and H. Hosono, J. Am. Chem. Soc. **130**, 3296 (2008).

[29] G. R. Stewart, Rev. Mod. Phys. **83**, 1589 (2011).

[30] W. Malaeb, T. Yoshida, A. Fujimori, M. Kubota, K. Ono, K. Kihou, P. M. Shirage, H. Kito, A. Iyo, H. Eisaki, Y. Nakajima, T. Tamegai, and R. Arita, J. Phys. Soc. Jpn. **78**, 123706 (2009).

[31] H. Q. Yuan, J. Singleton, F. F. Balakirev, S. A. Baily, G. F. Chen, J. L. Luo, and N. L. Wang, Nature **457**, 565 (2009).

[32] I. I. Mazin, D. J. Singh, M. D. Johannes, and M. H. Du, Phys. Rev. Lett. **101**, 057003 (2008).

[33] L. P. Gor'kov and E. I. Rashba, Phys. Rev. Lett. **87**, 037004 (2001).

[34] E. Bauer, G. Hilscher, H. Michor, M. Sieberer, E. Scheidt, A. Gribanov, Y. Seropegin, P. Rogl, W. Song, J.-G. Park, D. Adroja, A. Amato, M. Nicklas, G. Sparn, M. Yogi, and Y. Kitaoka, Czech. J. Phys. **54**, 401 (2004).

[35] E. Bauer, G. Hilscher, H. Michor, C. Paul, E. W. Scheidt, A. Gribanov, Y. Seropegin, H. Noël, M. Sigrist, and P. Rogl, Phys. Rev. Lett. **92**, 027003 (2004).

[36] E. Bauer and M. Sigrist, *Non-Centrosymmetric Superconductors: Introduction and Overview*, Lecture notes in physics (Springer-Verlag Berlin Heidelberg, 2012).

[37] N. Metoki, K. Kaneko, T. D. Matsuda, A. Galatanu, T. Takeuchi, S. Hashimoto, T. Ueda, R. Settai, Y. Ōnuki, and N. Bernhoeft, J. Phys. Condens. Matter **16**, L207 (2004).

[38] T. Willers, B. Fåk, N. Hollmann, P. O. Körner, Z. Hu, A. Tanaka, D. Schmitz, M. Enderle, G. Lapertot, L. H. Tjeng, and A. Severing, Phys. Rev. B **80**, 115106 (2009).

[39] A. Amato, E. Bauer, and C. Baines, Phys. Rev. B **71**, 092501 (2005).

[40] K. Izawa, Y. Kasahara, Y. Matsuda, K. Behnia, T. Yasuda, R. Settai, and Y. Ōnuki, Phys. Rev. Lett. **94**, 197002 (2005).

[41] T. Takeuchi, T. Yasuda, M. Tsujino, H. Shishido, R. Settai, H. Harima, and Y. Ōnuki, J. Phys. Soc. Jpn. **76**, 014702 (2007).

[42] R. L. Ribeiro, I. Bonalde, Y. Haga, R. Settai, and Y. nuki, J. Phys. Soc. Jpn. **78**, 115002 (2009).

[43] M. Yogi, H. Mukuda, Y. Kitaoka, S. Hashimoto, T. Yasuda, R. Settai, T. D. Matsuda, Y. Haga, Y. nuki, P. Rogl, and E. Bauer, Journal of the Physical Society of Japan **75**, 013709 (2006).

[44] P. W. Anderson, Phys. Rev. B **30**, 4000 (1984).

[45] P. A. Frigeri, D. F. Agterberg, A. Koga, and M. Sigrist, Phys. Rev. Lett. **92**, 097001 (2004).

[46] D. F. Agterberg, P. A. Frigeri, R. P. Kaur, A. Koga, and M. Sigrist, Physica B **378-380**, 351 (2006), Proceedings of the International Conference on Strongly Correlated Electron Systems 2005".

[47] N. Kimura, K. Ito, K. Saitoh, Y. Umeda, H. Aoki, and T. Terashima, Phys. Rev. Lett. **95**, 247004 (2005).

[48] I. Sugitani, Y. Okuda, H. Shishido, T. Yamada, A. Thamizhavel, E. Yamamoto, T. D. Matsuda, Y. Haga, T. Takeuchi, R. Settai, and Y. Ōnuki, J. Phys. Soc. Jpn. **75**, 043703 (2006).

[49] R. Settai, I. Sugitani, Y. Okuda, A. Thamizhavel, M. Nakashima, Y. Ōnuki, and H. Harima, J. Magn. Magn. Mater. **310**, 844 (2007).

[50] F. Honda, I. Bonalde, S. Yoshiuchi, Y. Hirose, T. Nakamura, K. Shimizu, R. Settai, and Y. Ōnuki, Physica C **470, Supplement 1**, S543 (2010).

[51] N. Kimura, Y. Muro, and H. Aoki, J. Phys. Soc. Jpn. **76**, 051010 (2007).

[52] Y. Muro, D. Eom, N. Takeda, and M. Ishikawa, J. Phys. Soc. Jpn. **67**, 3601 (1998).

[53] N. Aso, H. Miyano, H. Yoshizawa, N. Kimura, T. Komatsubara, and H. Aoki, J. Magn. Magn. Mater. **310**, 602 (2007).

[54] T. Terashima, Y. Takahide, T. Matsumoto, S. Uji, N. Kimura, H. Aoki, and H. Harima, Phys. Rev. B **76**, 054506 (2007).

[55] T. Terashima, M. Kimata, S. Uji, T. Sugawara, N. Kimura, H. Aoki, and H. Harima, Phys. Rev. B **78**, 205107 (2008).

[56] Y. Muro, M. Ishikawa, K. Hirota, Z. Hiroi, N. Takeda, N. Kimura, and H. Aoki, J. Phys. Soc. Jpn. **76**, 033706 (2007).

[57] N. Egetenmeyer, J. L. Gavilano, A. Maisuradze, S. Gerber, D. E. MacLaughlin, G. Seyfarth, D. Andreica, A. Desilets-Benoit, A. D. Bianchi, C. Baines, R. Khasanov, Z. Fisk, and M. Kenzelmann, Phys. Rev. Lett. **108**, 177204 (2012).

[58] T. Ohkochi, T. Toshimitsu, H. Yamagami, S.-i. Fujimori, A. Yasui, Y. Takeda, T. Okane, Y. Saitoh, A. Fujimori, Y. Miyauchi, Y. Okuda, R. Settai, and Y. nuki, J. Phys. Soc. Jpn. **78**, 084802 (2009).

[59] N. Aso, M. Takahashi, H. Yoshizawa, H. Iida, N. Kimura, and H. Aoki, J. Phys. Soc. Jpn **80**, 095004 (2011).

[60] A. Thamizhavel, T. Takeuchi, T. D. Matsuda, Y. Haga, K. Sugiyama, R. Settai, and Y. Ōnuki, J. Phys. Soc. Jpn. **74**, 1858 (2005).

[61] A. Thamizhavel, H. Shishido, Y. Okuda, H. Harima, T. D. Matsuda, Y. Haga, R. Settai, and Y. Ōnuki, J. Phys. Soc. Jpn. **75**, 044711 (2006).

[62] I. Sheikin, P. Rodiere, R. Settai, and Y. Ōnuki, J. Phys. Soc. Jpn. **80**, SA020 (2011).

[63] T. Kawai, H. Muranaka, M.-A. Measson, T. Shimoda, Y. Doi, T. D. Matsuda, Y. Haga, G. Knebel, G. Lapertot, D. Aoki, J. Flouquet, T. Takeuchi, R. Settai, and Y. Ōnuki, J. Phys. Soc. Jpn. **77**, 064716 (2008).

[64] T. Kawai, Y. Okuda, H. Shishido, A. Thamizhavel, T. D. Matsuda, Y. Haga, M. Nakashima, T. Takeuchi, M. Hedo, Y. Uwatoko, R. Settai, and Y. nuki, J. Phys. Soc. Jpn. **76**, 014710 (2007).

[65] J. Kitagawa, Y. Muro, N. Takeda, and M. Ishikawa, J. Phys. Soc. Jpn. **66**, 2163 (1997).

[66] T. Kawai, M. Nakashima, Y. Okuda, H. Shishido, T. Shimoda, T. D. Matsuda, Y. Haga, T. Takeuchi, M. Hedo, Y. Uwatoko, R. Settai, and Y. nuki, J. Phys. Soc. Jpn. **76**, 166 (2007).

[67] S. Doniach, Physica B+C **91**, 231 (1977).

[68] N. Kimura, K. Ito, H. Aoki, S. Uji, and T. Terashima, Phys. Rev. Lett. **98**, 197001 (2007).

[69] R. Settai, Y. Miyauchi, T. Takeuchi, F. Lévy, I. Sheikin, and Y. Ōnuki, J. Phys. Soc. Jpn. **77**, 073705 (2008).

[70] Y. Tada, N. Kawakami, and S. Fujimoto, Phys. Rev. Lett. **101**, 267006 (2008).

[71] Y. Tada, N. Kawakami, and S. Fujimoto, Physica Status Solidi B **247**, 621 (2010).

[72] P. A. Frigeri, D. F. Agterberg, and M. Sigrist, New J. Phys. **6**, 115 (2004).

[73] T. Akazawa, H. Hidaka, T. Fujiwara, T. C. Kobayashi, E. Yamamoto, Y. Haga, R. Settai, and Y. Ōnuki, J. Phys. Condens. Matter **16**, L29 (2004).

[74] J. S. Kim, D. J. Mixson, D. J. Burnette, T. Jones, P. Kumar, B. Andraka, G. R. Stewart, V. Craciun, W. Acree, H. Q. Yuan, D. Vandervelde, and M. B. Salamon, Phys. Rev. B **71**, 212505 (2005).

[75] S. Fujimoto, J. Phys. Soc. Jpn. **75**, 083704 (2006).

[76] S. Fujimoto, J. Phys. Soc. Jpn. **76**, 051008 (2007).

[77] J. Chen and H. Q. Yuan, J. Phys.: Conf. Ser. **400**, 022010 (2012).

[78] K. Togano, P. Badica, Y. Nakamori, S. Orimo, H. Takeya, and K. Hirata, Phys. Rev. Lett. **93**, 247004 (2004).

[79] P. Badica, T. Kondo, and K. Togano, J. Phys. Soc. Jpn **74**, 1014 (2005).

[80] H. Takeya, K. Hirata, K. Yamaura, K. Togano, M. El Massalami, R. Rapp, F. A. Chaves, and B. Ouladdiaf, Phys. Rev. B **72**, 104506 (2005).

[81] H. Takeya, M. ElMassalami, S. Kasahara, and K. Hirata, Phys. Rev. B **76**, 104506 (2007).

[82] H. Q. Yuan, D. F. Agterberg, N. Hayashi, P. Badica, D. Vandervelde, K. Togano, M. Sigrist, and M. B. Salamon, Phys. Rev. Lett. **97**, 017006 (2006).

[83] M. Nishiyama, Y. Inada, and G.-q. Zheng, Phys. Rev. Lett. **98**, 047002 (2007).

[84] S. P. Mukherjee and T. Takimoto, Phys. Rev. B **86**, 134526 (2012).

[85] W. Lee, H. Zeng, Y. Yao, and Y. Chen, Physica C: Superconductivity **266**, 138 (1996).

[86] I. Bonalde, R. L. Ribeiro, K. J. Syu, H. H. Sung, and W. H. Lee, New J. Phys. **13**, 123022 (2011).

[87] J. Chen, L. Jiao, J. L. Zhang, Y. Chen, L. Yang, M. Nicklas, F. Steglich, and H. Q. Yuan, New J. Phys. **15**, 053005 (2013).

[88] A. D. Hillier, J. Quintanilla, and R. Cywinski, Phys. Rev. Lett. **102**, 117007 (2009).

[89] M. Sigrist, AIP Conf. Proc. **789**, 165 (2005).

[90] J. Quintanilla, A. D. Hillier, J. F. Annett, and R. Cywinski, Phys. Rev. B **82**, 174511 (2010).

[91] A. D. Hillier, J. Quintanilla, B. Mazidian, J. F. Annett, and R. Cywinski, Phys. Rev. Lett. **109**, 097001 (2012).

[92] A. D. Hillier, B. Mazidian, J. Quintanilla, J. F. Annett, D. M. Paul, G. Balakrishnan, and M. R. Lees, Phys. Rev. Lett. **112**, 107002 (2014).

[93] B. Joshi, A. Thamizhavel, and S. Ramakrishnan, Phys. Rev. B **84**, 064518 (2011).

[94] M. Mondal, B. Joshi, S. Kumar, A. Kamlapure, S. C. Ganguli, A. Thamizhavel, S. S. Mandal, S. Ramakrishnan, and P. Raychaudhuri, Phys. Rev. B **86**, 094520 (2012).

[95] L. Jiao, J. L. Zhang, Y. Chen, Z. F. Weng, Y. M. Shao, J. Y. Feng, X. Lu, B. Joshi, A. Thamizhavel, S. Ramakrishnan, and H. Q. Yuan, Phys. Rev. B **89**, 060507 (2014).

[96] T. Shibayama, M. Nohara, H. A. Katori, Y. Okamoto, Z. Hiroi, and H. Takagi, J. Phys. Soc. Jpn. **76**, 073708 (2007).

[97] K. Wakui, S. Akutagawa, N. Kase, K. Kawashima, T. Muranaka, Y. Iwahori, J. Abe, and J. Akimitsu, J. Phys. Soc. Jpn. **78**, 034710 (2009).

[98] P. K. Biswas, M. R. Lees, A. D. Hillier, R. I. Smith, W. G. Marshall, and D. M. Paul, Phys. Rev. B **84**, 184529 (2011).

[99] C. S. Lue, H. F. Liu, C. N. Kuo, P. S. Shih, J.-Y. Lin, Y. K. Kuo, M. W. Chu, T.-L. Hung, and Y. Y. Chen, Supercond. Sci. Technol. **26**, 055011 (2013).

[100] K. Miliyanchuk, F. Kneidinger, C. Blaas-Schenner, D. Reith, R. Podloucky, P. Rogl, T. Khan, L. Salamakha, G. Hilscher, H. Michor, E. Bauer, and A. D. Hillier, Journal of Physics: Conference Series **273**, 012078 (2011).

[101] E. Bauer, R. T. Khan, H. Michor, E. Royanian, A. Grytsiv, N. Melnychenko-Koblyuk, P. Rogl, D. Reith, R. Podloucky, E.-W. Scheidt, W. Wolf, and M. Marsman, Phys. Rev. B **80**, 064504 (2009).

[102] G. Eguchi, D. C. Peets, M. Kriener, Y. Maeno, E. Nishibori, Y. Kumazawa, K. Banno, S. Maki, and H. Sawa, Phys. Rev. B **83**, 024512 (2011).

[103] V. K. Anand, A. D. Hillier, D. T. Adroja, A. M. Strydom, H. Michor, K. A. McEwen, and B. D. Rainford, Phys. Rev. B **83**, 064522 (2011).

[104] M.-A. Méasson, H. Muranaka, T. Matsuda, T. Kawai, Y. Haga, G. Knebel, D. Aoki, G. Lapertot, F. Honda, R. Settai, J.-P. Brison, J. Flouquet, K. Shimizu, and Y. Ōnuki, Physica C **470, Supplement 1**, S536 (2010).

[105] J. Chen, M. B. Salamon, S. Akutagawa, J. Akimitsu, J. Singleton, J. L. Zhang, L. Jiao, and H. Q. Yuan, Phys. Rev. B **83**, 144529 (2011).

[106] G. Amano, S. Akutagawa, T. Muranaka, Y. Zenitani, and J. Akimitsu, Journal of the Physical Society of Japan **73**, 530 (2004).

[107] S. Kuroiwa, Y. Saura, J. Akimitsu, M. Hiraishi, M. Miyazaki, K. H. Satoh, S. Takeshita, and R. Kadono, Phys. Rev. Lett. **100**, 097002 (2008).

[108] P. K. Biswas, A. D. Hillier, M. R. Lees, and D. M. Paul, Phys. Rev. B **85**, 134505 (2012).

[109] S. Blundell, *Magnetism in Condensed Matter*, Oxford Master Series In Condensed Matter (Oxford University Press, Oxford, 2001).

[110] M. Matsumoto, M. J. Han, J. Otsuki, and S. Y. Savrasov, Phys. Rev. Lett. **103**, 096403 (2009).

[111] K. W. H. Stevens, Proceedings of the Physical Society. Section A **65**, 209 (1952).

[112] M. Hutchings, in *Solid State Physics: Advances in Research and Applications*, Vol. 16, edited by F. Seitz and D. Turnbull (Academic Press, 1964) pp. 227 – 273.

[113] G. Marusi, N. V. Mushnikov, L. Pareti, M. Solzi, and A. E. Ermakov, J. Phys. Condens. Matter **2**, 7317 (1990).

[114] A. Thamizhavel, H. Nakashima, T. Shiromoto, Y. Obiraki, T. D. Matsuda, Y. Haga, S. Ramakrishnan, T. Takeuchi, R. Settai, and Y. Ōnuki, J. Phys. Soc. Jpn. **74**, 2617 (2005).

[115] J. Jensen and A. Mackintosh, *Rare Earth Magnetism: Structures and Excitations*, International series of monographs on physics (Clarendon Press, Oxford, 1991).

[116] D. I. Khomskii, *Basic Aspects of the Quantum Theory of Solids: Order and Elementary Excitations* (Cambridge University Press, Cambridge, 2010).

[117] J. R. Schrieffer and P. A. Wolff, Phys. Rev. **149**, 491 (1966).

[118] P. Coleman, in *Handbook of Magnetism and Advanced Magnetic Materials*, edited by H. Kronmüller and S. Parkin (John Wiley and Sons, 2004).

[119] G. R. Stewart, Rev. Mod. Phys. **56**, 755 (1984).

[120] Q. Si and F. Steglich, Science **329**, 1161 (2010).

[121] W. Meissner and R. Ochsenfeld, Naturwissenschaften **21**, 787 (1933).

[122] M. Cyrot and P. D., *Introduction to Superconductivity and High-Tc Materials* (World Scientific Publishing, Singapore, 2010).

[123] A. Aharoni, J. Appl. Phys **83**, 3432 (1998).

[124] E. H. Brandt, Phys. Rev. B **68**, 054506 (2003).

[125] A. A. Abrikosov, Sov. Phys. JETP **5**, 1174 (1957).

[126] W. H. Kleiner, L. M. Roth, and S. H. Autler, Phys. Rev. **133**, A1226 (1964).

[127] A. Maisuradze, R. Khasanov, A. Shengelaya, and H. Keller, J. Phys. Condens. Matter **21**, 075701 (2009).

[128] E. H. Brandt, Rep. Prog. Phys. **58**, 1465 (1995).

[129] E. H. Brandt, Physica B **404**, 695 (2009).

[130] L. P. Gor'kov, Sov. Phys. JETP **36**, 1364 (1959).

[131] L. P. Lèvy, *Magnetism and Superconductivity* (Springer-Verlag Berlin Heidelberg, 2000).

[132] L. N. Cooper, Phys. Rev. **104**, 1189 (1956).

[133] B. Mühlschlegel, Z. Phys. **155**, 313 (1959).

[134] A. Carrington and F. Manzano, Physica C **385**, 205 (2003).

[135] H. Padamsee, J. Neighbor, and C. Shiffman, J. Low Temp. Phys. **12**, 387 (1973).

[136] D. C. Johnston, Supercond. Sci. Technol. **26**, 115011 (2013).

[137] W. L. McMillan, Phys. Rev. **167**, 331 (1968).

[138] M. Sigrist, AIP Conf. Proc. **789**, 165 (2005).

[139] A. P. Mackenzie and Y. Maeno, Physica B **280**, 2148 (2000).

[140] M. Sigrist, AIP Conf. Proc. **1162** (2009).

[141] M. Sigrist, D. Agterberg, P. Frigeri, N. Hayashi, R. Kaur, A. Koga, I. Milat, K. Wakabayashi, and Y. Yanase, J. Magn. Magn. Mater. **310**, 536 (2007).

[142] P. A. Frigeri, D. F. Agterberg, I. Milat, and M. Sigrist, Eur. Phys. B **54**, 435 (2006).

[143] C. Kittel, *Introduction to Solid State Physics*, 7th ed. (John Wiley and Sons, New York, 1996).

[144] F. Bouquet, Y. Wang, R. A. Fisher, D. G. Hinks, J. D. Jorgensen, A. Junod, and N. E. Phillips, Europhys. Lett. **56**, 856 (2001).

[145] J. B. Ketterson and S. N. Song, *Superconductivity* (Cambridge University Press, Cambridge, 1999).

[146] P. K. Biswas, G. Balakrishnan, D. M. Paul, C. V. Tomy, M. R. Lees, and A. D. Hillier, Phys. Rev. B **81**, 092510 (2010).

[147] M. Tinkham, *Introduction to Superconductivity*, 2nd ed. (McGraw-Hill, New York, 1996).

[148] A. M. Clogston, Phys. Rev. Lett. **9**, 266 (1962).

[149] N. R. Werthamer, E. Helfand, and P. C. Hohenberg, Phys. Rev. **147**, 295 (1966).

[150] B. H. Toby, Powder Diffr. **21**, 67 (2006).

[151] A. Coelho, *TOPAS-Academic* (Coelho Software, Brisbane, 2007).

[152] B. H. Toby, J. Appl. Cryst. **34**, 210 (2001).

[153] J. Rodrìguez-Carvajal, Physica B **192**, 55 (1993).

[154] B. T. M. Willis and C. J. Carlile, *Experimental Neutron Scattering* (Oxford University Press, Oxford, 2009).

[155] T. Hahn, ed., *International Tables for Crystallography*, 4th ed. (Kluwer Academic Publishers, Dordrecht, 1995).

[156] A. Wills, J. Phys. IV France **11**, 133 (2001).

[157] A. Wills, Physica B **276-278**, 680 (2000).

[158] G. L. Squires, *Introduction to the Theory of Thermal Neutron Scattering*, 3rd ed. (Cambridge University Press, Cambridge, 2012).

[159] E. Bauer, Adv. Phys. **40**, 417 (1991).

[160] K. W. Becker, P. Fulde, and J. Keller, Z. Phys. B **28**, 9 (1977).

[161] A. Krimmel, A. Severing, A. Murani, A. Grauel, and S. Horn, Physica B **180-181**, 191 (1992).

[162] A. D. Hillier, D. T. Adroja, P. Manuel, V. K. Anand, J. W. Taylor, K. A. McEwen, B. D. Rainford, and M. M. Koza, Phys. Rev. B **85**, 134405 (2012).

[163] E. D. Bauer, A. D. Christianson, J. M. Lawrence, E. A. Goremychkin, N. O. Moreno, N. J. Curro, F. R. Trouw, J. L. Sarrao, J. D. Thompson, R. J. McQueeney, W. Bao, and R. Osborn, J. Appl. Phys. **95**, 7201 (2004).

[164] P. C. Canfield and Z. Fisk, Philos. Mag. B **65**, 1117 (1992).

[165] R. C. Weast and M. J. Astle, *Handbook of Chemistry and Physics*, 62nd ed. (CRC Press, Florida, 1981).

[166] M. McElfresh, "Fundamentals of magnetism and magnetic measurements," Quantum Design.

[167] N. Shirakawa, H. Horinouchi, and Y. Yoshida, J. Magn. Magn. Mater. **272-276, Supplement**, E149 (2004), proceedings of the International Conference on Magnetism (ICM 2003).

[168] J. Lashley, M. Hundley, A. Migliori, J. Sarrao, P. Pagliuso, T. Darling, M. Jaime, J. Cooley, W. Hults, L. Morales, D. Thoma, J. Smith, J. Boerio-Goates, B. Woodfield, G. Stewart, R. Fisher, and N. Phillips, Cryogenics **43**, 369 (2003).

[169] `http://www.ill.eu/instruments-support/instruments-groups/instruments/d10/`.

[170] `http://www.ill.eu/instruments-support/instruments-groups/instruments/in6`.

[171] S. J. Blundell, Contemp. Phys. **40**, 175 (1999).

[172] A. Yaouanc and M. Dalmas de Rèotier, *Muon Spin Rotation, Relaxation and Resonance*, International Series of Monographs on Physics 147 (Oxford University Press, Oxford, 2011).

[173] K. Nagamine, *Introductory Muon Science* (Cambridge University Press, Cambridge, 2003).

[174] V. K. Pecharsky, O.-B. Hyun, and K. A. Gschneidner, Phys. Rev. B **47**, 11839 (1993).

[175] K. Kaneko, N. Metoki, T. Takeuchi, T. D. Matsuda, Y. Haga, A. Thamizhavel, R. Settai, and Y. Ōnuki, J. Phys.: Conf. Ser. **150**, 042082 (2009).

[176] A. Das, R. K. Kremer, R. Pöttgen, and B. Ouladdiaf, Physica B **378-380**, 837 (2006).

[177] G. Knebel, D. Aoki, G. Lapertot, B. Salce, J. Flouquet, T. Kawai, H. Muranaka, R. Settai, and Y. Ōnuki, J. Phys. Soc. Jpn. **78**, 074714 (2009).

[178] M. Mizoo, T. Nishioka, H. Kato, and M. Matsumura, J. Phys.: Conf. Ser. **273**, 012009 (2011).

[179] D. Eom, M. Ishikawa, J. Kitagawa, and N. Takeda, J. Phys. Soc. Jpn. **67**, 2495 (1998).

[180] K. Kanai, T. Terashima, D. H. Eom, M. Ishikawa, and S. Shin, Phys. Rev. B **60**, R9900 (1999).

[181] V. Krishnamurthy, K. Nagamine, I. Watanabe, K. Nishiyama, S. Ohira, M. Ishikawa, D. Eom, and T. Ishikawa, Physica B **289-290**, 47 (2000).

[182] K. Kanai, T. Terashima, D. Eom, M. Ishikawa, and S. Shin, Physica B **281-282**, 734 (2000).

[183] V. V. Krishnamurthy, K. Nagamine, I. Watanabe, K. Nishiyama, S. Ohira, M. Ishikawa, D. H. Eom, T. Ishikawa, and T. M. Briere, Phys. Rev. Lett. **88**, 046402 (2002).

[184] M.-A. Méasson, H. Muranaka, T. Kawai, Y. Ota, K. Sugiyama, M. Hagiwara, K. Kindo, T. Takeuchi, K. Shimizu, F. Honda, R. Settai, and Y. Ōnuki, J. Phys. Soc. Jpn. **78**, 124713 (2009).

[185] A. Schenck, in *Muon Science*, edited by S. L. Lee, S. H. Kilcoyne, and R. Cywinski (Taylor and Francis, New York, 1999).

[186] P. Seiden, Physics Letters A **28**, 239 (1968).

[187] N. Bykovetz, A. Hoser, J. Klein, C. L. Lin, and M. S. Seehra, J. Appl. Phys. **111**, 07E145 (2012).

[188] F. L. Pratt, J. Phys. Condens. Matter **19**, 456207 (2007).

[189] S. Maekawa, S. Kashiba, S. Takahashi, and M. Tachiki, J. Magn. Magn. Mater. **52**, 149 (1985).

[190] D. Schmitt, J. Phys. F: Met. Phys. **9**, 1745 (1979).

[191] D. Schmitt, J. Phys. F: Met. Phys. **9**, 1759 (1979).

[192] B. Rainford, D. Adroja, A. Neville, and D. Fort, Physica B: Proceedings of the International Conference on Strongly Correlated Electron Systems **206-207**, 209 (1995).

[193] D. T. Adroja, A. D. Hillier, V. K. Anand, E. A. Goremychkin, K. A. McEwen, B. D. Rainford, V. V. Krishnamurthy, and G. Balakrishnan, ISIS Facility Experimental Report, RB820238 (2009).

[194] T. Kawai, H. Muranaka, M.-A. Measson, T. Shimoda, Y. Doi, T. D. Matsuda, Y. Haga, G. Knebel, G. Lapertot, D. Aoki, J. Flouquet, T. Takeuchi, R. Settai, and Y. Ōnuki, J. Phys. Soc. Jpn. **77**, 064716 (2008).

[195] T. Kawai, *Split Fermi Surface Properties and Superconductivity in the Non-centrosymmetric Crystal Structure*, Ph.D. thesis, University of Osaka (2008).

[196] D. T. Adroja, K. A. McEwen, J. G. Park, A. D. Hillier, N. Takeda, P. S. Riseborough, and T. Takabatake, J. Optoelectron. Adv. M. **10**, 1564 (2008).

[197] M. Bouvier, P. Lethuillier, and D. Schmitt, Phys. Rev. B **43**, 13137 (1991).

[198] P. S. Riseborough, Adv. Phys. **49**, 257 (2000).

[199] R. Viennois, L. Girard, L. C. Chapon, D. T. Adroja, R. I. Bewley, D. Ravot, P. S. Riseborough, and S. Paschen, Phys. Rev. B **76**, 174438 (2007).

[200] R. Viennois, D. Ravot, F. Terki, C. Hernandez, S. Charar, P. Haen, S. Paschen, and F. Steglich, J. Magn. Magn. Mater. **272 - 276, Supplement**, E113 (2004), proceedings of the International Conference on Magnetism (ICM 2003).

[201] V. R. Fanelli, *Inelastic Neutron Scattering Study of the Intermediate Valence Compounds CePd3 and YbAl3*, Ph.D. thesis, University of California, Irvine (2009).

[202] J. M. Lawrence, P. S. Riseborough, C. H. Booth, J. L. Sarrao, J. D. Thompson, and R. Osborn, Phys. Rev. B **63**, 054427 (2001).

[203] D. T. Adroja, J.-G. Park, E. A. Goremychkin, K. A. McEwen, N. Takeda, B. D. Rainford, K. S. Knight, J. W. Taylor, J. Park, H. C. Walker, R. Osborn, and P. S. Riseborough, Phys. Rev. B **75**, 014418 (2007).

[204] R. Osborn, E. A. Goremychkin, I. L. Sashin, and A. P. Murani, J. Appl. Phys. **85**, 5344 (1999).

[205] A. D. Christianson, V. R. Fanelli, J. M. Lawrence, E. A. Goremychkin, R. Osborn, E. D. Bauer, J. L. Sarrao, J. D. Thompson, C. D. Frost, and J. L. Zarestky, Phys. Rev. Lett. **96**, 117206 (2006).

[206] C. Carlile and M. Adams, Physica B **182**, 431 (1992).

[207] D. T. Adroja, A. del Moral, C. de la Fuente, A. Fraile, E. A. Goremychkin, J. W. Taylor, A. D. Hillier, and F. Fernandez-Alonso, Phys. Rev. Lett. **108**, 216402 (2012).

[208] N. Kumar, S. K. Dhar, A. Thamizhavel, P. Bonville, and P. Manfrinetti, Phys. Rev. B **81**, 144414 (2010).

[209] B. Rainford and G. Daniell, Hyperfine Interact. **87**, 1129 (1994).

[210] A. C. Hannon, Nuclear Instruments and Methods in Physics Research Section A: Accelerators, Spectrometers, Detectors and Associated Equipment **551**, 88 (2005).

[211] J. Faber and T. Fawcett, Acta Cryst. **B58**, 325 (2002).

[212] V. K. Anand, H. Kim, M. A. Tanatar, R. Prozorov, and D. C. Johnston, Phys. Rev. B **87**, 224510 (2013).

[213] M. Zehetmayer, Supercond. Sci. Technol. **26**, 043001 (2013).

[214] G. Eguchi, F. Kneidinger, L. Salamakha, S. Yonezawa, Y. Maeno, and E. Bauer, J. Phys. Soc. Jpn. **81**, 074711 (2012).

[215] E. Bucher, F. Heiniger, J. Muheim, and J. Muller, Rev. Mod. Phys. **36**, 146 (1964).

[216] A. Knapton, J. Less-Common Met. **1**, 480 (1959).

[217] J. Chen, L. Jiao, J. L. Zhang, Y. Chen, L. Yang, M. Nicklas, F. Steglich, and H. Q. Yuan, Phys. Rev. B **88**, 144510 (2013).

[218] R. Steadman and P. M. Nuttall, Acta Cryst. **17**, 62 (1964).

[219] A. B. Karki, Y. M. Xiong, N. Haldolaarachchige, S. Stadler, I. Vekhter, P. W. Adams, D. P. Young, W. A. Phelan, and J. Y. Chan, Phys. Rev. B **83**, 144525 (2011).

[220] C. S. Lue, T. H. Su, H. F. Liu, and B.-L. Young, Phys. Rev. B **84**, 052509 (2011).

[221] R. P. Singh, M. Smidman, M. R. Lees, D. M. Paul, and G. Balakrishnan, J. Cryst. Growth **361**, 129 (2012).